

General Disclaimer

One or more of the Following Statements may affect this Document

- This document has been reproduced from the best copy furnished by the organizational source. It is being released in the interest of making available as much information as possible.
- This document may contain data, which exceeds the sheet parameters. It was furnished in this condition by the organizational source and is the best copy available.
- This document may contain tone-on-tone or color graphs, charts and/or pictures, which have been reproduced in black and white.
- This document is paginated as submitted by the original source.
- Portions of this document are not fully legible due to the historical nature of some of the material. However, it is the best reproduction available from the original submission.



(NASA-CR-134830) TWO-STAGE, LOW NOISE
ADVANCED TECHNOLOGY FAN. 4: AERODYNAMIC
FINAL REPORT (Pratt and Whitney Aircraft)
177 p HC \$7.50

CSCl 21E

N76-26197

Unclassified
42229

G3/07

TWO-STAGE, LOW NOISE ADVANCED TECHNOLOGY FAN
IV. AERODYNAMIC FINAL REPORT

by

K.G. Harley and M.J. Keenan

PRATT & WHITNEY AIRCRAFT DIVISION
UNITED TECHNOLOGIES CORPORATION

September 1975



prepared for

NATIONAL AERONAUTICS AND SPACE ADMINISTRATION
NASA-LEWIS RESEARCH CENTER
CONTRACT NAS3-16811

1. Report No. NASA CR-134830	2. Government Accession No.	3. Recipient's Catalog No.	
4. Title and Subtitle Two-Stage, Low Noise Advanced Technology Fan IV. Aerodynamic Final Report		5. Report Date September 1975	
6. Performing Organization Code		7. Author(s) K. G. Harley and M. J. Keenan	
8. Performing Organization Report No. PWA-5304		9. Performing Organization Name and Address Pratt & Whitney Aircraft Division United Technologies Corporation East Hartford, Connecticut 06108	
10. Work Unit No.		11. Contract or Grant No. NAS3-16811	
12. Sponsoring Agency Name and Address National Aerodynamics and Space Administration Washington, D.C. 20546		13. Type of Report and Period Covered Contractor Report	
14. Sponsoring Agency Code			
15. Supplementary Notes Final Report (Aerodynamics) -- Program Manager: L. J. Herrig, Fluid System Components Division Technical Advisor: M. F. Heidmann, V/STOL and Noise Division NASA-Lewis Research Center, Cleveland, Ohio 44135			
16. Abstract A two-stage research fan was tested to provide technology for designing a turbofan engine for an advanced, long range commercial transport having a cruise Mach number of 0.85 - 0.9 and a noise level 20 EPNdB below current requirements. The fan design tip speed was 365.8 m/sec [1200 ft/sec]; the hub/tip ratio was 0.4; the design pressure ratio was 1.9; and the design specific flow was 209.2 kg/sec/m ² [42.85 lbm/sec/ft ²]. Two fan-versions were tested: a baseline configuration, and an acoustically treated configuration with a sonic inlet device. The baseline version was tested with uniform inlet flow and with tip-radial and hub-radial inlet flow distortions. The baseline fan with uniform inlet flow attained an efficiency of 86.4% at design speed, but the stall margin was low. Tip-radial distortion increased stall margin 4 percentage points at design speed and reduced peak efficiency one percentage point. Hub-radial distortion decreased stall margin 4 percentage points at all speeds and reduced peak efficiency at design speed 8 percentage points. At design speed, the sonic inlet in the cruise position reduced stall margin one percentage point and efficiency 1.5 to 4.5 percentage points. The sonic inlet in the approach position reduced stall margin 2 percentage points.			
17. Key Words (Suggested by Author(s)) Quiet Fan Two-Stage Fan Aerodynamic Performance Low Tip Speed		18. Distribution Statement Commercial Transport 0.9 Cruise Mach Number Unclassified - Unlimited	
19. Security Classif. (of this report) Unclassified	20. Security Classif. (of this page) Unclassified	21. No. of Pages 177	22. Price*

FOREWORD

The work described herein was conducted by the Pratt & Whitney Aircraft Division of United Technologies Corporation for the National Aeronautics and Space Administration, Lewis Research Center, under NASA Contract NAS3-16811. The program was completed under the management of NASA Project Managers Messrs. L. J. Herrig and W. L. Beede, Fluid System Components Division and Mr. W. A. Benser, Assistant Branch Chief. The Pratt & Whitney Aircraft Program Manager was Mr. H. V. Marman and the Assistant Program Manager was Mr. P. A. Odegard.

TABLE OF CONTENTS

	Page
SUMMARY	1
INTRODUCTION	2
APPARATUS AND PROCEDURE	3
TWO-STAGE FAN RIG	3
Aerodynamic Design	3
Velocity Vectors	4
Airfoil Design	4
Structural Design	6
Fan Inlet Design	7
TEST FACILITY	7
INSTRUMENTATION AND CALIBRATION	8
DATA REDUCTION TECHNIQUES	12
Performance Parameter Calculations	12
TEST PROCEDURE	14
RESULTS AND DISCUSSION	16
BASELINE CONFIGURATION	16
Uniform Inlet Flow	16
Radially Distorted Inlet Flow	23
STALL INVESTIGATION	25
ACOUSTICALLY TREATED CONFIGURATION	29
Performance of the Sonic Inlet Device	29
System Performance of Fan and Sonic Inlet	32
Performance of Fan Alone	33
Exit Duct Loss	33
REMARKS	34
SUMMARY OF RESULTS	34
APPENDIX	
SYMBOLS AND PARAMETERS	37
REFERENCES	43
DISTRIBUTION LIST	171

LIST OF ILLUSTRATIONS

Figure	Title	Page
1	Two-Stage Fan, Baseline Configuration	45
2	Baseline Standard and Sonic Inlet Geometries	45
3	Aerial View of Outdoor Test Facility	46
4	Schematic of Fan Rig, Gas Generator and Free-Turbine	46
5	Typical Instrumentation	47
6	Axial Location of Instrumentation and Calculation Planes	48
7	Circumferential Location of Instrumentation	49
8	Fan Overall Performance With Uniform Inlet Flow	50
9	Fan Overall Performance at Design Speed With Uniform Inlet Flow	51
10	First-Stage Performance With Uniform Inlet Flow	51
11	First-Stage Rotor Performance With Uniform Inlet Flow	52
12	Pressure Coefficient and Adiabatic Efficiency <i>VERSUS FLOW</i> Coefficient for Uniform Inlet Flow, First Stage	53
13	Pressure Coefficient and Adiabatic Efficiency Versus Flow Coefficient for Uniform Inlet Flow, First-Stage Rotor	54
14	Pressure Coefficient and Adiabatic Efficiency Versus Flow Coefficient for Uniform Inlet Flow, Second Stage	55
15	Pressure Coefficient and Adiabatic Efficiency Versus Flow Coefficient for Uniform Inlet Flow, Second-Stage Rotor	56
16	Stator Total Pressure Recovery Versus Stator Inlet Corrected Flow	57
17	Fan Overall Pressure Ratio and Efficiency Versus Span for Near Design Data Points	58
18	Rotor and Stage Pressure Ratio Versus Span for Near Design Data Points	59
19	Rotor and Stage Efficiency Versus Span for Near Design Data Points	60

LIST OF ILLUSTRATIONS (Cont'd)

Figure	Title	Page
20	Blade Row Inlet Meridional Velocity Versus Span for Near Design Points	61
21	Spanwise Distribution of Loss Coefficient, Diffusion Factor, and Deviation and Incidence Angles for Near Design Data Point, First-Stage Rotor	62
22	Spanwise Distributions of Loss Coefficient, Diffusion Factor, and Deviation and Incidence Angles for Near Design Data Point, First-Stage Stator	63
23	Spanwise Distributions of Loss Coefficient, Diffusion Factor, and Deviation and Incidence Angles for Near Design Data Point, Second-Stage Rotor	64
24	Spanwise Distributions of Loss Coefficient, Diffusion Factor, and Deviation and Incidence Angles for Near Design Data Point, Second-Stage Stator	65
25	Spanwise Distribution of Loss for the First-Stage Rotor and a Similar Low Speed Rotor	66
26	Calculated Flow Velocity on Suction Surface and Pressure Surfaces at the Hub of the First-Stage Rotor and a Similar Low Speed Rotor	66
27	Blade-Element Performance, Baseline Configuration, Uniform Inlet Flow – First-Stage Rotor	67
28	Blade-Element Performance, Baseline Configuration, Uniform Inlet Flow – First-Stage Stator	78
29	Blade-Element Performance, Baseline Configuration, Uniform Inlet Flow – Second-Stage Rotor	89
30	Blade-Element Performance, Baseline Configuration, Uniform Inlet Flow – Second-Stage Stator	99
31	Hub and Tip Radial-Distortion Screens	109
32	Fan Inlet Total Pressure Ratio Versus Span for Radially Distorted Inlet Flow	110
33	Inlet Total Pressure Distortion Parameter Versus Inlet Flow for Radial Distortions	111
34	Fan Overall Performance With Tip Radially Distorted Inlet Flow	111

LIST OF ILLUSTRATIONS (Cont'd)

Figure	Title	Page
35	First-Stage Performance With Tip Radially Distorted Inlet Flow	112
36	Blade Row Inlet Meridional Velocity Versus Span for Tip Radially Distorted Inlet Flow	113
37	Fan Overall Pressure Ratio Versus Span for Tip Radially Distorted Inlet Flow	114
38	Blade-Element Performance, Baseline Configuration, Tip Radially Distorted Inlet Flow — First-Stage Rotor	115
39	Blade-Element Performance, Baseline Configuration, Tip Radially Distorted Inlet Flow — First-Stage Stator	120
40	Blade-Element Performance, Baseline Configuration, Tip Radially Distorted Inlet Flow — Second-Stage Rotor	125
41	Blade-Element Performance, Baseline Configuration, Tip Radially Distorted Inlet Flow — Second-Stage Stator	130
42	Fan Overall Performance With Hub Radially Distorted Inlet Flow	135
43	First-Stage Performance With Hub Radially Distorted Inlet Flow	136
44	Blade Row Inlet Meridional Velocity Versus Span for Hub Radially Distorted Inlet Flow	137
45	Overall Fan and First-Stage Pressure Ratio Versus Span for Hub Radially Distorted Inlet Flow	138
46	Hot-Film Traces at Stator Inlets, Uniform Inlet Flow, Baseline Configuration, 90 Percent of Design Speed	139
47	Strain-Gage Traces of Blade During Uniform Inlet Flow, Baseline Configuration, 100 Percent of Design Speed	140
48	Hot-Film Traces at Stator Inlets, Uniform Inlet Flow, 50 Percent of Design of Speed	141
49	Hot-Film Traces at Stator Inlets, Tip Radially Distorted Inlet Flow, 100 Percent of Design Speed	142
50	Hot-Film Traces at Stator Inlets, Tip Radially Distorted Inlet Flow, 63 Percent of Design Speed	143

LIST OF ILLUSTRATIONS (Cont'd)

Figure	Title	Page
51	Diffusion Factor of First-Stage Rotor and Stator Versus Weight Flow, Baseline Configuration, Uniform Inlet Flow, 13 Percent Span	144
52	Calculated Meridional Velocity Along Inner and Outer Casing Wall, Baseline Configuration, Uniform Inlet Flow	145
53	Inner Casing Wall Loading Between the First-Stage Rotor and First-Stage Stator and Between the First-Stage Stator and Second-Stage Rotor, Baseline Configuration, Uniform Inlet Flow	146
54	Radial Distributions of Pressure Recoveries of the Baseline and Sonic Configurations	147
55	Measured Mass Averaged Recovery of Sonic Inlet	148
56	Axial Distribution of Static Pressure on the Sonic Inlet – Throat Mach Number 1.0	149
57	Axial Distribution of Static Pressure on the Inner and Outer Surface of the Sonic Inlet – Throat Mach Number Subsonic	150
58	Power Spectral Density Measured Downstream of the Sonic Inlet, Approach Configuration, 0.9 Throat Mach Number, Three Percent Span From Hub	151
59	Radial Distribution of Turbulence Levels Measured Downstream of Sonic Inlet	152
60a	System Performance of Fan and Sonic Inlet Compared to Baseline (Shakedown) – Approach Sonic Inlet Position	153
60b	System Performance of Fan and Sonic Inlet Compared to Baseline (Shakedown) – Takeoff Sonic Inlet Position	154
60c	System Performance of Fan and Sonic Inlet Compared to Baseline (Shakedown) – Cruise Sonic Position	155
61	Stall Line Comparison With and Without Sonic Inlet	156
62a	Fan Alone Performance Considering Sonic Inlet as Source of Distortion Compared to Baseline (Shakedown) – Approach Sonic Position	157
62b	Fan Alone Performance Considering Sonic Inlet as Sources of Distortion Compared to Baseline (Shakedown) – Takeoff Sonic Inlet Position	158

LIST OF ILLUSTRATIONS (Cont'd)

Figure	Title	Page
62c	Fan Alone Performance Considering Sonic Inlet as Source of Distortion Compared to Baseline (Shakedown) — Cruise Sonic Inlet Position	159
63	Stall Line of Fan Only, Showing Effect of Sonic Inlet	160
64	Rotor and Stage Pressure Ratio Versus Span for a Near Design Point With Sonic Inlet in Cruise Position	161
65	Rotor and Stage Efficiency Versus Span for a Near Design Point With Sonic Inlet in Cruise Position	162
66	Spanwise Distribution of Loss Coefficient, Diffusion Factor, and Deviation and Incidence Angles for Data Point During Cruise Sonic Inlet Tests — First-Stage Rotor	163
67	Spanwise Distribution of Loss Coefficient, Diffusion Factor, and Deviation and Incidence Angles for Data Point During Cruise Sonic Inlet Tests — First-Stage Stator	164
68	Spanwise Distribution of Loss Coefficient, Diffusion Factor, and Deviation and Incidence Angles for Data Point During Cruise Sonic Inlet Tests — Second-Stage Rotor	165
69	Spanwise Distribution of Loss Coefficient, Diffusion Factor, and Deviation and Incidence Angles for Data Point During Cruise Sonic Inlet Tests — Second-Stage Stator	166
70	Fan Overall Pressure Ratio and Adiabatic Efficiency for Near Design Point With Sonic Inlet in Cruise Position	167
71	Overall Performance of Fan Alone at Design Speed Comparing Tests of Check Run, Shakedown, Performance, and Cruise Sonic Inlet	168
72	Fan Discharge Duct Recovery With and Without Acoustic Ring and Treatment	169
73	Spanwise Recovery of Fan Discharge Duct, Showing Effect of Acoustic Ring and Treatment	169

LIST OF TABLES

Table	Title	Page
I	General Design Parameters	3
II	Blade and Vane Geometry Parameters	5
III	Performance and Blade Element Instrumentation	9
IV	Transient Data Instrumentation	11
V	Parameters Input to Flowfield Program	13
VI	Maximum Blade-Element Diffusion Factors Near Stall at Design Speed Compared to Other Fans	27
VII	Comparison of Design Maximum Wall Loading Parameters	28
VIII	Inlet Total Pressure Recoveries Compared to Design Predictions	30

TWO-STAGE, LOW NOISE ADVANCED TECHNOLOGY FAN

IV. AERODYNAMIC FINAL REPORT

K. G. Harley and M. J. Keenan

SUMMARY

This report presents the results of a test program to demonstrate a fan for a turbofan engine for a commercial long-range advanced technology transport (ATT) aircraft having a cruise Mach number between 0.85 and 0.9 with the potential of achieving noise levels of FAR 36 minus 15 to 20 EPNdB. An earlier study had determined that the optimum fan for this application was a low tip speed, low hub tip ratio, two-stage fan having a pressure ratio of 1.9. In this study it was predicted that the basic unsuppressed engine installation noise characteristics would meet FAR Part 36 limits. A noise level of 20 EPNdB below FAR 36 limits was predicted with advanced technology inlet and discharge duct acoustic suppression and use of special aircraft noise-abatement flight operations.

Previous fan noise work by both NASA and Pratt & Whitney Aircraft have shown that fan noise is dependent on both fan tip speed and blade loading. A low design tip speed and low blade loadings result in low generated noise levels over the entire fan operating range. To obtain the fan pressure ratios required for optimum cycles, single-stage fans must either be designed for moderate tip speed with high blade loading, or moderate blade loading with high tip speed. Performance, noise, and economic analyses showed that a two-stage fan is the preferred approach. A major objective of this program was to verify predicted low noise levels for a two-stage fan having a low fan tip speed and moderate blade loadings, plus application of effective inlet and discharge acoustical treatment.

A 0.836m [32.9 in.] diameter scaled version of the fan was built and tested. The overall pressure ratio of 1.9 was broken down into a 1.46 pressure ratio first stage and a 1.30 pressure ratio second stage. The hub/tip ratio was 0.4, the 1st-stage rotor design tip speed was 365.8 m/sec [1200 ft/sec], and the design specific flow was 209.2 kg/sec/m² [42.85 lbm/sec/ft²]. The fan also incorporated noise control design features including: large blade-vane axial spacings, no inlet guide vane, and selected numbers of blades and vanes to provide cut-off of fundamental rotor blade frequencies.

Two versions of the fan were tested: 1) a baseline configuration having standard inlet cowling, and 2) an acoustically treated configuration having an inlet device that could be adjusted to obtain sonic inlet flow for approach and takeoff, and provide high flow capacity for cruise conditions.

The baseline fan with the standard inlet cowling attained an efficiency of 86.4% at design speed, but stalled before reaching the design pressure ratio. This premature stall was due either to excessive aerodynamic loading on the hub wall between the 1st-stage rotor and stator, poor flow conditions in the 1st-stage rotor hub region, or a combination of these factors. Above 90% of design speed the stall line fell below the design operating line. A 20% stall margin was measured at 63% of design speed. Attempts to improve the stall

margin by restaggering the 1st-stage stator open five degrees were only marginally successful. Fan pressure ratio at design speed increased from 1.87 to 1.90, but fan efficiency decreased 1.5 percentage points. Maximum corrected flow at design speed exceeded design flow. The pressure ratio-flow characteristic would have passed very near the design point if it were not for the premature stall.

At design speed, a 0.155 ($\Delta P/P_{max}$) tip-radial distortion resulted in a stall margin 4% over the stall limit with uniform inlet flow, and reduced peak efficiency one percentage point. At 63% of design speed, tip-radial distortion reduced the stall margin appreciably. The tip distortion was completely attenuated, principally by the first stage.

A 0.17 ($\Delta P/P_{max}$) hub-radial distortion reduced stall margin at all speeds when compared to the stall limit for uniform inlet flow. Fan peak efficiency at design speed also was reduced eight percentage points. The hub distortion was partially attenuated, principally by the second stage.

At design speed, the sonic inlet device in the cruise position penalized system efficiency from 1.5 percentage points near stall to 4.5 percentage points at open throttle. The total pressure recovery of the sonic inlet device in the cruise position was 0.9819 near stall and 0.9796 at open throttle. The effects of the sonic inlet on the stall margin of the fan would have been acceptable if the fan had achieved its design stall margin.

Total pressure recovery of the acoustically treated exit duct with the acoustic ring and wall treatment was 0.9655. This was approximately 1.3% below the recovery for the untreated duct.

Based on the tests reported herein, the concept of low tip speed and blade loading in a two-stage fan design and its performance objectives are considered achievable. The tests demonstrated that fan flow and efficiency goals were met and the sonic inlet device reduced inlet noise without causing unacceptable performance penalties. A higher stall margin could be obtained by redesigning the hub region of the first stage where stalls originated.

INTRODUCTION

A fan research program has been conducted by P&WA for the NASA-Lewis Research Center under Contract NAS3-16811. The purpose of the program was to develop fan technology for application in turbofan engines for an advanced long-range commercial transport with a cruise Mach number between 0.85 and 0.9 and a noise level 20 EPNdB below current requirements (i.e., FAR 36 minus 20 EPNdB). To achieve these goals with only minimum weight and performance penalties, fans included in such engines must incorporate features both to minimize the generation of noise and to obtain the maximum suppression of the noise generated.

The optimum fan for such a transport was established in an earlier study (ref. 1). The study showed the optimum configuration to be a low tip-speed, two-stage fan with a low hub/tip ratio, a pressure ratio of approximately 1.9, and a tip speed of 365.8 m/sec [1200 ft/sec].

To document the aerodynamic and acoustic performance of the fan, a 0.836 m [32.90 in.] diameter scale-model of the fan was designed, fabricated, and tested. The fan incorporated several important noise control features that had been employed in single-stage fans, but had never been fully applied to two-stage designs. These features included moderate tip speed and pressure rise per stage, absence of inlet guide vanes, substantial spacing between rotors and stators, and proper relationships of the number of rotor blades and stator vanes. The rig was designed to permit the vane angles to be reset on the stand. The rig was also designed to allow the blade-vane spacings to be changed, but this capability was not utilized during the program. Other noise suppression features included use of acoustic treatment in the interstage casing walls, a fan discharge duct with treated walls and a treated splitter-ring, and a sonic inlet device employing a translating centerbody. Details of these design features are presented in reference 2.

The aerodynamic performance data were obtained for a baseline, essentially untreated configuration and for a version of the fan having full noise-suppression equipment. The aerodynamic performance data obtained from the tests are presented and discussed in this report. Overall aerodynamic performance and blade-element data tabulations and data relating to turbulence levels generated by the sonic inlet are provided in reference 3. The acoustic data are presented in reference 4, and the acoustic results are discussed in reference 5.

Symbols and parameters appearing in this report are defined in the appendix.

APPARATUS AND PROCEDURE

TWO-STAGE FAN RIG

Aerodynamic Design

The fan configuration (Figure 1) was influenced by acoustic considerations as much as by aerodynamic considerations. Design features to reduce noise included low tip speeds, moderate blade loadings, proper relationships between numbers of blades and vanes, and axial spacings of two aerodynamic chord lengths between blade rows. Because of the low tip-speeds and moderate loadings, two stages were required to provide the desired pressure ratio. A summary of the general design parameters is provided in Table I.

TABLE I - GENERAL DESIGN PARAMETERS

Corrected Speed, $NA\sqrt{\theta}$ = 8367 rpm [876.2 rad/sec]

Corrected Flow, $W\sqrt{\theta/\delta}$ = 96.39 kg/sec [212.5 lbm/sec]

Specific Corrected Flow, $W\sqrt{\theta/\delta}/A = 209.2 \text{ kg/sec/m}^2$ [42.85 lbm/sec/ft²]

Tip Diameter = 0.836 meters [32.90 inches]

Hub-Tip Ratio = 0.4

Tip Speed = 365.8 m/sec [1200 ft/sec]

TABLE I - GENERAL DESIGN PARAMETERS (Cont'd)

	Pressure Ratio		Adiabatic Efficiency (%)	
	Local	Cumulative	Local	Cumulative
Rotor 1	1.485	1.485	89.5	89.5
Stator 1	0.984	1.461	—	85.6
Rotor 2	1.317	1.924	90.9	87.3
Stator 2	0.987	1.898	—	85.3

Velocity Vectors

The fan was designed with a constant tip diameter to allow the entire flowpath convergence to be taken on the hub to prevent excessive hub-loadings; to reduce the large past-axial turnings inherent in a low speed, low hub/tip ratio rotor; and to facilitate possible future changes in blade row spacing. The 1st-stage rotor was designed to turn the flow approximately 30 degrees past axial at the hub, and the 2nd-stage rotor was designed for no past-axial turning. The fan exit flow (stator 2 exit) was axial, and the designed exit Mach number was approximately 0.45. Design velocity vectors and flow conditions were calculated by means of a streamline analysis computation system which provided an axisymmetric, compressible flow solution of continuity, energy, and radial equilibrium equations. Streamline curvature, enthalpy, and entropy gradient terms were included in the equilibrium equation; viscosity terms were neglected. Flow blockages were used to account for boundary layers on flowpath walls and for the presence of the partspan shroud on each rotor. Blockages were applied equally to all stream tubes at calculation stations. Design velocity vectors and overall performance parameters are included in the design blade-element data given in reference 2.

Airfoil Design

A summary of rotor and stator blade parameters is provided in Table II.

Ratios of numbers-of-blades to numbers-of-vanes were selected to prevent propagation of blade-vane interaction noise. Because of the large number of vanes relative to the number of blades, the stators had higher aspect ratios and solidities than the rotors. The hub chord lengths were determined primarily by mechanical considerations, and the tip chord lengths were chosen to provide the desired solidity levels. The airfoil series were selected for low loss at design Mach numbers.

TABLE II – BLADE AND VANE GEOMETRY PARAMETERS

	Rotor 1	Stator 1	Rotor 2	Stator 2
Number of Airfoils	28	62	35	76
Airfoil Series ¹	MCA	MCA	MCA	65/CA
Aspect Ratio ²	2.75	5.03	2.54	3.89
Aspect Ratio ³	2.19	3.81	2.21	3.73
Taper Ratio ⁴	1.232	1.099	1.028	0.9709
Hub Chord - meter [inch]	0.0897 [3.530]	0.0513 [2.020]	0.0859 [3.382]	0.0489 [1.930]
Tip Chord - meter [inch]	0.1105 [4.350]	0.0564 [2.220]	0.0883 [3.476]	0.0475 [1.8707]
Tip Solidity	1.18	1.33	1.18	1.38
Hub Solidity	2.28	2.50	2.14	2.46

NOTES: 1 MCA (multiple-circular-arc) and 65/CA (circular-arc mean line with a 65 series thickness distribution)

2 Average length/axially projected hub chord

3 Average length/chord at tip

4 Tip chord/hub chord

ROTOR BLADE DESIGN

Multiple-circular-arc (MCA) airfoils were selected for the rotor blades based on successful experience with these airfoils in the transonic and high subsonic Mach number regimes. Maximum-thickness to chord ratios were selected to provide mechanical stability while maintaining an adequate flow area in the channels between blades. Rotor leading and trailing edge metal angles were determined by applying incidence and deviation criteria to the design inlet and exit relative flow-angles. When the inlet relative Mach number exceeded one, the airfoil section was designed with an incidence angle of approximately 1.5 degrees to the suction surface at a point halfway between the leading edge and the point from which a Mach wave emanated that met the leading edge of the following blade (ref. 6). Subsonic sections were designed with incidence angles that were consistent with low loss data from previous tests and also provided smooth distributions of blade geometry. Design deviation-angles were calculated using a P&WA cascade system modified by correction factors based on applicable rotor test data. Design incidence and deviation angles are included in the design blade-element data given in reference 2. Channels between adjacent blades were sized to provide sufficient flow capacity while allowing rotor sections to operate near minimum loss. The design minimum critical-area ratio (A/A^*) in channels of both rotors was set at approximately 1.03 over

most of the span. Additional area was provided near partspan shrouds to compensate for the shroud blockage. Tabulations of rotor airfoil geometry on conical surfaces approximating design streamlines of revolution are provided in reference 2.

STATOR VANE DESIGN

In order to minimize the propagation of blade-vane interaction noise, the number of vanes for each stator was selected in accordance with the relationship $s=2r + 6$ where s is the number of vanes in the stator and r is the number of blades in the preceding rotor. This relationship is based on the Tyler-Sofrin criterion (ref. 7) which states that if the number of stator vanes is greater than twice the number of rotor blades, interaction noise generated at subsonic tip-speeds will decay within the inlet and exit ducts of a fan.

High stator vane aspect ratios were used to avoid excessive solidity. Blade thickness-to-chord ratios were selected which were somewhat higher than in previous NASA fans in order to satisfy flutter criteria at these high aspect ratios. MCA airfoils were used for the 1st-stage stator to provide the control of channel areas necessary for low loss at the high subsonic Mach numbers encountered at the hub. The 2nd-stage stator was designed with 65/CA vanes (circular arc meanlines with 65 series thickness distribution) since this vane operates at Mach numbers below 0.65, a regime where 65/CA airfoils have low losses. Stator leading and trailing edge metal angles for both stators were based on the P&WA cascade system modified by correction factors based on applicable test data. Design incidence and deviation angles are included in the design blade-element data given in reference 2.

Minimum values of critical-area ratio (A/A^*) in channels between 1st-stage stator vanes were determined using a correlation of capture-area/throat-area at minimum loss as a function of stator inlet Mach number (ref. 6). Channel area was not considered a critical design parameter for the lower Mach number, 2nd-stage stator vanes. Tabulations of stator airfoil geometry on design conical surfaces are provided in reference 2.

Structural Design

The structural design included calculation of blade-disk frequencies and resonances with rig excitations, steady-state stresses, blade and vane flutter parameters, rig critical speeds, and full rotor system response due to imbalance. The materials chosen were:

ITEM	MATERIAL
1st-stage blade	AMS 4973F (Titanium alloy)
2nd-stage blade	AMS 4928 (Titanium alloy)
1st-stage and 2nd-stage vanes	AMS 5613 (Stainless steel)
disks, hubs, spacer, and seals	AMS 5616 (Stainless steel)

Partspan shrouds were required on both rotors to avoid first bending resonances with one and with two excitations per revolution. The airfoil geometry and shroud location were chosen to provide the best compromise between high speed margin with a 3E resonance (3E = 3 excitations per rotor revolution) and the speed at which a 4E resonance would occur. The 1st-stage and 2nd-stage blade shroud locations were 66.5 percent and 60 percent span from the hub, respectively. Conventional "dovetail" attachments were selected for the blades of both rotors.

Both the 1st-stage and 2nd-stage vanes were made mechanically adjustable for stagger angle changes by means of the vane arms and unison rings mounted externally on the rig cases.

An oil damper was chosen for the 1st-stage bearing to reduce the sensitivity and resulting deflection of the rotor to imbalance.

The rig flowpath design incorporated constant diameter hub and tip duct sections between blade rows to facilitate changes in axial spacing if required. The outer rig case was split to facilitate on-stand acoustic configuration changes. The inner and outer structural cases were designed to provide growth capability for acoustic treatment thickness.

Fan Inlet Design

Two inlet configurations (Figure 2) were selected for evaluation in this program: a standard inlet cowling and a sonic inlet configuration with an axially translating plug or centerbody.

The standard inlet cowling was used for the baseline tests. This inlet was designed to provide a one-dimensional throat Mach number of 0.68 at the cruise operating condition. The inlet-length to fan-tip diameter ratio was 1.03, and the overall contraction ratio ($A_{highlight}/A_{throat}$) was 1.65. The highlight of the inlet cowling is shown in Figure 2 and is defined as the furthest forward point on the cowl.

The sonic inlet configuration provided a means of controlling area to achieve throat Mach numbers that would provide some magnitude of noise suppression over a range of fan operating conditions. In addition, the sonic inlet required a relatively short inlet length without excessive boundary layer growth or possibly separation. A translating centerbody inlet geometry was selected. The sonic inlet in the approach, takeoff, and cruise configuration is shown in Figure 2. For the tests reported herein, positioning of the centerbody was accomplished by means of axial spacers.

Details of both inlet designs are provided in reference 2.

TEST FACILITY

The tests were conducted in an outdoor facility located in a remote area of Bradley International Airport, Windsor Locks, Connecticut. An aerial view of the site is shown in Figure 3.

The test rig was equipped with a gas turbine engine, positioned at an acute angle to the rig centerline, which included a free-turbine (Figure 4) that could provide 1.2×10^7 watts [1.6×10^4 hp] to the test fan at speeds from 4,000 rpm to 8,000 rpm.

For the aerodynamic tests, a portable inlet plenum chamber and a flow measuring nozzle were positioned in front of the fan. A wire-mesh screen was located in the plenum to provide a uniform total-pressure field in the rear half of the inlet plenum for the airflow entering the fan through the bellmouth or the sonic inlet. A variable annulus area exit nozzle was used to throttle the fan.

Since the rotor was cantilevered, the test rig did not have inlet struts, permitting unobstructed flow into the fan for noise tests. By utilizing aft mounted telemetry for transmitting rotor strain-gage signals, the slip-ring support struts were also eliminated.

Inlet distortion patterns were generated by means of screens $0.0127 \times 0.0127 \times 0.00107$ m [$0.5 \times 0.5 \times 0.042$ in.] mesh. The distortion screens were attached to a 0.0259×0.0259 m [1×1 in.] mesh base screen which was attached to 12 equally spaced struts located 0.84 m [33 in.] upstream of the rotor leading edge.

INSTRUMENTATION AND CALIBRATION

All measurements were read as millivolts and converted to engineering units by an automatic data acquisition system. Both the millivolt and engineering units were recorded.

Pressures were measured by means of transducers. The accuracy of these measurements was ± 0.1 percent of the transducer full-scale value. Pressures from sensors upstream of the 1st-stage rotor were measured using 10.34×10^4 N/m² [15 lbf/in.²] full-scale transducers. Pressures from sensors located rearward from the 1st-stage rotor leading edge were measured using 17.24×10^4 N/m² [25 lbf/in.²], 34.47×10^4 N/m² [50 lbf/in.²], and 68.95×10^4 N/m² [100 lbf/in.²] full-scale transducers.

All temperatures were measured with chromel-alumel, type K thermocouples. Separate wire calibrations of temperatures versus millivolts were used for each thermocouple. Overall rms accuracy, including the aerodynamic corrections described below, was estimated to be $\pm 0.56^\circ$ K [$\pm 1^\circ$ R].

Blade tip clearances were monitored by means of two proximity detectors located over the tips of each rotor blade at midchord.

To measure the airflow to the fan, a calibrated nozzle designed to ISO¹ standards was utilized. The airflow measurements for the aerodynamic performance tests were taken directly from the calibrated nozzle and were accurate to within one percent. For the acoustic tests, the flow measuring nozzle and plenum had to be removed, and the flow was determined using a correlation of fan inlet corrected flow versus the ratio of inlet static-pressure-to-total-pressure from tests for which the flow nozzle had been installed.

(1) International Organization for Standardization

Rotor shaft vibrations were measured with accelerometers. Critical parts (stationary and rotating) were strain-gaged to determine levels of vibratory stress over the operating range of the fan.

The compressor speed was measured by means of an impulse type pickup. The pickup was an electromagnetic device which counted the gear teeth that passed within an interval of time and converted the count to RPM. Between 4,000 rpm and 12,000 rpm, the accuracy was within 0.2 percent.

Total temperature measurements were corrected using calibrations of temperature recovery versus Mach number for individual sensors. A correction was also made for pressure level, using calibrations given by Glawe, Simms, and Stickney (ref. 8).

Wedge probes for measuring total pressure, static pressure, and air angle were calibrated for Mach number as a function of indicated ratio of static-pressure-to-total-pressure with pitch angle as a parameter. Total pressure recovery and air yaw angle corrections were calibrated as functions of Mach number and pitch angle. All total pressures measured in supersonic flow were corrected for shock loss. The corrected Mach number and total pressure were then used in conjunction with standard tables of air properties to calculate static pressure. The corrected air-angles were accurate with 1.0 degree.

Combination probes were used to measure total and static pressures, total temperature, and air angle. Corrections were based on probe calibrations similar to those for wedge probes but with the additional calibration of total temperature recovery versus Mach number.

Typical instrumentation is shown in Figure 5. The axial and circumferential positions of the instrumentation are shown in Figures 6 and 7, respectively. The instrumentation used to measure overall and blade element performance is listed in Table III. The parameters that were recorded continually during transient excursions into stall are listed in Table IV.

Aerodynamic data were obtained at ten radial locations at each of stations 7, 8, 14, 15, and 18 and at eleven radial locations at station 11 (Figure 7). These radial locations coincided with the percents of span for which blade-element data are given. The diameters at which the streamlines pass the leading and trailing edges of each blade row are identified in reference 3.

TABLE III — PERFORMANCE AND BLADE ELEMENT INSTRUMENTATION

INSTRUMENT PLANE		PARAMETER	TYPE — QUANTITY
STA. NO.	LOCATION		
0	Inlet	p	8 pressure taps in bellmouth 5 pressure in plenum (barometer for noise tests)
1.3	Bellmouth Inlet	p	10 pressure taps on OD wall, 5 axial location, 180° apart
1.3	Sonic Inlet	p	30 pressure taps on OD wall, 30 on ID wall, 15 axial locations, 180° apart

TABLE III (Cont'd)

INSTRUMENT PLANE		PARAMETER	TYPE - QUANTITY
STA. NO.	LOCATION		
4	Fan Inlet (Approx. $\frac{1}{2}$ chord upstream)	p	4 pressure taps on OD wall, approximately 90° apart
4	Fan Inlet	P, p & β	2 wedge probes, 180° apart, radial traverse.
4	Fan Inlet	p	2 radial rakes, with sensors at 10, 30, 50, 70, and 90 percent span (distortion tests only).
7	Rotor One Exit (Approx. $\frac{1}{2}$ chord downstream)	p	4 pressure taps on O.D. wall and 4 on I.D. wall, approximately 90° apart.
7	Rotor One Exit (Approx. $\frac{1}{2}$ chord downstream)	P, p, T, & β	1 NASA combination probe, radial traverse.
8	Stator One Inlet (Approx. $\frac{1}{2}$ chord Upstream)	p	4 pressure taps on O.D. wall and 4 on I.D. wall, approximately 90° apart.
8	Stator One Inlet	P, p, T & β	1 NASA combination probe, radial traverse.
11	Stator One Exit (Approx. $\frac{1}{2}$ chord downstream)	p	4 pressure taps on O.D. wall and 4 on I.D. wall, approximately 90° apart.
11	Stator One Exit	P, p, & β	1 wedge probe, radial traverse.
11	Stator One Exit	P & T	1 radial rake, 11 P sensors, 11 T sensors, circumferential traverse across one vane gap.
14	Rotor Two Exit (Approx. $\frac{1}{2}$ chord downstream)	p	4 pressure taps on O.D. wall and 4 on I.D. wall, approximately 90° apart.
14	Rotor Two Exit	P, p, T & β	1 NASA combination probe, radial traverse.
15	Stator Two Inlet (Approx. $\frac{1}{2}$ chord upstream)	p	4 pressure taps on O.D. wall and 4 on I.D. wall, approximately 90° apart.
15	Stator Two Inlet	P, p, T, & β	1 NASA combination probe, radial traverse.
18	Stator Two Exit (Approx. $\frac{1}{2}$ chord downstream)	p	4 pressure taps on O.D. wall and 4 on I.D. wall, approximately 90° apart.
18	Stator Two Exit	P & T	2 radial rakes, each with 10 P sensors and 10 T sensors, approximately 180° apart, circumferential traverse across one vane gap.
18	Stator Two Exit	P, p, & β	2 wedge probes, approximately 180° apart, radial traverse.

TABLE III (Cont'd)

INSTRUMENT PLAN		PARAMETER	TYPE - QUANTITY
STA. NO.	LOCATION		
19	Leading Edge of Strut Case	P	5 P sensors, one each on five exit struts, 72° apart
20-21	Splitter	p	7 pressure taps on O.D. wall in exit duct, equally spaced axially, one circumferential location.
20-21	Splitter	p	5 pressure taps on upper surface of splitter and 5 on lower surface, equally spaced axially, one circumferential location.
22	Splitter Exit (½ passage height downstream)	P	2 radial rakes, each with 28 sensors, located 147° apart.
22	Splitter Exit	p	2 pressure taps on O.D. wall and 2 on I.D. wall adjacent to radial rakes.

TABLE IV - TRANSIENT DATA INSTRUMENTATION

Station	Instrument Plane Location	Type & QUANTITY
4	1st-stage rotor inlet	One radial traverse kulite probe (sonic inlet configuration tests only)
---	1st-stage rotor tip	Two proximity pickups 120° apart at blade maximum thickness
8	1st-stage stator inlet	One rake with three rapid-response transducers at 25%, 50%, and 85% span from the hub (rotating stall test only).
---	2nd-stage rotor tip	Two proximity pickups 120° apart at blade maximum thickness.
15	2nd-stage stator inlet	One rake with three rapid-response transducers at 25%, 50%, and 85% span from hub (rotating stall tests only).
---	Rotor Blades	Several strain-gages on each rotor
---	Stator vanes	Several strain-gages on each stator

DATA REDUCTION TECHNIQUES

All steady-state performance data were automatically recorded in millivolts on computer cards and then converted to engineering units, corrected, and used to calculate overall and blade-element parameters. Circumferential distributions of total temperature obtained from circumferential traverses of pole rakes at the 1st-stage and 2nd-stage stator exits were mass-flow averaged at each radial position using the corresponding measured circumferential distribution of total pressure and a constant circumferential static pressure determined by linearly interpolating between wedge probe radial-measurements or between inner and outer wall static tap measurements. A circumferentially mass-flow averaged total pressure was also calculated at each radial position using the same procedure. The highest value from the circumferential total pressure distribution measured behind adjacent stator vanes at each radial location was chosen to represent the free-stream or stator inlet pressure at the appropriate percent of span. The circumferentially mass-flow averaged temperatures and the free-stream total pressures were in good agreement with values measured upstream of the stators.

Redundant measurements were made with similar instrumentation taken at the same axial locations but at different circumferential positions, and these measurements were arithmetically averaged.

Performance Parameter Calculations

Total pressure and temperatures were ratioed to the compressor inlet values (station 4). Compressor inlet total pressure was assumed to be equal to the inlet plenum pressure for tests with uniform inlet flow. For tests with distorted inlet flows, overall pressures were ratioed to the mass-flow average of the total pressures measured by the radial 5-element rakes at the fan inlet station 4. For tests with the sonic inlet, two sets of overall performance parameters were calculated: 1) with total pressures ratioed to plenum pressure giving an overall systems performance, i.e., P_{18}/P_0 , and 2) with total pressure ratioed to mass-flow averaged total pressure with wedge probes at the 1st-stage rotor inlet. Method 2 identifies the fan-only performance during sonic inlet testing. Temperatures were always ratioed to plenum temperature.

Overall and blade-element performance parameters for uniform and radially distorted inlet flows were calculated by means of a streamline analysis computer program. All parameters were corrected to standard-day conditions. Inputs to the flowfield program are listed in Table V.

For the flowfield analysis, a blockage factor was used at each axial location to account for the endwall boundary layer and shroud blockages. The design blockages were evaluated for the near-design operating point by comparing the calculated static pressure with measured test values. The agreement was good, and the design blockages were used throughout the data reduction except at the inlet to the 1st-stage rotor with the sonic inlet where total pressure measurements were sufficiently detailed so that blockage corrections were not necessary.

TABLE V — PARAMETERS INPUT TO FLOWFIELD PROGRAM

LOCATION	PARAMETERS
Compressor Inlet (Station 0, Figure 6)	1) Corrected mass flow 2) Corrected rotor speed 3) Constant radial total pressure
Rotor 1 Inlet Instrument Plane (Station 4)	1) Total pressure ratio* versus radius 2) Constant radial blockage factor
Stator 1 Inlet (Station 9)	1) Total pressure ratio versus radius 2) Constant radial blockage factor
Stator 1 Exit Instrument Plane (Station 11)	1) Total temperature ratio versus radius 2) Total pressure ratio versus radius 3) Constant radial blockage factor 4) Absolute air angle versus radius
Stator 2 Inlet (Station 16)	1) Total pressure ratio versus radius 2) Constant radial blockage factor
Stator 2 Exit Instrument Plane (Station 18)	1) Total temperature ratio versus radius 2) Total pressure ratio versus radius 3) Constant radial blockage factor 4) Absolute air angle versus radius

*Ratio equals 1.0 for baseline configuration, uniform inlet flow tests. Ratio equals local value of P_4/P_0 for tests with sonic inlet configuration or with distorted inlet flow.

All static pressure distributions and air angles behind the rotors were calculated by assuming axisymmetric flow and using mass-flow continuity, radial equilibrium, and energy equations. Curvature, enthalpy, and entropy gradient terms were included in the equilibrium calculations. Aerodynamic conditions at the blade edges were calculated by translating the measured data from the instrument plane along streamlines to blade edges. Blade element parameters were calculated for airfoil sections lying on conical surfaces defined by the intersections of design streamlines and the blade edges. These streamlines passed through the 1st- and 2nd-stage stator exit instrument planes at diameters close to the average of the pressure and temperature sensor diameters on the pole rakes, the primary input source to the streamline program.

Blade-edge stations for the flowfield calculation were input as curved lines which closely approximate the profiles of the manufactured blade edges. In addition to the blade element parameters, the output of the flowfield analysis program included overall performance of the 1st-stage rotor, the entire first stage, the 2nd-stage rotor, and the entire two-stage fan. Blade-element performance data for uniform and radially distorted flow tests are tabulated in reference 3.

TEST PROCEDURE

The program consisted of both aerodynamic and acoustic testing. Because of the cost of changing configurations, the aerodynamic and acoustic tests were intermixed. In addition, the acoustic wall treatment was not removed during any portion of the tests. Instead, untreated walls were simulated by covering the treated walls with an aluminum faced adhesive with the edges rolled over and secured by adjacent cases.

The sequence of testing was as follows:

- 1) Acoustic tests of the baseline fan with standard inlet cowling and interstage acoustic-treatment.⁽¹⁾
- 2) Aerodynamic tests of the above configuration with uniform inlet flow.
- 3) Aerodynamic, uniform inlet flow tests of the fan with the sonic inlet installed and with acoustic treatment in the inlet, interstage, and aft ducts. These tests were conducted with the sonic inlet in the cruise, takeoff, and approach configurations.
- 4) Acoustic tests of the above fan configurations.
- 5) Aerodynamic tests of the baseline fan with tip-radial inlet flow distortion and interstage acoustic treatment.⁽¹⁾
- 6) Aerodynamic tests of the baseline fan with hub-radial inlet flow distortion and interstage acoustic treatment.⁽¹⁾

Shakedown tests of each configuration were conducted prior to detailed testing. The purpose of the shakedown tests was to locate unsafe operating regions, to define stability limits, and to check instrumentation and data recording systems.

No significant vibrations due to rotor critical speeds were detected. Blade and vane resonances limited operation only during sonic inlet tests of Mach numbers of 0.9 and 1.0. At these conditions high stresses prevented throttling the fan to the stall line.

The shakedown tests included rotating-stall surveys in which the signals from rapid response transducers and strain-gages were recorded as the fan was throttled into stall. Initial tests at 50 percent, 70 percent, 100 percent, and 105 percent of design speed showed inadequate stall margin at higher speeds. A second series of tests was run at 50 percent and 100 percent of design speed. During this series the 1st-stage stator vanes were opened five degrees to evaluate the effects on stall margin. Upon completion of the series, the stator vanes were returned to the nominal setting and the 50 percent, 70 percent, 80 percent, 90 percent, 100 percent, and 105 percent of design speed operating points were documented. This completed the shakedown tests of the basic fan.

(1) It was originally planned to cover the interstage treatment for this test. However, during the first set of initial shakedown tests, the interstage treatment cover started to peel and was removed to eliminate the danger of damaging the fan and the effects on the data of the partially peeled covering.

These shakedown tests did not include radial traverses with the combination or wedge probes. To determine whether these probes would interfere with other measurements, an operating point at design speed was run and measurements from these traverse probes were recorded separately and also simultaneously with other measurements. The results of this investigation showed that all measurements could be recorded simultaneously. However, circumferential and radial traversing were recorded separately for all subsequent tests because of limitations in the data equipment.

Detailed performance tests were conducted to determine the aerodynamic performance of each of the aforementioned configurations. These tests were fully documented and included operation at 50 percent, 63 percent, 76 percent, 80 percent, 94 percent, 100 percent, and 105 percent of design speed.

The baseline tests were followed by tests with the sonic inlet installed and the acoustic treatment exposed. These tests were conducted with the sonic inlet in the approach, takeoff, and cruise position. These sonic inlet arrangements were obtained by axially repositioning the centerbody by means of spacer blocks.

Operating points were chosen along constant speed lines with back pressure and flow being varied and also along constant flow lines with back pressure and speed being varied. The purpose of the constant flow line tests was to provide performance data at specified Mach numbers at the throat of the sonic inlet.

For the approach configuration, constant speed lines of 63 percent and 77 percent were run. In addition, constant flow lines representing throat Mach numbers of 0.8 and 0.9 were run.

For the takeoff configuration, constant flow lines representing Mach numbers of 0.8 and 1.0 were run.

For the cruise configuration, constant speed lines at 94 percent and 100 percent were run.

In addition to documenting the performance of the fan stage, measurements were also taken to document the performance of the sonic inlet and the acoustically treated exit duct. Dynamic pressure and static and total pressure measurements were documented to determine losses and flow stability.

With completion of the sonic inlet tests, the sonic inlet was removed and the standard inlet cowling reinstalled. A series of operating points was then run at design speed. The purpose of this series was to determine if the baseline performance obtained earlier could be repeated. These tests were run without the bellmouth and flow measuring nozzles.

Tip-radial distortion tests were conducted at 63 percent, 90 percent, and 100 percent of design speed. The distortion pattern was generated by means of screens placed 0.838 meters [33 inches] forward of the 1st-stage rotor.

The hub-radial distortion investigation included measurements obtained with shakedown instrumentation at 50 percent, 63 percent, 94 percent, and 100 percent of design speed. Full instrumentation was used at wide open throttle and at design speed only.

After 90 percent of the aerodynamic and acoustic programs was completed and during hub radially distorted inlet flow tests, an inlet total pressure probe rake failed. The failure caused sufficient damage to both the 1st-stage and 2nd-stage rotors and to the 1st-stage stator to necessitate termination of the test program. An investigation revealed that the failure was caused by a fatigue crack which had originated at the base of the rake adjacent to the support boss (Figure 5). The investigation was thorough and included microscopic examination, spectrographic analysis, and a vibration analysis. The failure most likely occurred because of high localized stresses at the leading edge resulting from first mode bending caused by the fan rig 1E (1st mode shaft resonance excitation).

RESULTS AND DISCUSSION

BASELINE CONFIGURATION

The baseline configuration with the standard inlet cowling in place is shown in Figure 1. This configuration was tested with uniform inlet flow and with hub and tip radially distorted inlet flows. In this configuration the interstage acoustic treatment was exposed, but the aft duct acoustic treatment was taped to provide a smooth surface.

Uniform Inlet Flow

OVERALL FAN PERFORMANCE

The overall performance of the two-stage fan is shown in Figure 8; complete tabulations of overall performance parameters are given in reference 3.

The peak adiabatic efficiency at design speed was 86.4% compared to the designed efficiency of 85.3%. This efficiency was attained on two occasions during shakedown tests. The peak adiabatic efficiency at design speed during the performance documentation tests was 85.0% although the same instrumentation and data reduction techniques were used. The highest peak adiabatic efficiency was 87.5%, obtained at 90 percent of design speed during shakedown testing. During performance testing, the highest adiabatic efficiency was 86%, obtained at 80 percent and 94 percent of design speed. No data were taken at 90 percent of design speed during this phase of the testing. Peak efficiency at 63 percent of design speed was 85.0% and at 105 percent speed was 82.5% for both shakedown and performance tests. As noted, fan efficiency was higher during the shakedown testing than during performance documentation testing (Figures 8 and 9). The high efficiency was attained both before the 1st-stage stator was opened 5 degrees and after it was reset at the design value; no erroneous data was found in either test point. The higher performance value was also more consistent with the data obtained during distortion tests and during tests with the sonic inlet. The sonic inlet and the distortion tests are discussed in separate sections of the report.

The fan stalled at design speed at a pressure ratio of 1.873 which is lower than the design pressure ratio of 1.9. The stall-free range at design speed was disappointingly small. The stall line for speeds above 90 percent of design speed was below the design operating line (Figure 8). A stall margin of 20% was obtained at 63 percent speed. An attempt was made during shakedown testing to raise fan pressure ratio by increasing the work input from the 2nd-stage rotor since the stall appeared to have occurred in the first stage. The 1st-stage stator was opened 5 degrees (reset in a position to decrease preswirl into the 2nd-stage rotor), but this attempt was only marginally successful, as shown by Figure 9. Stall pressure ratio increased to 1.902 which is slightly more than the design pressure ratio; however, efficiency decreased by approximately 1.5 percentage points. As this loss in efficiency was considered excessive for the small gain in pressure ratio, the 1st-stage stator was reset to the design stagger-angle. Because stall at high speed was the most serious problem of this fan, stall is discussed in detail in a separate section of the report.

The fan flow was very near the design goal, as indicated by extrapolating the design speed-line to the design pressure-ratio (Figure 8). Very high flows per unit annulus area were obtained. Specific flow at the inlet to the 1st-stage rotor reached 211.3 kg/sec-m^2 [$42.25 \text{ lbm/sec-ft}^2$] at design speed and 219.2 kg/sec-m^2 [$44.9 \text{ lbm/sec-ft}^2$] at 105 percent of design speed.

OVERALL PERFORMANCE OF THE FIRST STAGE AND FIRST-STAGE ROTOR

Overall performance of the first stage and of the 1st-stage rotor is shown on Figures 10 and 11, respectively. These figures show the curves of pressure-ratio-versus-flow approaching the design point at design speed. The first stage attained an efficiency of 87.0% at design speed. Maximum first stage and 1st-stage rotor efficiency occurred near the stall point. The maximum efficiency decreased at 105 percent speed, but there was no marked change in maximum efficiency as speed was decreased below the design value. The high values of efficiency for the baseline data at 50 percent of design speed can probably be attributed to data inaccuracies as a result of the very low rise in temperatures at that speed.

NONDIMENSIONAL PERFORMANCE DATA

Pressure coefficients and adiabatic efficiencies for the first stage and 1st-stage rotor are presented as functions of flow coefficient in Figures 12 and 13, respectively.

At low speeds the first stage and the 1st-stage rotor operated over a wide range of flow coefficients. But at high speeds the stage and the rotor operated in a narrow range of flow coefficients. This narrowing effect is common to high specific flow stages.

First-stage pressure coefficients at all speeds increased steadily with decreasing flow coefficient, although the stage operated on the low flow side of peak efficiency at partspeed (Figure 12). At 50 percent and 63 percent of design speed, the first-stage pressure coefficients attained values that were higher than the design value. The design pressure-coefficients were not attained at design speed by either the first stage or the 1st-stage rotor.

The cluster of low pressure-coefficient data at high flow with the 1st-stage stator opened 5 degrees, in contrast to the more evenly distributed, high-level pressure coefficient data for the nominal stator setting (Figure 12), shows that the corrected-flow limit of the 2nd-stage, rather than the throttle, was controlling first-stage pressure when the 1st-stage stator was opened. The lower level of pressure coefficients obtained when the 1st-stage stator was opened (Figure 12) shows that the loading of 1st-stage rotor was reduced. The 1st-stage stator losses were not high at any operating condition, as can be seen by comparing the 1st-stage rotor and the first-stage pressure coefficients and efficiencies. The low level of the 1st-stage stator loss indicates that this stator did not choke.

The second stage and 2nd-stage rotor pressure coefficients and adiabatic efficiencies are shown versus flow coefficients in Figures 14 and 15. This stage and rotor reached the design pressure coefficients only when the 1st-stage stator was opened 5 degrees. The fact that higher pressure coefficients were obtained with the opened stator indicates that the second stage must have been operating below its loading limit when the 1st-stage stator was set at the design stagger-angle. The pressure coefficient curve of the second stage shows no evidence of flattening which is often a characteristic of a stage that is approaching loading limit. The first stage shows more evidence of flattening than the second stage. The large difference in pressure coefficients between the second stage and 2nd-stage rotor and between efficiencies at open throttle points indicates that the 2nd-stage stator was choked at this operating condition. The 2nd-stage stator choke losses are shown in Figure 16a which presents the ratio of stator-exit to stator-inlet total pressure as a function of stator-inlet corrected flow. The pressure recoveries for the 1st-stage stator are shown on Figure 16b. No choke conditions are indicated for the 1st-stage stator for either the nominal or the reset vane angles.

BLADE SPANWISE PERFORMANCE

The spanwise distributions of total pressure ratio and adiabatic efficiency at the fan exit for a near design point operating condition are shown in Figure 17. This is also the near-stall point. Adiabatic efficiency tends to be lower than design in the hub region and higher than design in the tip region. The partspan shrouds appear to have a small adverse effect on efficiency near 60 percent span. Because stall occurred at a pressure ratio somewhat less than design, the general level of pressure ratio shown on Figure 17 is also low. A comparison of the shapes of the experimental and design curves, however, shows a deficiency of pressure ratio near the hub and a somewhat higher pressure ratio near the tip.

Spanwise distributions of total pressure at the exits of the individual rotors and stages are compared to the design profiles in Figure 18. The first stage and 1st-stage rotor show lower than design pressure ratios in the hub region and near or somewhat higher than design pressure ratios in the tip region. The second stage and 2nd-stage rotor show higher pressure ratios for the hub region. But, as shown on Figure 17, the second stage hub did not completely compensate for the pressure ratio deficiency of the first-stage hub section.

Spanwise efficiency profiles for the near-design data point are compared to design profiles for individual rotors and stages in Figure 19. Agreement with design predictions was generally good except near the endwalls. The tip-region efficiencies of both stages were higher than predicted. An effect of the 1st-stage rotor partspan shroud on efficiency at 66 percent span was noted. There appears to be little effect of the 2nd-stage rotor partspan shroud which was located at 60 percent span.

The first-stage hub efficiency indicated in Figure 19 was unexpectedly low while the second-stage hub efficiency shown was too high (greater than 100%). However, the accumulative efficiency at the fan exit (Figure 17) was reasonable. Intrafan data were examined in detail to determine if the first-stage pressure and temperature measurements were correct. Measurements from radial traverses at the 1st-stage rotor exit and stator inlet were used to recalculate 1st-stage rotor performance. In general the efficiency profiles obtained corroborated the profiles obtained with the primary instrumentation (circumferential traverses with the 1st-stage stator exit pole rakes). The spanwise profiles of efficiency obtained with the radial traverses are also shown in Figure 19.

Meridional velocity profiles at the entrance of each blade row are presented in Figure 20. The level was higher than design at the fan inlet because of higher-than-design corrected flow. There was, however, a small deficiency of flow at the hub as compared to the tip. Levels were generally higher than design for the other blade rows because of a combination of high inlet-flow and low pressure-ratio. Low meridional velocities in the hub regions were amplified downstream of the fan inlet as a consequence of the local defect in pressure ratio at the hub of the 1st-stage rotor.

Figures 21 through 24 give spanwise profiles of loss coefficient, diffusion factor, deviation angle, and incidence angle to the leading edge for each of the four blade rows for the near-design test point. Loss coefficients for each blade row were in reasonable agreement with predictions except in the hub region of both rotors. The most significant differences between test and predicted blade-element performance were the high loss coefficient at the hub of the 1st-stage rotor and the low loss coefficients at the hub of the 2nd-stage rotor.

These questionable distributions of loss coefficient may be the result of limitations in the method employed to reduce the data. The data was reduced by a standard method that does not account for the radial transport of boundary layer fluid in that it is assumed that the flow is axisymmetric and that particle paths do not cross streamlines. However, a radial flow of sufficient magnitude to account for these questionable results may have occurred within the boundary layer on the rotor blades. The 1st-stage rotor had past-axial relative flow at the exit in the hub region which caused the exit mainstream flow to have a higher tangential, or swirl, velocity than the blade boundary layers. The higher swirl velocity would generate a steeper radial gradient of static pressure in the mainstream flow than the gradient in the blade boundary layer where swirl velocity approaches blade speed. The pressure field imposed on the boundary layer would draw boundary layer fluid toward the hub at the exit of the 1st-stage rotor. Because the 2nd-stage rotor had no past-axial flow, the blade speed was always higher than the tangential flow velocity. The resulting difference in radial static pressure gradients on the 2nd-stage rotor would draw boundary layer material away from the hub. Thus, the high loss at the hub of the 1st-stage rotor can be the result

of an inward flow of low energy fluid within the boundary layer, and the low-loss at the hub of the 2nd-stage rotor can be the result of an outward flow of boundary layer fluid. The relatively high loss region at approximately 20 percent span at the exit of the 2nd-stage rotor may be the result of this radial outflow of hub region, boundary layer fluid. Radial flow within blade boundary-layers is discussed in reference 9.

The high loss coefficient at the hub of the 1st-stage rotor does not appear to have been entirely the result of past-axial exit flow at the hub since this loss coefficient was higher than the loss coefficient obtained in tests of a similar "low-speed" fan-rotor that had even greater past-axial turning (ref. 10 & 11). Figure 25 compares spanwise profiles of loss coefficient for these two rotors and shows that the 1st-stage rotor of this fan had approximately 50 percent higher loss coefficient at 5 percent span than the reference-10 rotor.

Calculated surface-velocities versus chord are presented for the hub sections of both rotors in Figure 26. The velocities on the surfaces of both blades were calculated for design flow conditions using the potential flow method described in reference 12. Total suction surface diffusion, defined as the maximum velocity to exit velocity on the suction surface, is comparable. The rate of diffusion for the 1st-stage rotor, however, is higher. The higher rate of diffusion concentrated toward the rear of the blade could cause higher losses and may have had adverse effects on secondary flows which could have led to higher losses when compared to the rotor of reference 10. The more gradual diffusion on the low-speed rotor was achieved by having the peak suction surface velocity near the leading edge. The 1st-stage rotor, however, requires a higher critical Mach number than the "low-speed" rotor because of its higher blade speed. Moving the peak suction surface velocity forward would have reduced the diffusion rate, but would have had the effect of reducing the critical Mach number as well. However, a more optimum design might have been achieved if the critical Mach number was compromised for less rearwall diffusion.

Incidence angles for the 1st-stage rotor were lower than design over the outer 70 percent of span because the corrected flow for this test point was higher than the design value. The lowest flow obtained was higher than the design flow due to premature stall. If, however, design flow had been attained, it is believed that near design incidence angles would have been obtained over most of the blade span.

Diffusion factors were near design predictions and well below the loading level usually associated with stall. Deviation angles for the 1st-stage rotor were nearly four degrees lower than the design estimate at 14 percent span. The extra turning increased the temperature rise (work input) at this location by only six percent because of the low blade-speed near the hub.

Deviation angles for the 1st stage stator (Figure 22) were approximately two degrees more than the design estimate. This deviation increased the preswirl into 2nd-stage rotor, causing a reduction in 2nd-stage rotor work input. The losses for the 1st-stage stator were only slightly higher than design estimates, except in the wake of the partspan shroud at the 1st-stage rotor, where the losses were noticeably higher. Diffusion factors were lower than design levels, except in the pressure defect region at the hub. As these blade loading levels are well below loadings documented in other fan tests (ref. 13 and 14), the 1st-stage stator loading levels are not considered a probable cause of stall.

The loss coefficients for the 2nd-stage rotor (Figure 23) agreed well with design predictions, except at the hub where the loss coefficients were unreasonably low.

The 2nd-stage rotor diffusion factors were below design values and well below the 1st-stage rotor loadings. This was true for all spanwise locations. Deviation angles were approximately three degrees below the design estimate at 86 percent span and three degrees above the design estimate at 5 percent span. These variations did not have a significant effect on the pressure ratio profile of the 2nd-stage rotor, as shown by Figure 18.

Incidence angles for the 2nd-stage rotor from 10 percent span to the tip were two to three degrees lower than design because of the higher-than-design corrected flow into this rotor, the excess preswirl due to insufficient turning in the 1st-stage stator, and the flow shift due to the pressure defect at the hub. Incidence angles were higher than design values at the hub because of this pressure defect.

The loss coefficients for the 2nd-stage stator (Figure 24) agreed well with design values. Incidence angles and diffusion factors were generally lower than design values. Deviation angles in the tip region were approximately three degrees greater than design estimates.

BLADE-ELEMENT PERFORMANCE

Blade-element plots of loss coefficient, diffusion factor, and deviation angles versus incidence are presented in Figures 27 through 30 for the performance documentation data obtained with the baseline inlet configuration with uniform inlet flow. The data obtained during performance documentation tests included radial traverse measurements which were recorded immediately following the recording of measurements from the circumferential traversing pole rakes. The blade-element performance plots in this report are based on the performance documentation tests rather than data from shakedown testing. The data is presented at eleven radial locations for the 1st-stage rotor and stator and at ten radial locations for the 2nd-stage rotor and stator. Complete tabulations of blade-element and velocity-vector data are given in reference 3. Discussion of these plots is concentrated on the effects of incidence angle and of speed, which are not shown by the spanwise distributions for the near-design data point.

First-Stage Rotor

Blade-element performance for the 1st-stage rotor is shown in Figure 27. Because the stall-free range at high speeds was very small, the range of incidence angles at high speeds was

very narrow and limited to low incidence angles. At low speeds the incidence angle range was larger and shifted in the direction of higher incidence angles. This shift to higher incidence angles at low speed is not unusual when the aft stages of a multistage compressor control the flow capacity at low speeds.

The high losses at the hub of the 1st-stage rotor occurred over the entire range of incidence-angle and speed. The scatter in the loss coefficient data at the hub was probably due to the large wakes at the rotor hub. But smooth curves of loss coefficient versus incidence were obtained from 23 percent span to the tip. The highest losses occurred at higher speeds at negative incidence angles.

Deviation angles in general were lowest near design incidence angles. The deviation angles increased with decreasing incidence angles at high speeds at 62 percent, 68 percent, and 74 percent span (the region of the partspan shroud). This abrupt rise in deviation angle together with the increased loss coefficient appears to define a negative incidence limit, indicating a choke condition at high speeds.

Blade diffusion factor levels remained relatively constant at all spans throughout the incidence and speed range and never exceeded a value of 0.51 which is below values normally associated with stall.

First-Stage Stator

The blade-element parameters for the 1st-stage stator are shown in Figure 28. The data were concentrated in a narrow range of incidence angles at high speeds because stall limited the range of fan operation. At the tip, most incidence angles were lower than design predictions. The loss coefficient curves for all spanwise locations were flat, and there were no indications of an impending choke or stall. Deviation angles at the hub of the 1st-stage stator were slightly larger than design and increased with increased incidence. The rate of increasing deviation with increasing incidence was higher at the hub than at the tip. The scatter in the deviation angle data increased toward the tip, with a trend toward higher deviation angles in high speed data. Diffusion factors for the 1st-stage stator were higher at low speeds than at high speeds and occurred at higher incidence angles. Even at the low speeds, however, loadings were below the levels associated with stall.

Second-Stage Rotor

Blade-element parameters for the 2nd-stage rotor are shown in Figure 29. The loss coefficients obtained at 5 percent span were unrealistically low over most of the incidence and speed range. The loss coefficients increased with decreasing incidence at all spanwise positions at high speeds. Choking is indicated by the rapid rate of increasing loss coefficients with decreasing incidence angle for tip sections at high speed. The more gradual rise for hub sections indicates a negative incidence-angle problem but not choking. The evenly spread data points on the first-stage, nondimensional performance plots (Figure 12) show that local choking had no significant effect on the flow capacity of the 2nd-stage rotor.

Incidence angles for the 2nd-stage rotor were low at all spanwise positions and, except at midspan, were less than design. The low incidence angles resulted largely from the higher-than-design corrected flow from the first stage and in part from the larger-than-design deviation angles measured for the 1st-stage stator. In the upper part of the span, the incidence angle range was quite narrow.

Blade diffusion factors near the tip increased rapidly with increasing incidence angle, but never exceed 0.37 at any spanwise position at any speed.

The deviation angles generally increased with increasing incidence angle from the hub to 39 percent of span. At 95 percent span, the dominant trend was an increasing deviation angle with decreasing incidence, indicating a tendency to choke. Deviation angle data was scattered at the hub, but fell into tighter bands near the tip.

Second-Stage Stator

The blade-element parameters for the 2nd-stage stator are shown in Figure 30. Minimum loss coefficients were generally lower than design estimates for this 65/CA vane. Loss coefficients increased with decreasing incidence angles at all spanwise locations and increased sharply at 13 percent, 21 percent and 30 percent span, particularly at higher speeds. This abrupt increase in loss coefficients indicates stator choke and is consistent with Figure 16a which shows that the overall stator total pressure ratio dropped as choke was encountered. Incidence angles at high speeds were confined to low angles because of a lack of stall range.

At low speeds the multistage effect of front-stage stall and rear-stage choke maintained the lower range of incidence angles. Loss coefficient data appears to define minimum loss levels at all speeds and spanwise locations. The low losses occurred at design incidence angles at all spanwise positions. Diffusion factors increased gradually with increasing incidence angle at all spanwise positions and never exceeded 0.44. Deviation angles showed very little effect of incidence angle or of speed, except near the hub for those data points where high loss coefficients indicate choke. The apparent sharp decrease in deviation angles for these points was probably due to large wakes from the stator which affected the angle measurements.

Radially Distorted Inlet Flow

Radial distortions of total pressure at the fan face were generated by screens (Figure 31) placed 0.838 m [33 in.] forward of the 1st-stage rotor. Distortion patterns generated by the screens at design speed with wide open and near-stall throttle settings are shown in Figure 32. The distortion parameter, $P_{\max} - P_{\min} / P_{\max}$, is shown in Figure 33 as a function of percent design inlet corrected flow for both hub and tip distortions. The largest hub distortion parameter was 0.17 and the largest for the tip was 0.155.

TIP DISTORTED FLOW

Fan and first-stage overall performance with tip radially distorted flow is shown in Figures 34 and 35, respectively. Performance with uniform inlet flow from shakedown tests is shown by dashed lines for comparison. Complete data tabulations are given in reference 3. Figure

34 shows that the stall line was higher with the tip distortion at high speeds and lower at low speeds. At design speed with tip radial distortion, a positive stall margin of 4% over the stall limit with uniform inlet flow was obtained. This improvement included both a higher pressure ratio and lower flow at stall. At 63 percent of design speed where the blade tip region was critical, tip distortion resulted in an appreciable decrease in stall margin. Figure 35 shows that the first stage — which initiated stalls at high speeds with uniform inlet flow — operated at lower corrected flows at 90 percent and 100 percent speeds with the tip distortion, but the first-stage maximum pressure ratio was not changed. The increased overall fan pressure ratio was due to the second stage which operated at a lower corrected flow and a higher pressure ratio than with uniform inlet flow.

The improved stall-line at high speed with the tip distortion indicates that the hub stalled with uniform inlet flow and that forcing additional flow toward the hub by means of the distortion relieved critical loadings. The spanwise profiles of meridional velocity are presented in Figure 36 for the near stall point at design speed with tip inlet flow distortion. Data from a similar point for uniform inlet flow is shown for comparison. Figure 36 shows that tip distortion resulted in a much larger flow shift towards the hub in the first stage than in the second stage. This radial shift of flow towards the hub of the first stage relieved the loading in the first-stage hub region and improved the stall or surge margin at high speeds. The data with tip inlet flow distortion substantiates the theory that the premature high speed surge with uniform inlet flow was initiated in the first-stage hub region.

Attenuation of the tip distortion is shown in Figure 37 by a comparison of the radial total pressure profiles from the uniform and distorted inlet flow tests. These data are for near stall conditions at design speed. The shaded symbols represent the absolute distribution of pressure ratio for a distorted inlet flow, where local pressures were divided by the fan inlet average pressure. In the plot of fan overall pressure ratio, the shaded symbols of the distortion inlet flow show a profile similar to that of the nondistorted data, indicating that the fan had effectively attenuated inlet tip distortion. In fact, most of the attenuation occurred in the first stage. The unshaded symbols represent pressure ratio along streamlines and show that an increase in tip pressure ratio in the first stage was necessary in order to produce the first stage attenuation. The second stage contributed much less pressure rise at the tip.

Maximum overall efficiency with tip-radial inlet flow distortion at design speed was approximately one percentage point below that obtained during the baseline shakedown tests (Figure 34) and was approximately equal to that shown on Figure 8 for the baseline performance tests.

Blade element performance parameters for each blade row at five radial positions are shown in Figures 38 through 41. The 1st-stage rotor tip (88 percent span) operated at slightly higher positive incidence with tip distortion than with uniform inlet flow, and had only a small increase in loss due to the tip distortion. The highest diffusion factor (0.56) also occurred at the tip of the 1st-stage rotor. The data for the 1st-stage stator were obtained over an increased incidence angle range, approximately 10 degrees higher at design speed at 88 percent span than with uniform inlet flow. The loadings of the 1st-stage stator increased slightly over the values for uniform inlet flows, giving a peak diffusion factor of 0.42 at 88 percent span. Loss coefficient levels did not increase due to tip distortion.

Second-stage blade-element loadings and incidence angles were lower than for the first stage. Both second-stage blade rows showed increasing loss with decreasing incidence angles, indicating that even with tip distortion the second stage was closer to choke than to stall.

HUB DISTORTED FLOW

Overall performance of the fan and the first stage with hub radially distorted flow is shown in Figures 42 and 43, respectively. The performance with uniform inlet flow from the baseline shakedown tests is shown by dashed lines for comparison. Complete data tabulations are given in reference 3.

Figure 42 shows that at all speeds the stall line was lower with hub distortion than with uniform inlet flow. The lower stall-line was the result of lower pressure ratios at stall at all speeds. Lower stall flows at 100 percent and 94 percent speeds failed to offset the reduced pressure ratios. The hub radial flow distortion resulted in a negative stall margin of 4% at all speeds when compared to tests with uniform inlet flow. Figure 43 shows that the first-stage pressure ratio was lower at all speeds with the hub distortion.

Spanwise profiles of meridional flow velocity for hub distortion are compared to those for uniform-inlet profiles in Figure 44. Both data points were obtained at design speed at an open throttle setting and both have nearly equal pressure ratios. The figure shows that flow was diverted from the hub, which was the region of critical loadings in both stages, and that both rotors tended to attenuate velocity distortion with the 2nd-stage rotor having the greater effect.

Profiles of pressure ratio for the first stage and overall fan are shown in Figure 45. The figure shows that most of the pressure distortion was attenuated at the fan exit (solid symbols), with only a small pressure defect remaining at the hub. The profile at the exit of the first-stage, however, retained a significant defect at the hub. Streamline values of pressure ratio (open symbols) showed that whatever attenuation was achieved in the first stage was the result of reduced pressure ratio in the undistorted flow outboard of midspan. The second stage was very effective in attenuating the large distortion. The defect on the hub wall of the first stage and the loss of stall margin was consistent with the theory that premature surge at high speeds with uniform inlet flow was initiated in the first-stage hub region.

Fan-overall peak efficiency was reduced approximately eight percentage points by the hub distortion at design speed. Efficiency reductions were less severe at lower speeds, dropping to approximately five percentage points at 50 percent speed. Flow capacity was also reduced nine percent at high speeds, where maximum flow was limited by the fan. At low speeds the flow was system limited, and the effect of hub distortion on maximum flow could not be evaluated.

STALL INVESTIGATION

The most serious performance problem of this fan was the low stall-limit line at high speeds. The stall limit or upper limit of pressure ratio attainable by a fan or compressor is limited by rotating stall, system surge, or blade or vane vibratory stress. At high speeds with uniform inlet flow and at all speeds with hub inlet flow distortion, surge was the limiting phenomenon for the subject fan. Reference 16 shows that surge can be initiated when the

slope of the static-pressure/flow characteristic curve becomes highly positive. The initiation of a flow separation from either a wall between the blade rows or from one of the blade rows could cause a sufficient drop in overall static pressure ratio to induce system surge. Alternately, this discontinuity in static pressure could be due to increased losses or to unloading of one or more blade rows due to a radial flow shift.

In an effort to determine the cause of the low stall limit line at high speeds, records from rapid response transducers and strain gages, qualitative effects of radial distortions, and blade-element and intrafan flow distribution data were reviewed.

Pressure fluctuations near the hub, at midspan, and near the tip at both stator-inlet traverse stations were recorded as the fan was stalled. The fluctuations were measured by hot-film sensors and recorded by means of rapid response transducers.

An excerpt from a record taken during stall at 90 percent speed during uniform inlet flow tests is shown in Figure 46. The figure shows that flow instabilities first occurred near the hub and at the entrance to the 1st-stage stator. At the time this signal was recorded, the fan surged (rapid change in pressure ratio and flow).

Records of strain-gage signals versus time during stall were also reviewed to determine which blade or vane first showed high vibratory stresses. An excerpt from a stress record made as the fan was stalled at design speed is shown in Figure 47. The figure shows that high stresses occurred on the 1st-stage stator before occurring on the 2nd-stage rotor or stator. The rise in the 1st-stage rotor stress (not shown) also occurred after the rise in 1st-stage stator stress.

There was no evidence that hub instabilities caused stalls at low speeds with uniform inlet flow, see Figure 48. Fan overall flow and pressure were stable in stall (no surges), but the pressure fluctuations obtained from the hot films clearly indicated rotating stall.

Stalls with tip distortion did not appear to have been instigated at the first-stage hub. At high speeds, stalls were accompanied by surge, without periodic patterns of rotating stall, see Figure 49. Rotating stall did occur at lower speeds, Figure 50, and flow instability appeared to have started at the tip of the first stage. The limited stall range at low speeds during tip distortion tests probably was caused by excessive loading at the tip of the 1st-stage rotor or stator.

Stalls with hub distortion showed no clear indications of rotating stall at either high or low speeds, and were accompanied by surges similar to stalls at high speed with uniform inlet flow.

Tip radial distortion raised the stall line at high speeds, and hub radial distortion lowered the stall line (Figure 34 and 42). These effects strongly support the hot-film records which show that the initial breakdown of flow at high speeds occurred at the hub.

The overall fan pressure ratio was increased by opening the 1st-stage stator (Figure 8). The increased pressure ratio was created by the second stage when the 1st-stage stator was opened, proving that the loading limit of the second stage had not been reached during the tests with the nominal setting stator. This effect is consistent with the hot film and strain-gage records which indicate that the first stage initiated stalls.

Blade-element data (Figures 21 to 24) showed that the first stage was the more highly loaded stage and that the higher loadings occurred near the hub. Figure 51 presents diffusion factors at 13 percent span from the hub of the 1st-stage rotor and stator versus corrected flow, with speed as a parameter. Near-stall data points were very close to stall flows and, therefore, the near-stall diffusion factors were a good representation of loading at stall. In Table VI, maximum blade-element diffusion factors at stall at design speed for the subject fan are compared to values documented in tests of similar fans. These other fans had aspect ratios similar to the subject fan and rotor tip speeds which bracket the tip speed of this fan.

TABLE VI — MAXIMUM BLADE-ELEMENT DIFFUSION FACTORS[†]
NEAR STALL AT DESIGN SPEED COMPARED TO OTHER FANS

Location	NAS316811 (1200 ft/sec) Fan	442 m/sec [1450 ft/sec] Two-Stage Fan (ref. 13)	304.8 m/sec [1000 ft/sec] Fan Stage (ref. 11)
Rotor 1	0.5166	0.5906	0.6012
Stator 1	0.4804	0.5583	0.6016
Rotor 2	0.3475	0.6376	
Stator 2	0.3911	0.5589	

[†]Excluding the inner and outer 10% span

The two-stage fan of reference 13 had small axial spacing between rotors, and stators and the single-stage fan of reference 11 had large axial spacings. All three fans had similar instrumentation, and the data were reduced using substantially the same procedures and techniques. Highest diffusion factors for the subject fan were well below the limits encountered in the similar fans. Based on this comparison, it is improbable that stall was caused by excessive loadings on blades or vanes. The more rapid rate of diffusion near the rear of the 1st-stage rotor hub (Figure 25) may have resulted in abrupt flow separation or had an adverse effect on secondary flows which prevented attainment of the loading levels achieved by the other two fans.

Wall loadings were also investigated as a possible cause of stall. High loadings on the inner wall resulted from the use of cylindrical spacers in the flowpath to obtain desired axial spacings between blades and vanes. Inner wall curvature entering a cylindrical section increased meridional velocity; and curvature at the end of a cylindrical section reduced meridional velocity, imposing an adverse pressure gradient on the wall. Plots of meridional velocity versus axial location along the inner and outer casing walls between blade rows for the near-stall (also near-design) data point and for design conditions are presented in Figure 52. These wall velocities were calculated using the flowfield analysis procedures discussed under Data Reduction Techniques. Comparisons with values calculated from wall static pressures at the instrument stations gave good agreement with values calculated from the

flowfield analysis. Velocity levels on the inner wall between the 1st- and 2nd-stage rotors were lower than design because high loss at the hub of the 1st-stage rotor caused lower-than-design total pressure. The largest velocity deceleration (i.e., wall loading) occurred between the 1st-stage rotor and stator on the inner wall. This loading was evaluated in terms of the wall loading parameter, $1 - V_m^2 \text{ min}/V_m^2 \text{ max}$, where the $V_m \text{ min}$ occurs downstream of $V_m \text{ max}$. Maximum wall loading for the design distribution of meridional velocity was 0.580 which is much higher than previous experience. Table VII compares design wall loadings for this fan to those of other compressors that had high wall-loadings.

TABLE VII – COMPARISON OF DESIGN MAXIMUM WALL LOADING PARAMETERS

Fan	Max Wall Loading $1 - (V_m^2 \text{ min}/V_m^2 \text{ max})$	Location
Transonic Stator MCA-A (ref. 15)	0.482	hub between rotor and stator
304.8 m/sec [1000 ft/sec] (ref. 11)	0.466	hub between rotor and stator
Subject Fan	0.580	hub between rotor 1 and stator 1

The values of wall loading between the 1st-stage rotor and stator and between the 1st-stage stator and 2nd-stage rotor are plotted in Figure 53 as functions of airflow for tests with uniform inlet flow. At speeds below 94 percent of design, stalls occurred when the wall loading between the 1st-stage rotor and stator reached 0.60. Loadings at 94 percent, 100 percent, and 105 percent of design speed were concentrated between 0.55 and 0.60, but did not show a continuous trend of increasing wall loading with decreasing flow. Blade-element loss coefficient data for the hub of the 1st-stage rotor at high speeds also showed significant scatter (Figure 27). This scatter indicates that obtaining accurate measurements was a problem, probably because of large wakes from the hub of the 1st-stage rotor. In addition to this measurement difficulty, the wall loading parameter was extremely sensitive to small differences in velocity; for example, at design speed a change of 3 m/sec [9.84 ft/sec] in velocity changed the loading parameter by 0.025. The combination of measurement difficulty and parameter sensitivity probably produced the scatter in the high speed wall loading data shown in Figure 53. The data, however, is sufficiently accurate to justify the existence of extremely high wall loadings between the 1st-stage rotor exit and 1st-stage stator inlet.

The major findings of the investigation of stall at high speed with uniform inlet flow are:

- 1) The rapid-response records and radial distortion data show that the stalls were initiated at the hub.
- 2) Tests with the 1st-stage stator opened showed that stall was initiated in the first stage. Rapid-response transducer and strain-gage records also indicate that the stalls were initiated in the first stage, either in the stator or between the rotor and stator.

- 3) Rotor and stator hub diffusion factors never approached stalling levels which had been attained in other fan and compressor stages.
- 4) Loading on the hub wall between the 1st-stage rotor and stator was much higher than previous experience. Stalls occurred consistently at or near a wall loading parameter of 0.6.
- 5) System surge prevented lower flows and higher pressure ratios from being attained at high speeds with uniform inlet flow and at all speeds with hub inlet flow distortion.

Based on these findings, one possible cause of stall at high speed during tests with uniform inlet flow might be the high wall-loading on the hub between 1st-stage rotor and 1st-stage stator. This high wall-loading was primarily the result of design velocity distributions and was augmented by the velocity defect on the hub at the 1st-stage exit station. The 1st-stage rotor, however, may also have been the cause of premature stall at high speeds. The high loading in the aft region of the 1st-stage rotor hub section could have resulted in either a sudden blade section or corner flow separation of sufficient magnitude to trigger the surges observed, or might have precipitated a major flow separation from the interblade hub wall. Therefore, the high speed stall margin limitations can be attributed to the first-stage hub and interblade region, but the exact source of the problem has not been defined.

ACOUSTICALLY TREATED CONFIGURATION

Aerodynamic performance tests were conducted on the fan with a sonic inlet and acoustically treated linings on exit duct walls and with an acoustically treated ring installed in the exit duct. The sonic inlet had an adjustable centerbody whose position determined the inlet throat area (Figure 2). Performance was documented by tests with the sonic inlet centerbody in the approach, takeoff, and cruise positions. In this section of the report, total pressure losses in the sonic inlet are described and the effect of the inlet on fan performance is discussed. The discussion treats performance of the fan inlet system and of the fan alone, considering the inlet as a source of distortion.

Performance of the Sonic Inlet Device

The aerodynamic objective of the sonic inlet design was to provide a variable throat area with acceptable performance and which could be choked for approach and takeoff flow conditions. Inlet performance was assessed in terms of overall total pressure recovery, total pressure profile, degree of flow separation, and a reasonable level of turbulence at the fan face.

Measurements of inlet total pressure were made with wedge probes radially traversed at the fan face. These traverses were made at midgap between support struts for the centerbody casing. The total pressure loss of the struts was estimated and added to the measured loss of the inlet to provide a representation of the overall sonic inlet recovery. Radial profiles of total pressure recovery are shown in Figure 54 for the approach, takeoff, and cruise settings of the inlet centerbody at various levels of throat Mach number; in addition the profile obtained with the standard baseline inlet cowling is compared with the cruise configura-

tion profile. (The throat Mach number used herein was calculated from measured flow, throat area, and assumptions of uniform velocity and no boundary layer blockage.) The major difference between the profiles obtained with the baseline and cruise configurations was the pressure loss in the hub region due to the centerbody; there was no measureable loss due to the spinner used with the baseline configuration.

In general, none of the profiles indicated flow separation, and the trends and levels of pressure loss were reasonable. Mass averaged total pressure recoveries for these profiles, together with calculated strut losses, are compared to design predictions in Table VIII.

TABLE VIII - INLET TOTAL PRESSURE RECOVERIES COMPARED TO DESIGN PREDICTIONS

CONFIGURATION	THROAT MACH NO.	PERCENT		INLET RECOVERY (Estimated Strut) (Loss Included)	PREDICTED RECOVERY
		DESIGN CORRECTED FLOW	MEASURED MASS AVG. RECOVERY		
Approach	0.8	76.6	0.9883	0.9879	—
	0.9	79.1	0.9858	0.9853	0.9700
	1.0	79.7	0.9772	0.9767	—
Takeoff	0.8	89.5	0.9857	0.9851	—
	0.9	92.2	—	—	0.9750
	1.0	92.9	0.9763	0.9756	—
Cruise	0.65	96.3	0.9831	0.9822	—
	0.71	101.0	0.9797	0.9787	0.9870
Baseline Inlet	0.67	100.	0.9957		

Recoveries were higher than predicted for approach and takeoff configurations and lower than predicted for the cruise configuration.

The values of total pressure recovery given in reference 3 (data report) were based on measurements and were not adjusted for estimated strut losses. Nonadjusted values of mass-averaged recovery are shown as functions of inlet corrected flow in Figure 55 for the cruise, takeoff, and approach positions. This figure shows that for the same throat Mach number the approach configuration gave the highest recovery and the cruise configuration the lowest recovery.

Axial distributions of wall static pressure on the inner and outer surface of the sonic inlet are shown in Figure 56 for the choked condition at takeoff and approach positions. Static pressures at lower throat Mach numbers are shown in Figure 57 for the takeoff, approach, and cruise configurations.

The lowest static pressure (highest local Mach number) on the centerbody occurred with the sonic inlet choked in the takeoff configuration (Figure 56). A region of high loss near the hub (approximately 10 percent span) was seen at this choked, takeoff condition (Figure 54).

The lowest static pressures on the outer wall occurred at a throat Mach number of 0.71 with the centerbody in the cruise position (Figure 57). A region of high loss near the outer casing was seen for this operating condition (Figure 54).

Predicted and test static pressure distributions can be compared in Figures 57 for the cruise and approach positions. Predictions for the approach position were based on an annular diffuser flow analysis and were in good agreement with test values. The only significant difference occurred forward of 1.06 meters [41.8 inches] upstream of the fan face where the calculated contour had been blended into an assumed capture stream tube.

Predictions for the cruise position were based on a potential-flow analysis and were less accurate. This analysis operated on a limited number of sources and sinks along walls. The strength of these sources and sinks was determined by their spacing. In this application the spacing became too large, and the boundary condition of zero velocity normal to flowpath walls was not met. The high local velocity on the outer wall, which led to the poor pressure recovery, was not predicted. Despite this, no serious flow separation was noted.

The location of the lowest static pressure on the centerbody for all configurations was at the minimum or throat-area location. For the approach configuration and for the takeoff configuration at high mach number, the lowest static pressure occurred on both the centerbody and outer surfaces at the same axial location, corresponding to the minimum area. The lowest static pressure did not occur at the same axial location for both surfaces for the cruise configuration or for the takeoff configuration at lower Mach numbers, indicating that the maximum velocity from centerbody to outer casing was not radial.

Power-spectral-density plots — which are measurements of flow turbulence — were obtained for each sonic inlet position and converted to ΔP rms values. These plots for ten radial positions for each configuration are presented in reference 3; a typical plot at three percent span is shown in Figure 58. Spanwise profiles of turbulence for the design conditions are shown in Figure 59; the rotor-blade spikes have been eliminated from the plots. To provide a basis for comparison, the rms level for a typical, low turbulence, subsonic inlet is included in Figure 59.

The turbulence level outside the boundary layer with the approach and takeoff configurations was moderately higher than that with the typical subsonic inlet. For the cruise configuration, the turbulence levels outside the boundary layer were appreciably higher than for the approach and takeoff configurations. This cruise level was higher because the throat of this configuration was closer to the instrumentation and the turbulence generated at the throat had less distance in which to decay. The turbulence levels near the centerbody and cowl surfaces were generally higher than those in the free-stream because of the turbulence associated with shear in the boundary layer.

System Performance of Fan and Sonic Inlet

Performance tests were conducted with the sonic inlet in the approach, takeoff, and cruise configurations. In addition to the customary constant-speed-line data points, constant flow lines were run by adjusting the throttle to change fan pressure ratio while simultaneously adjusting speed to hold the desired corrected flow constant.

Overall performance of the system (i.e., fan and sonic inlet combined) is shown in Figures 60a, 60b, and 60c; performance with the baseline inlet (shakedown data) is shown by solid curves for comparison. The efficiency of the system is shown for each data point. Lines of constant efficiency were drawn for baseline data to provide a more convenient means of assessing efficiency penalties due to the sonic inlet. The sonic inlet in the approach position, Figure 60a, reduced efficiency by approximately five percentage points at a pressure ratio of 1.3 at 77 percent of design corrected speed (open throttle), which gave an inlet throat Mach number of 1.0. At an inlet Mach number of approximately 0.95 and with the pressure ratio increased to 1.42, the efficiency reduction decreased to approximately 3.5 percentage points. At lower flows and throat Mach number, the efficiency reduction was approximately two percentage points. For a throat Mach number of 0.9, the efficiency reduction near stall was less than two percentage points.

The system efficiency with the sonic inlet in the takeoff position at a throat Mach number of 1.0, Figure 60b, was approximately five percentage points lower than the baseline at open throttle. The efficiency penalty reduced to approximately two points near stall.

The efficiency penalty with the inlet in the cruise position, Figure 60c, was approximately 1.5 percentage points at design speed except at wide-open throttle where the efficiency penalty was approximately 4.5 percentage points.

Flow capacity of the system was reduced by approximately two percent at high speed. This reduction in flow capacity corresponded to the drop in total pressure recovery of the sonic inlet, but gave about the same corrected flow at the fan face as the baseline inlet performance test.

When compared to the baseline fan, a stall margin of minus two percent was obtained with the inlet/fan system with the centerbody in the approach position. With the centerbody in the takeoff and cruise positions, the comparative stall margins were minus one percent. These effects on stall margin would be acceptable if the fan had achieved design stall margin with the baseline inlet. A comparison of stall lines with and without the sonic inlet device is presented in Figure 61.

Performance of the Fan Alone

Overall performance of the fan, based on mass-flow averaged total pressure at the face of the fan, is shown in Figures 62a, 62b and 62c; performance with the baseline inlet (shakedown data) is shown for comparison for all three configurations, the pressure ratio, efficiency, and flow values were essentially the same as for the baseline inlet, and the stall line was, within measuring accuracy, the same as for the shakedown tests, Figure 63.

Spanwise profiles of pressure ratio (Figure 64) were nearly the same as for the baseline, except that the 1st-stage rotor produced higher pressure ratios locally at the hub and tip. Efficiency profiles were also similar, as shown in Figure 65. The higher efficiencies at the hub and tip of the 1st-stage rotor and the first stage accompanied the higher pressure ratios shown in Figure 64. The second-stage efficiency was also higher.

Blade-element spanwise parameters for the 1st-stage and 2nd-stage rotors and stators (Figures 66, 67, 68 and 69) were not significantly different from the baseline parameters. Figure 70 shows the efficiency and pressure ratios at the fan exit. The unshaded symbols represent the pressure ratio along streamlines from fan inlet to fan exit. The shaded symbols are ratios of local exit total pressure divided by the average inlet total pressure. The profiles of total pressure at the fan exit were nearly the same for the baseline tests.

The efficiency of the fan-alone during the sonic inlet tests was higher than that attained during either the shakedown or performance tests (Figure 71). In an effort to qualify these differences, checkpoints were run with the baseline inlet reinstalled. The efficiencies obtained during the checkpoint tests (Figure 71) did not reach the levels obtained during either the sonic inlet or the shakedown baseline tests. The checkpoint tests differed from the original performance tests in that the plenum was not used and the discharge duct had acoustically treated walls (tape removed) and the acoustic ring. These differences should have had little effect on the measured efficiency. For the checkpoint tests, corrected flow was estimated using a correlation of corrected flow versus the ratio of wall static pressure to free-stream pressure. These estimated flows are considered less accurate than those obtained from measurements made with the plenum and calibrated nozzle.

Exit Duct Loss

Total pressure recovery for the fan discharge duct is shown as a function of fan exit corrected flow in Figure 72. Recoveries are shown for configurations both with and without the acoustically treated walls and acoustic ring installed. The shaded symbol represents the near-design point with a total exit duct recovery of 0.9655. In this operating regime the acoustically treated exit duct gave a total pressure recovery approximately 1.3 percent lower than the untreated duct. The radial distribution of recovery for the additional acoustic treatment in the duct is shown in Figure 73. The acoustic ring created the larger portion of the loss.

REMARKS

The subject fan had good efficiency, but the high speed stall margin was inadequate. Although the exact cause of premature, high-speed stall or surge was not defined, the problem was shown to originate in the hub region of the first stage. The most probable source of premature stall was the high wall-loading on the hub between the 1st-stage rotor exit and the 1st-stage stator inlet. To minimize noise, the fan was designed with large axial spacings between blade rows with provisions for reducing this axial spacing by removal of spool pieces. Hub wall convergence was used across the blade rows to obtain acceptable loadings on the rotor and stator hub blade elements. These design concepts led to severe curvature at the entrance and exit of the intrablade row spaces and to high hub-wall loadings, particularly between the 1st-stage rotor and 1st-stage stator. In addition, the loading on the 1st-stage rotor hub was shifted rearward to control flow area margin for this blade section. A design for an actual engine application would not require adjustable axial spacings, therefore, more gradual wall curvatures could be used and a more optimum balance between wall loadings and hub blade element loadings achieved.

High loss at the hub of the 1st-stage rotor caused a velocity defect which contributed to the wall loading problem. A redesigned rotor root with a smoother rate of diffusion on blade surfaces should reduce the hub loss, thereby raising the velocity level and reducing wall loading at the hub.

SUMMARY OF RESULTS

- 1) The Quiet Two-Stage Fan attained an efficiency of 86.4% at design speed with the standard inlet cowling.
- 2) Based on a hypothetical operating line through the design point, the subject fan had a negative stall margin at all speeds above 90 percent of design speed, but had a 20 percent stall margin at 63 percent of design speed. Premature surge limited the flow range at high speed. This surge was caused by excessive loading on the hub wall between the 1st-stage rotor and stator, by poor flow conditions in the hub of the 1st-stage rotor, or by some combination of these factors.
- 3) Opening the 1st-stage stator five degrees increased the design speed stall pressure ratio from 1.87 to 1.90, but reduced fan efficiency 1.5 percentage points.
- 4) At design speed a 0.155 tip-radial distortion ($\Delta P/P_{max}$) resulted in a stall margin of four percent over the stall limit with uniform inlet flow, and reduced peak efficiency one percentage point. At 63 percent of design speed, tip-radial distortion reduced the stall margin appreciably. The tip distortion was completely attenuated, principally by the first stage.
- 5) At design speed and at lower speeds, a 0.17 hub-radial distortion ($\Delta P/P_{max}$) reduced stall margin four percent in comparison to the stall limit for uniform inlet flow. Fan peak efficiency at design speed was reduced eight percentage points. The hub distortion was partially attenuated, principally by the second stage.

- 6) At design speed, the fan efficiency with the sonic inlet in the cruise position was 1.5 to 4.5 percentage points lower than with the baseline configuration; the sonic inlet recovery was 0.9819 to 0.9796.
- 7) The effects on stall margin of the sonic inlet in approach, takeoff, and cruise positions were small. These effects on stall margin would be acceptable if the fan had achieved the design stall margin.
- 8) The addition of the acoustic ring and wall treatment reduced aft duct recovery 1.3 percentage points at near-design cruise operating conditions.

APPENDIX

SYMBOLS AND PARAMETERS

A	—	area, meters ² [inches ²]
A/A*	—	ratio of actual area to critical area (where local Mach number is 1.0)
D	—	diffusion factor or diameter
E	—	excitations per rotor revolution
EPNdB	—	effective perceived noise level, decibels
Hz	—	hertz (cycles per second)
ID	—	inside diameter, meters [inches]
i _{ss}	—	incidence angle, angle between inlet air direction and line tangent to blade suction surface at leading edge, degrees
i _m	—	incidence angle, angle between inlet air direction and line tangent to the mean camber line at leading edge, degrees
L	—	length
MCA	—	multiple-circular-arc
N	—	rotor speed, rpm
OD	—	outside diameter, meters [inches]
P	—	total pressure, N/m ² [lbf/ft ²]
p	—	static pressure, N/m ² [lbf/ft ²]
psi	—	pounds per square inch
T	—	total temperature, °K [°R]
V	—	velocity, m/sec (ft/sec)
V _m	—	meridional velocity ($V_r^2 + V_z^2$) ^{1/2} , m/sec [ft/sec]
W	—	mass flow rate, kg/sec [lbm/sec]
β	—	absolute air angle, $\cot^{-1}(V_m/V_\theta)$, degrees
β*	—	metal angle, on conical surface, between tangent to mean camber line and axial direction at leading edge and trailing edge; degrees
Δ Prms	—	differential root-mean-squared pressure integrated from the power spectral density measurements
δ	—	ratio of total pressure to standard pressure of 10.125×10^4 N/m ² [2116 lbf/ft ²]
δ°	—	deviation angle, exit air angle minus tangent to blade mean camber line at trailing edge, radians [degrees]
ε	—	angle between tangent to streamline projected on meridional plane and axial direction, degrees

PRECEDING PAGE BLANK NOT FILMED

η_{ad}	—	adiabatic efficiency, percent
θ	—	ratio of total temperature to standard temperature of 288.1°K [518.6°R]
$\bar{\omega}$	—	total pressure loss coefficient
65/CA	—	65 series thickness distribution on a circular arc mean line

Subscripts

des	—	design
r	—	radial direction
z	—	axial direction
θ	—	tangential direction
0	—	plenum chamber
4	—	instrument plane upstream of rotor 1
5	—	station at rotor 1 leading edge
6	—	station at rotor 1 trailing edge
7	—	instrument plane downstream of rotor 1
9	—	station at stator 1 leading edge
10	—	station at stator 1 trailing edge
11	—	instrument plane downstream of stator 1
12	—	station at rotor 2 leading edge
13	—	station at rotor 2 trailing edge
14	—	instrument plane downstream of rotor 2
15	—	instrument plane upstream of stator 2
16	—	station at stator 2 leading edge
17	—	station at stator 2 trailing edge
18	—	instrument plane downstream of stator 2
22	—	instrument plane downstream acoustic ring

Superscript

—	relative to moving blades
---	---------------------------

PERFORMANCE PARAMETERS

Incidence angle based on suction surface metal angle

$$i_{ss} = \beta'_5 - \beta^*_{ss5} \quad (\text{rotor 1})$$

$$i_{ss} = \beta_9 - \beta^*_{ss9} \quad (\text{stator 1})$$

$$i_m = \beta'_5 - \beta^*_{m5} \quad (\text{rotor 1})$$

$$i_m = \beta_9 - \beta^*_{m9} \quad (\text{stator 1})$$

a) Deviation angle

$$\delta^\circ = \beta'_6 - \beta^*_{66} \quad (\text{rotor 1})$$

$$\delta^\circ = \beta_{10} - \beta^*_{10} \quad (\text{stator 1})$$

b) Diffusion factor

$$D = 1 - \frac{V'_6}{V'_5} + \frac{r_6 V_{\theta 6} - r_5 V_{\theta 5}}{(r_6 + r_5) \sigma V'_5} \quad (\text{rotor 1})$$

$$D = 1 - \frac{V_{10}}{V_9} + \frac{r_9 V_{\theta 9} - r_{10} V_{\theta 10}}{(r_9 + r_{10}) \sigma V_9} \quad (\text{stator 1})$$

c) Loss coefficient

$$\bar{\omega} = \frac{P'_5 \left[\frac{T'_6}{T'_5} \right]^{\frac{\gamma}{\gamma-1}} - P'_6}{P'_5 - P_5} \quad (\text{rotor 1})$$

$$\bar{\omega} = \frac{P_9 - P_{10}}{P_9 - P_9} \quad (\text{stator 1})$$

d) Adiabatic efficiency

$$\eta_{ad} = \frac{\left[\frac{P_6}{P_5} \right]^{-\frac{\gamma-1}{\gamma}}}{\left[\frac{T_{10}}{T_0} \right]^{-1}} \quad (rotor 1)$$

$$\eta_{ad} = \frac{\left[\frac{P_{10}}{P_5} \right]^{-\frac{\gamma-1}{\gamma}}}{\left[\frac{T_{10}}{T_0} \right]^{-1}} \quad (stage 1)$$

e) Stall margin

$$SM = \left[\left(\frac{P_{18}/P_0}{W\sqrt{\theta_0}/\delta_0} \right)_{Stall} \left(\frac{W\sqrt{\theta_0}/\delta_0}{P_{18}/P_0} \right)_{Reference Point or Operating Point} \right]^{100}$$

Note: For cases with inlet flow distortion or for other cases where flow is evaluated at the fan inlet, replace the subscript 0 with 5.

f) Flow coefficient $\phi = \frac{V_z}{U_{\text{mean flow}}}$

g) Pressure coefficient $\psi = \frac{\Delta H_{\text{id}}}{U_{\text{mean}}^2}$

$$= \frac{\eta_{\text{ad}} \Delta T_{\text{actual}} C_p J g_c}{U_{\text{mean flow}}^2}$$

REFERENCES

1. Brines, G. L. : "Studies for Determining the Optimum Propulsion System Characteristics for use in a Long Range Transport Aircraft," NASA CR-120950, PWA-4449, July 1972.
2. Messenger, H. E. : Ruschak, J. T. and Sofrin, T. G. : "Two Stage Low Noise Advanced Technology Fan. I. Aerodynamic, Structural, and Acoustic Design", NASA CR-134662, PWA-5050, September, 1974.
3. Harley, K. G. and Odegard, P. A. : "Two-Stage, Low Noise Advanced Technology Fan, Volume II-Aerodynamic Data" NASA CR-134828, PWA-5258, September 1975.
4. Sofrin, T. G. and Riloff, N.: "Two-stage, Low Noise Advanced Technology Fan, Volume III – Acoustic Data Report", NASA CR-134829, PWA 5303, September 1975.
5. Sofrin, T. G. and Riloff, N.: "Two-Stage, Low Noise Advanced Technology Fan – V. Final Acoustic Report", NASA CR134831, PWA-5305, September 1975.
6. Keenan, M. J., and Bartok, J. A.: "Experimental Evaluation of Transonic Stators – Final Report," NASA CR-72298, PWA-3470, 1969.
7. Tyler, J. M. and Sofrin, T. G. : "Axial Flow Compressor Noise Studies," SAE Trans. Vol. 70, pp. 309-322, 1962.
8. Glawe, G. E.; Simms, F. S. and Stickney, T. N. : "Radiation and Recovery Corrections and Time Constants of Several Chromel-Alumel Thermocouple Probes at High Temperatures in High Velocity Gas Streams," NACA TN 3766, Oct. 1956.
9. Hanson, A.G. and Herzig, H. Z.: "Secondary Flows and Three-Dimensional Boundary Layer Effects, Aerodynamic Design of Axial-Flow Compressors," NASA SP-36, 1965, Ch. XV. pp. 385-411.
10. Monsarrat, N. T.; Keenan, M. J. and Tramm, P. C., "High Loading Low-Speed Fan Study – I. Design," NASA CR-72536, PWA-3535, July 1969.
11. Harley, K. G., Odegard, P. A., and Burdsall, E. A.: "High Loading Low Speed Fan Study – IV. Data and Performance with Redesign Stator and Including a Rotor Tip Casing Treatment," NASA CR-120866, PWA-4326, July 1972.
12. Katsanis, T. : "Fortran Program for Calculating Transonic Velocities on a Blade Stream Surface of a Turbomachine," NASA TN D-5427, Sept. 1969.
13. Messenger, H. E. and Keenan, M. J.: "Two Stage Fan – II. Data and Performance with Redesigned Second Stage Rotor Uniform and Distorted Inlet Flows," NASA CR-134710, PWA-5087, Oct. 1974.

PRECEDING PAGE BLANK NOT FILMED

14. Keenan, M. J. and Burdsall, E. A.: "High Loading, Low Speed Fan Study - V. Final Report," NASA CR-12 1138, PWA-4517, April 1973.
15. Keenan, M. J.; Harley, K. G. and Bogardus, G. A.: "Experimental Evaluation of Transonic Stators - Data and Performance Report, Multiple-Circular-Arc Stator A", NASA CR-5421, PWA-3260, 1968.
16. Bullock, R.O.; Wilcox, W.W.; and Moses, J.J.: "Experimental and Theoretical Studies of Surging in Continuous Flow Compressors", NACA Rep. 861, 1946. (Supersedes NACA TN 1213).

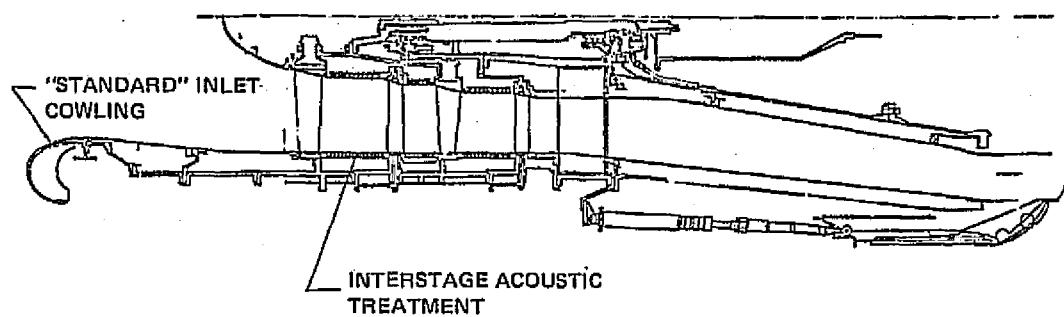


Figure 1 Two-Stage Fan, Baseline Configuration

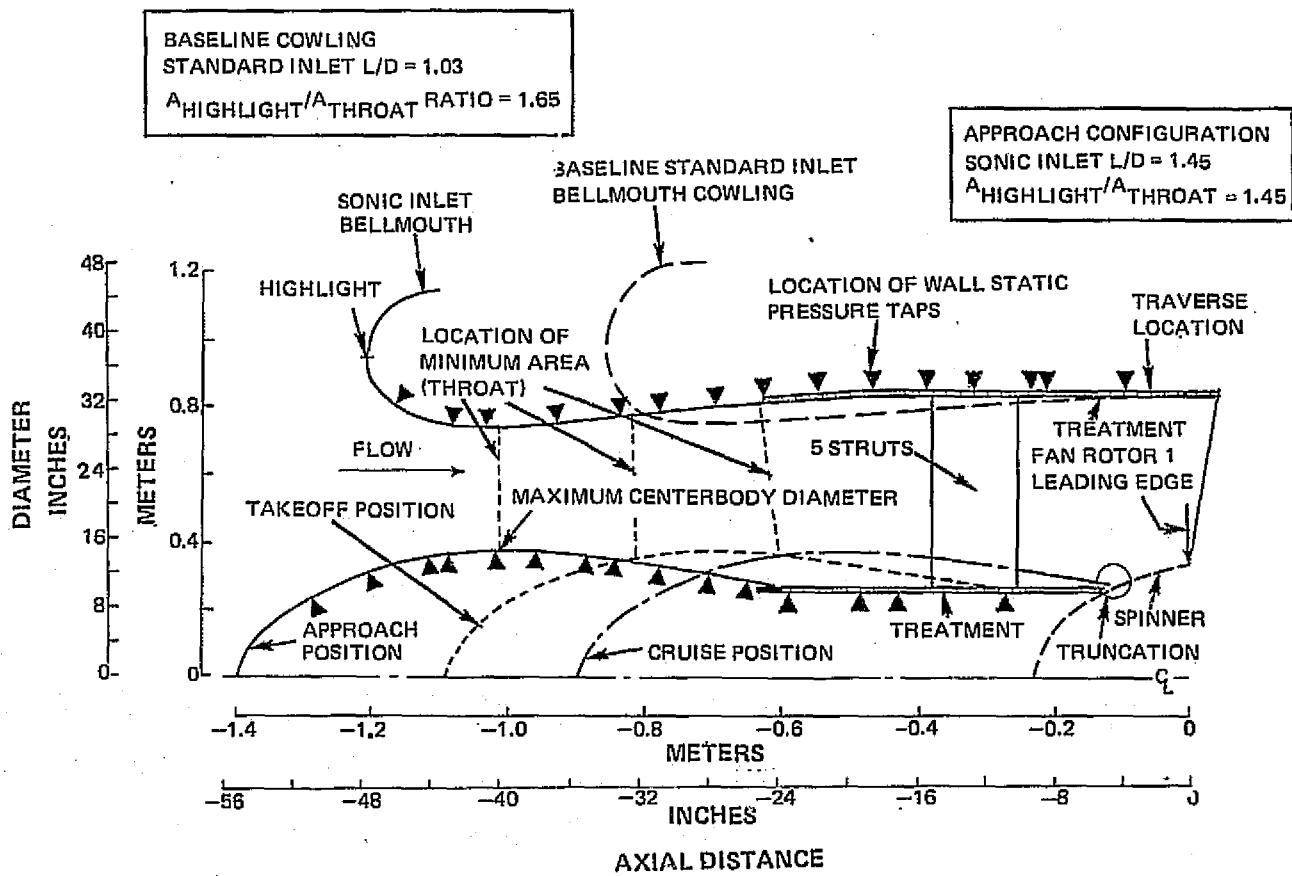


Figure 2 Baseline Standard and Sonic Inlet Geometries

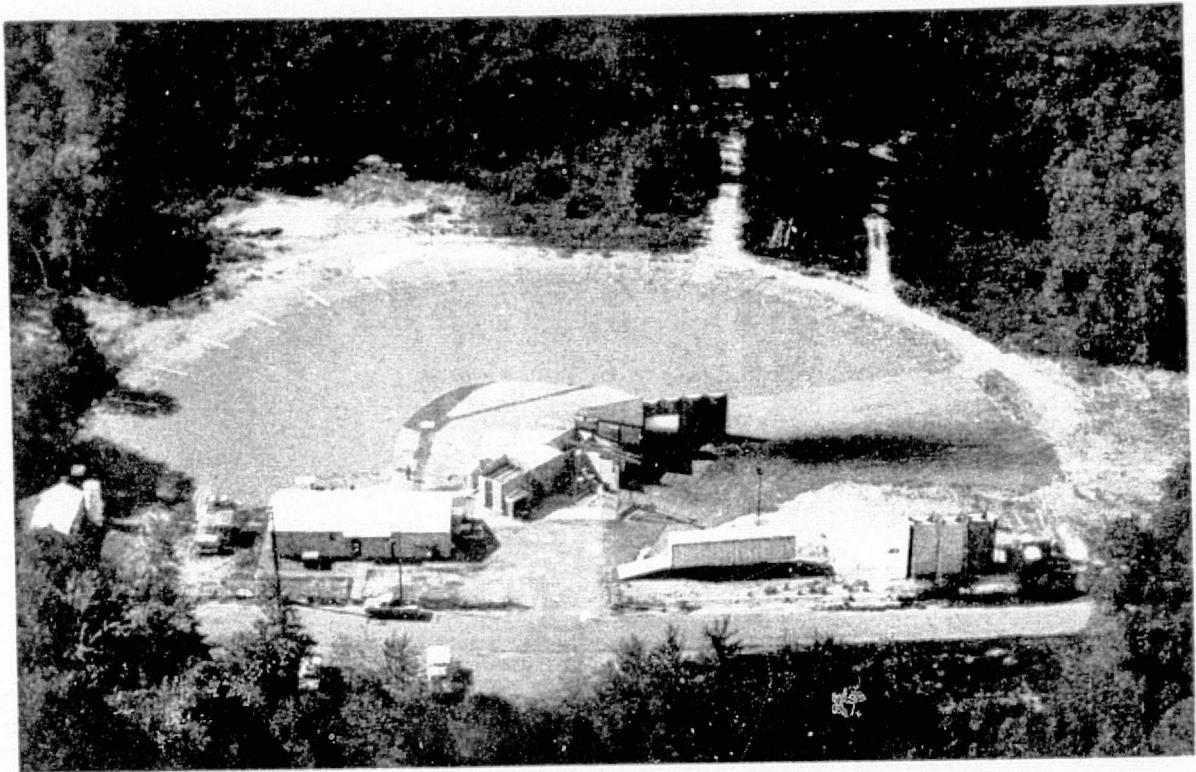


Figure 3 Aerial View of Outdoor Test Facility

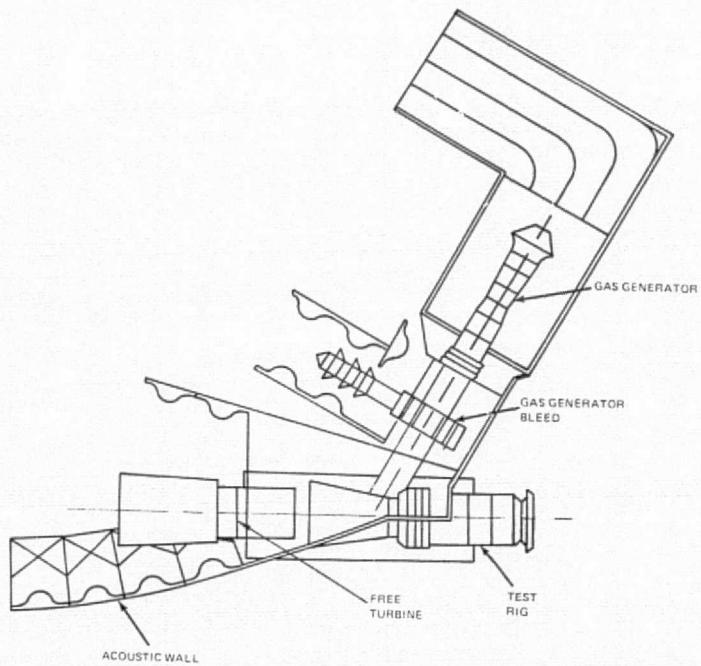
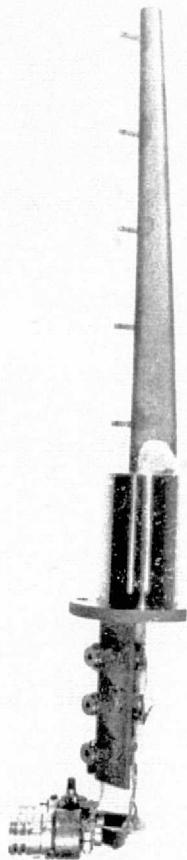
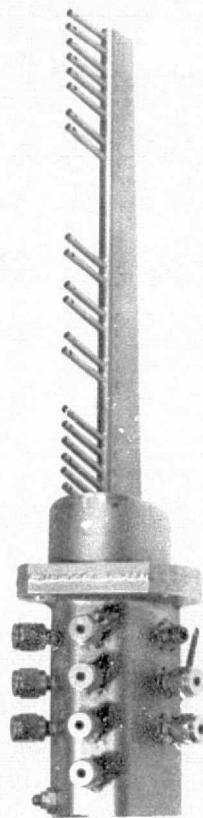


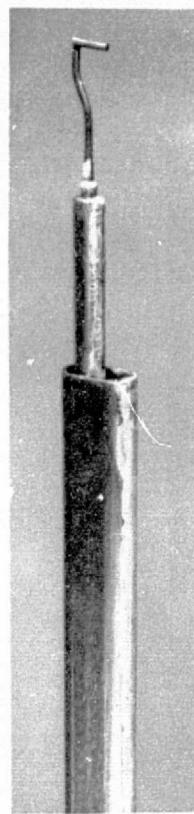
Figure 4 Schematic of Fan Rig, Gas Generator and Free-Turbine



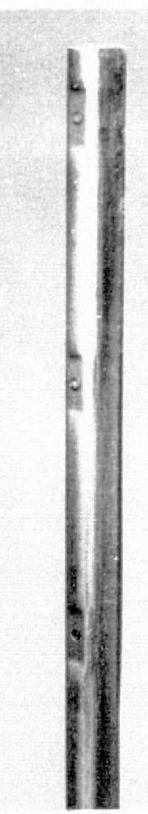
A. Fan Inlet Total Pressure Probe



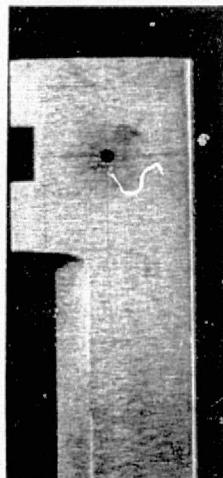
B. Stator Exit Temperature /Pressure Rake



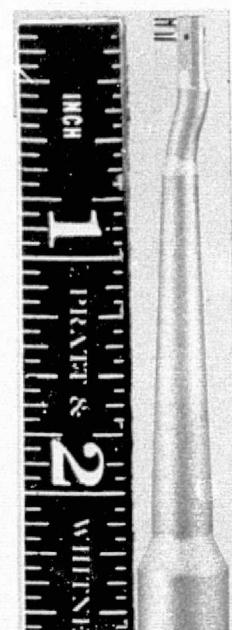
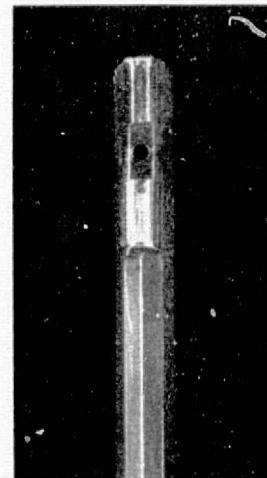
C. R1 L.E. Total Pressure Kulite Probe



D. Rotor T. E. Total Pressure Kulite Probe



E. Fan Inlet & Stator Exit Traverse Wedge Probes



F. Stator 1 Exit NASA Combination Probe

Figure 5 Typical Instrumentation

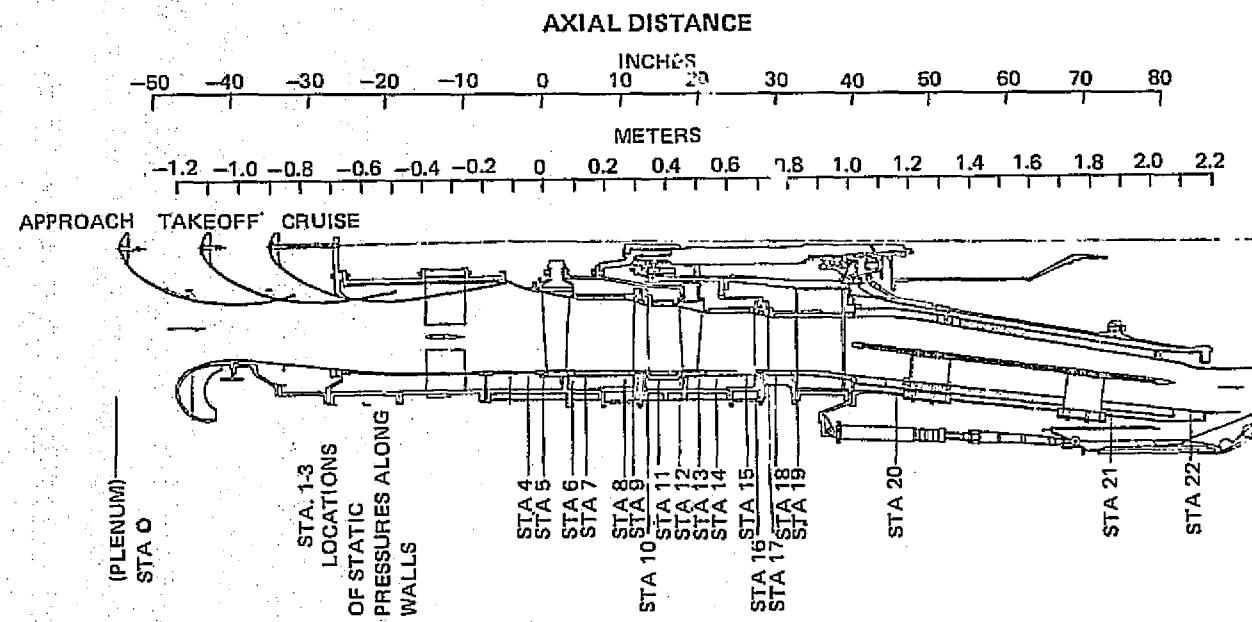


Figure 6 Axial Location of Instrumentation and Calculation Planes

- WALL STATIC PRESSURE
- ◇ WEDGE PROBE ~RADIAL TRAVERSE
- △ COMBINATION PROBE ~RADIAL TRAVERSE

- TOTAL PRESSURE AND TOTAL TEMPERATURE RADIAL RAKE, CIRCUMFERENTIAL TRAVERSE
- TOTAL PRESSURE RAKE

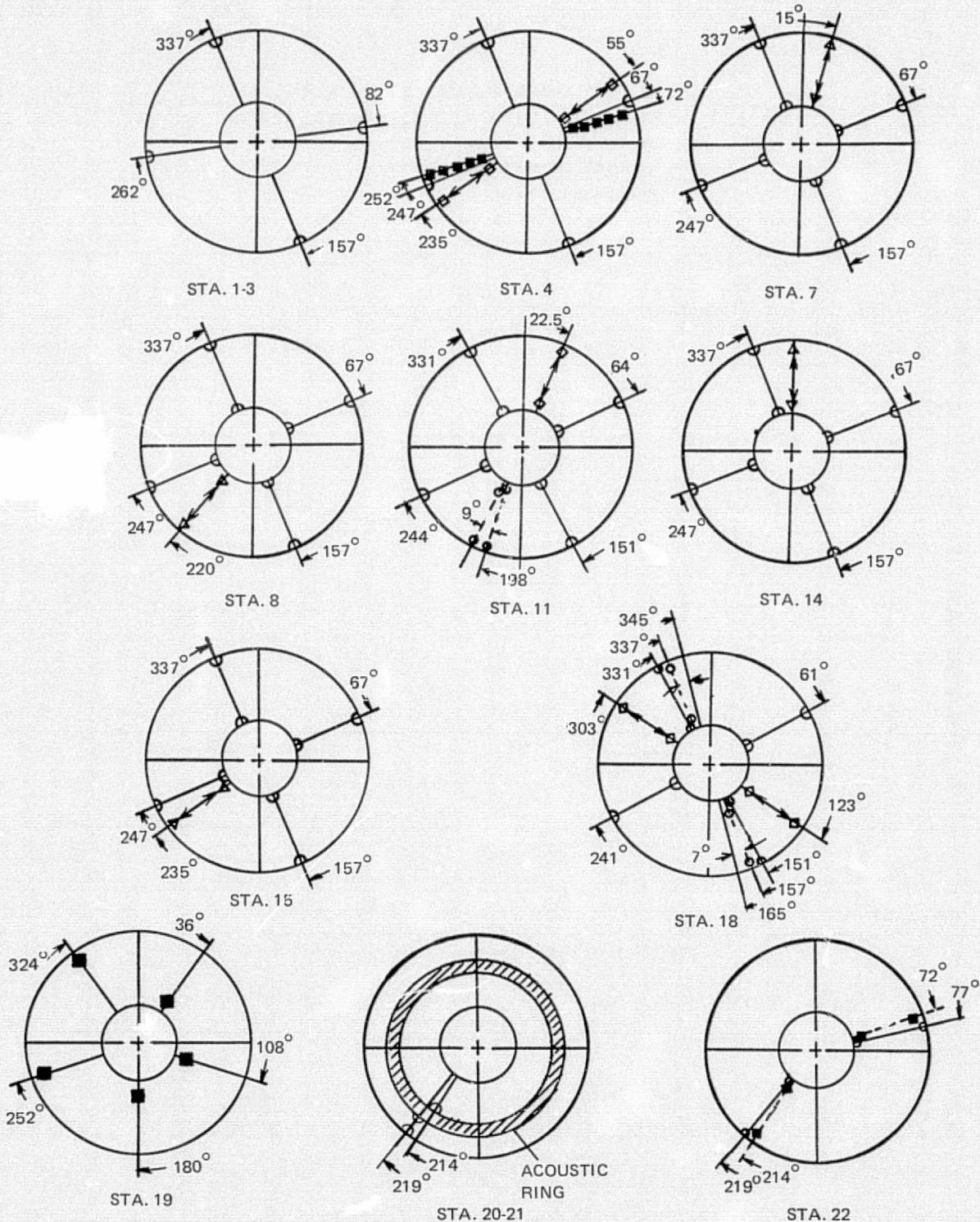


Figure 7 Circumferential Location of Instrumentation

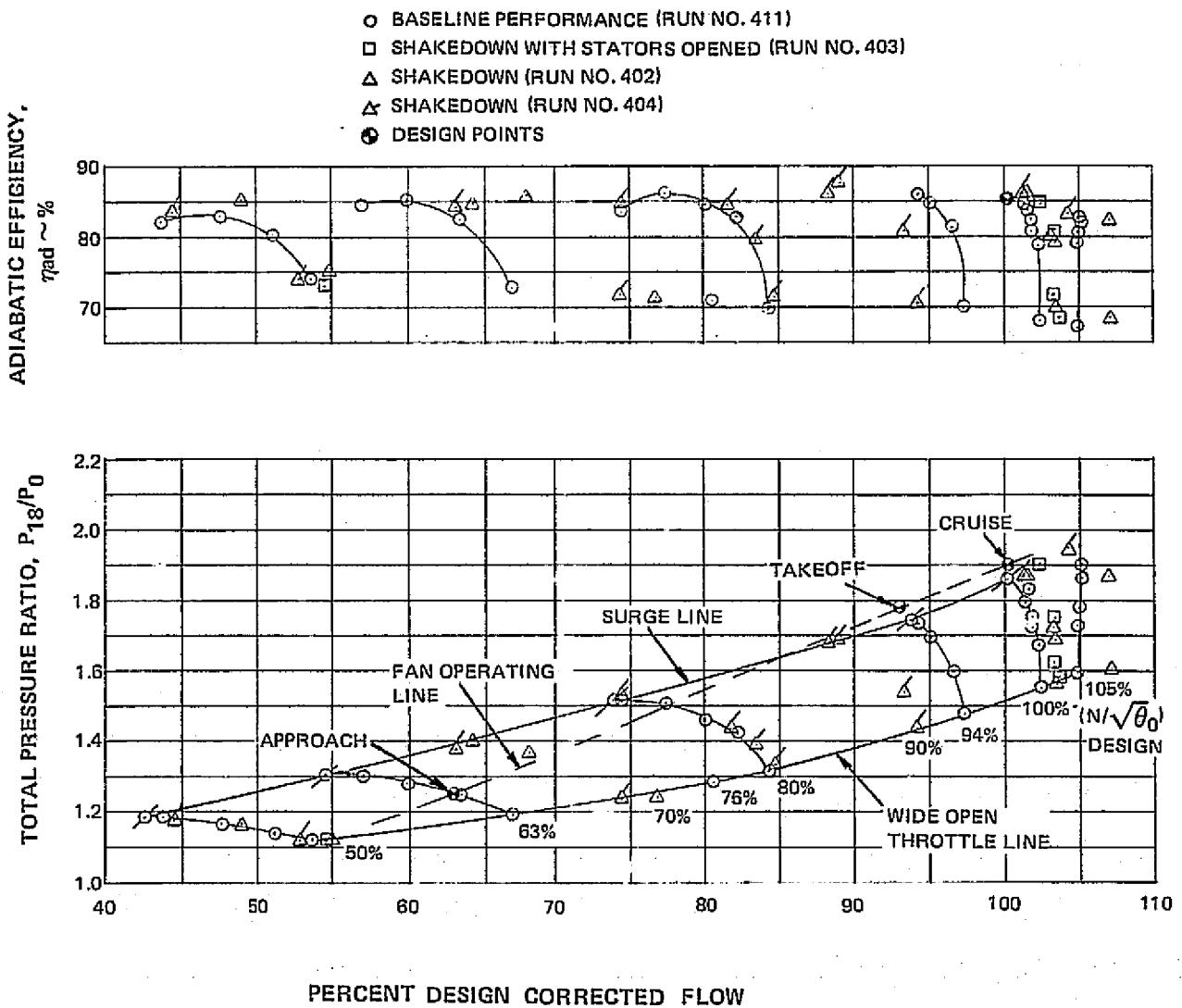


Figure 8 Fan Overall Performance With Uniform Inlet Flow

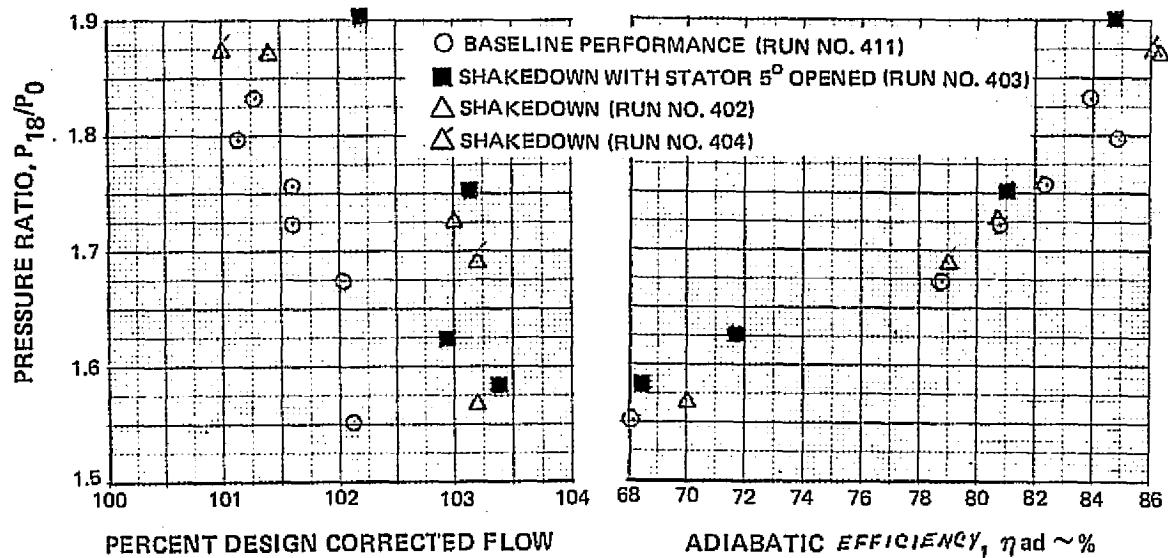


Figure 9 Fan Overall Performance at Design Speed With Uniform Inlet Flow

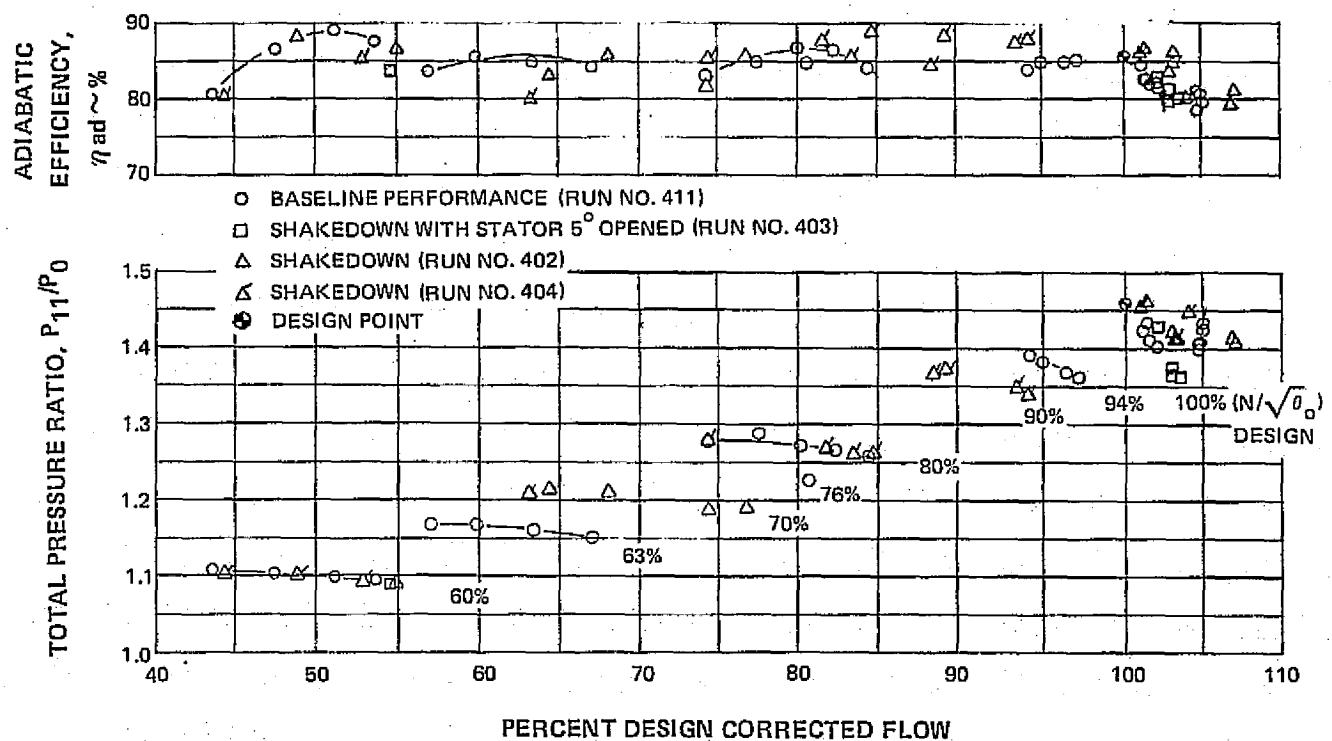


Figure 10 First-Stage Performance With Uniform Inlet Flow

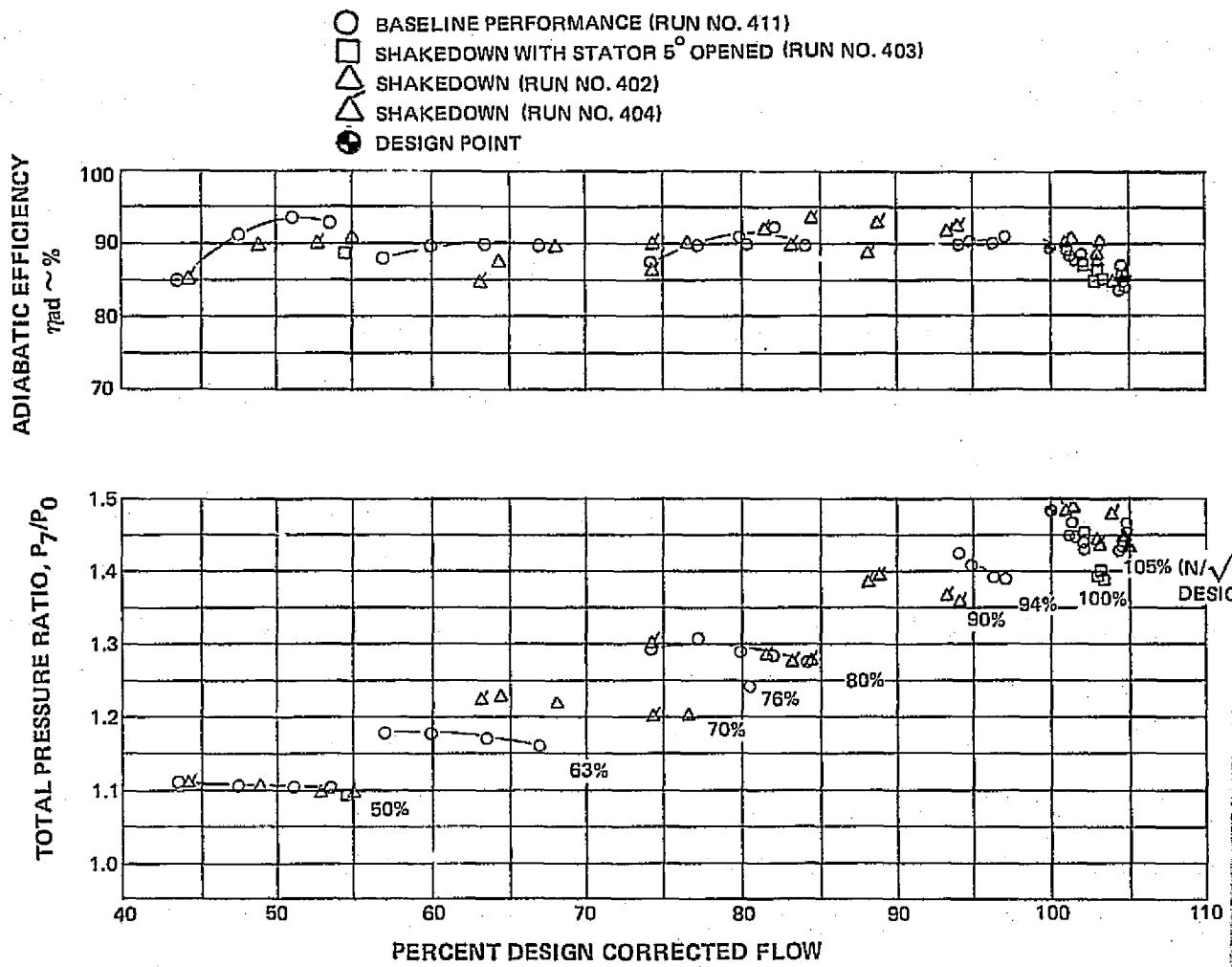
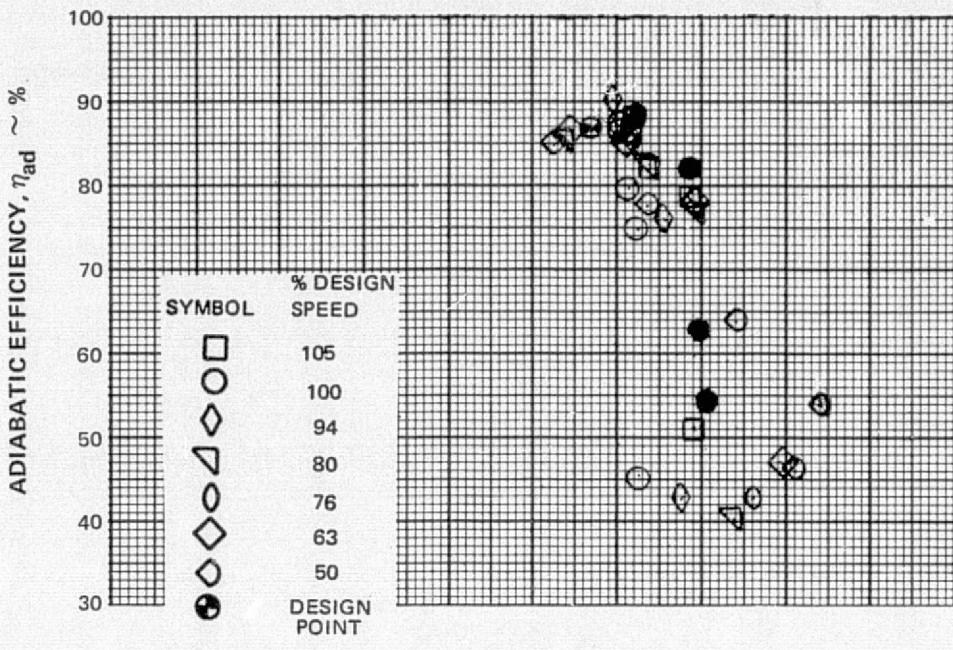


Figure 11 First-Stage Rotor Performance With Uniform Inlet Flow

"Page missing from available version"



OPEN SYMBOL – BASELINE PERFORMANCE (RUN NO. 411)

SOLID SYMBOL – SHAKEDOWN, STATOR 5° OPENED (RUN NO. 403)

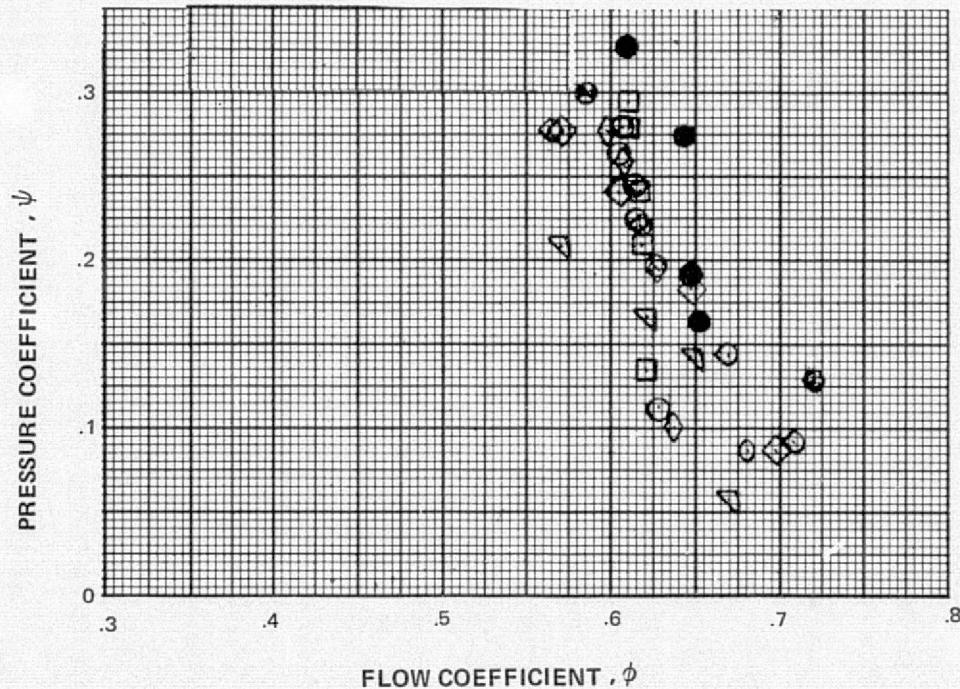


Figure 14 Pressure Coefficient and Adiabatic Efficiency Versus Flow Coefficient for Uniform Inlet Flow, Second Stage

PRECEDING PAGE BLANK NOT FILMED

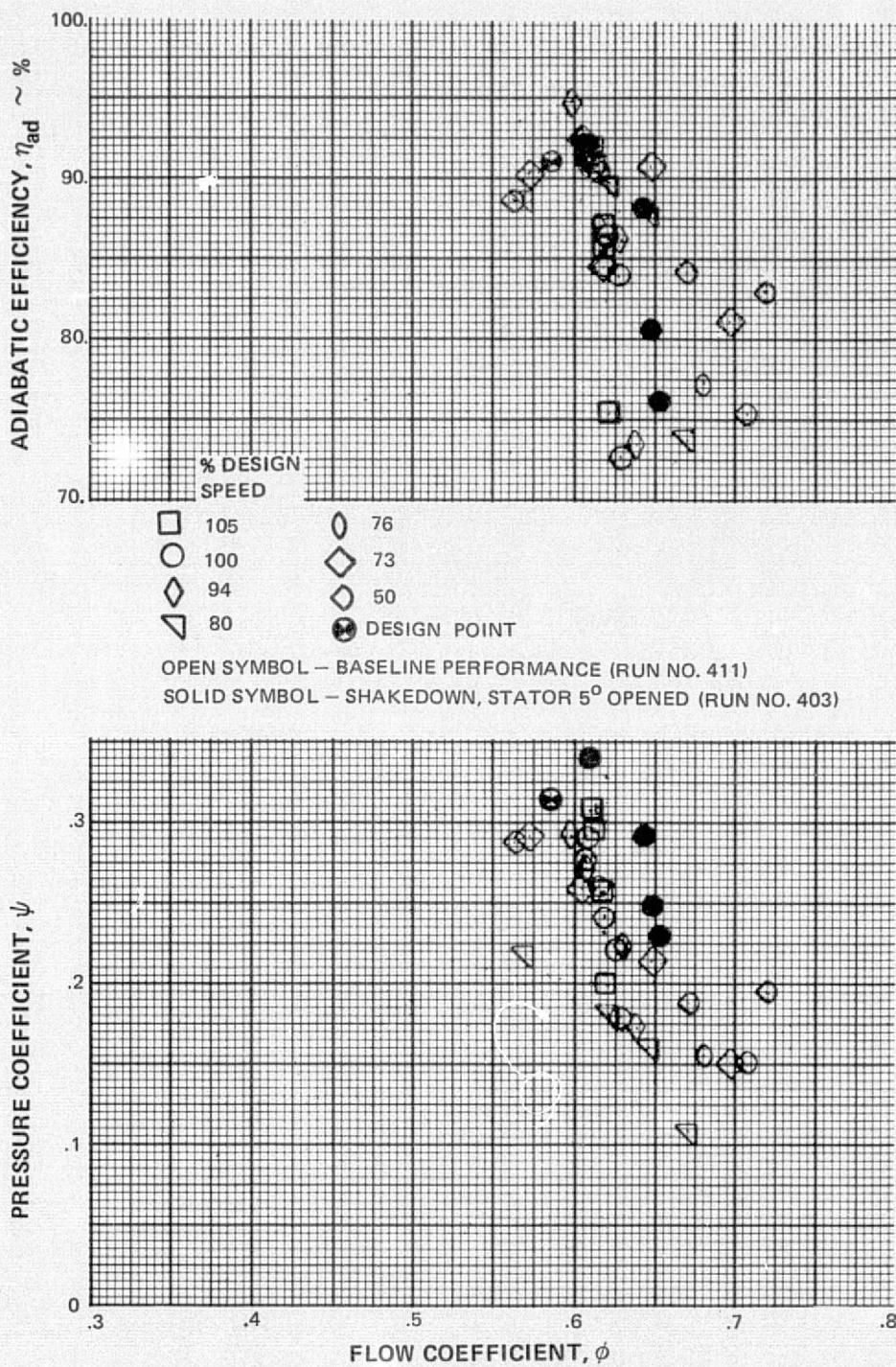


Figure 15 Pressure Coefficient and Adiabatic Efficiency Versus Flow Coefficient For Uniform Inlet Flow, Second-Stage Rotor

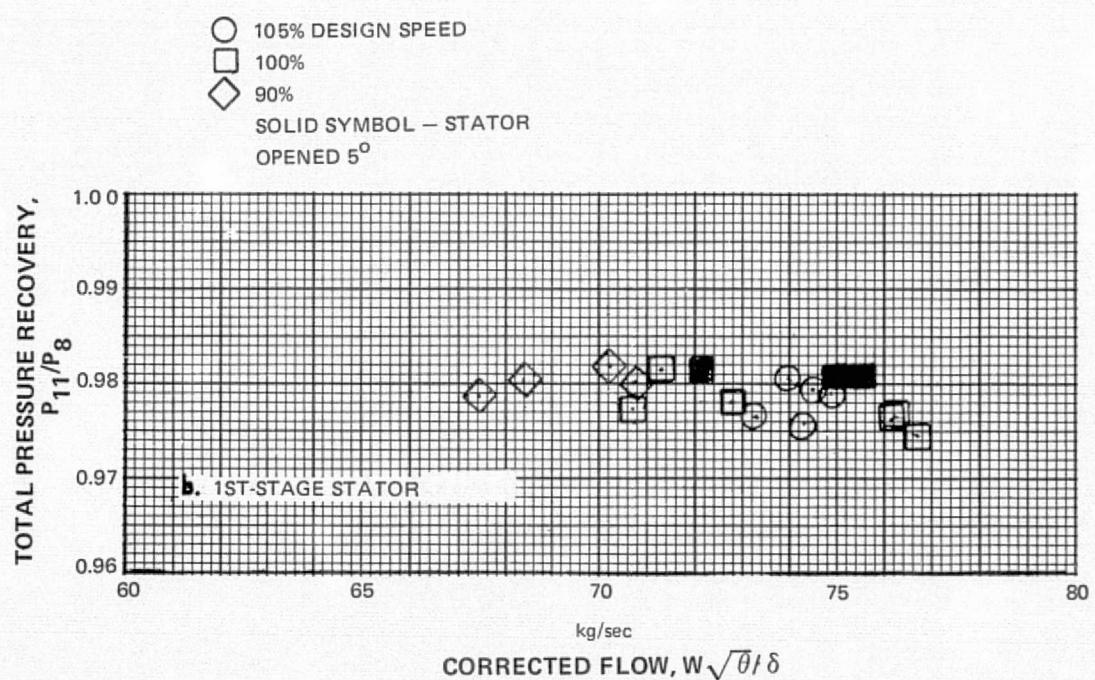
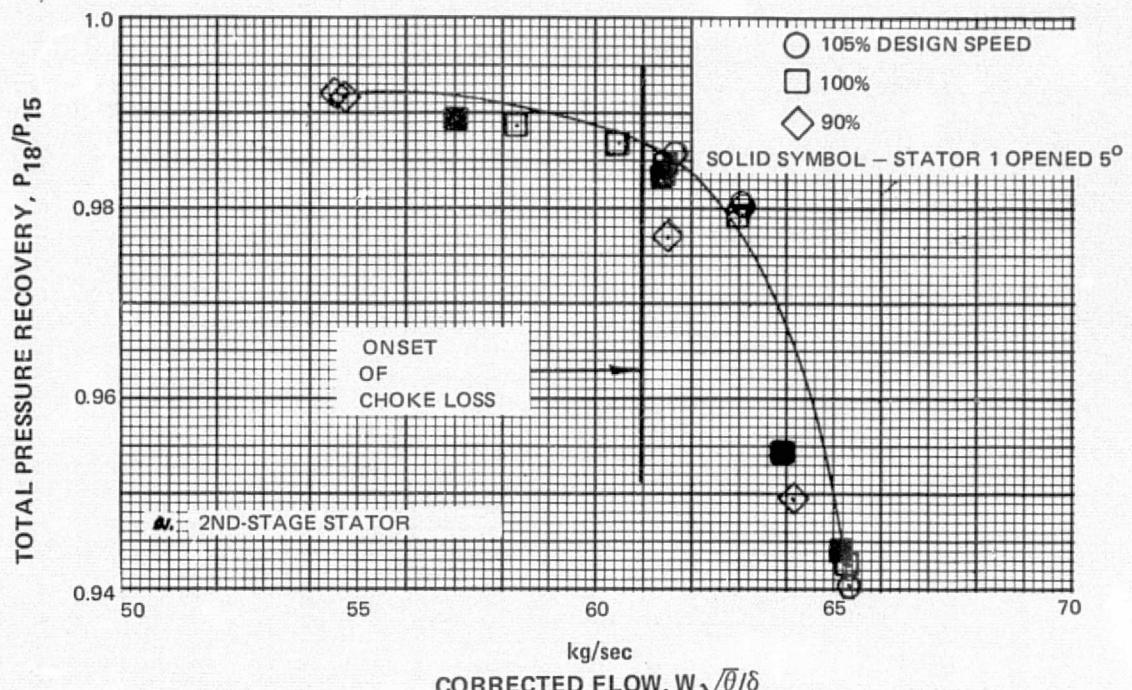


Figure 16 Stator Total Pressure Recovery Versus Stator Inlet Corrected Flow

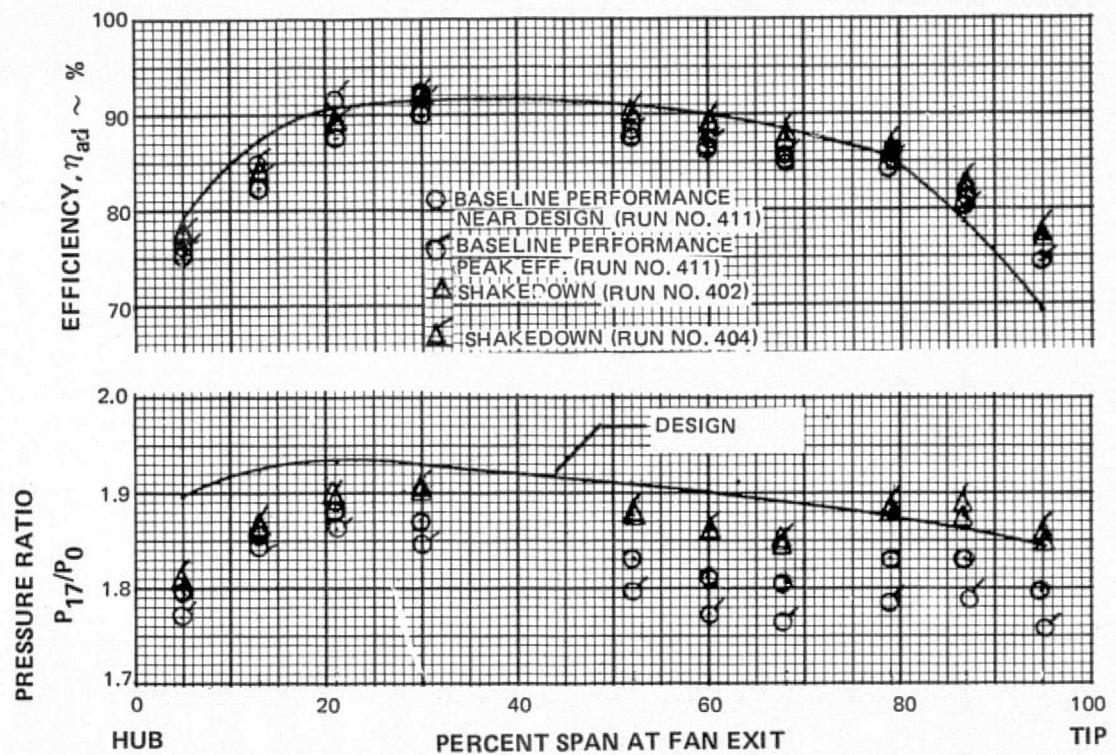


Figure 17 Fan Overall Pressure Ratio and Efficiency Versus Span for Near Design Data Points

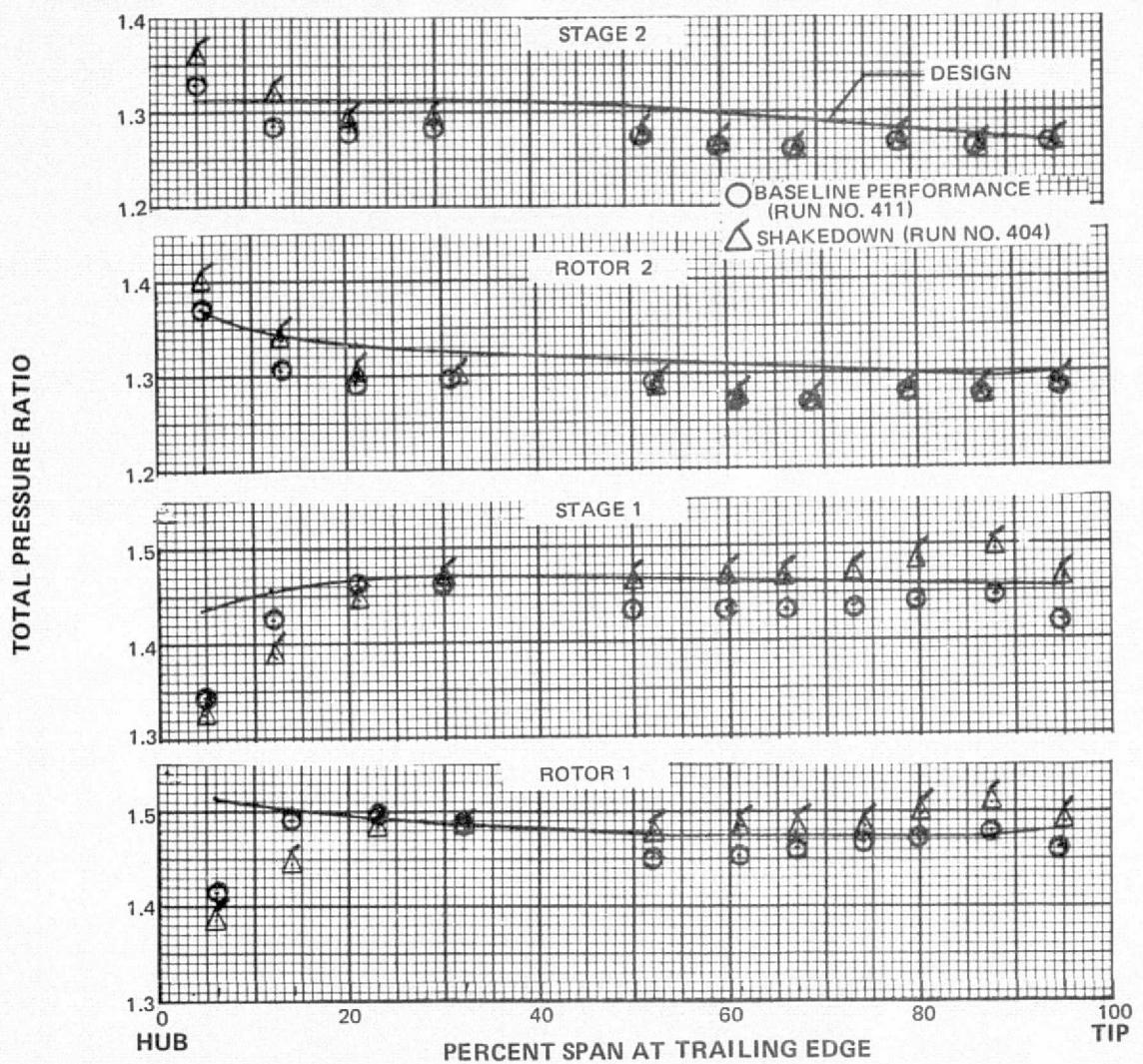


Figure 18 Rotor and Stage Pressure Ratio Versus Span for Near Design Data Points

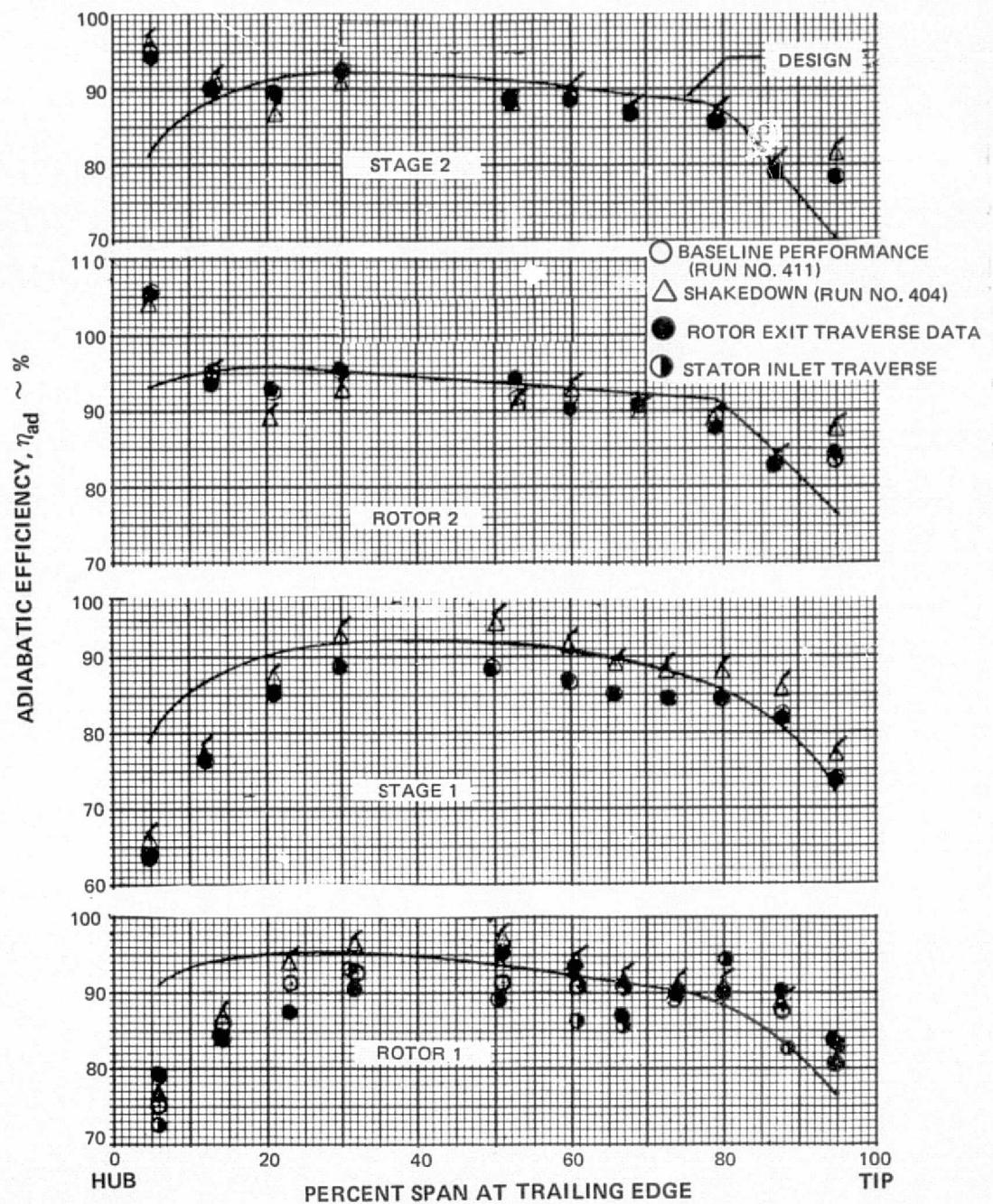


Figure 19 Rotor and Stage Efficiency Versus Span for Near Design Data Points

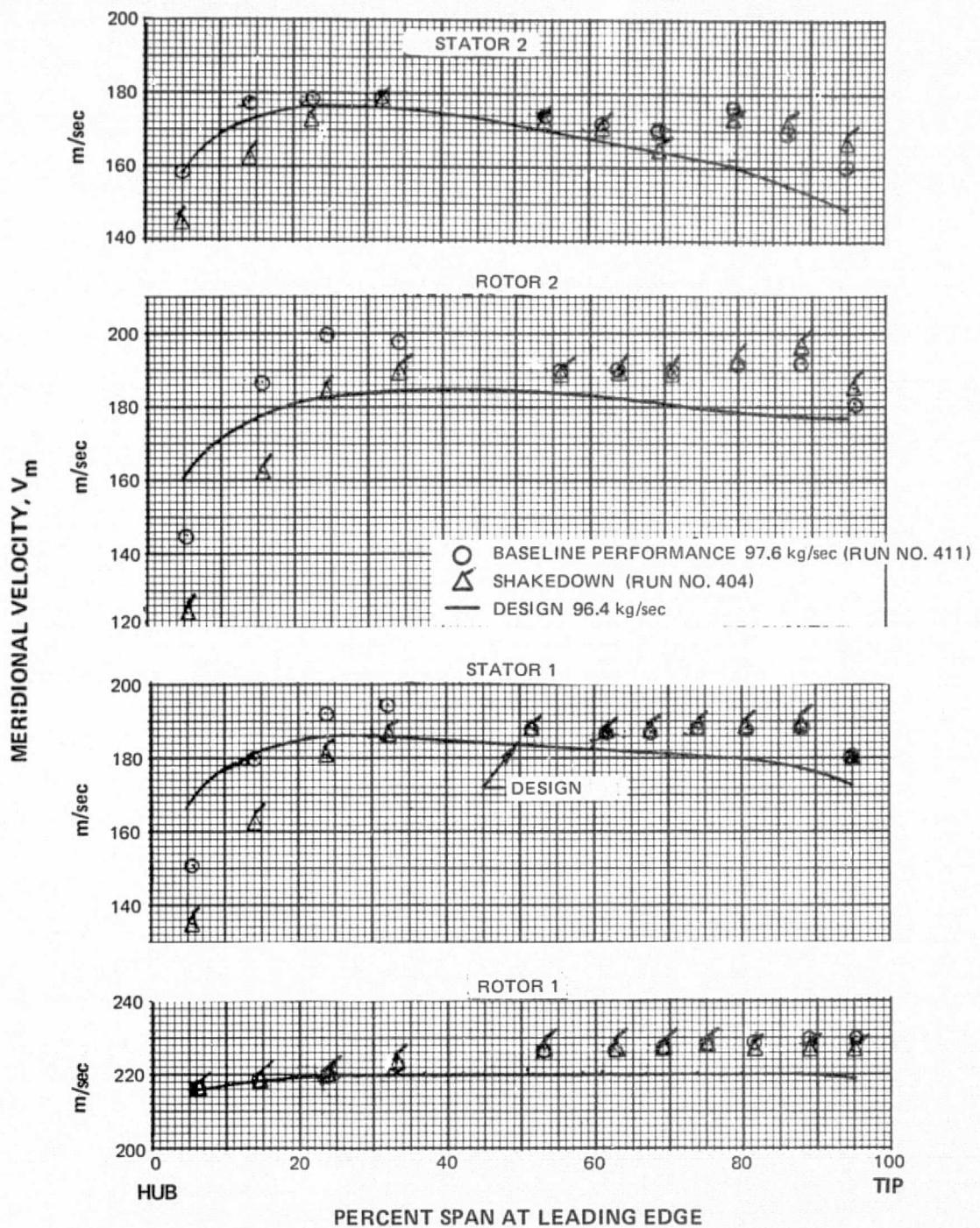


Figure 20 Blade Row Inlet Meridional Velocity Versus Span for Near Design Points

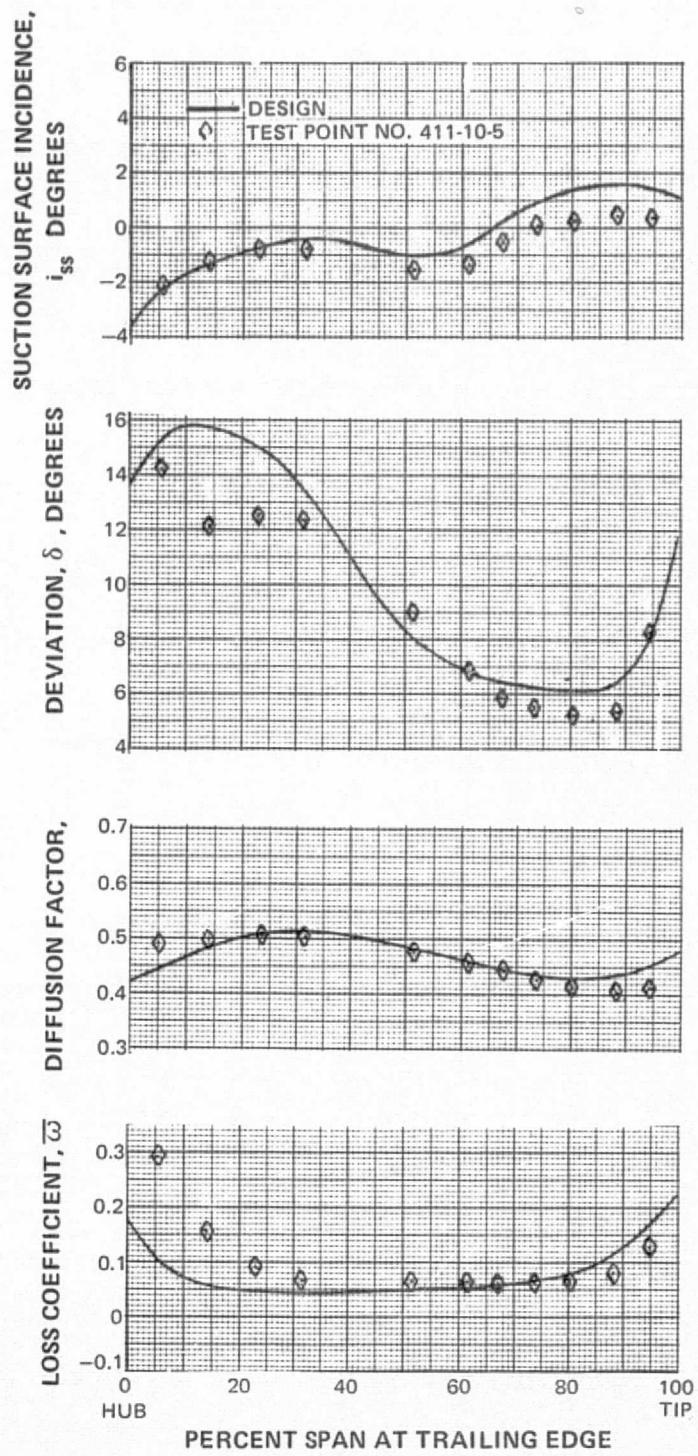


Figure 21 Spanwise Distribution of Loss Coefficient, Diffusion Factor, and Deviation and Incidence Angles for Near Design Data Point, First-Stage Rotor

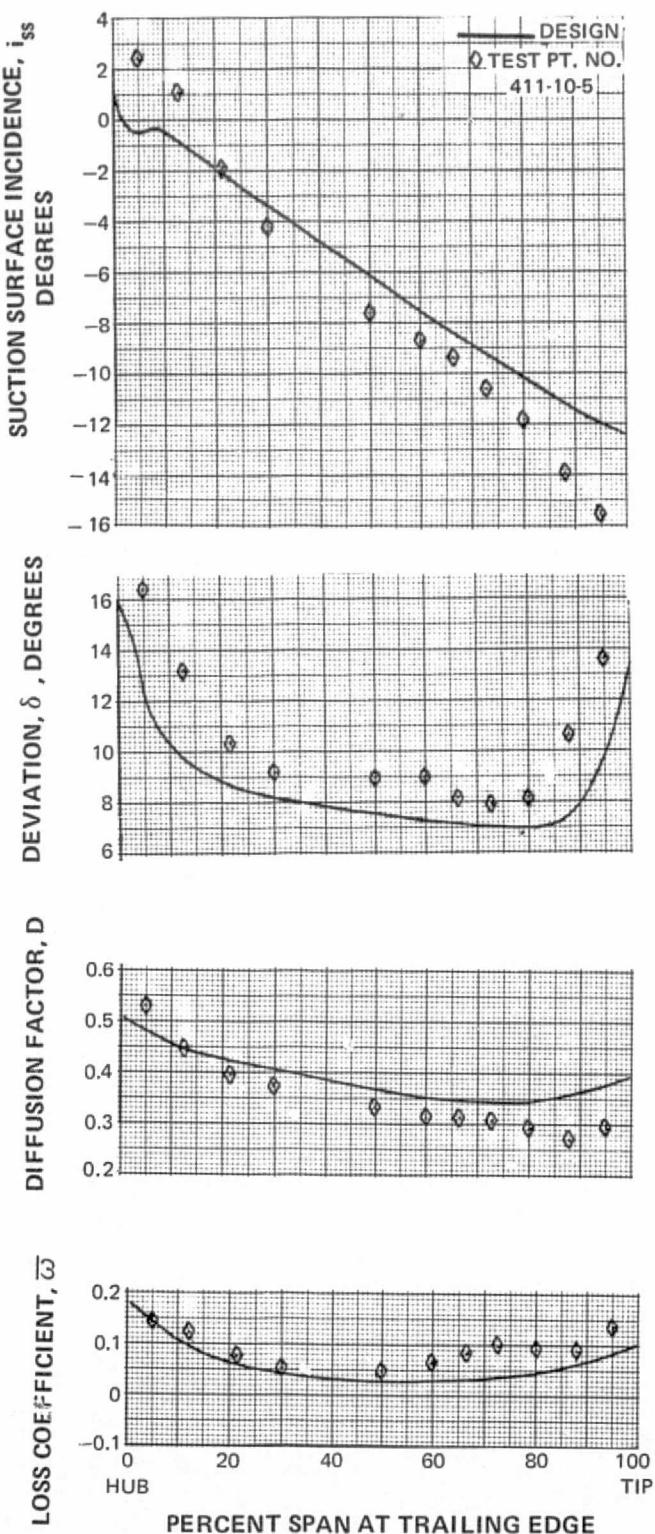


Figure 22 Spanwise Distributions of Loss Coefficient, Diffusion Factor, and Deviation and Incidence Angles for Near Design Data Point, First-Stage Stator

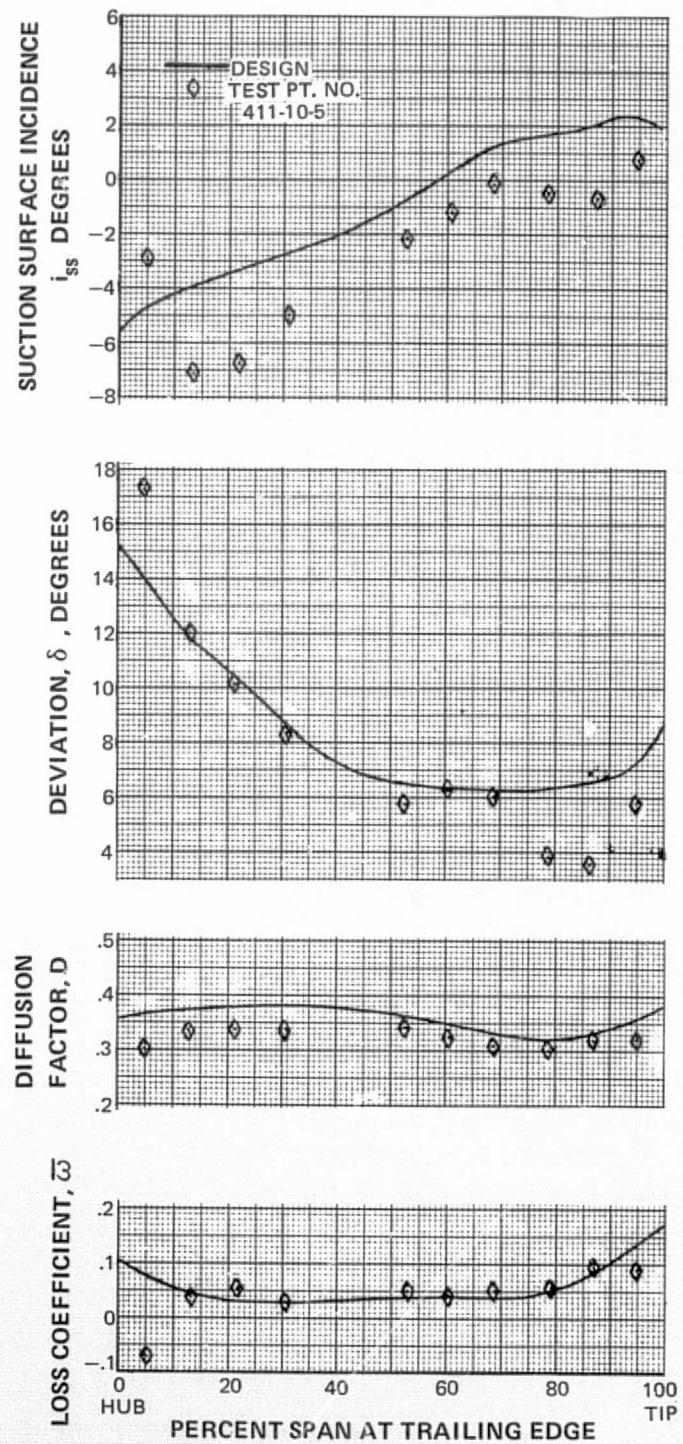


Figure 23 Spanwise Distributions of Loss Coefficient, Diffusion Factor, and Deviation and Incidence Angles for Near Design Data Point, Second-Stage Rotor

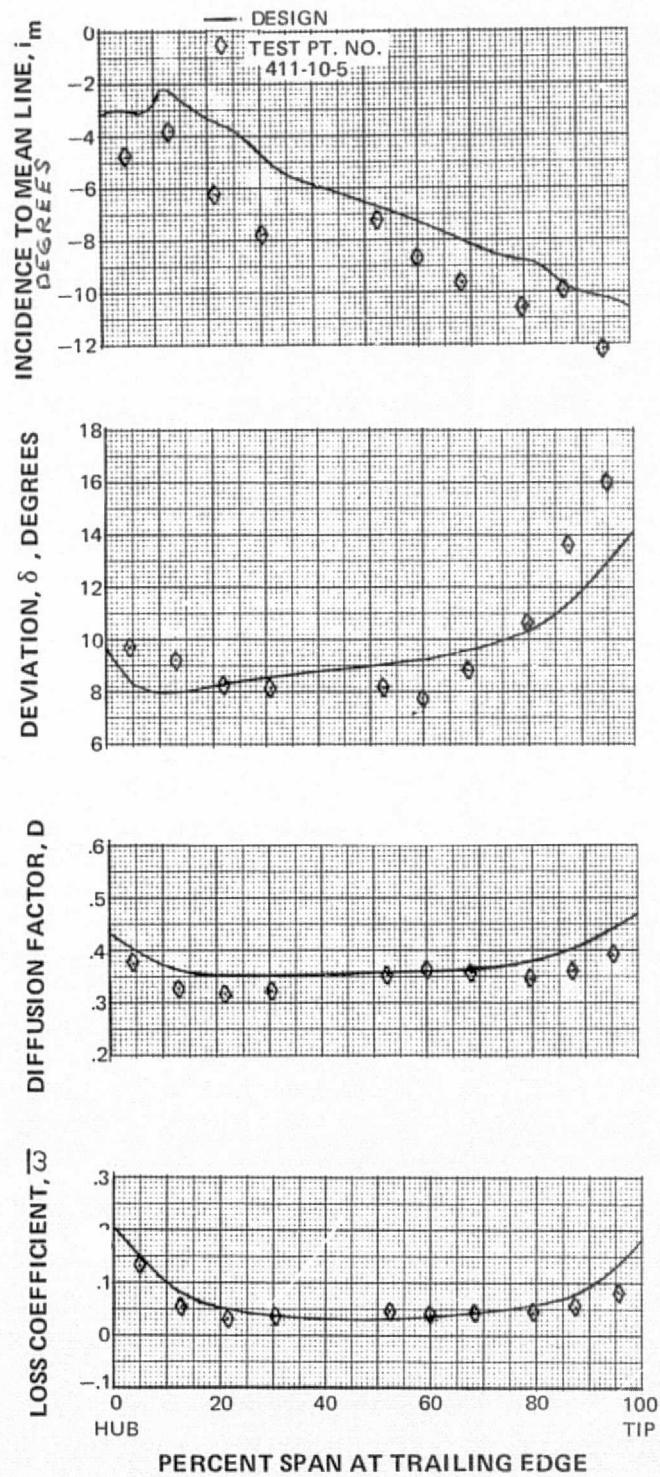


Figure 24 Spanwise Distributions of Loss Coefficient, Diffusion Factor, and Deviation and Incidence Angles for Near Design Data Point, Second-Stage Stator

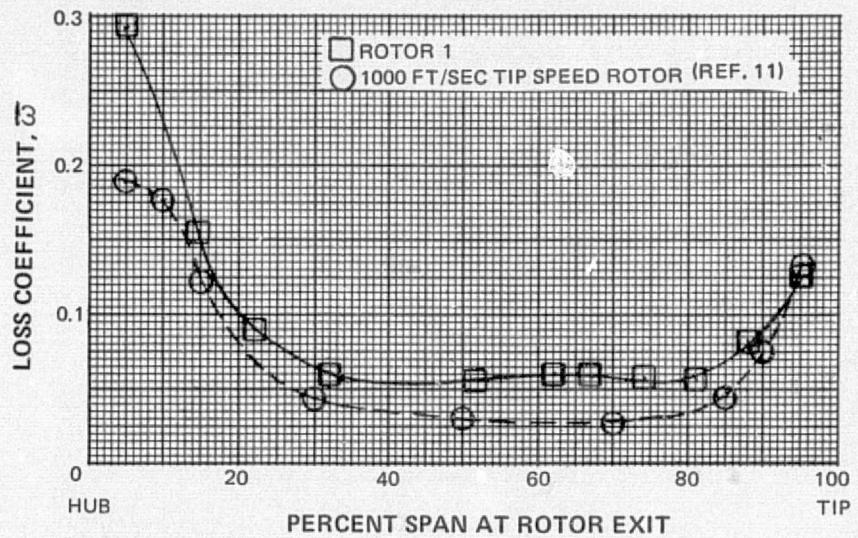


Figure 25 Spanwise Distribution of Loss for the First-Stage Rotor and a Similar Low Speed Rotor

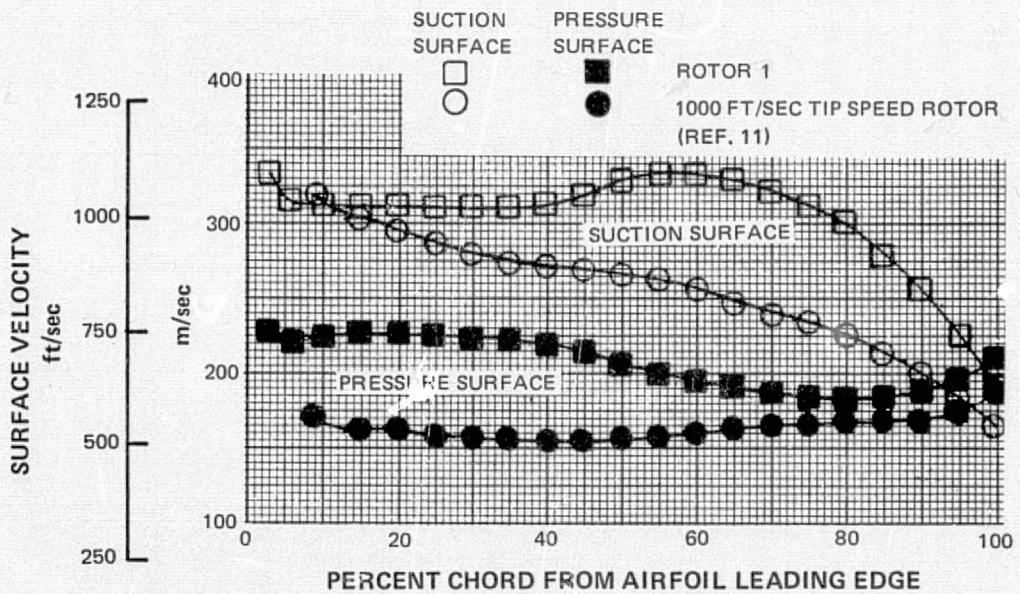


Figure 26 Calculated Flow Velocity on Suction Surface and Pressure Surfaces at the Hub of the First-Stage Rotor and a Similar Low Speed Rotor

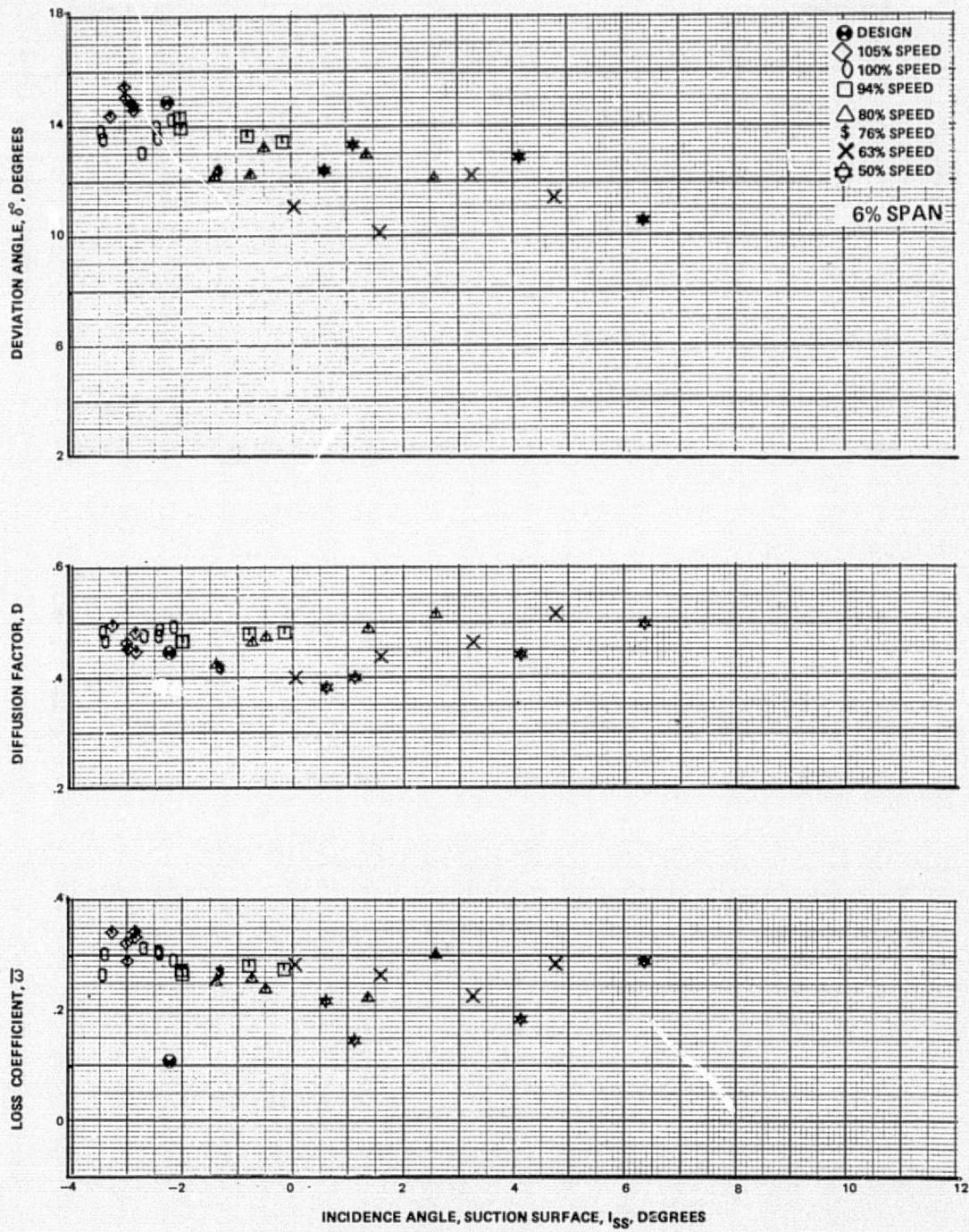


Figure 27a Blade-Element Performance, Baseline Configuration, Uniform in Inlet Flow – First-Stage Rotor

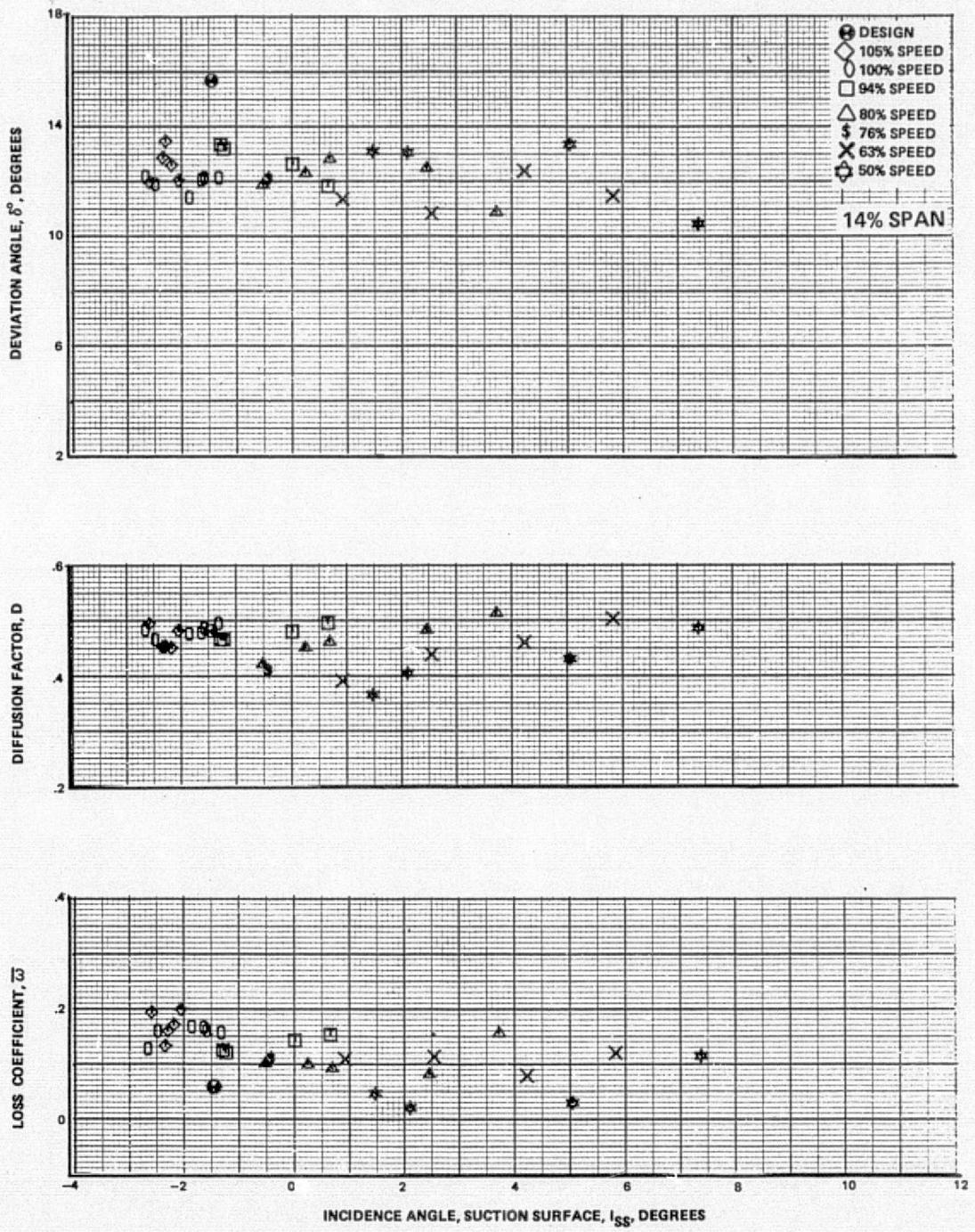


Figure 27b Blade-Element Performance, Baseline Configuration, Uniform in Inlet Flow – First-Stage Rotor

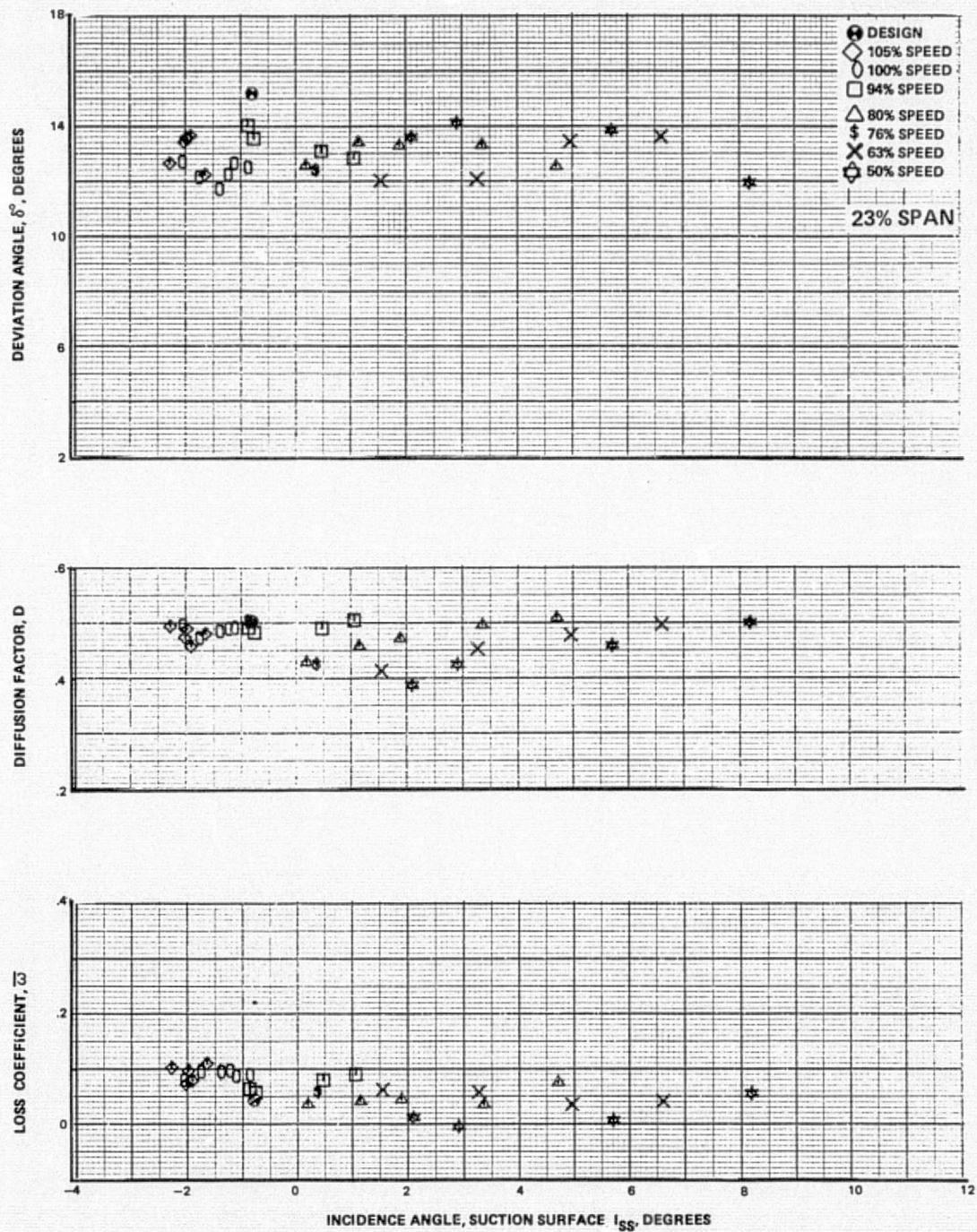


Figure 27c Blade-Element Performance, Baseline Configuration, Uniform in Inlet Flow—First-Stage Rotor

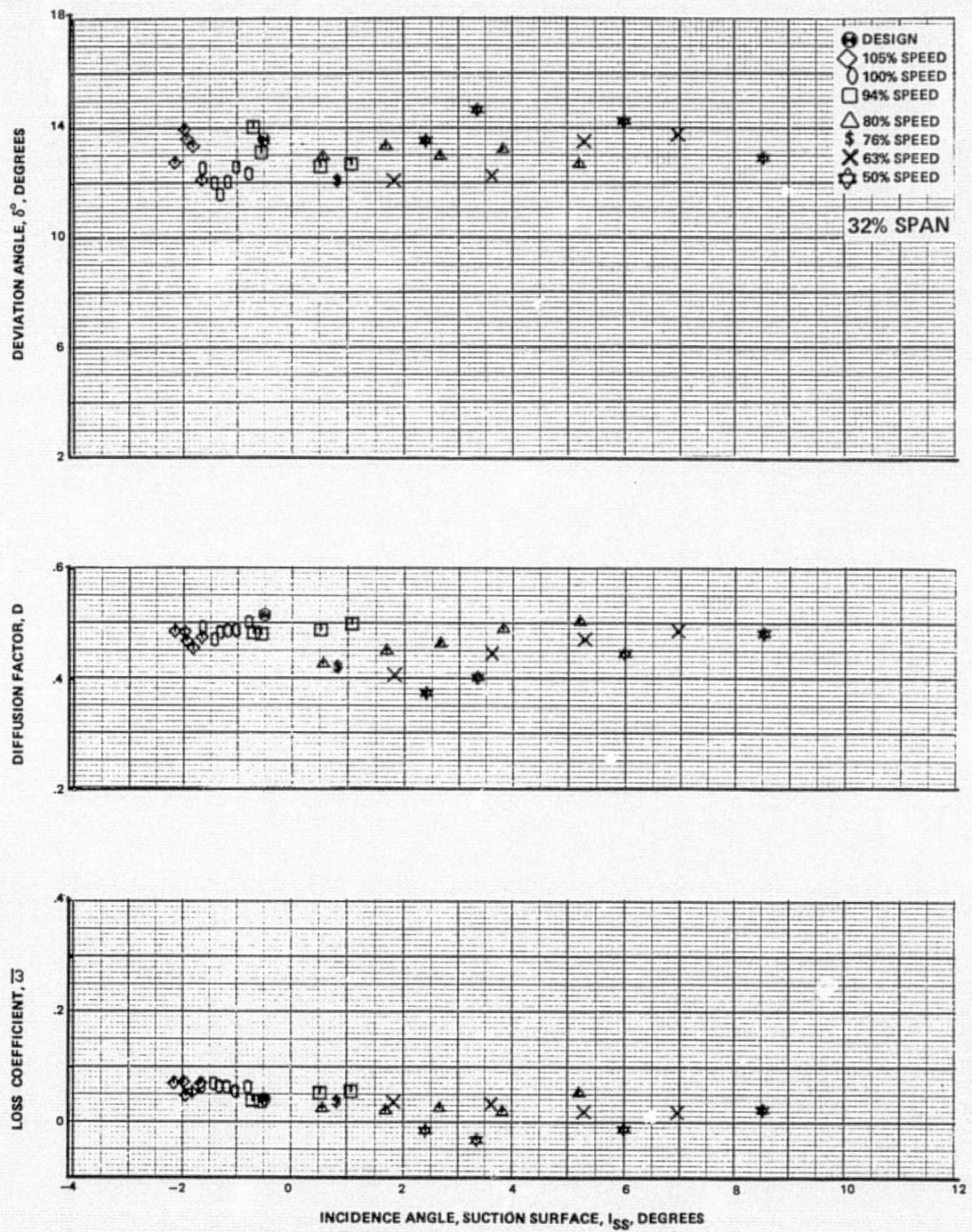


Figure 27d Blade-Element Performance, Baseline Configuration, Uniform in Inlet Flow – First-Stage Rotor

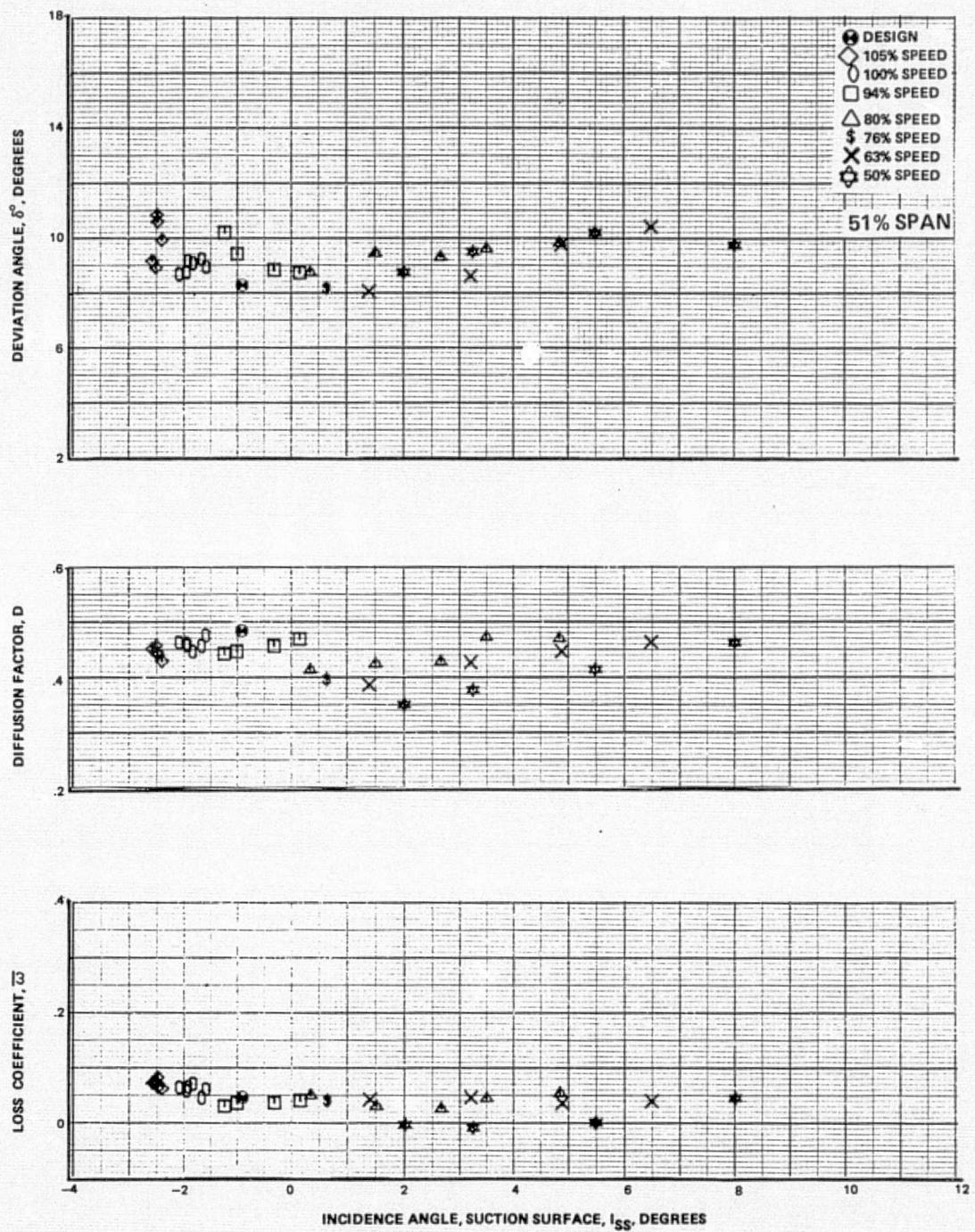


Figure 27e Blade-Element Performance, Baseline Configuration, Uniform in Inlet Flow – First-Stage Rotor

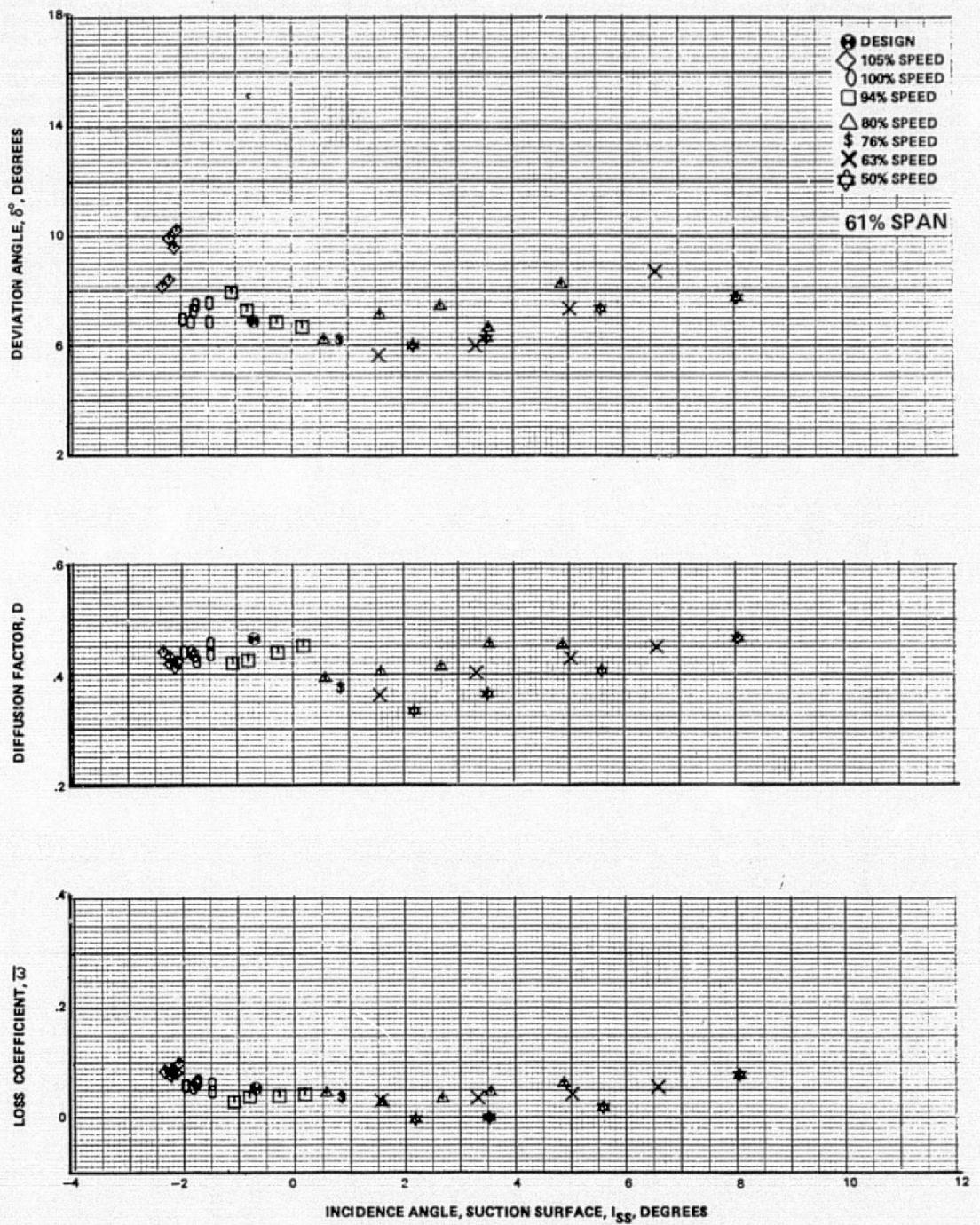


Figure 27f Blade-Element Performance, Baseline Configuration, Uniform in Inlet Flow – First-Stage Rotor

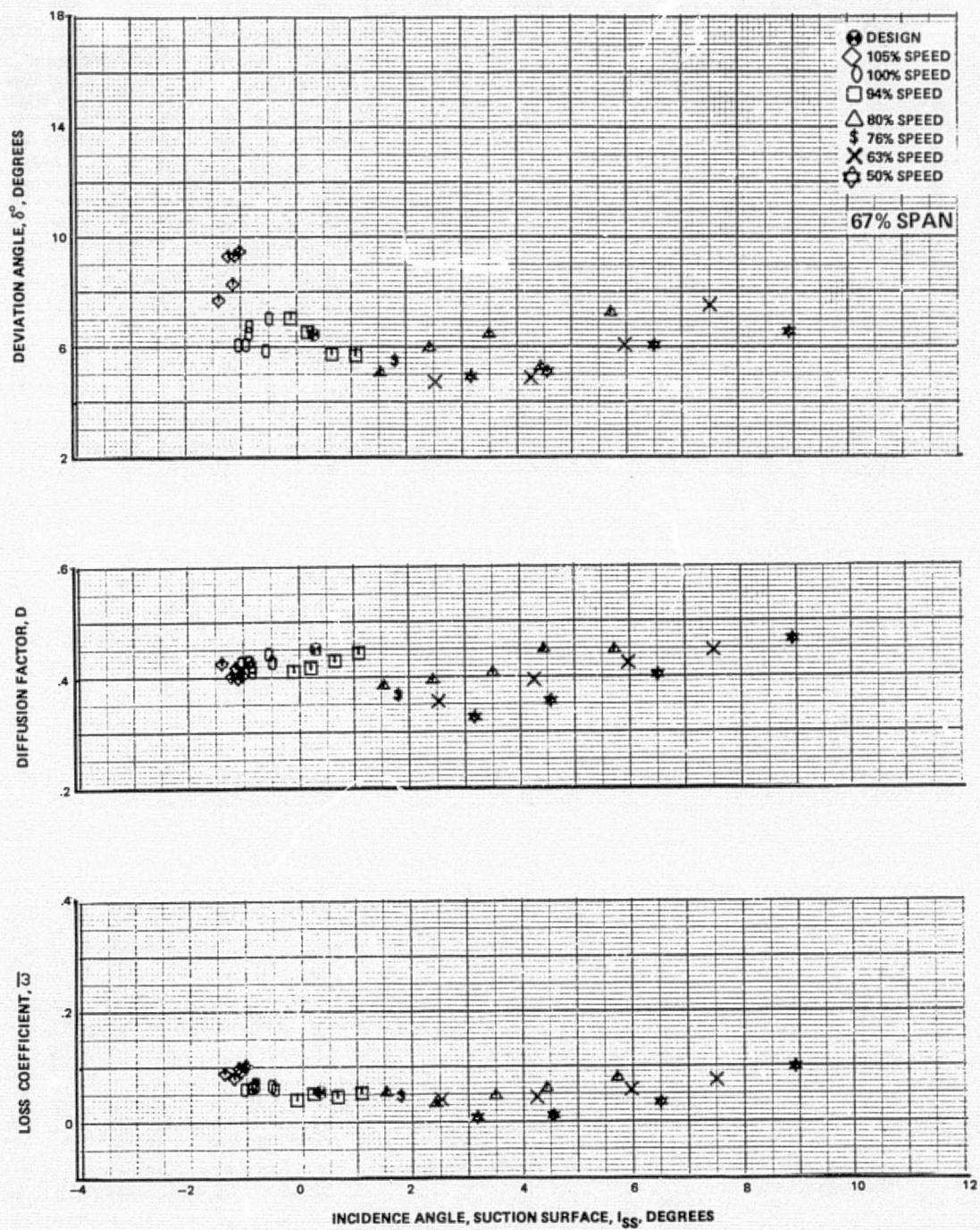


Figure 27g Blade-Element Performance, Baseline Configuration, Uniform in Inlet Flow – First-Stage Rotor

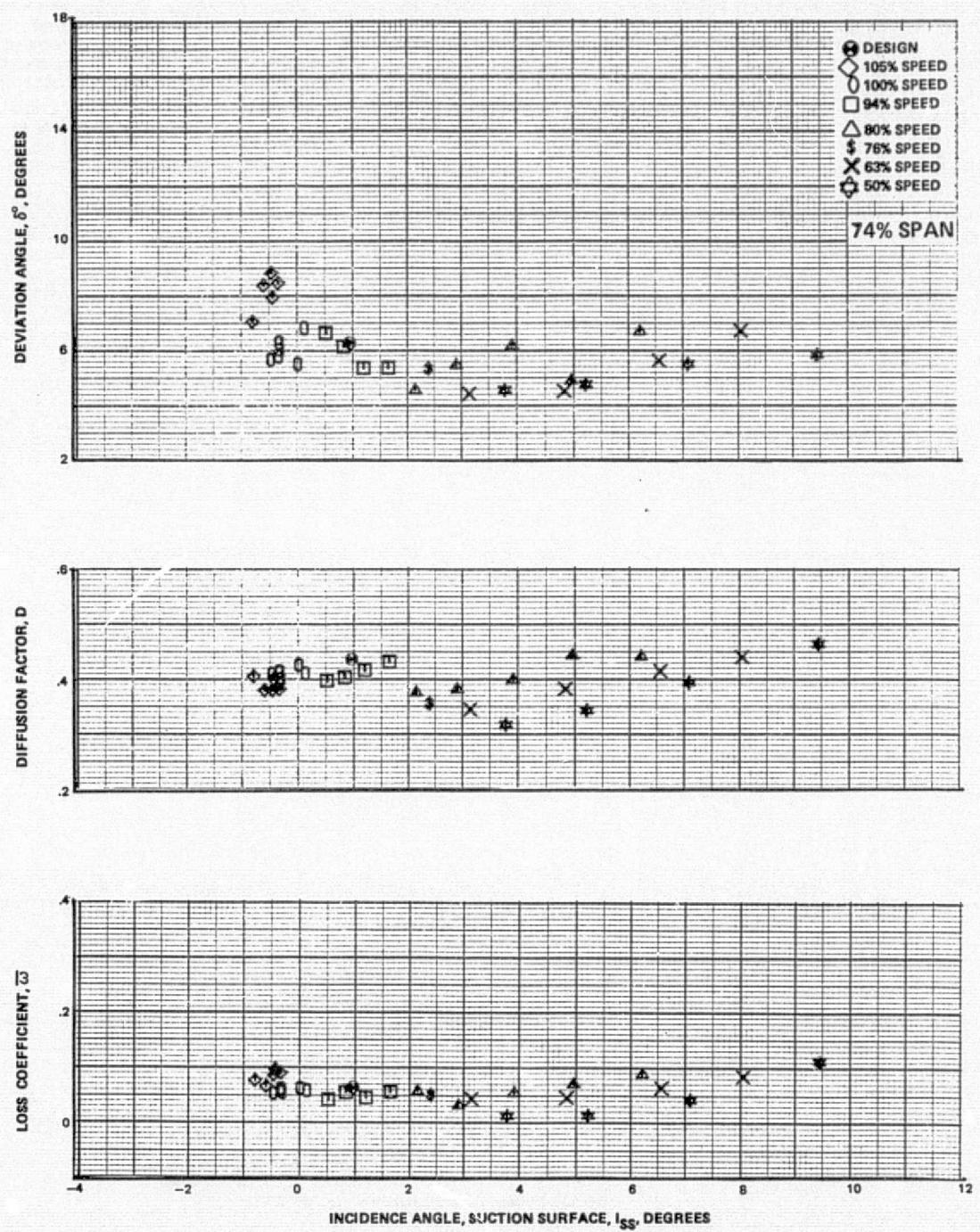


Figure 27h Blade-Element Performance, Baseline Configuration, Uniform in Inlet Flow – First-Stage Rotor

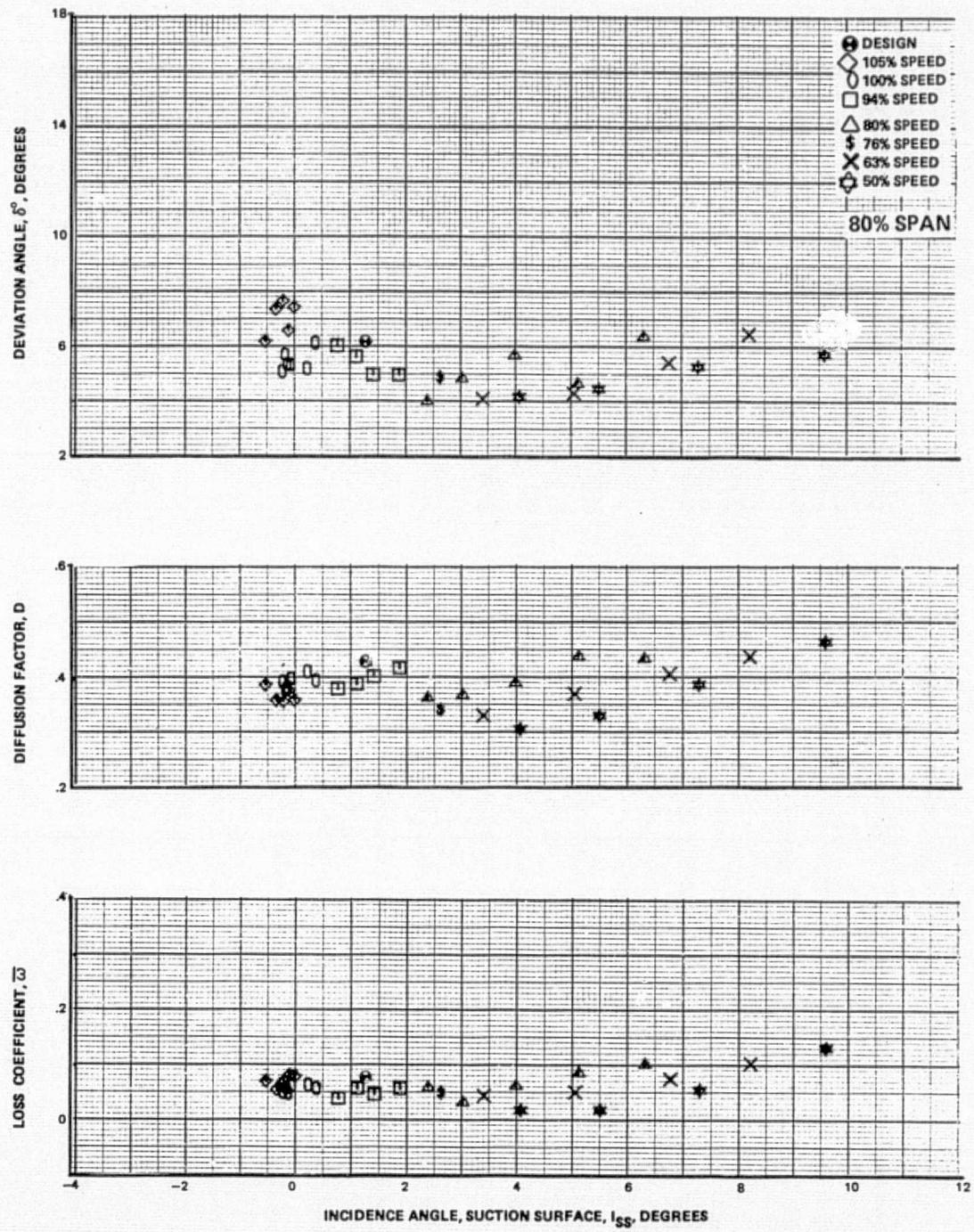


Figure 27i Blade-Element Performance, Baseline Configuration, Uniform in Inlet Flow – First-Stage Rotor

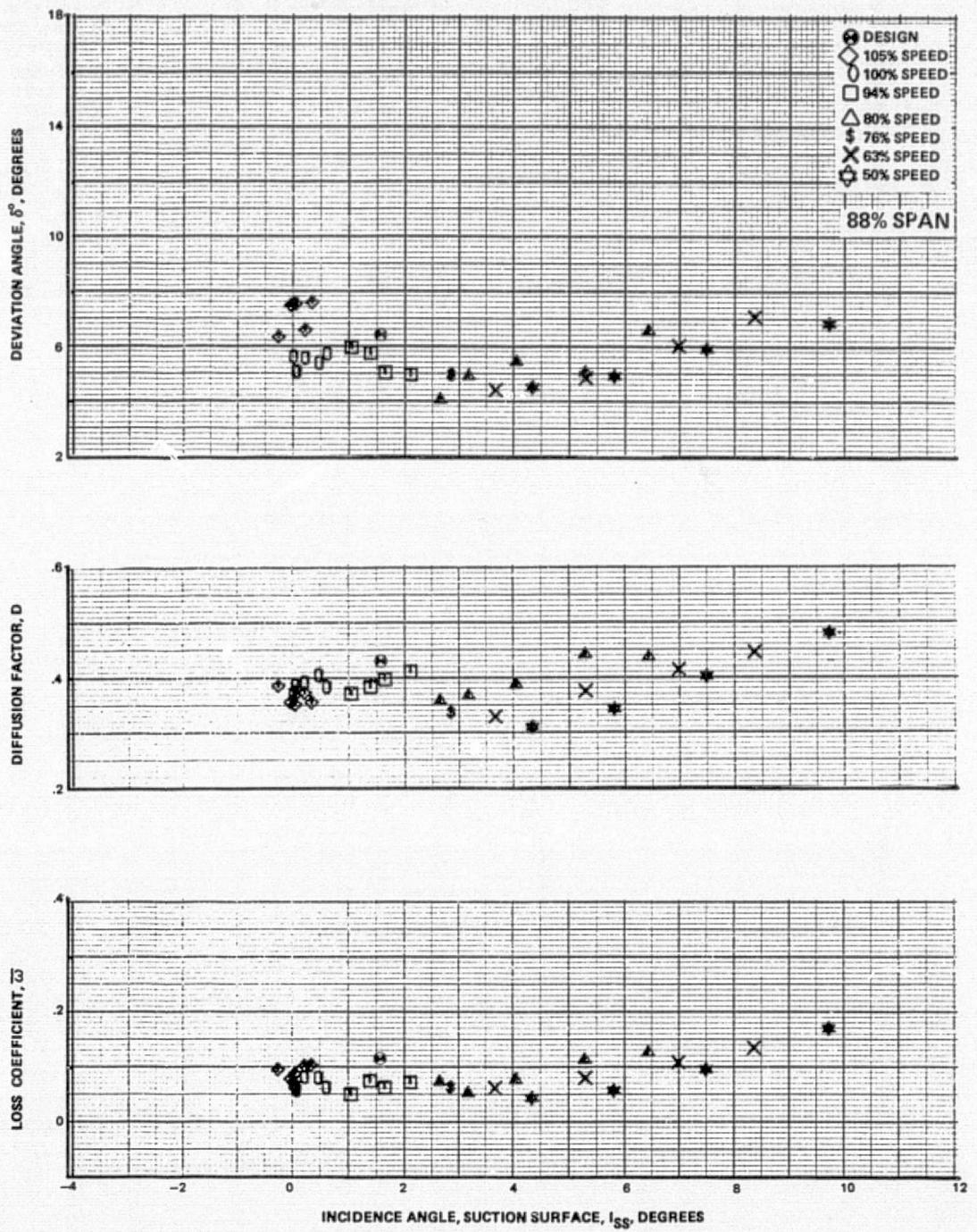


Figure 27j Blade-Element Performance, Baseline Configuration, Uniform in Inlet Flow – First-Stage Rotor

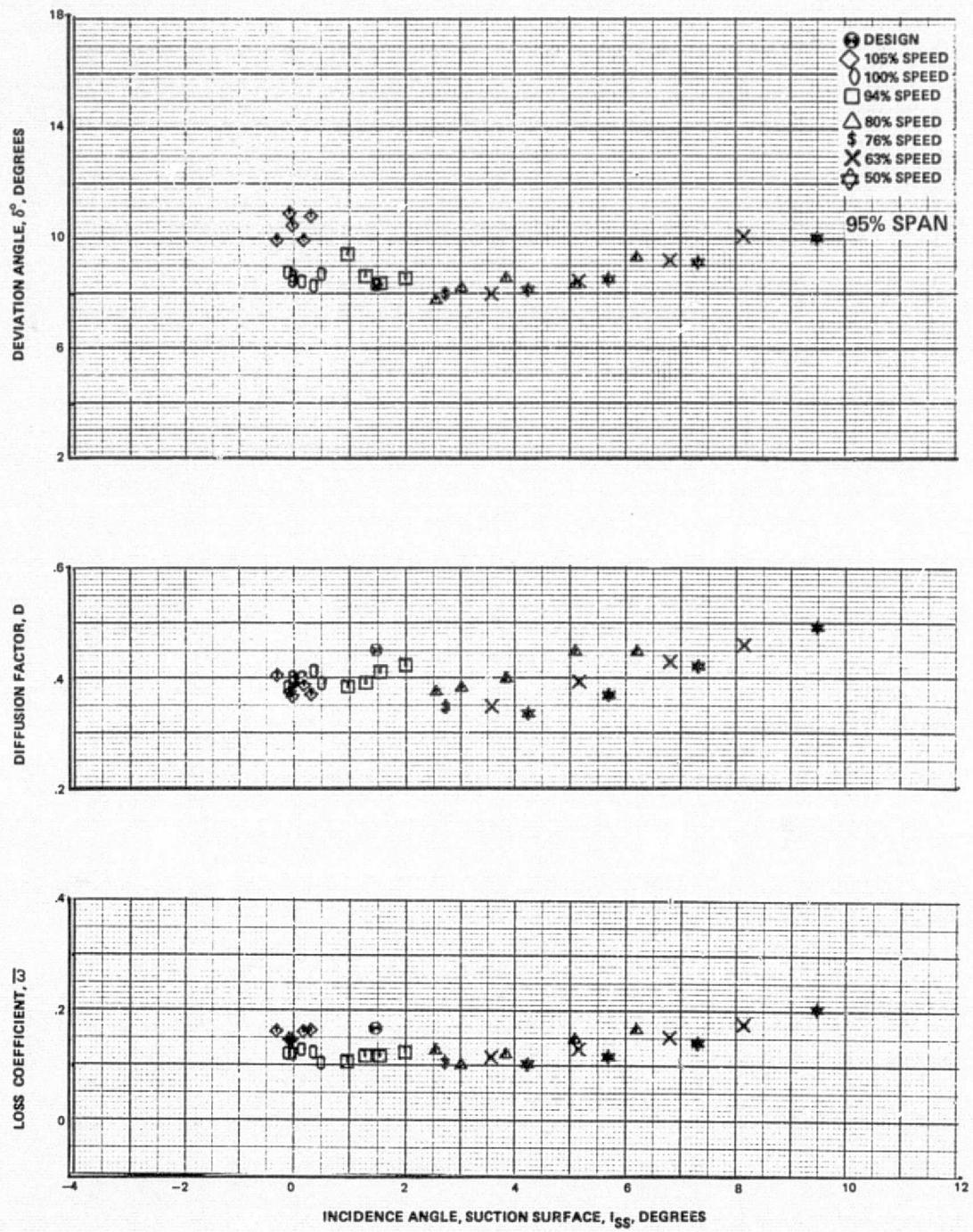


Figure 27k Blade-Element Performance, Baseline Configuration, Uniform in Inlet Flow – First-Stage Rotor

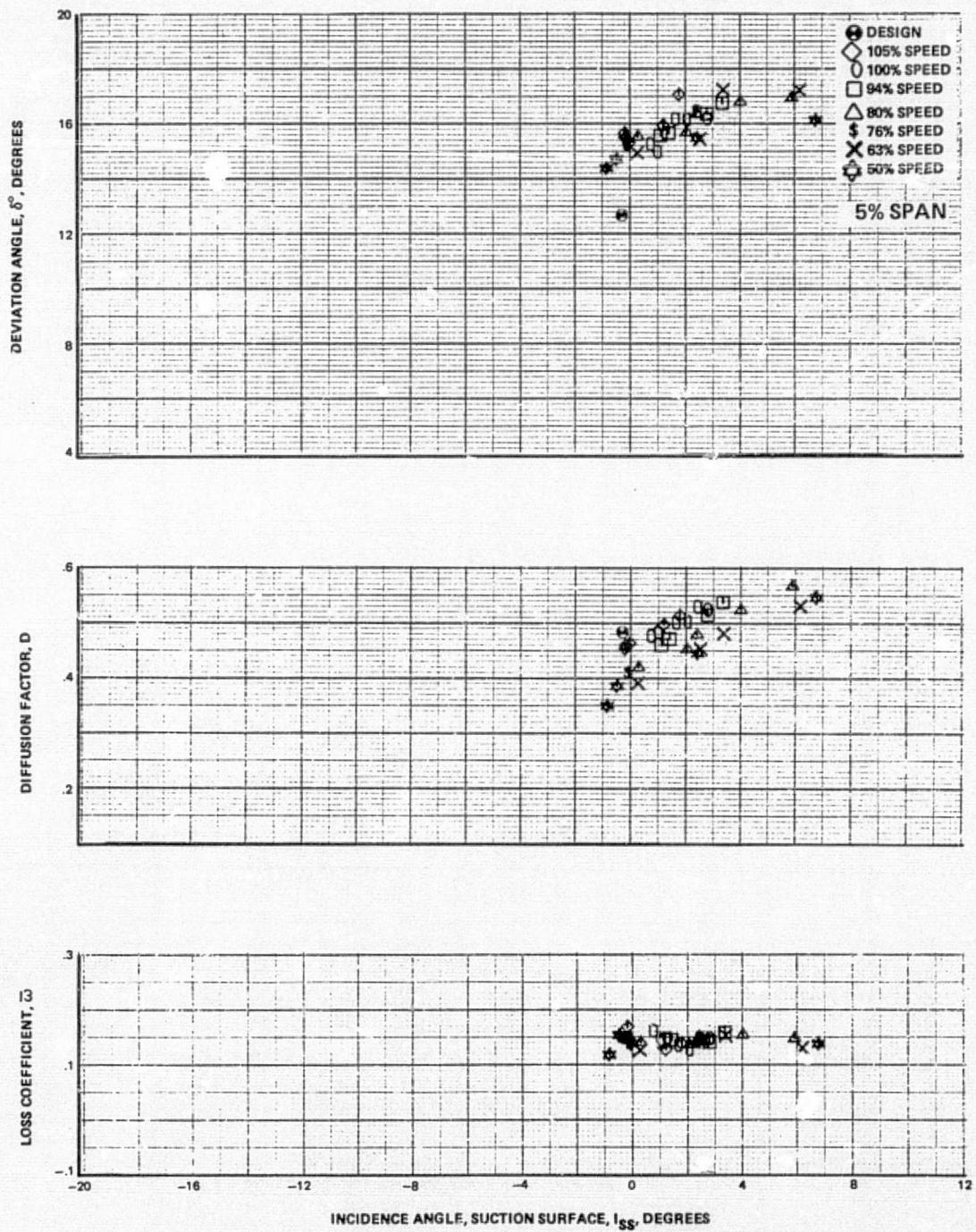


Figure 28a Blade-Element Performance, Baseline Configuration, Uniform Inlet Flow – First-Stage Stator

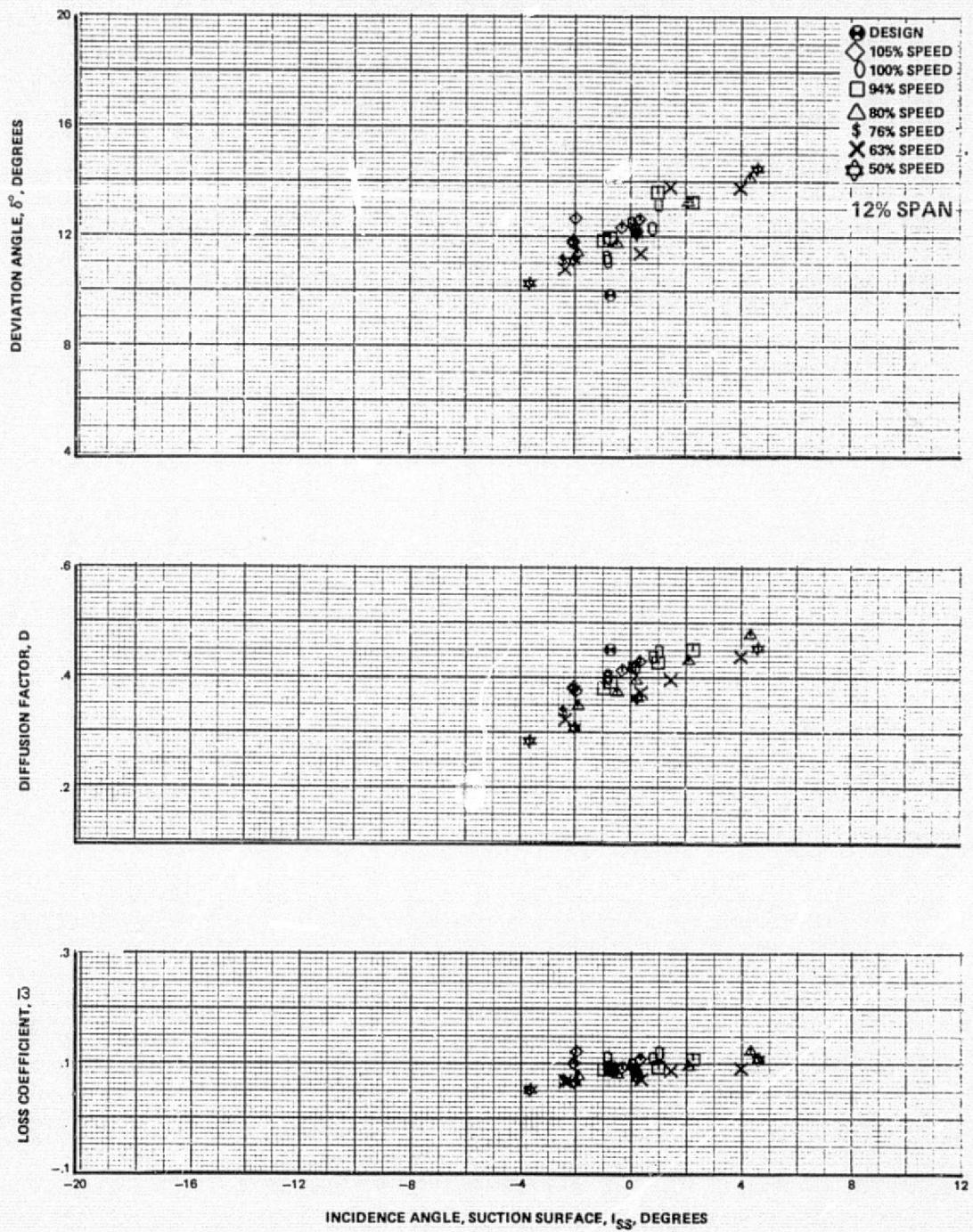


Figure 28b Blade-Element Performance, Baseline Configuration, Uniform Inlet Flow -- First-Stage Stator

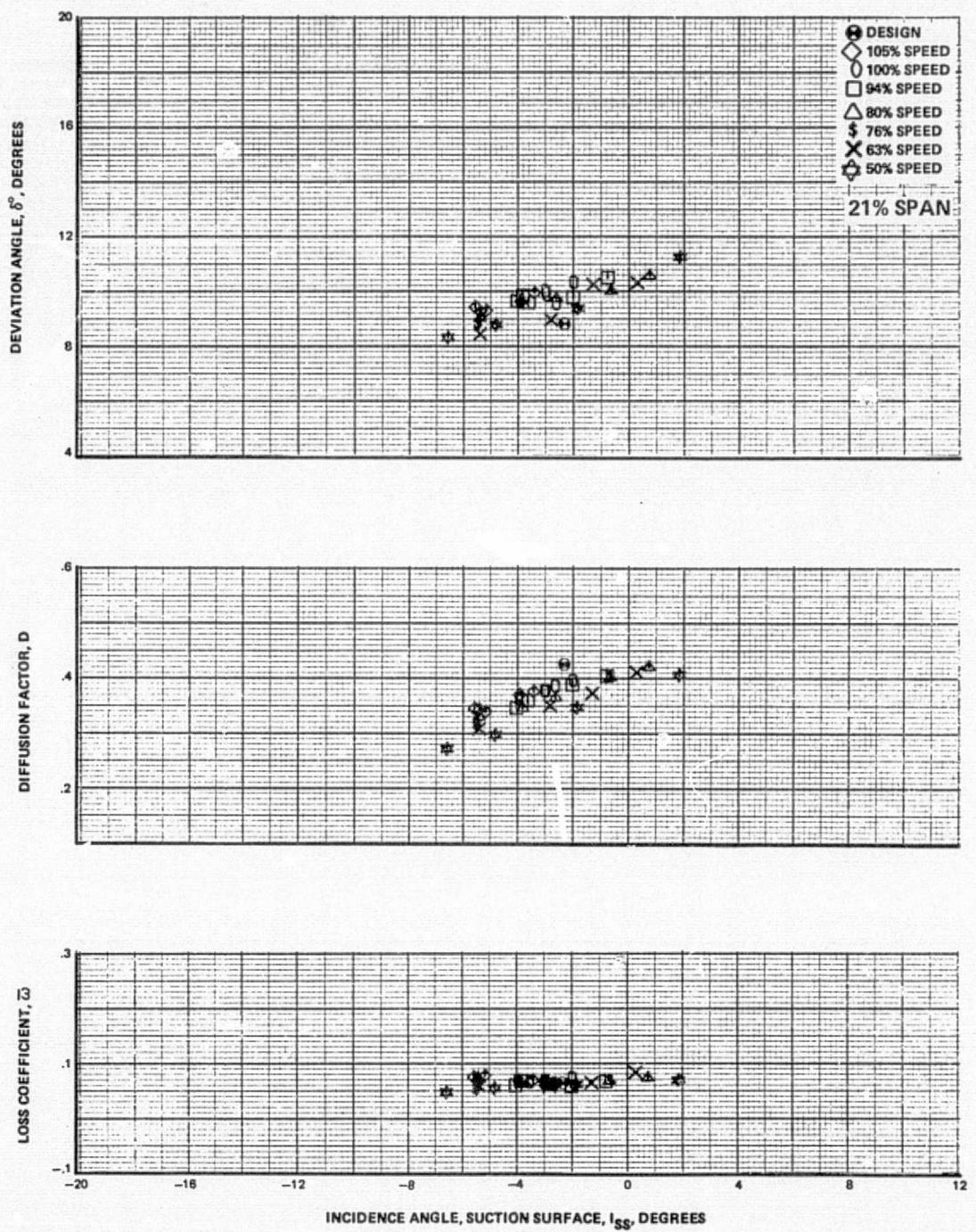


Figure 28c Blade-Element Performance, Baseline Configuration, Uniform Inlet Flow – First-Stage Stator

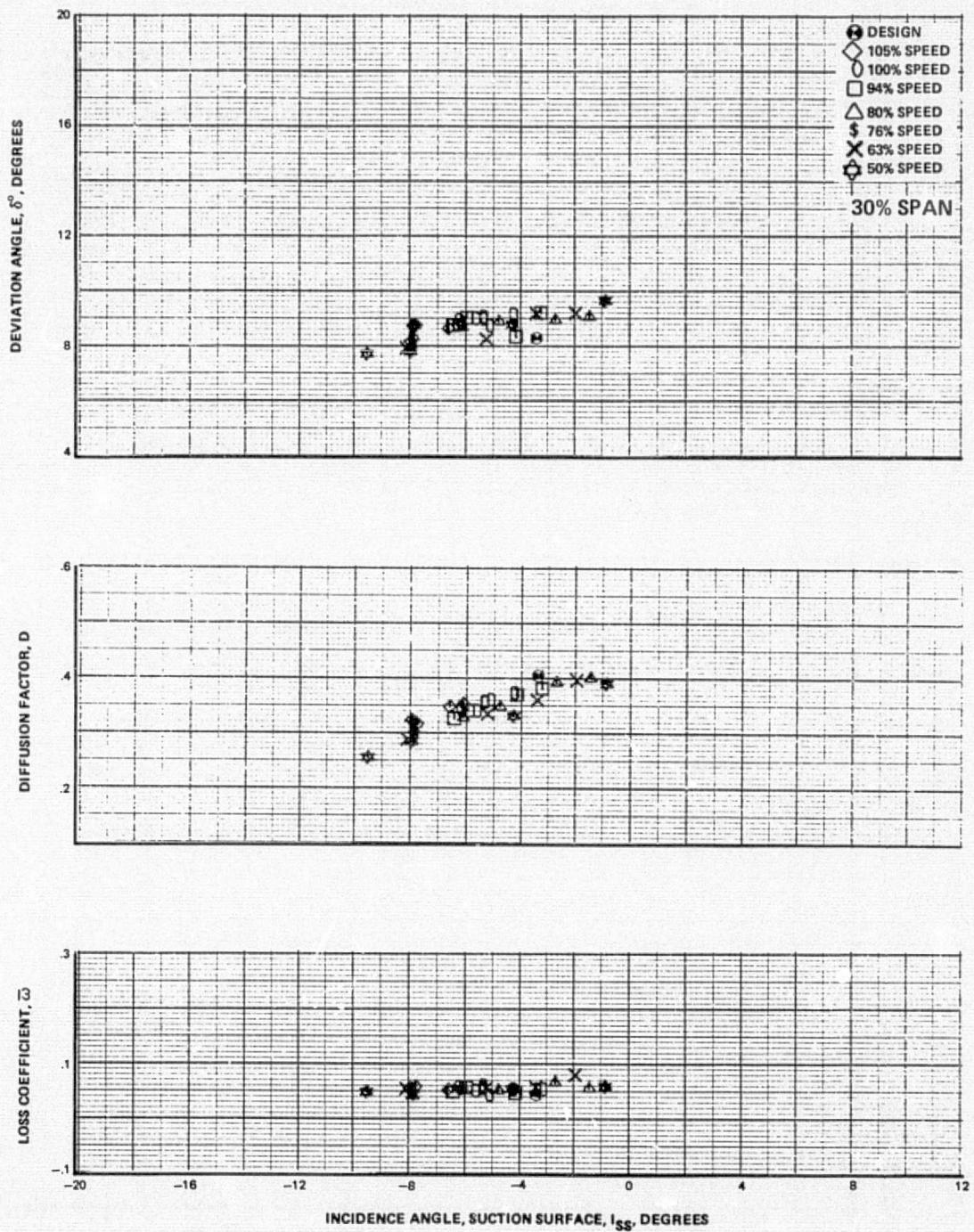


Figure 28d Blade-Element Performance, Baseline Configuration, Uniform Inlet Flow – First-Stage Stator

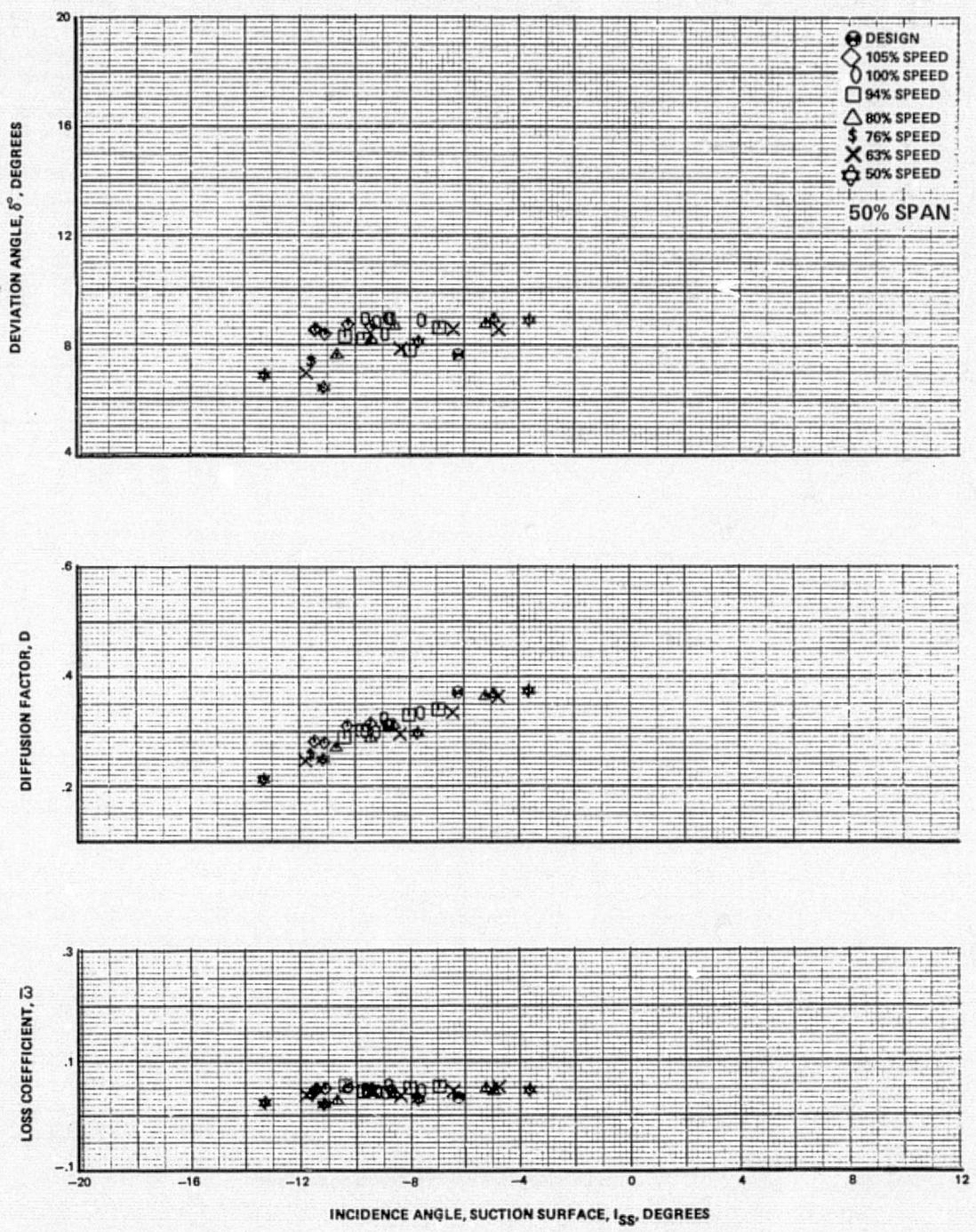


Figure 28e Blade-Element Performance, Baseline Configuration, Uniform Inlet Flow – First-Stage Stator

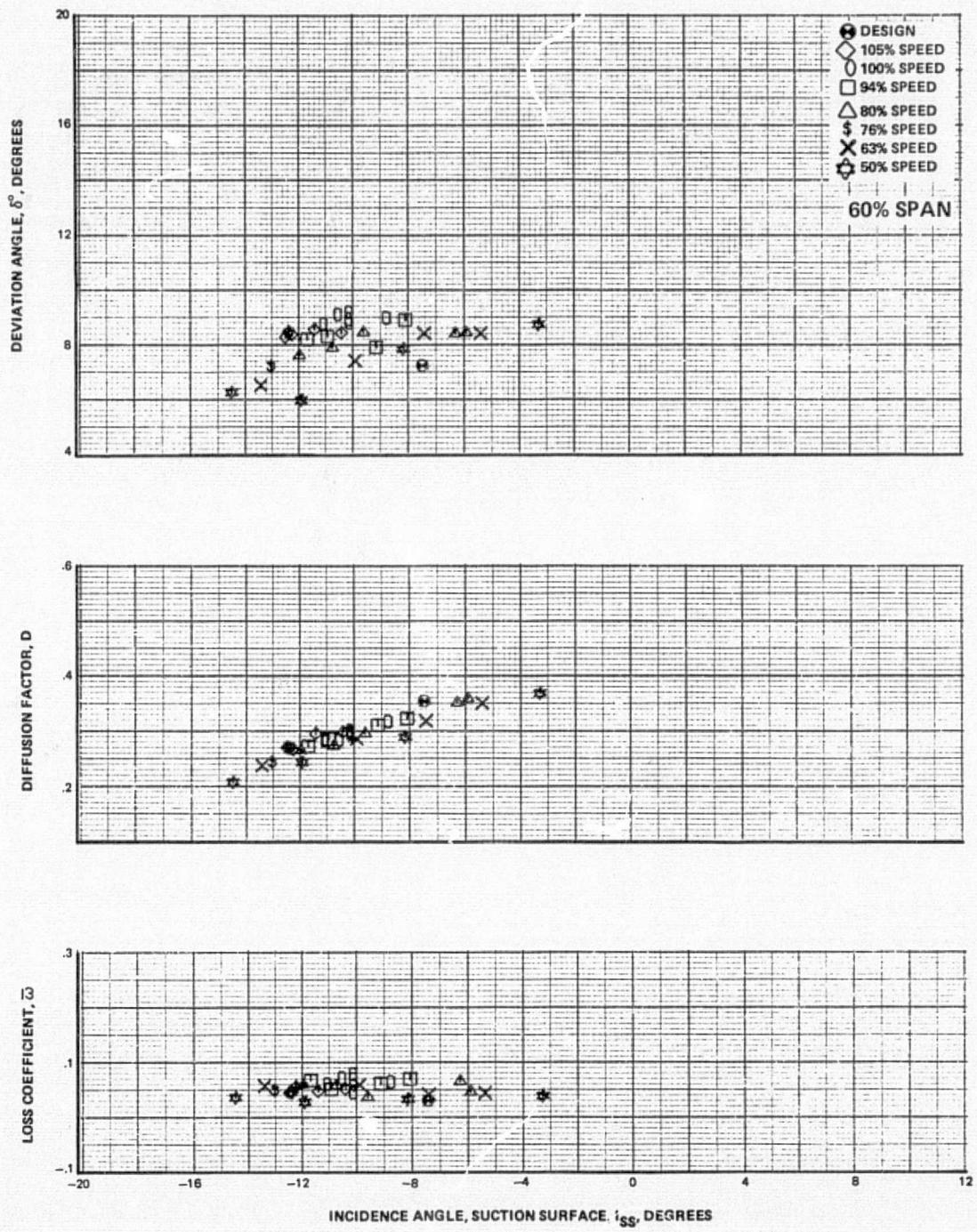


Figure 28f Blade-Element Performance, Baseline Configuration, Uniform Inlet Flow – First-Stage Stator

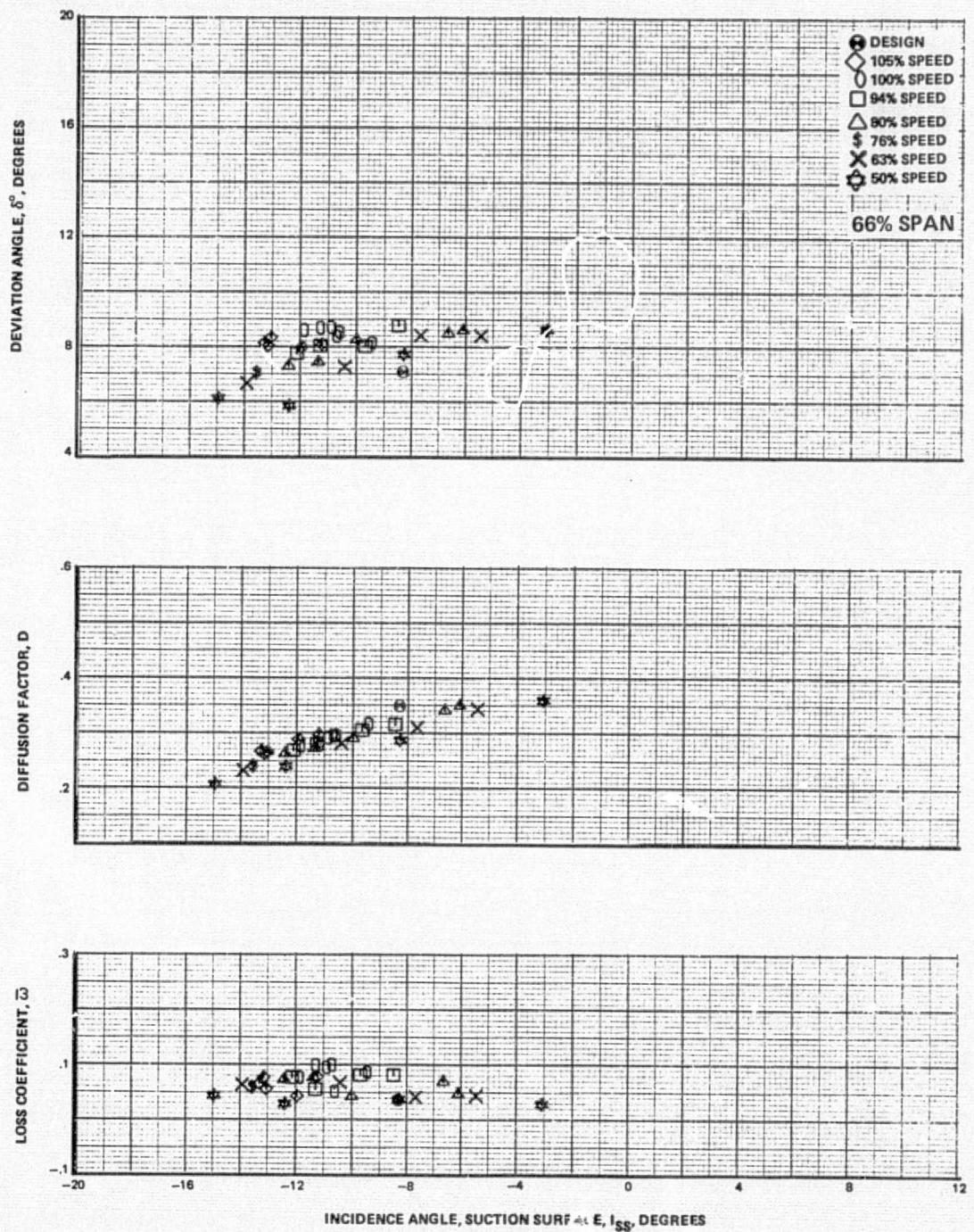


Figure 28g Blade-Element Performance, Baseline Configuration, Uniform Inlet Flow – First-Stage Stator

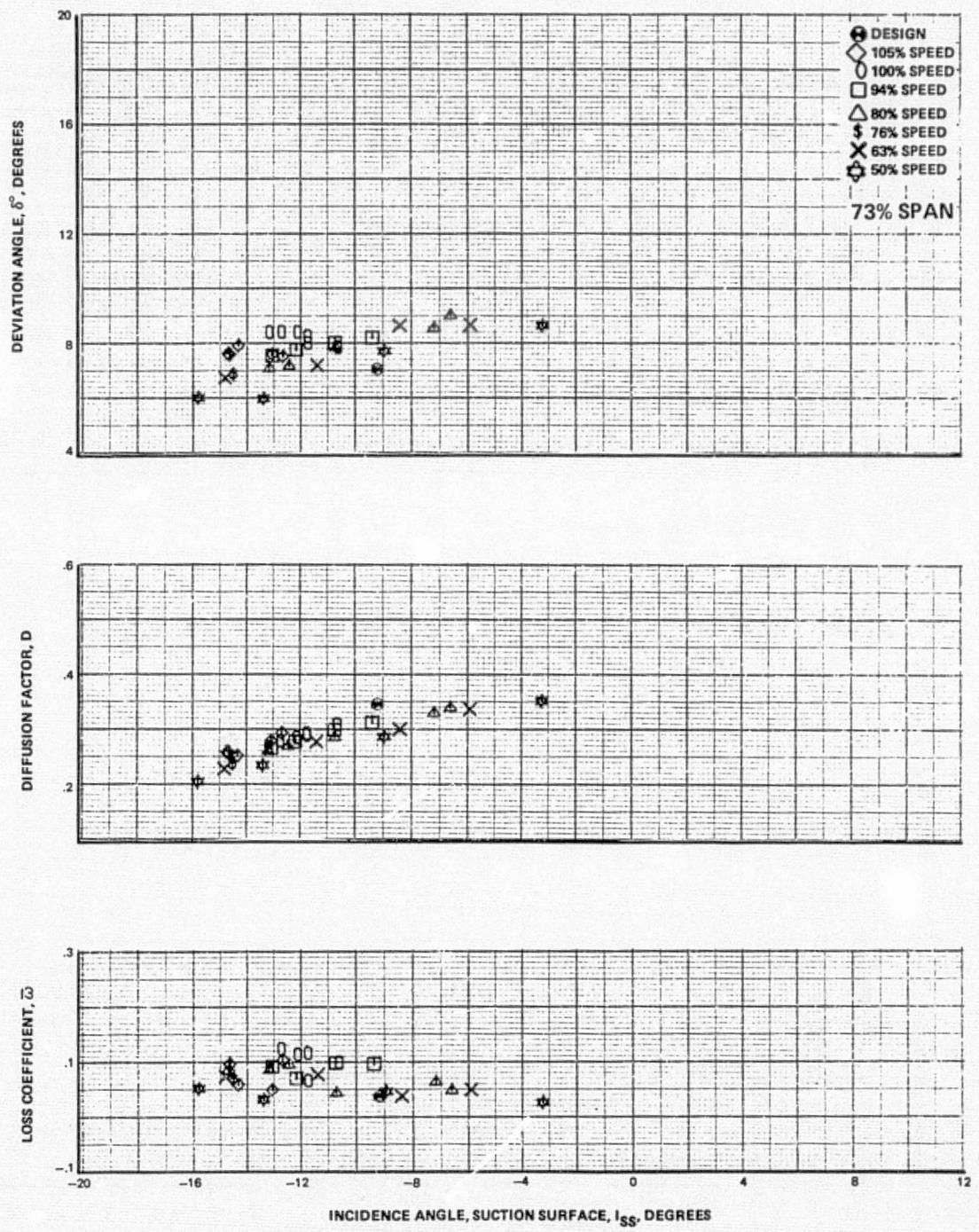


Figure 28h Blade-Element Performance, Baseline Configuration, Uniform Inlet Flow – First-Stage Stator

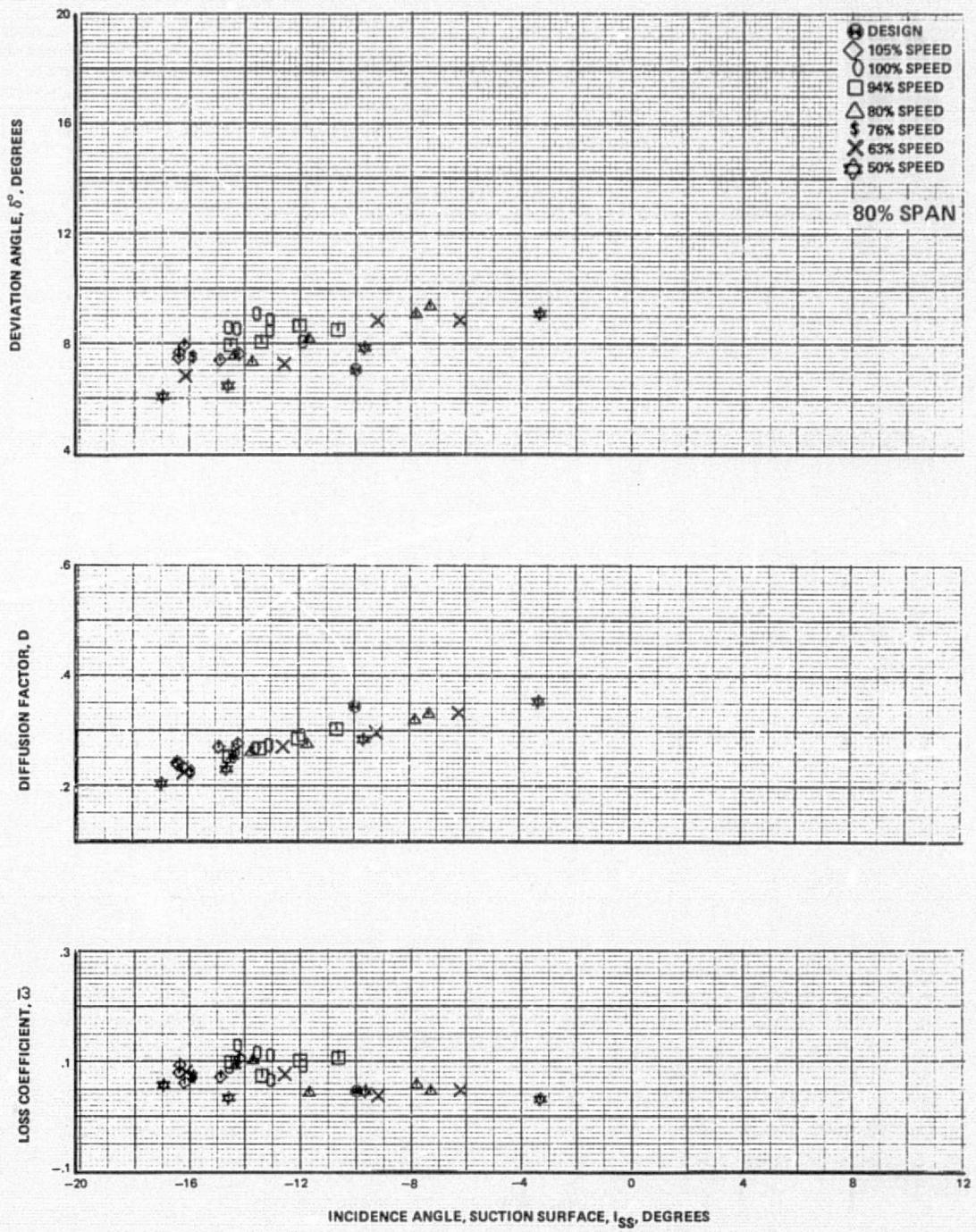


Figure 28i Blade-Element Performance, Baseline Configuration, Uniform Inlet Flow – First-Stage Stator

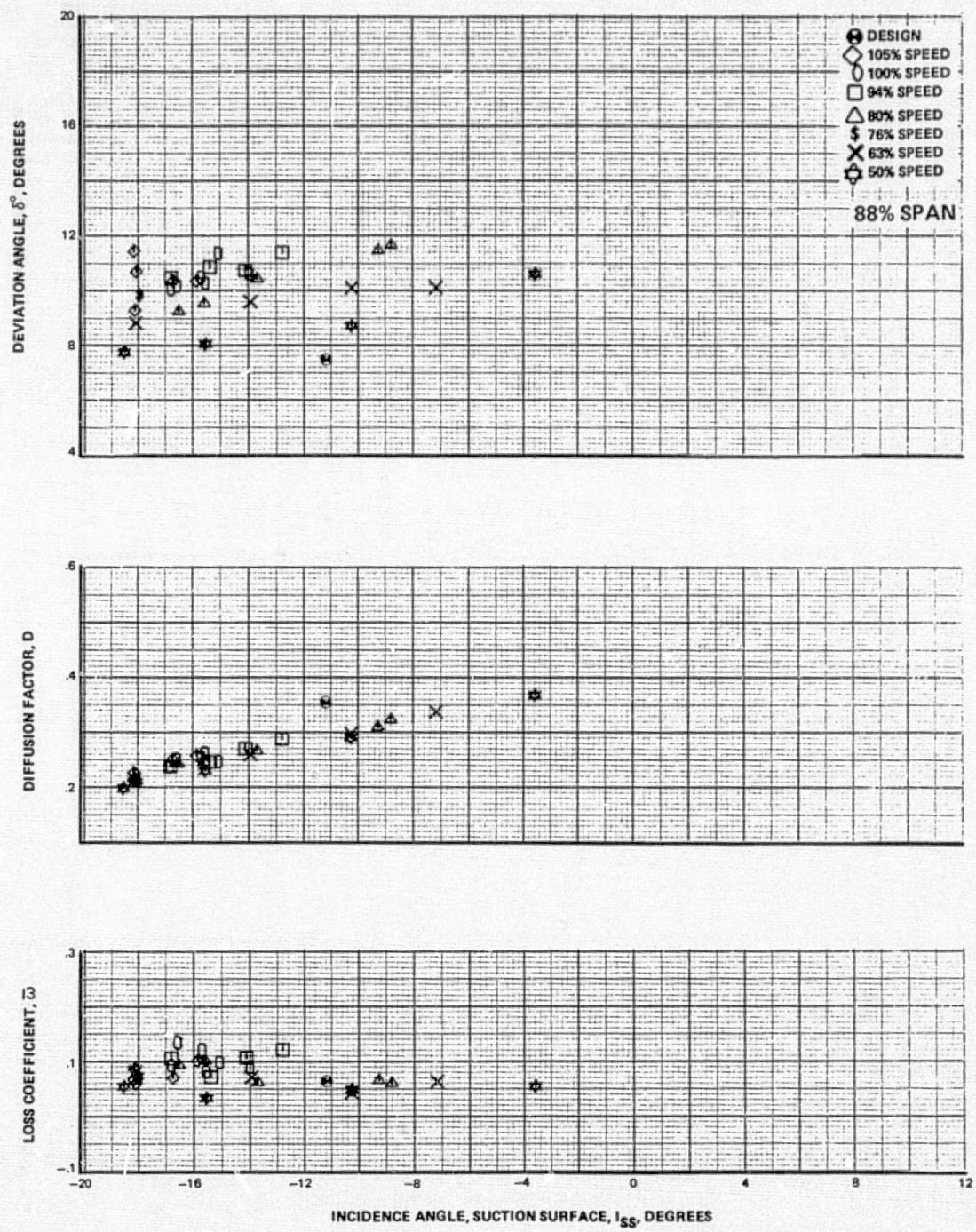


Figure 28j Blade-Element Performance, Baseline Configuration, Uniform Inlet Flow – First-Stage Stator

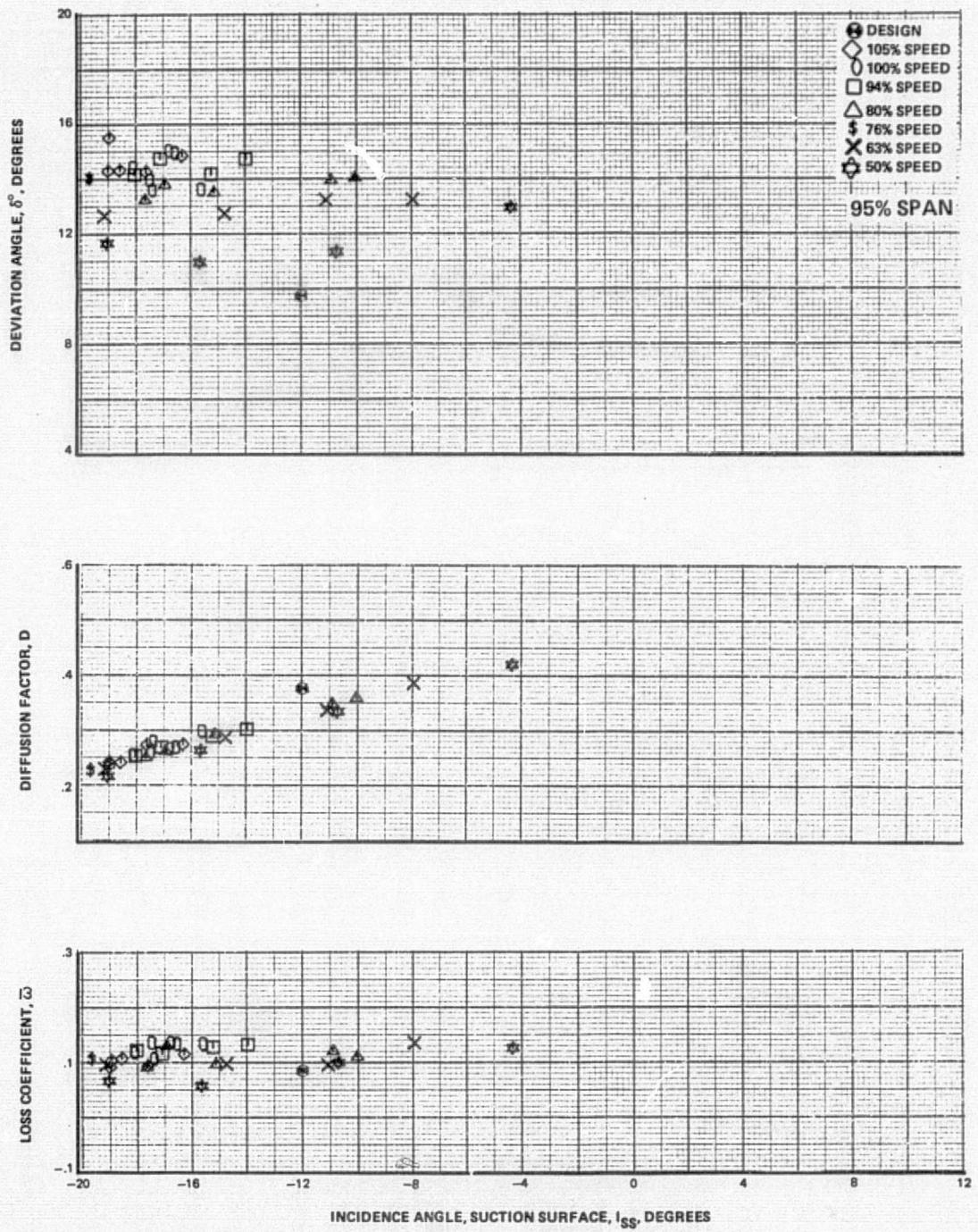


Figure 28k Blade-Element Performance, Baseline Configuration, Uniform Inlet Flow – First-Stage Stator

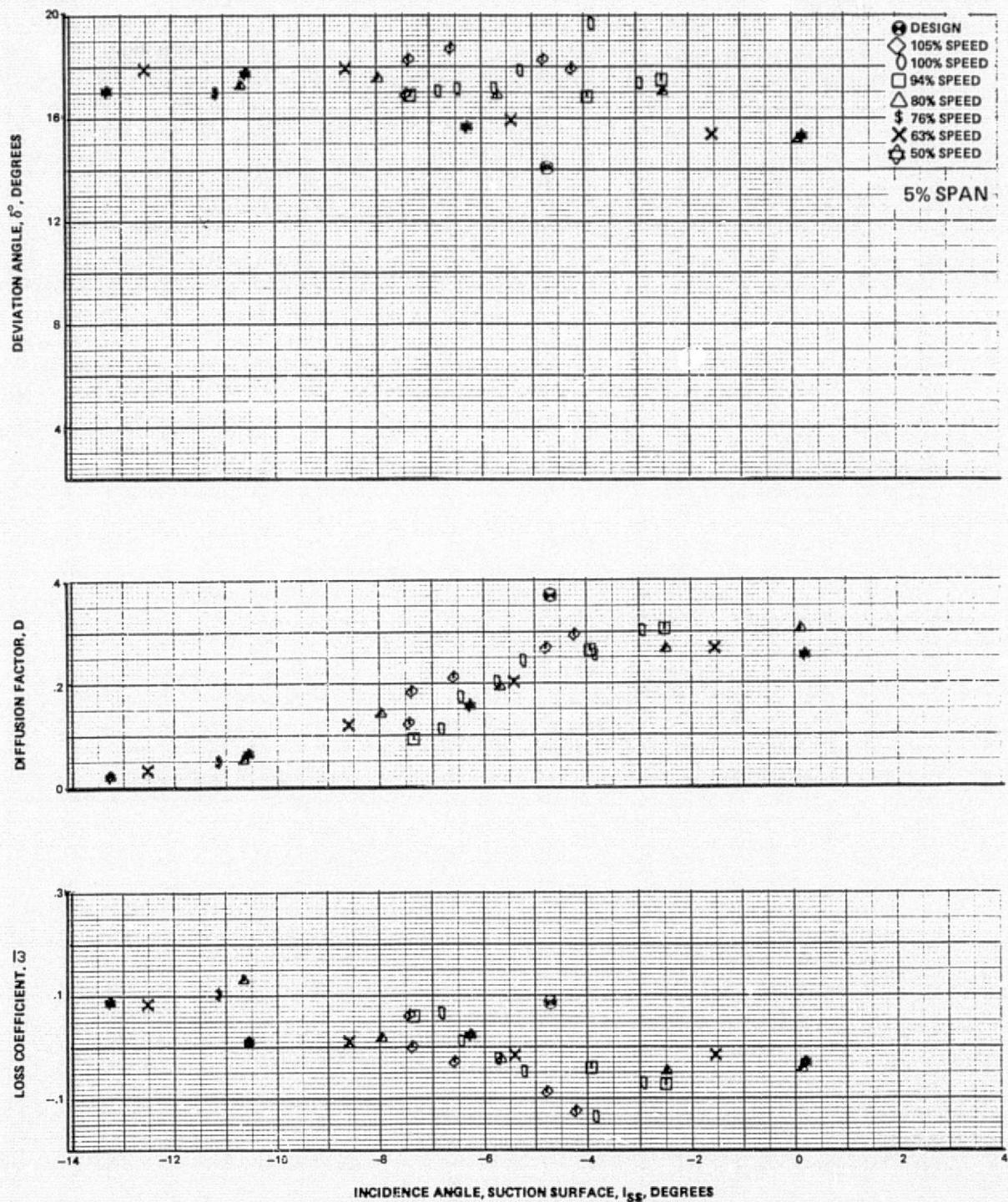


Figure 29a Blade-Element Performance, Baseline Configuration, Uniform Inlet Flow – Second-Stage Rotor

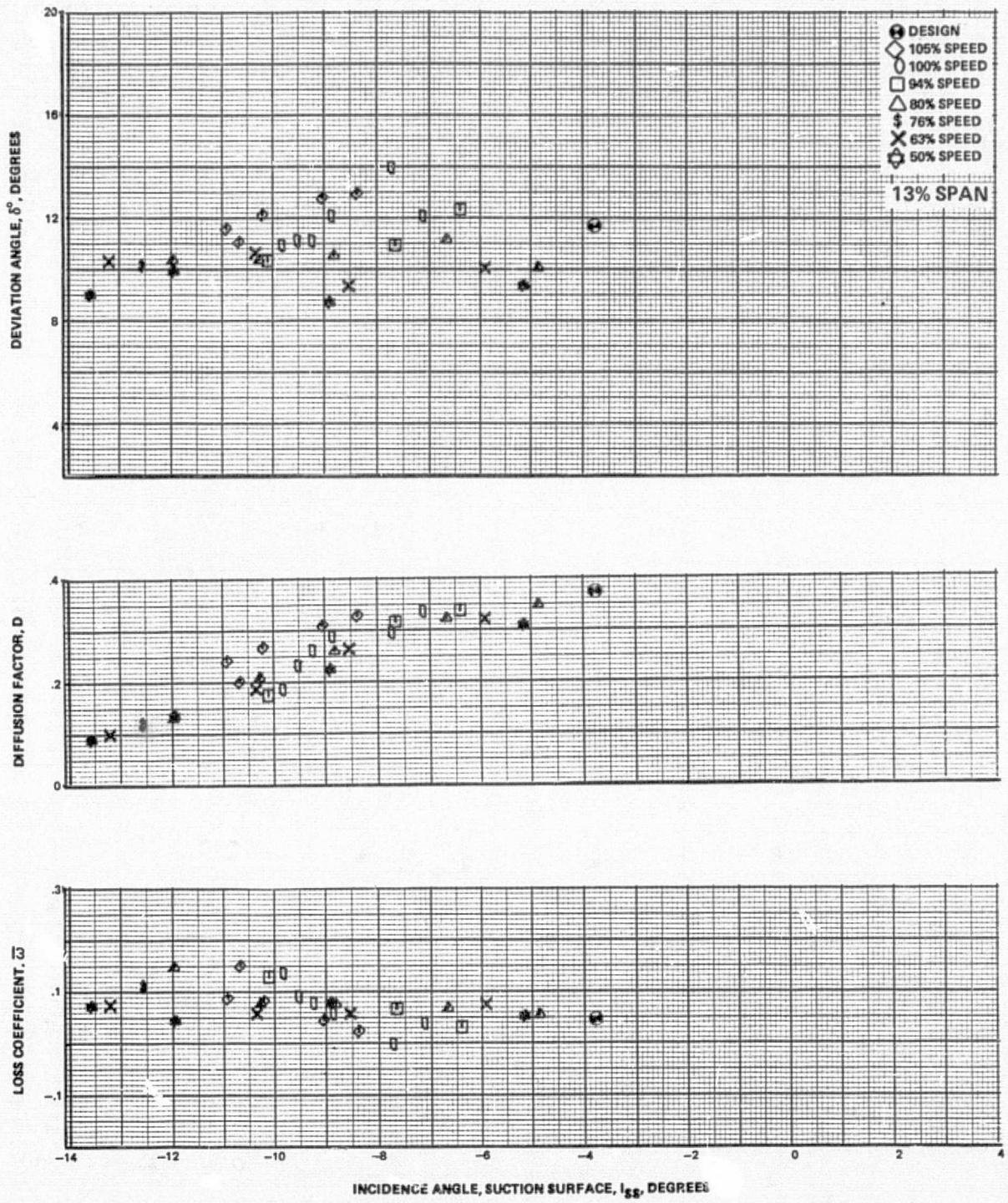


Figure 29b Blade-Element Performance, Baseline Configuration, Uniform Inlet Flow – Second-Stage Rotor

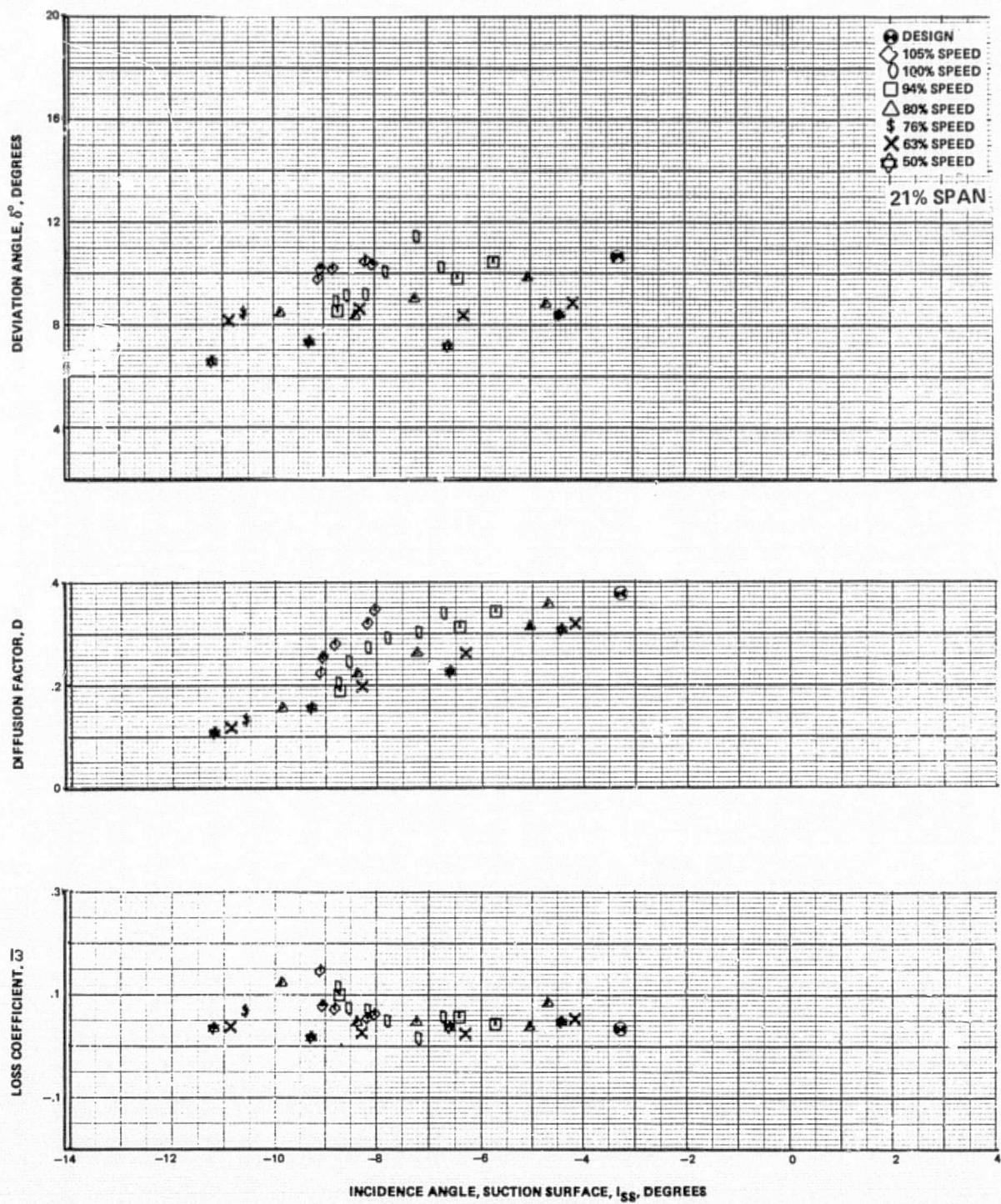


Figure 29c Blade-Element Performance, Baseline Configuration, Uniform Inlet Flow – Second-Stage Rotor

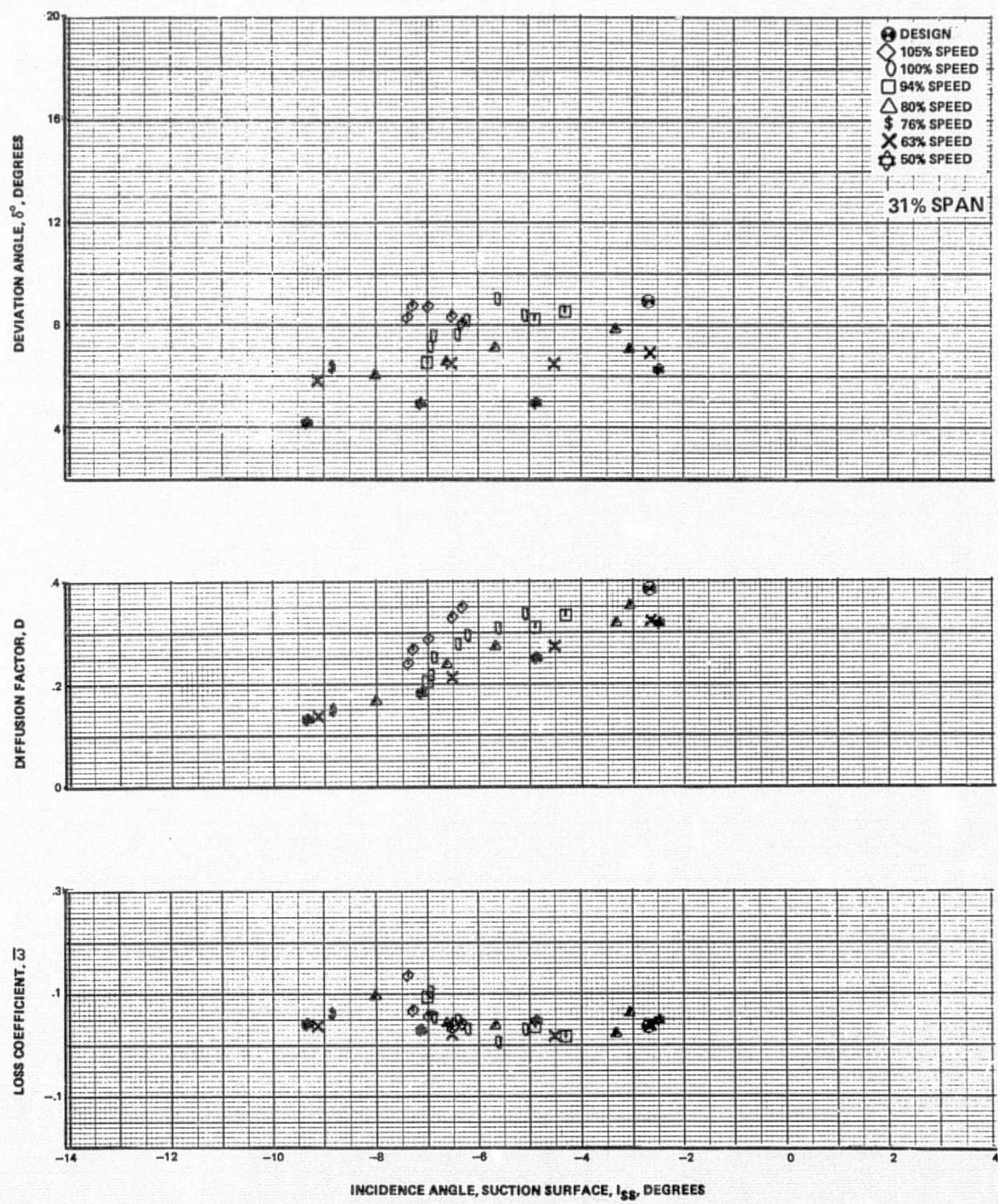


Figure 29d Blade-Element Performance, Baseline Configuration, Uniform Inlet Flow – Second-Stage Rotor

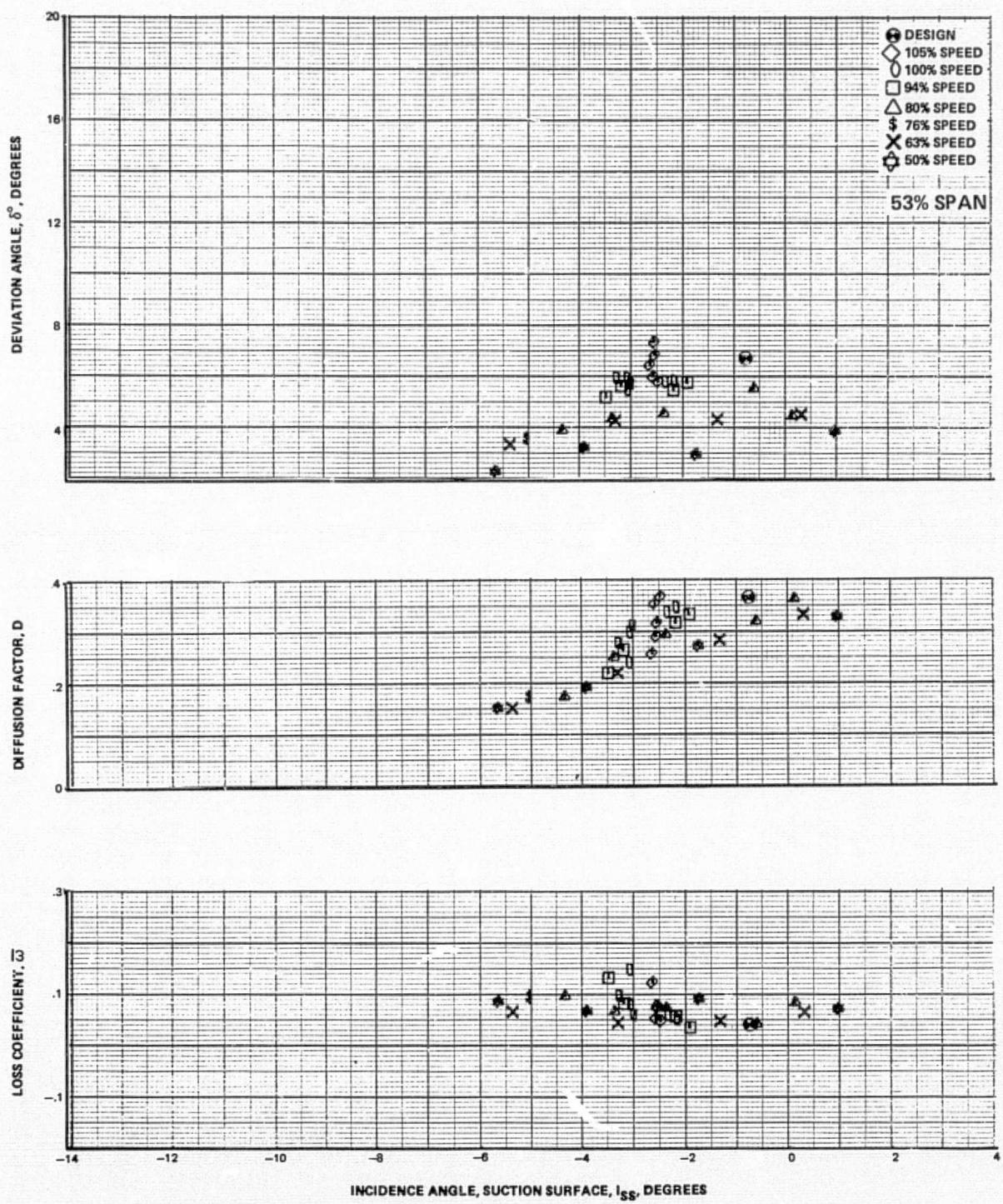


Figure 29e Blade-Element Performance, Baseline Configuration, Uniform Inlet Flow – Second-Stage Rotor

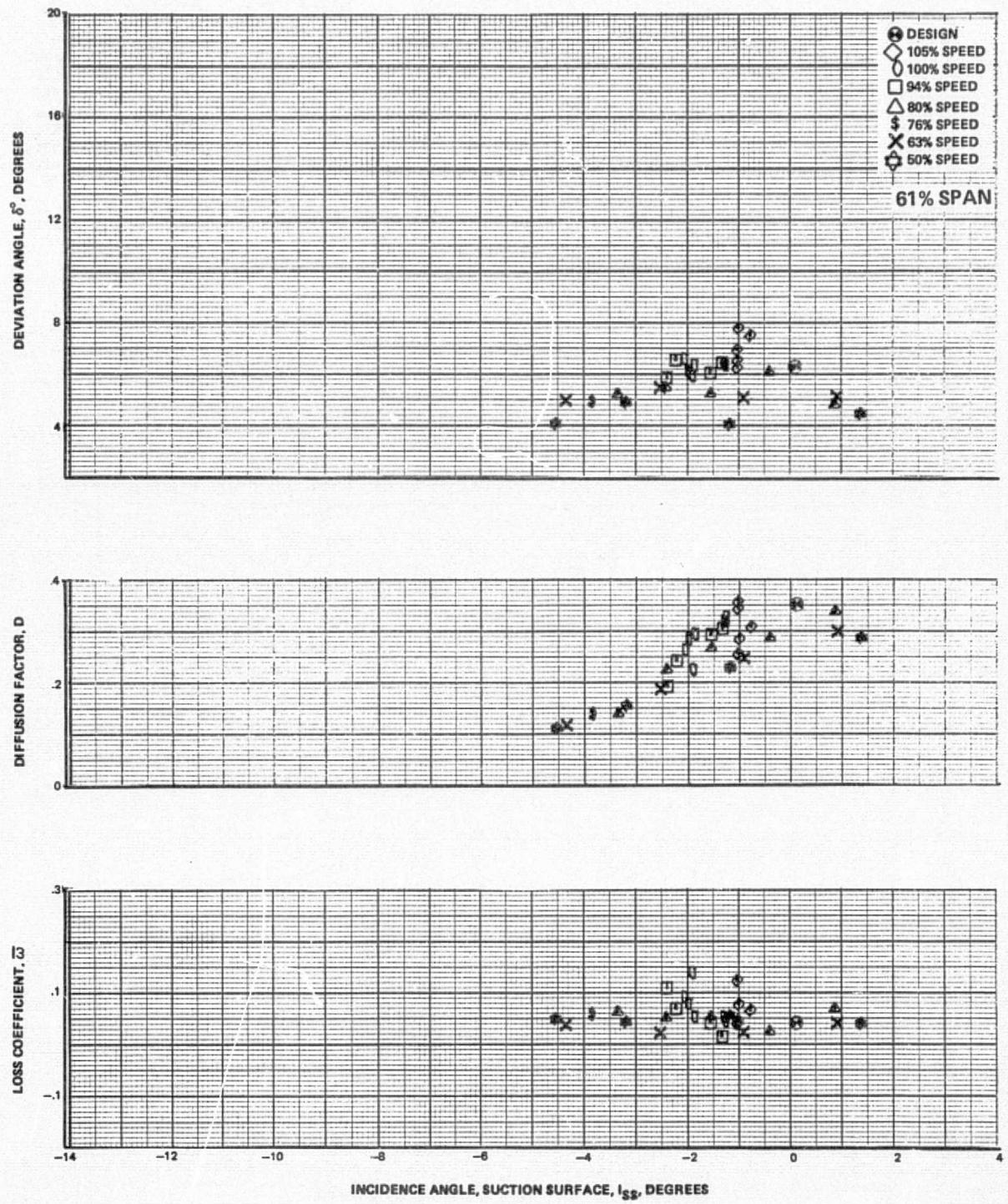


Figure 29f Blade-Element Performance, Baseline Configuration, Uniform Inlet Flow – Second-Stage Rotor

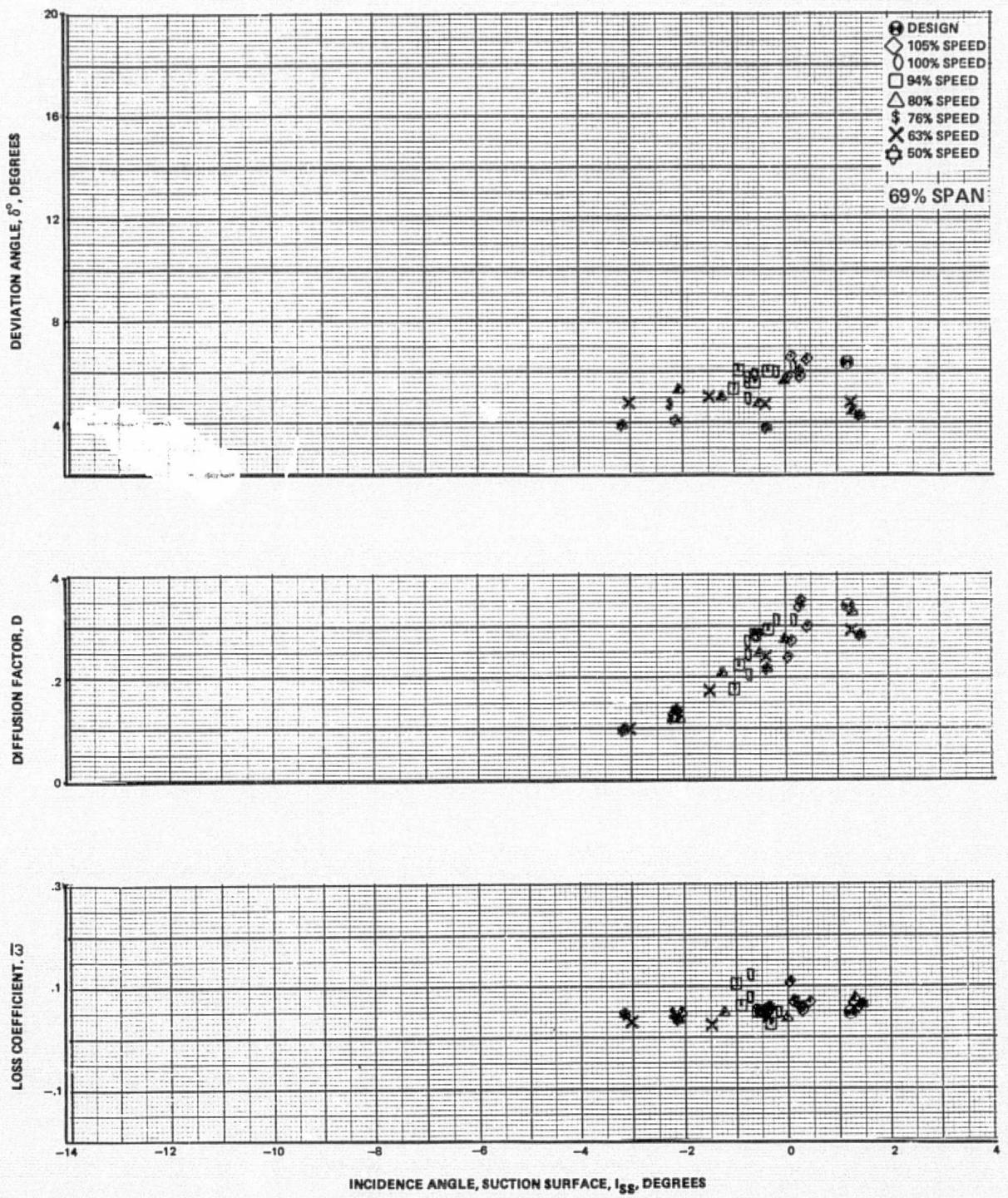


Figure 29g Blade-Element Performance, Baseline Configuration, Uniform Inlet Flow – Second-Stage Rotor

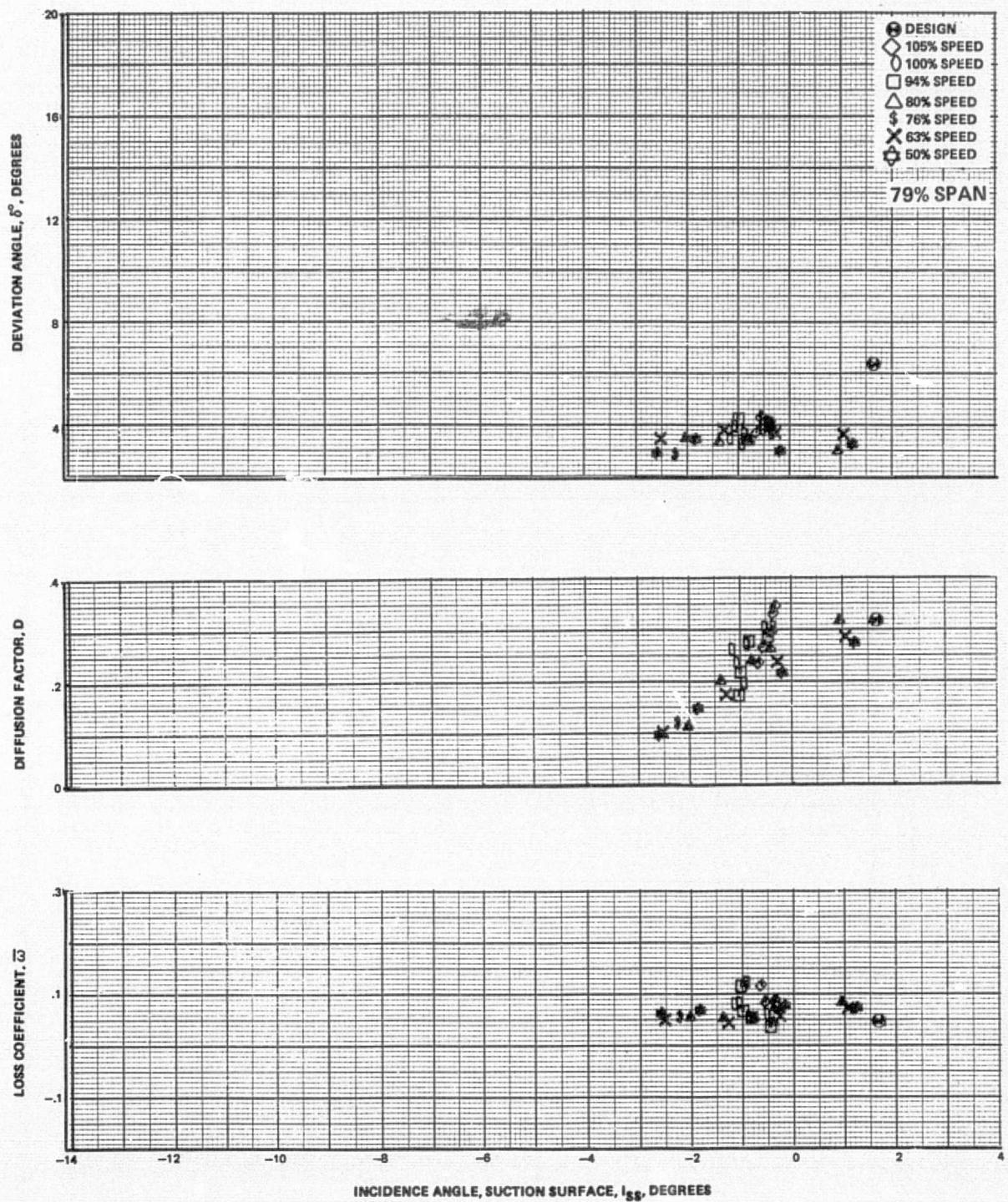


Figure 29h Blade-Element Performance, Baseline Configuration, Uniform Inlet Flow – Second-Stage Rotor

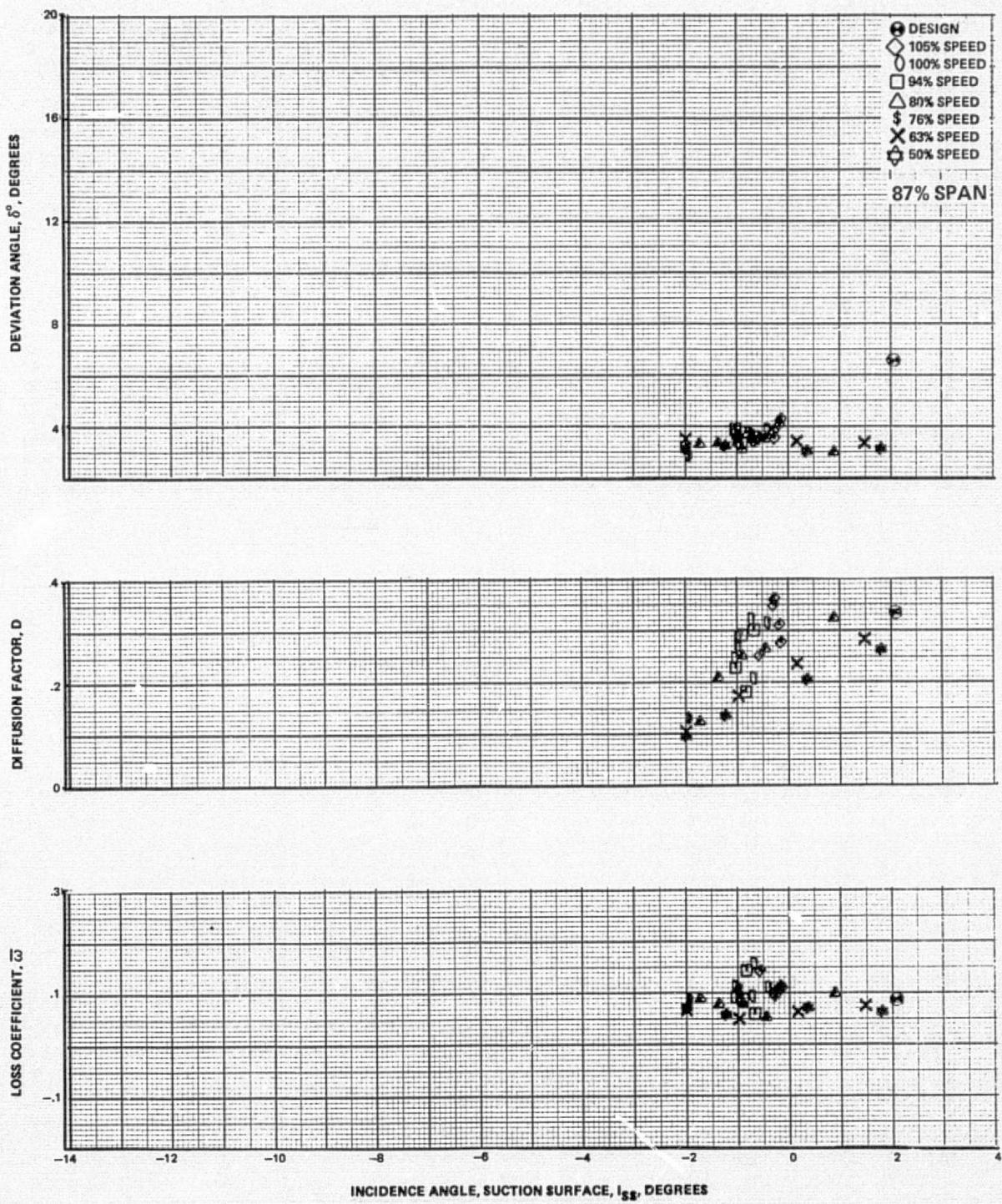


Figure 29i Blade-Element Performance, Baseline Configuration, Uniform Inlet Flow – Second-Stage Rotor

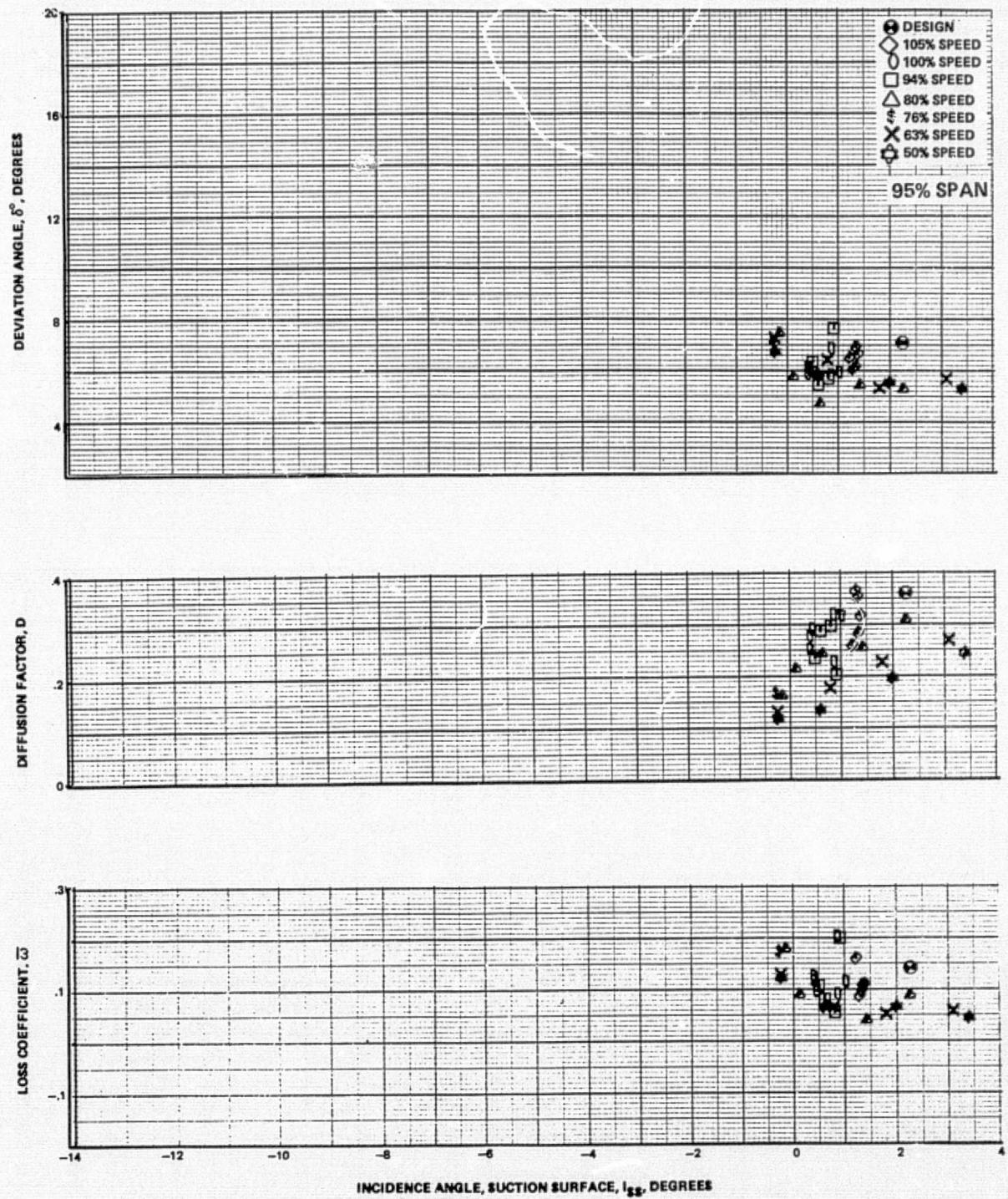


Figure 29j Blade-Element Performance, Baseline Configuration, Uniform Inlet Flow – Second-Stage Rotor

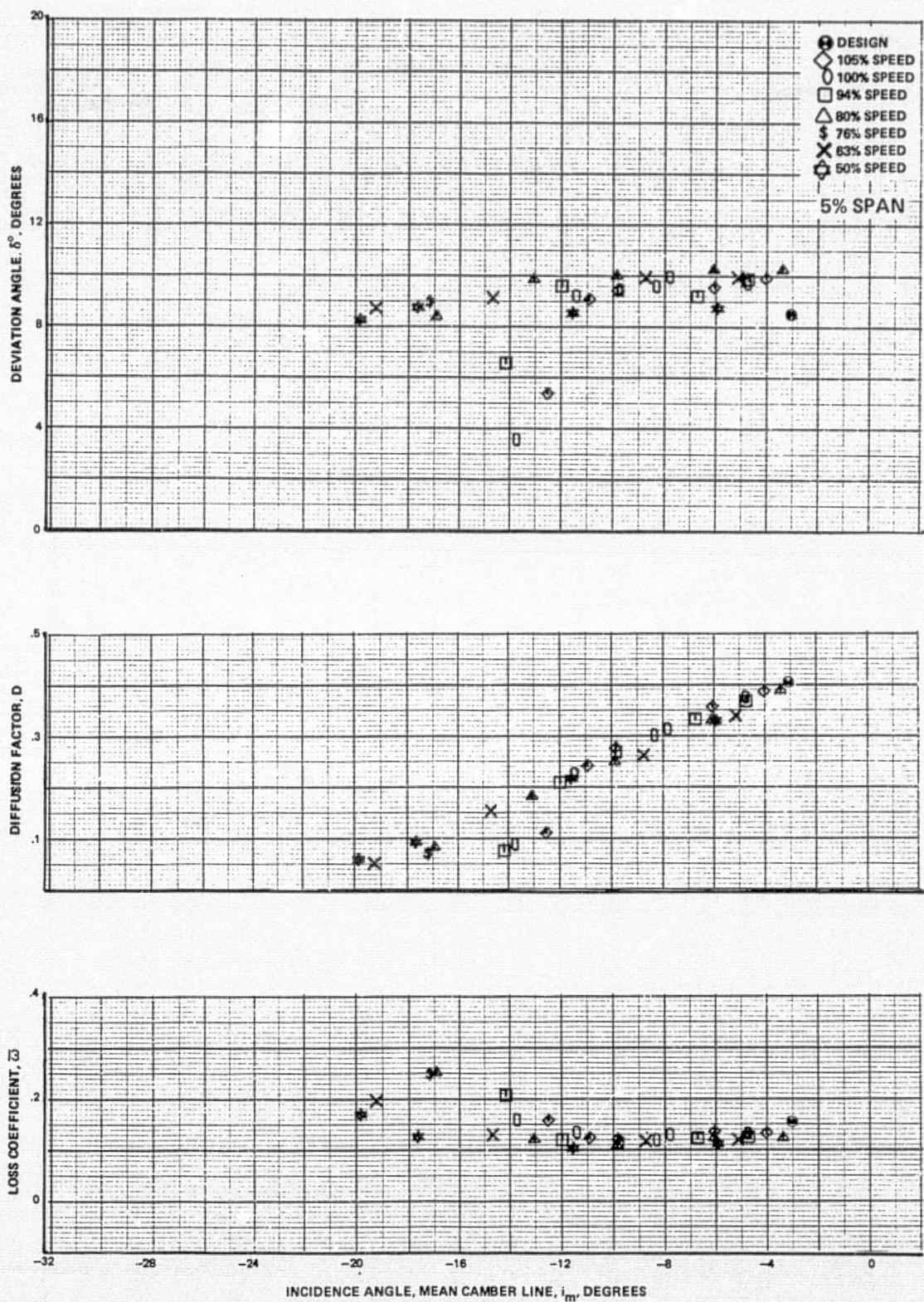


Figure 30a Blade-Element Performance, Baseline Configuration, Uniform Inlet Flow – Second-Stage Stator

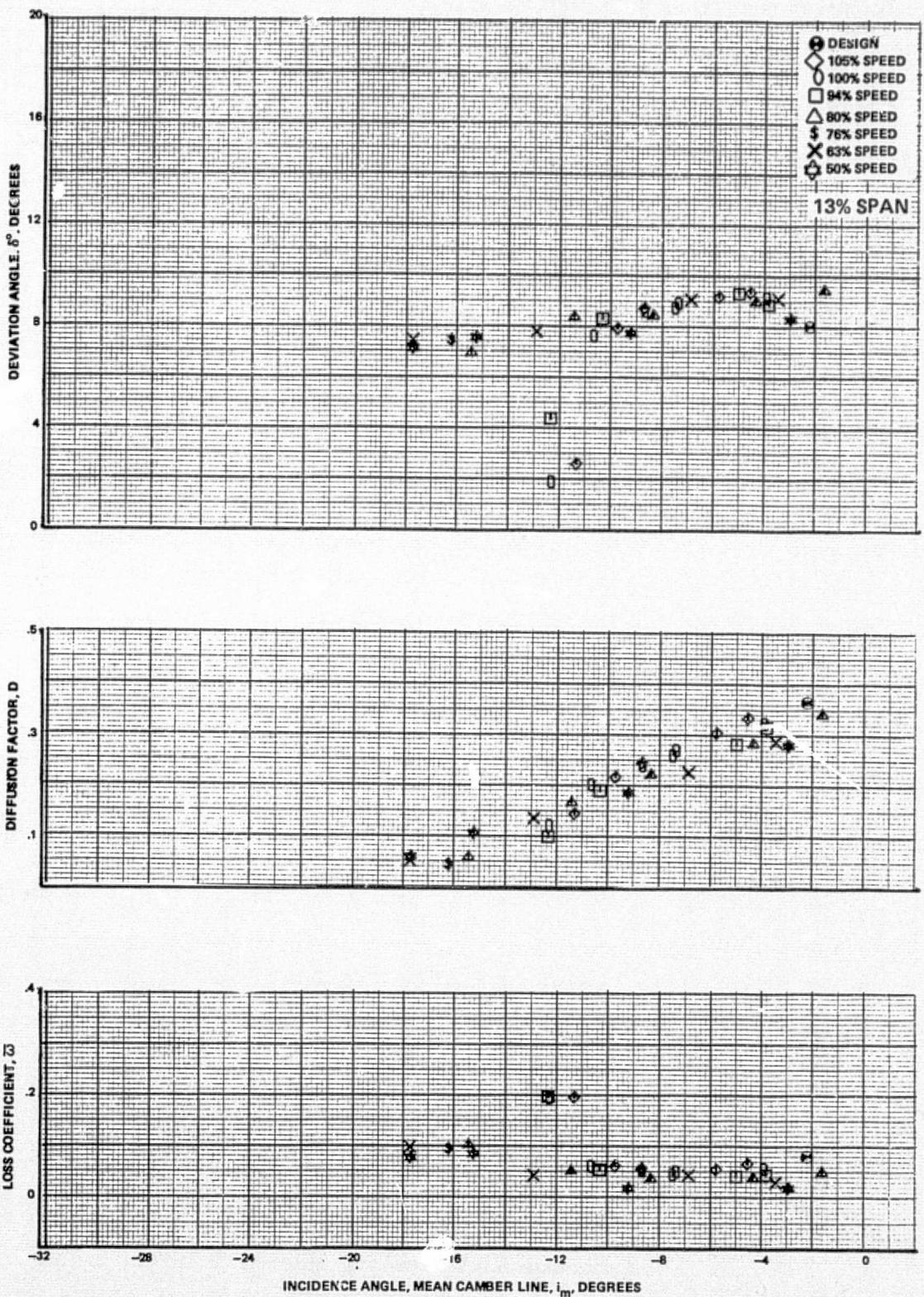


Figure 30b Blade-Element Performance, Baseline Configuration, Uniform Inlet Flow – Second-Stage Stator

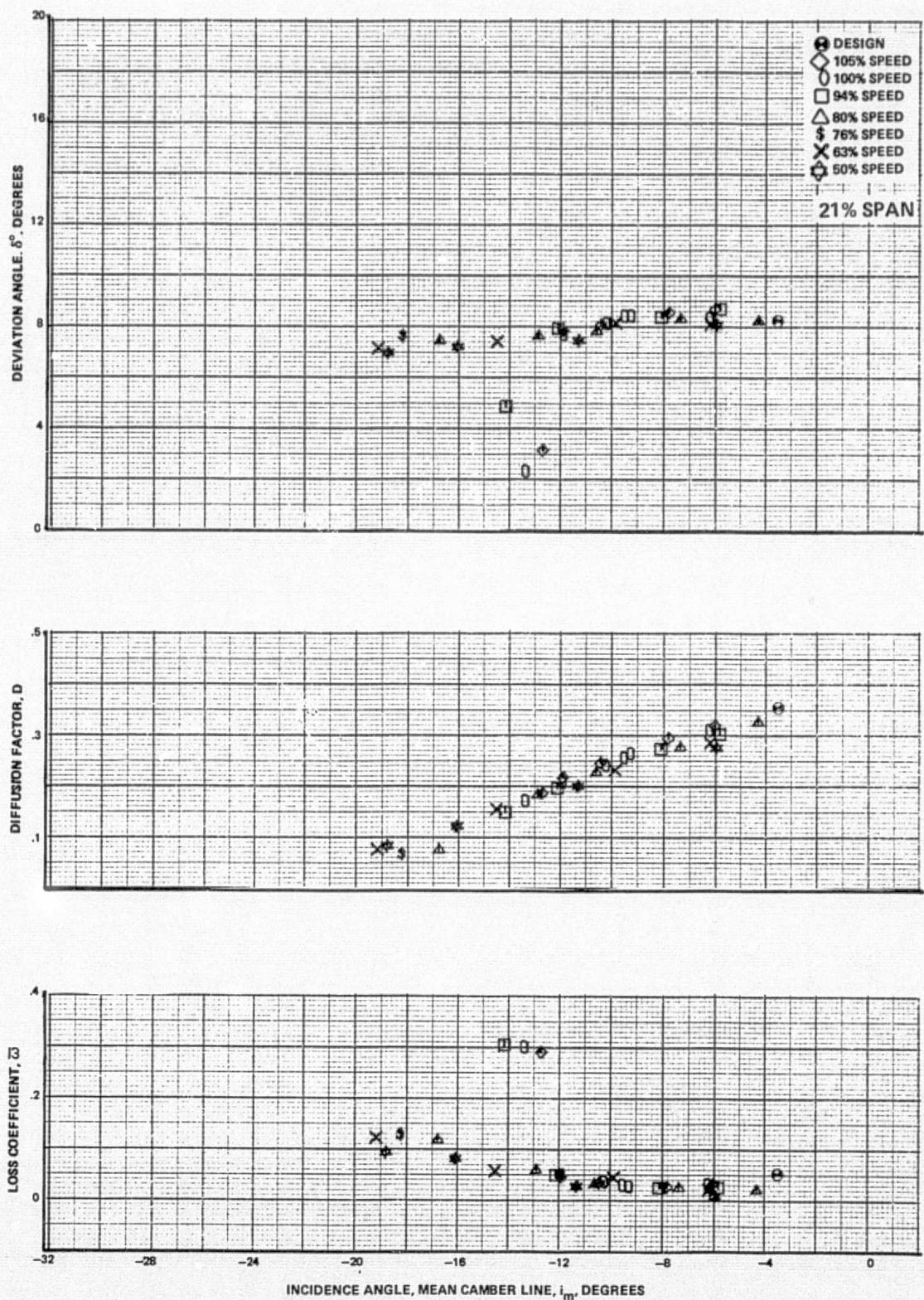


Figure 30c Blade-Element Performance, Baseline Configuration, Uniform Inlet Flow – Second-Stage Stator

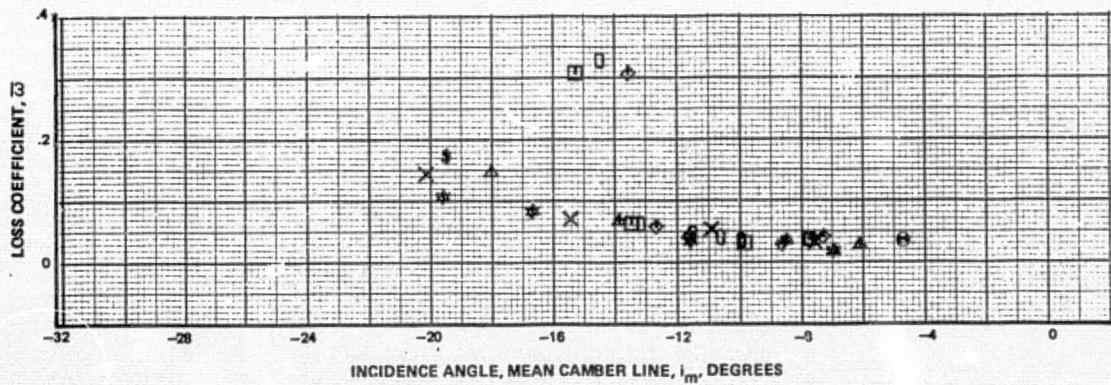
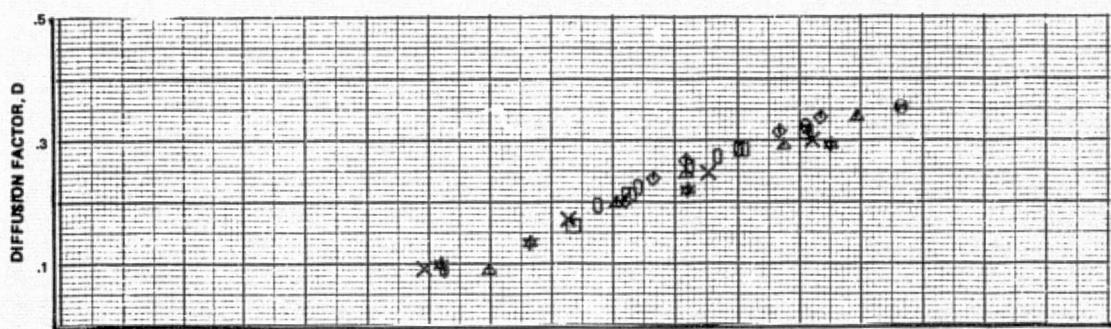
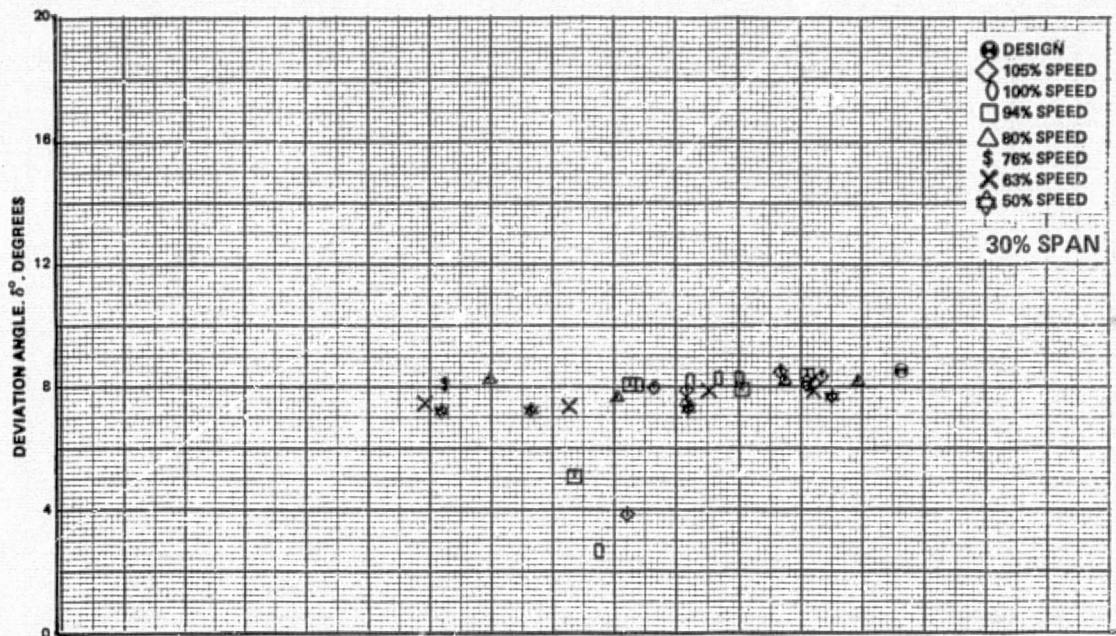


Figure 30d Blade-Element Performance, Baseline Configuration, Uniform Inlet Flow – Second-Stage Stator

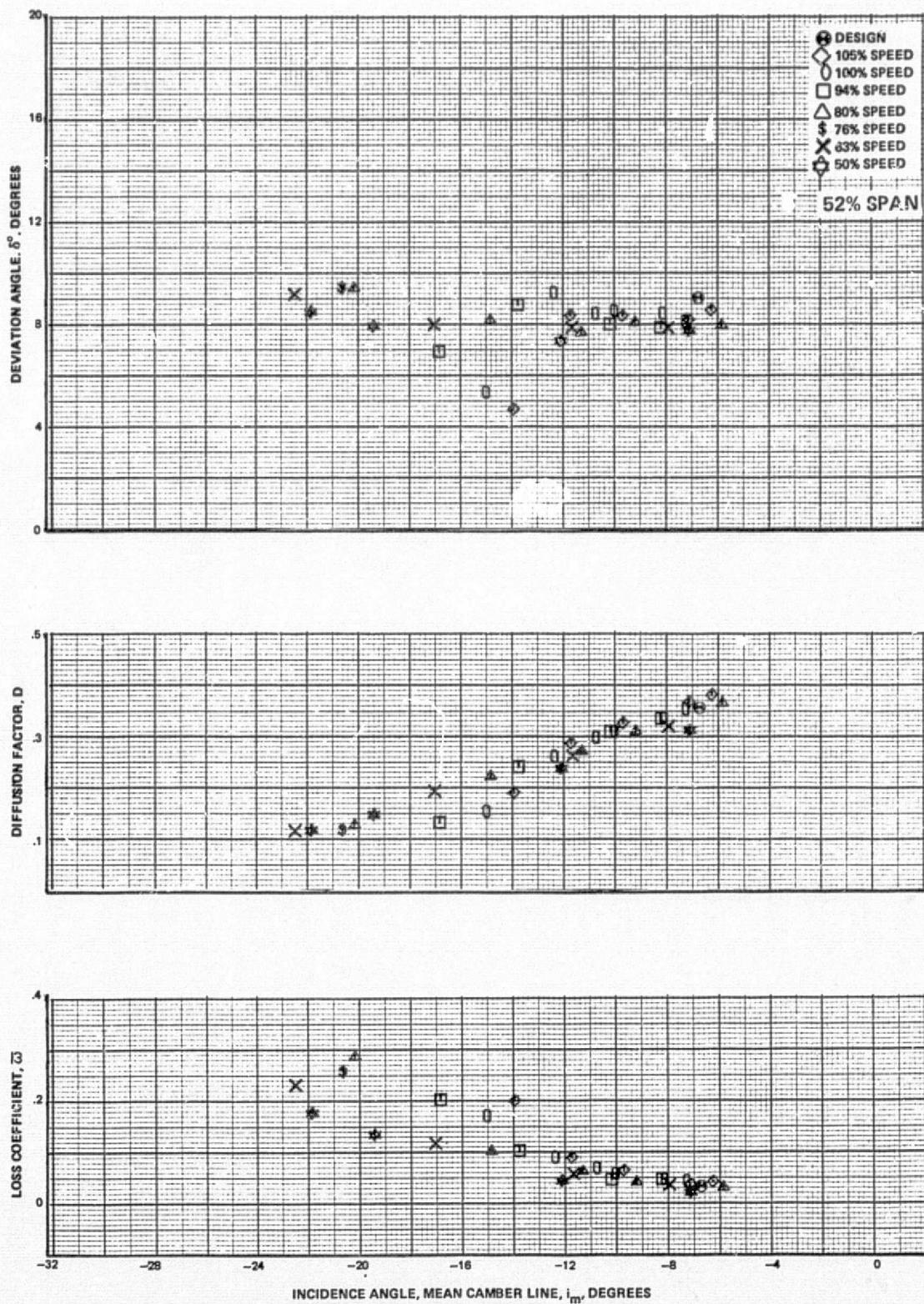


Figure 30e Blade-Element Performance, Baseline Configuration, Uniform Inlet Flow – Second-Stage Stator

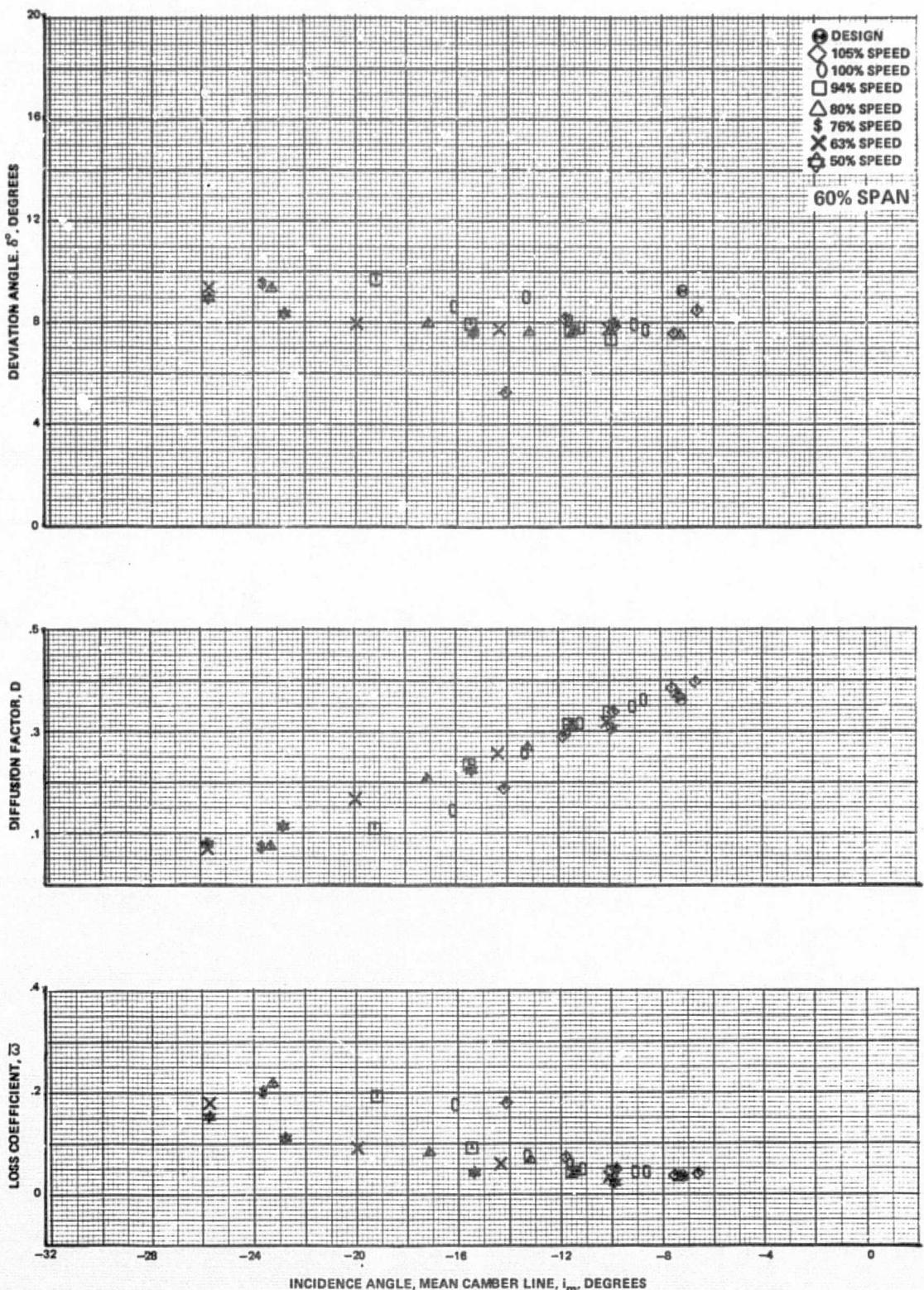


Figure 30f Blade-Element Performance, Baseline Configuration, Uniform Inlet Flow – Second-Stage Stator

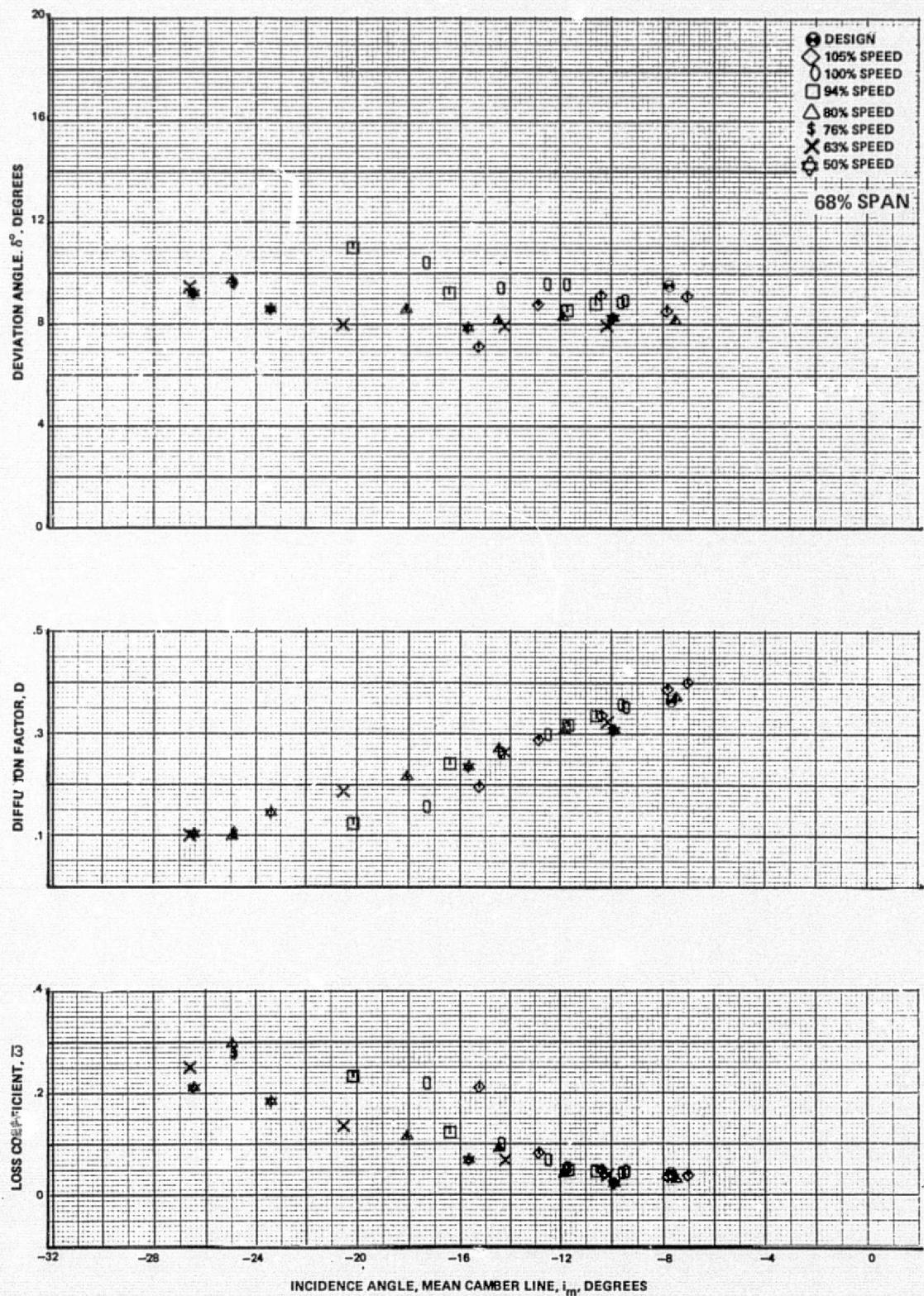


Figure 30g Blade-Element Performance, Baseline Configuration, Uniform Inlet Flow – Second-Stage Stator

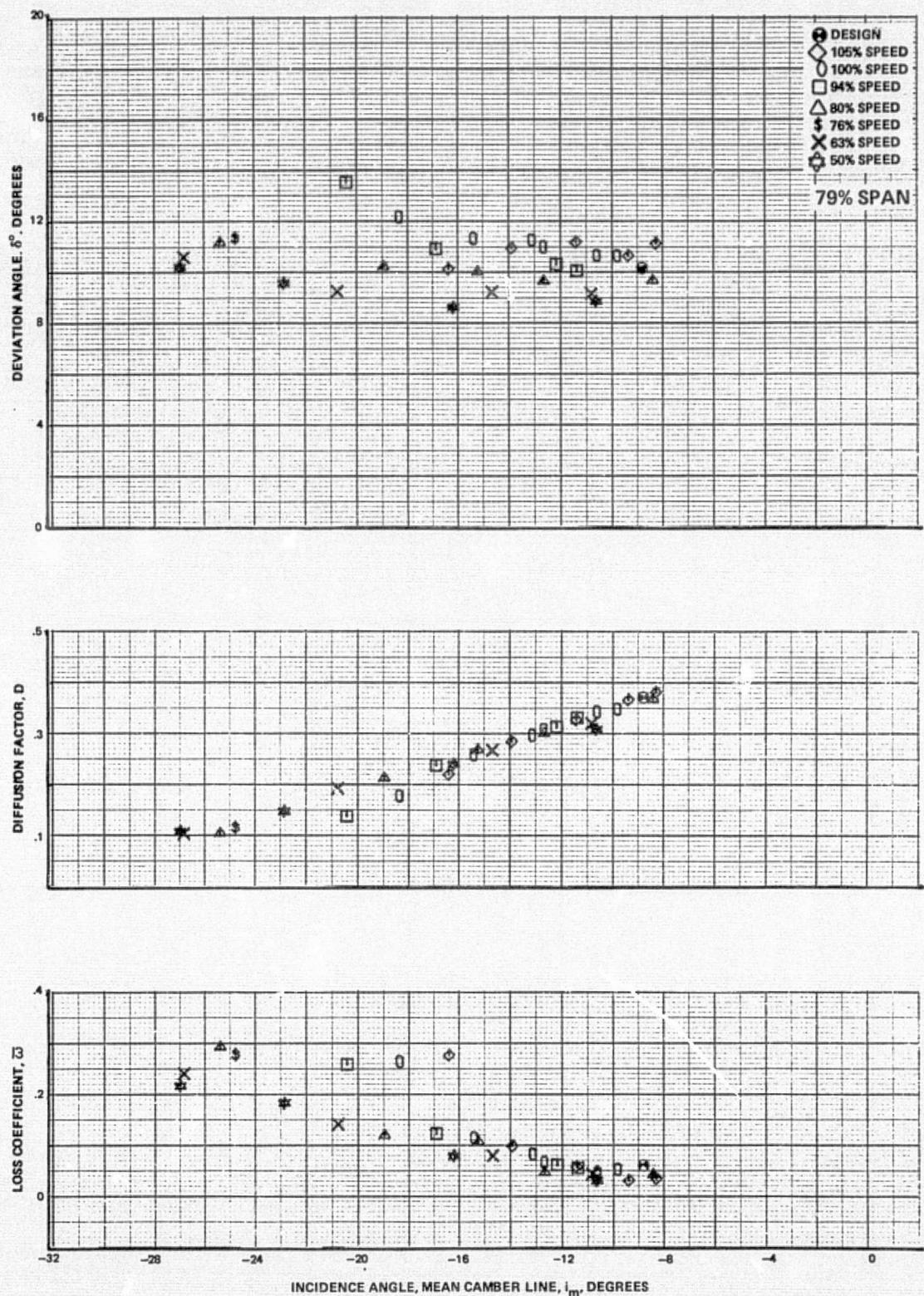


Figure 30h Blade-Element Performance, Baseline Configuration, Uniform Inlet Flow – Second-Stage Stator

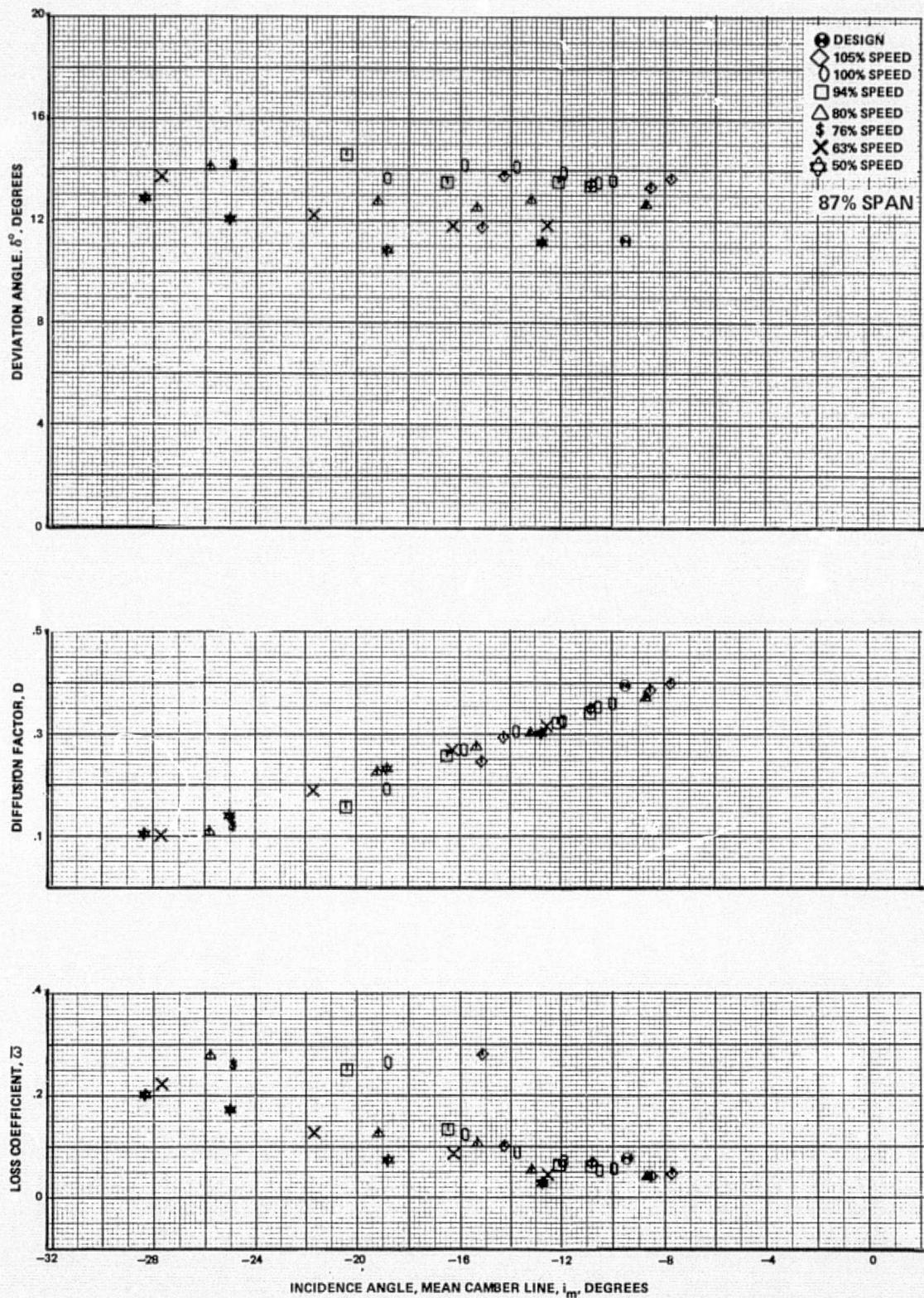


Figure 30i Blade-Element Performance, Baseline Configuration, Uniform Inlet Flow – Second-Stage Stator

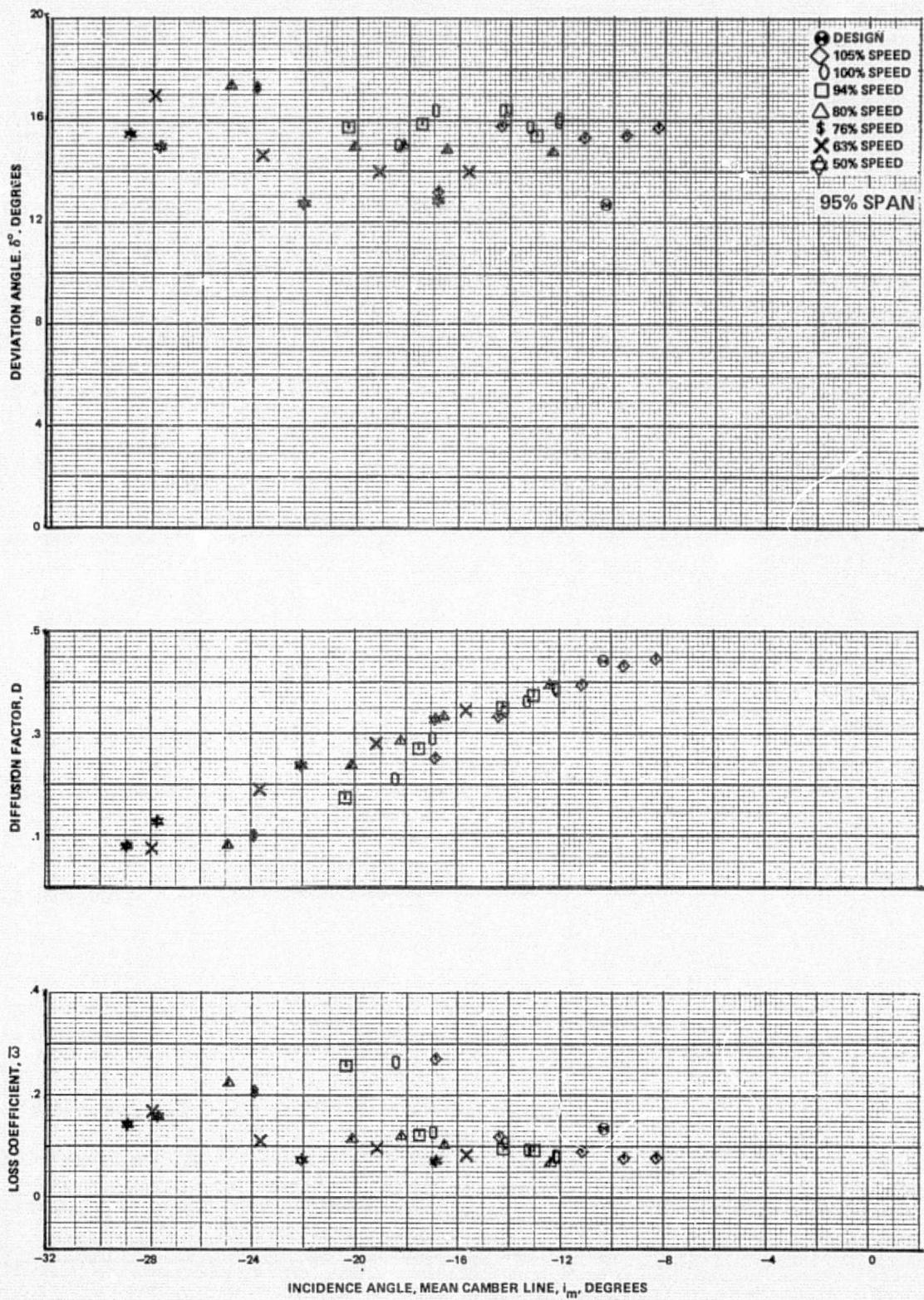


Figure 30j Blade-Element Performance, Baseline Configuration, Uniform Inlet Flow – Second-Stage Stator

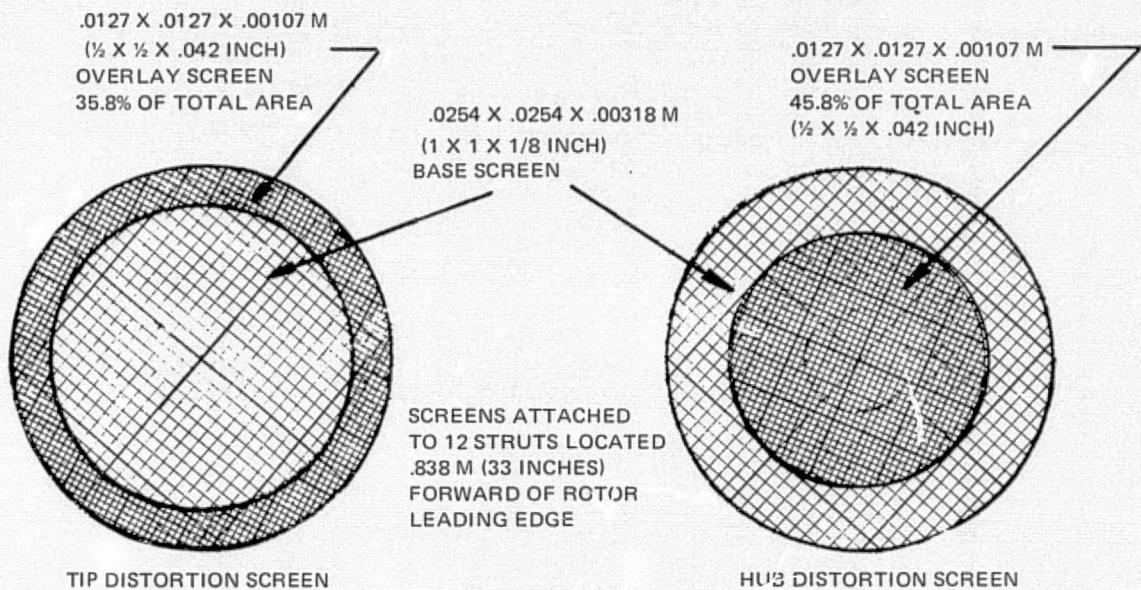


Figure 31 Hub and Tip Radial-Distortion Screens

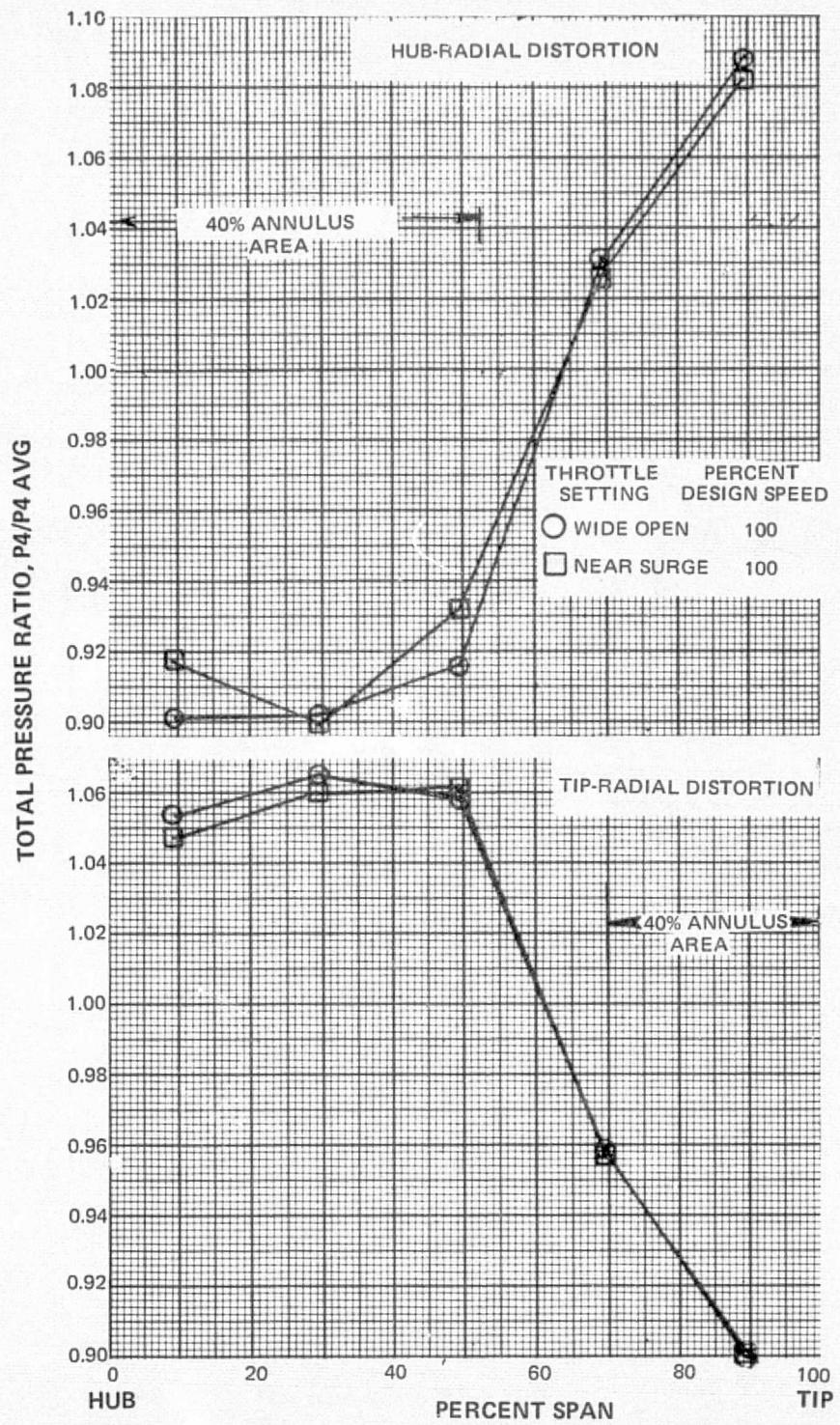


Figure 32 Fan Inlet Total Pressure Ratio Versus Span for Radially Distorted Inlet Flow

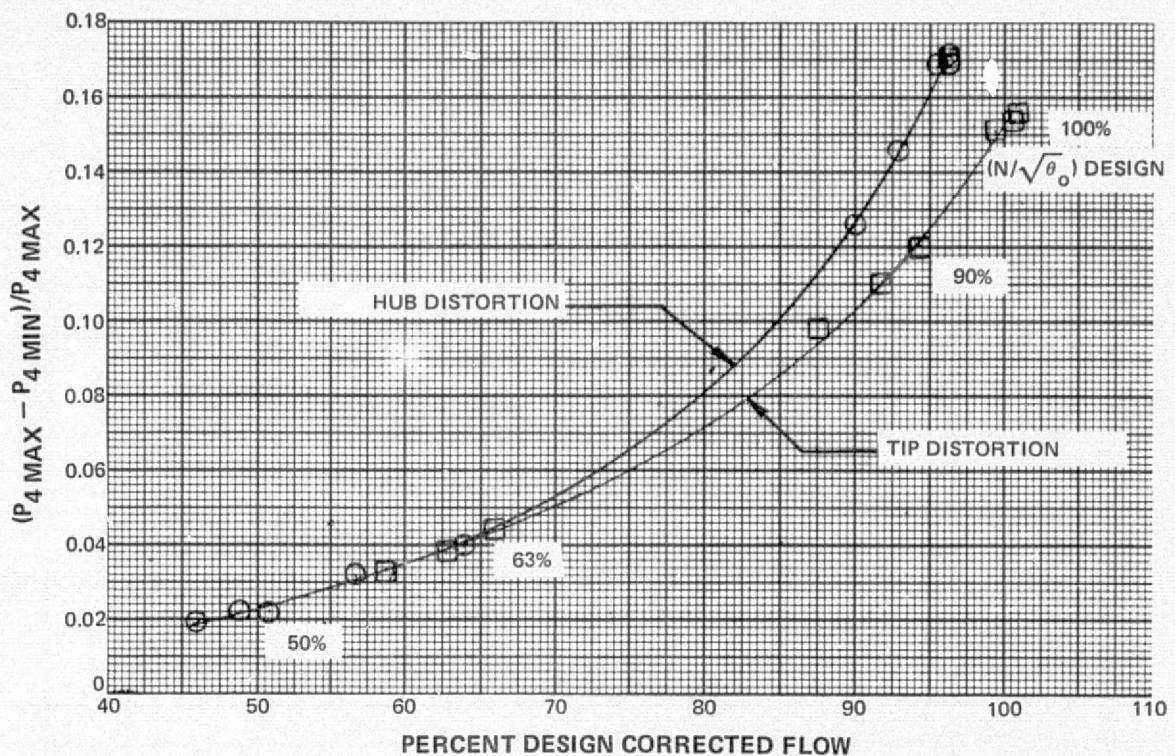


Figure 33 Inlet Total Pressure Distortion Parameter Versus Inlet Flow for Radial Distortions

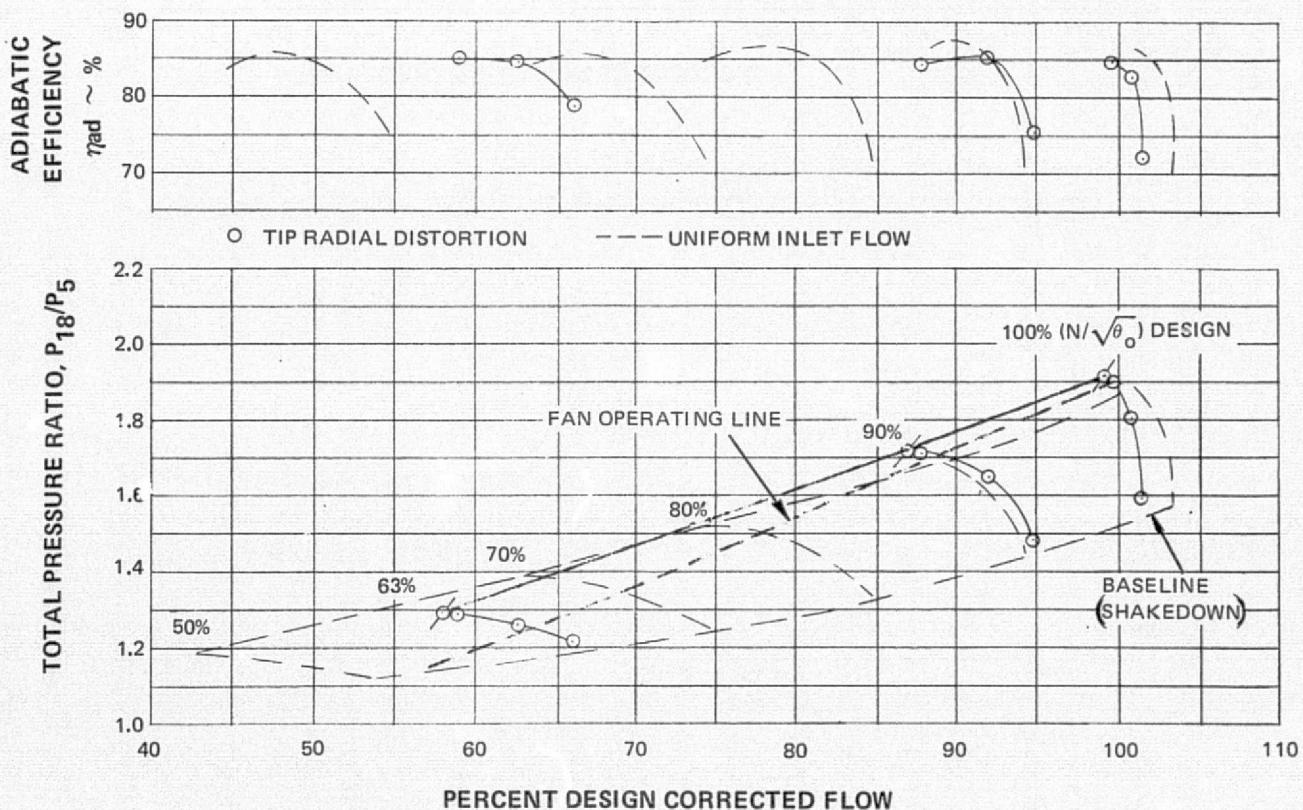


Figure 34 Fan Overall Performance With Tip Radially Distorted Inlet Flow

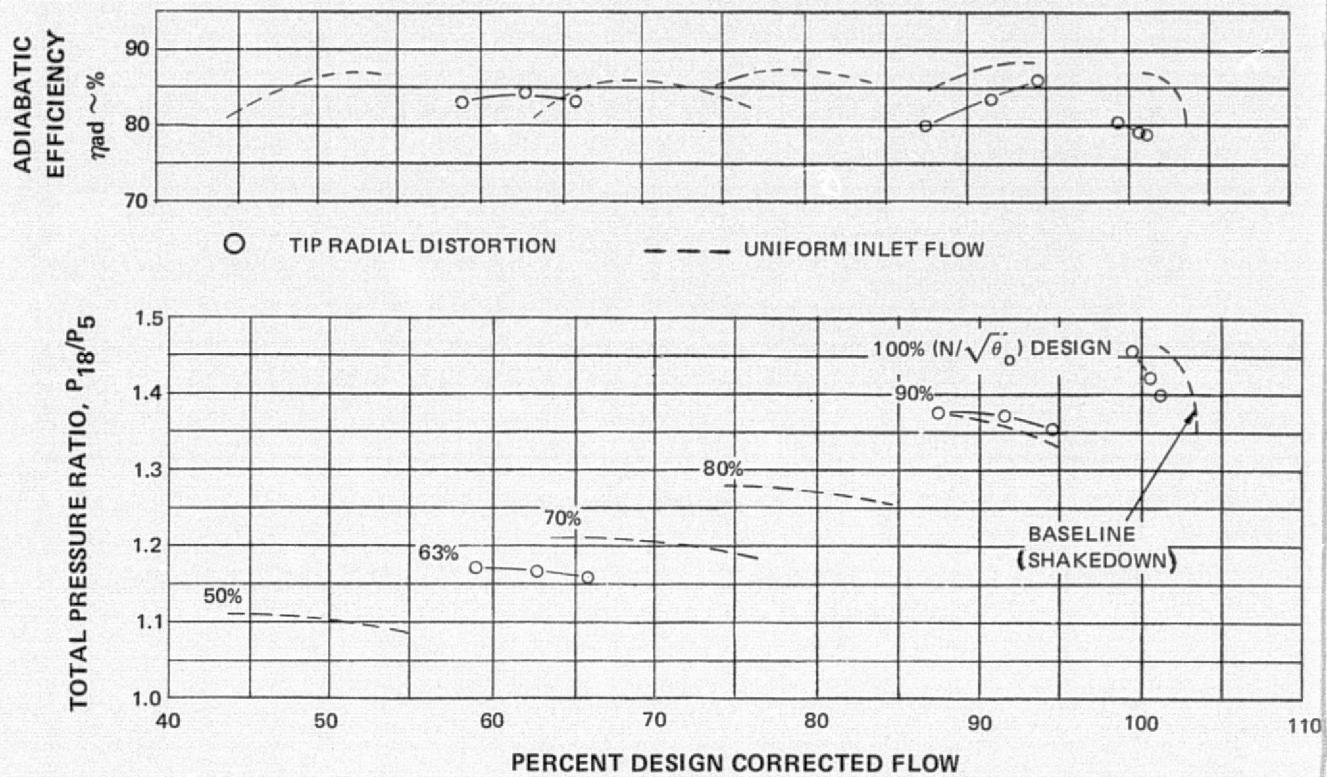


Figure 35 First-Stage Performance With Tip Radially Distorted Inlet Flow

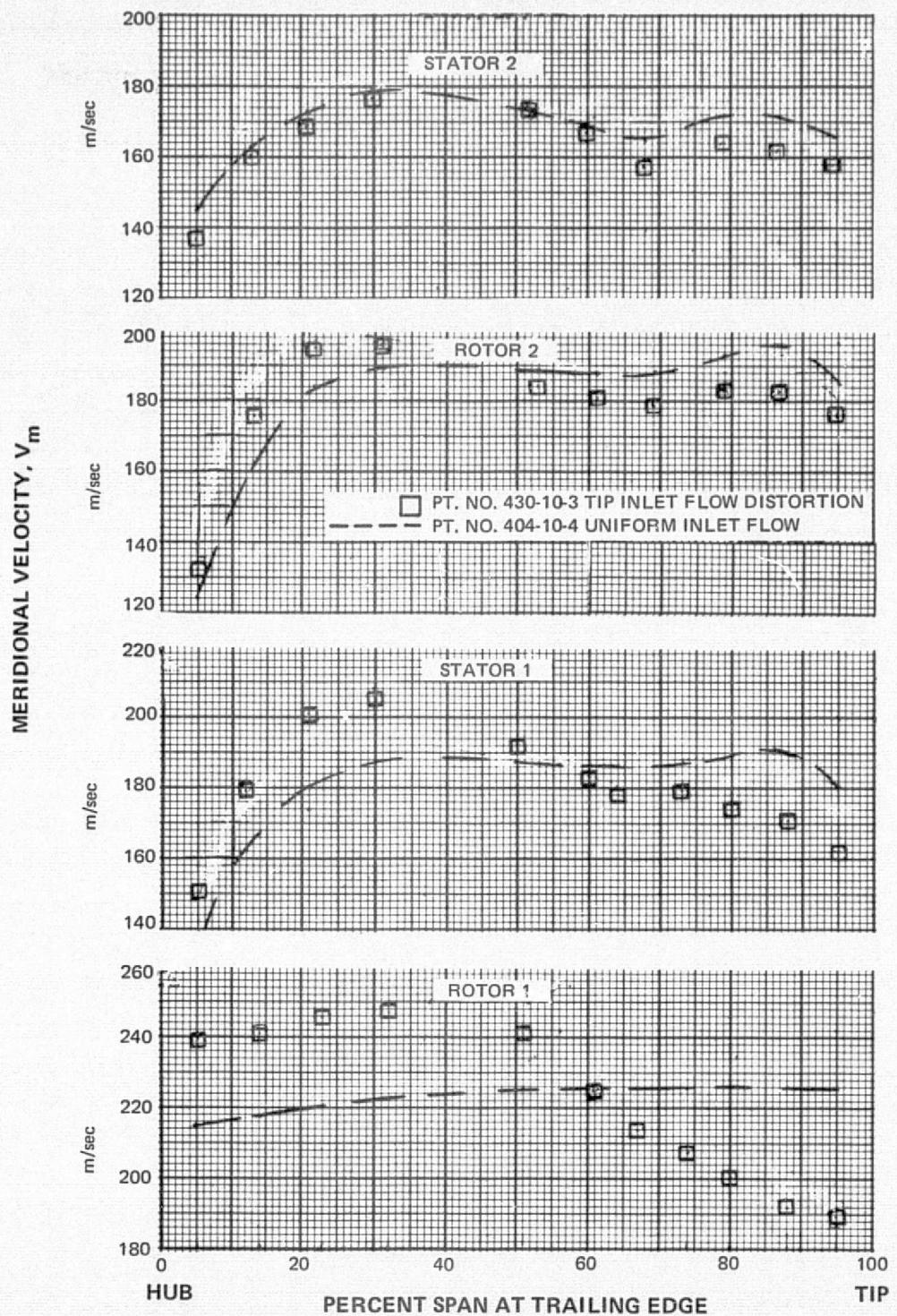


Figure 36 Blade Row Inlet Meridional Velocity Versus Span For Tip Radially Distorted Inlet Flow

NOTE: *UNSHADED SYMBOLS REPRESENT
PRESSURE ALONG STREAMLINE
FROM FAN INLET TO EXIT
*SHADED SYMBOLS REPRESENT THE
LOCAL FAN EXIT PRESSURE
DIVIDED BY THE AVERAGE FAN
INLET PRESSURE

□ PT. NO. 430-10-3
TIP INLET FLOW DISTORTION
— PT. NO. 404-10-4
UNIFORM INLET FLOW

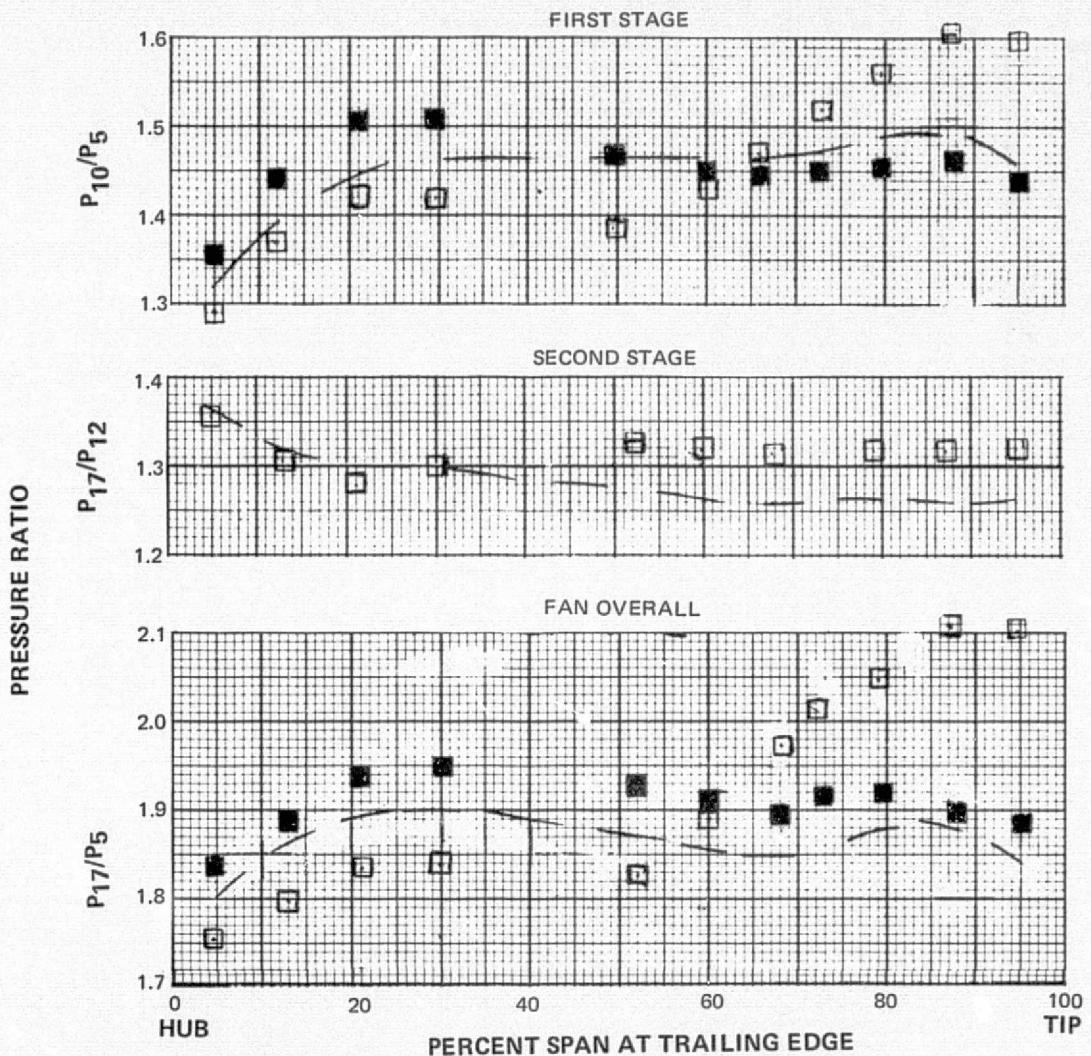


Figure 3 / Fan Overall Pressure Ratio Versus Span For Tip Radially Distorted Inlet Flow

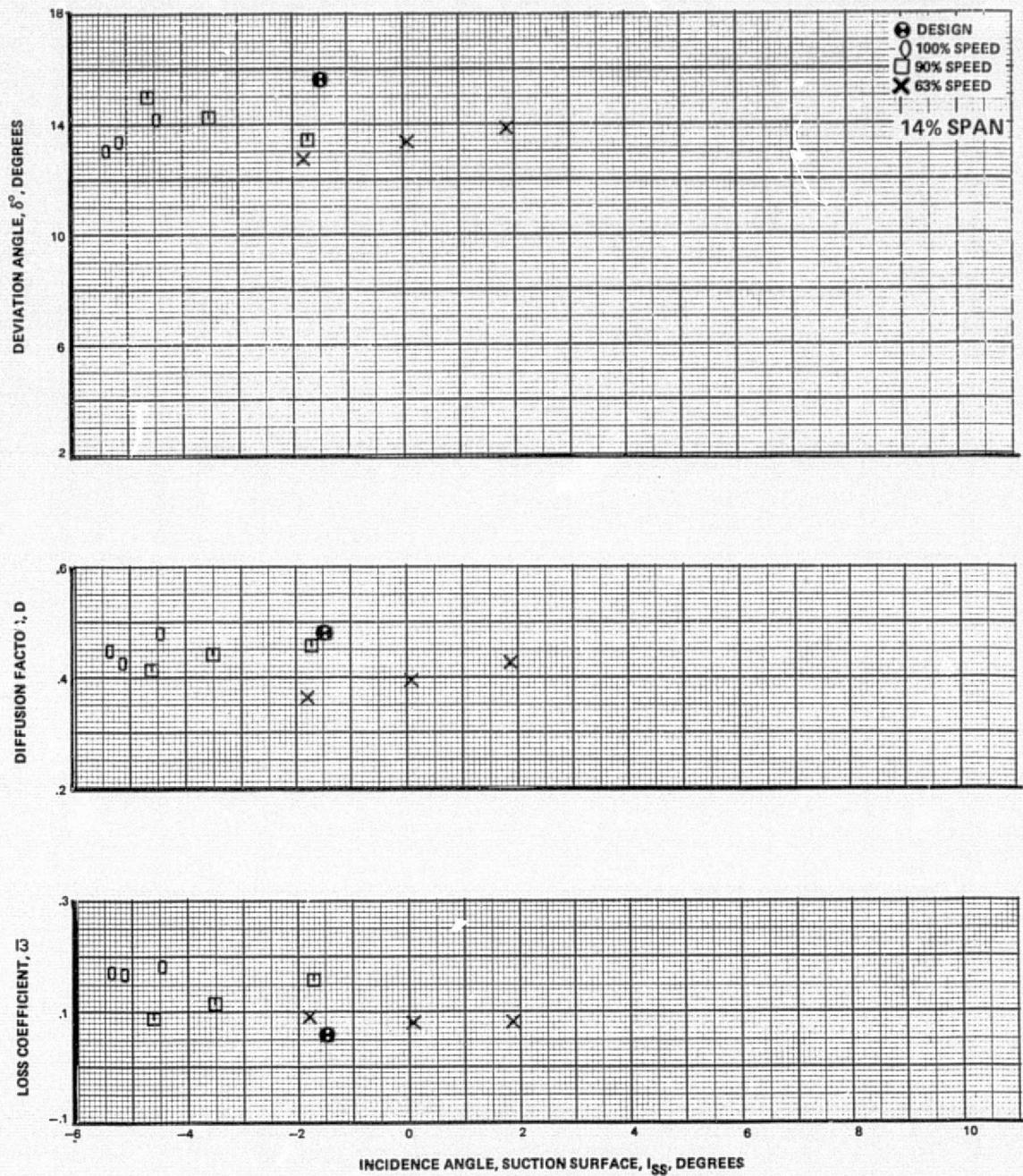


Figure 38a Blade-Element Performance, Baseline Configuration, Tip Radially Distorted Inlet Flow – First-Stage Rotor

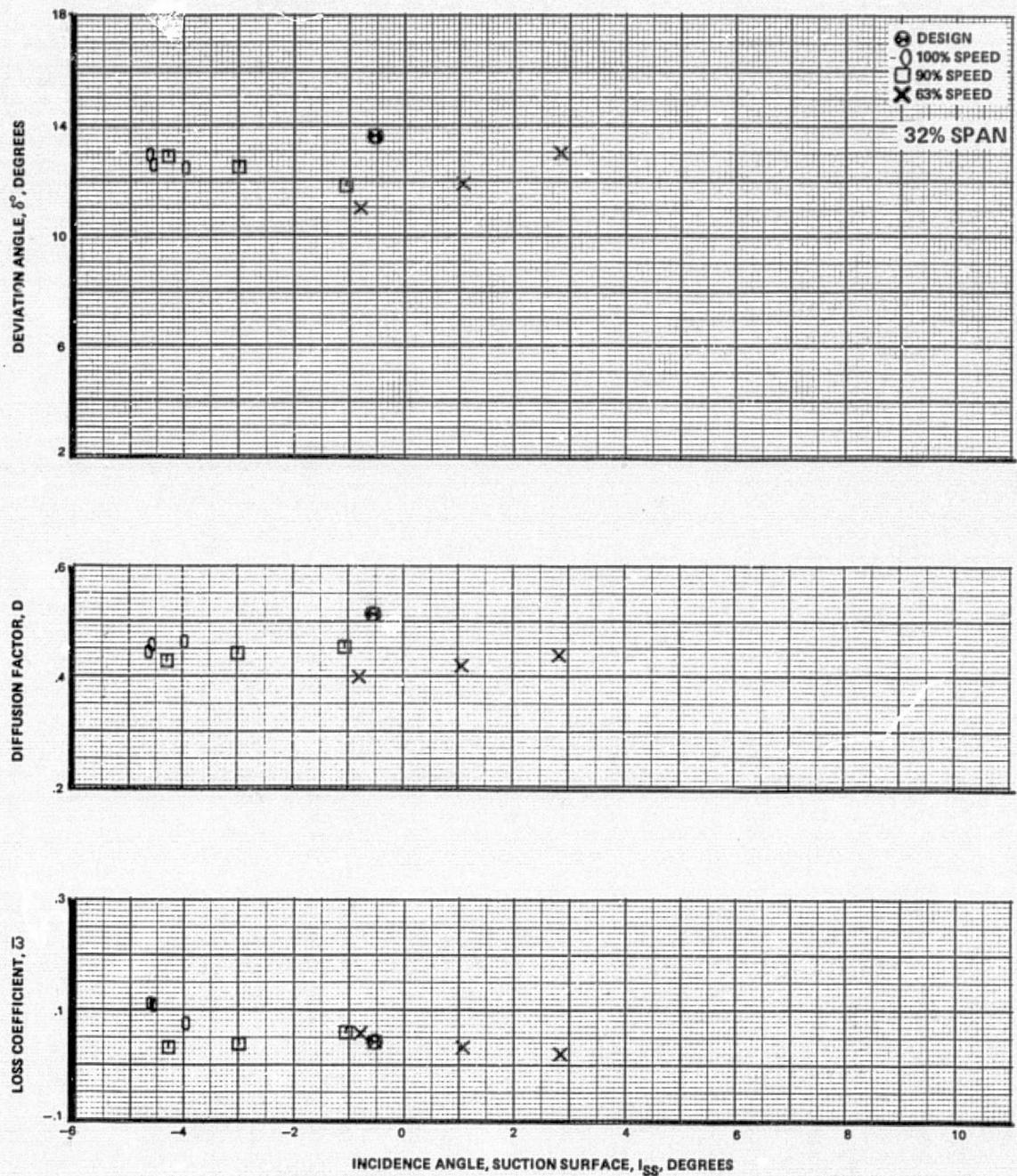


Figure 38b Blade-Element Performance, Baseline Configuration, Tip Radially Distorted Inlet Flow – First-Stage Rotor

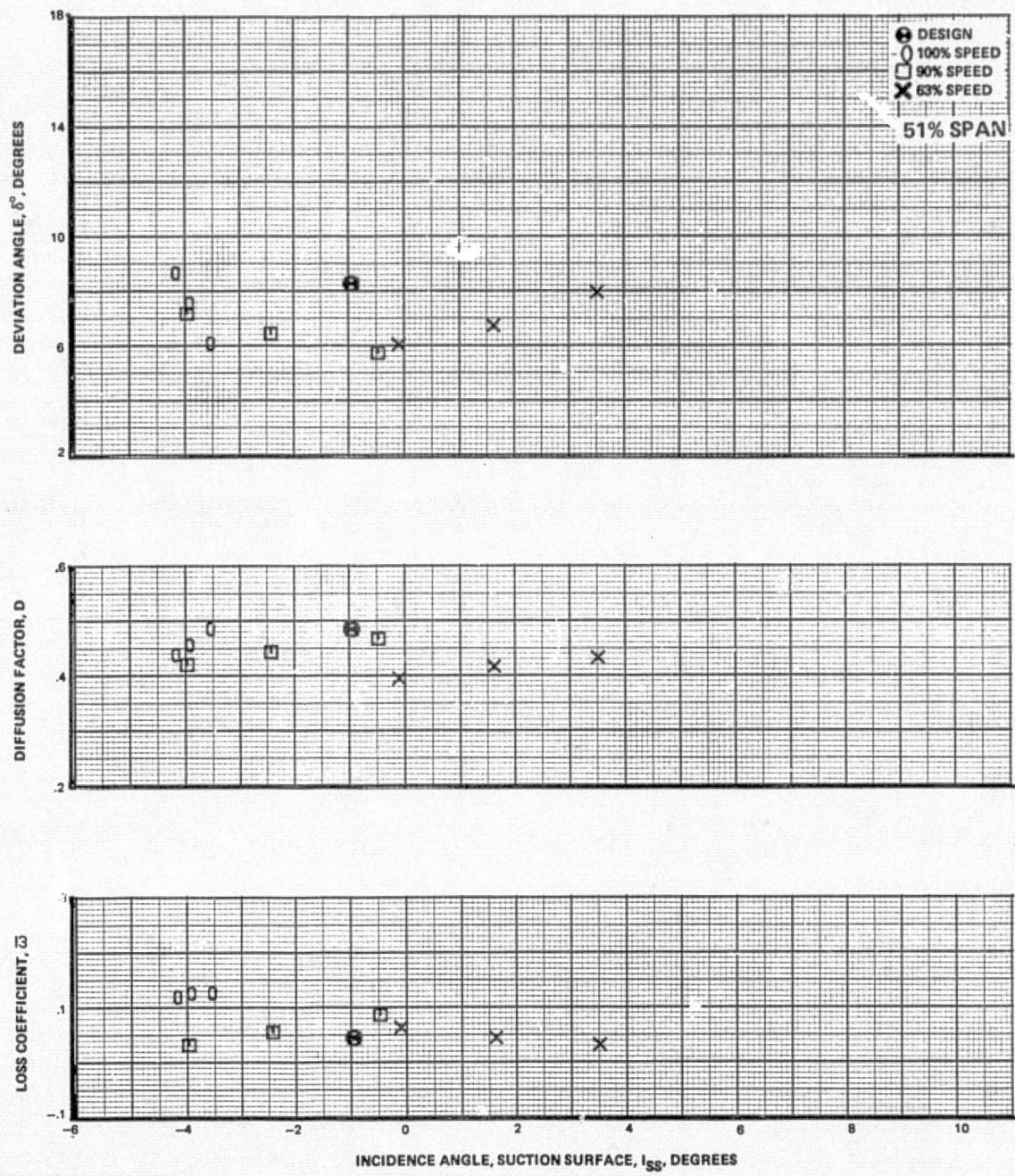


Figure 38c Blade-Element Performance, Baseline Configuration, Tip Radially Distorted Inlet Flow – First-Stage Rotor

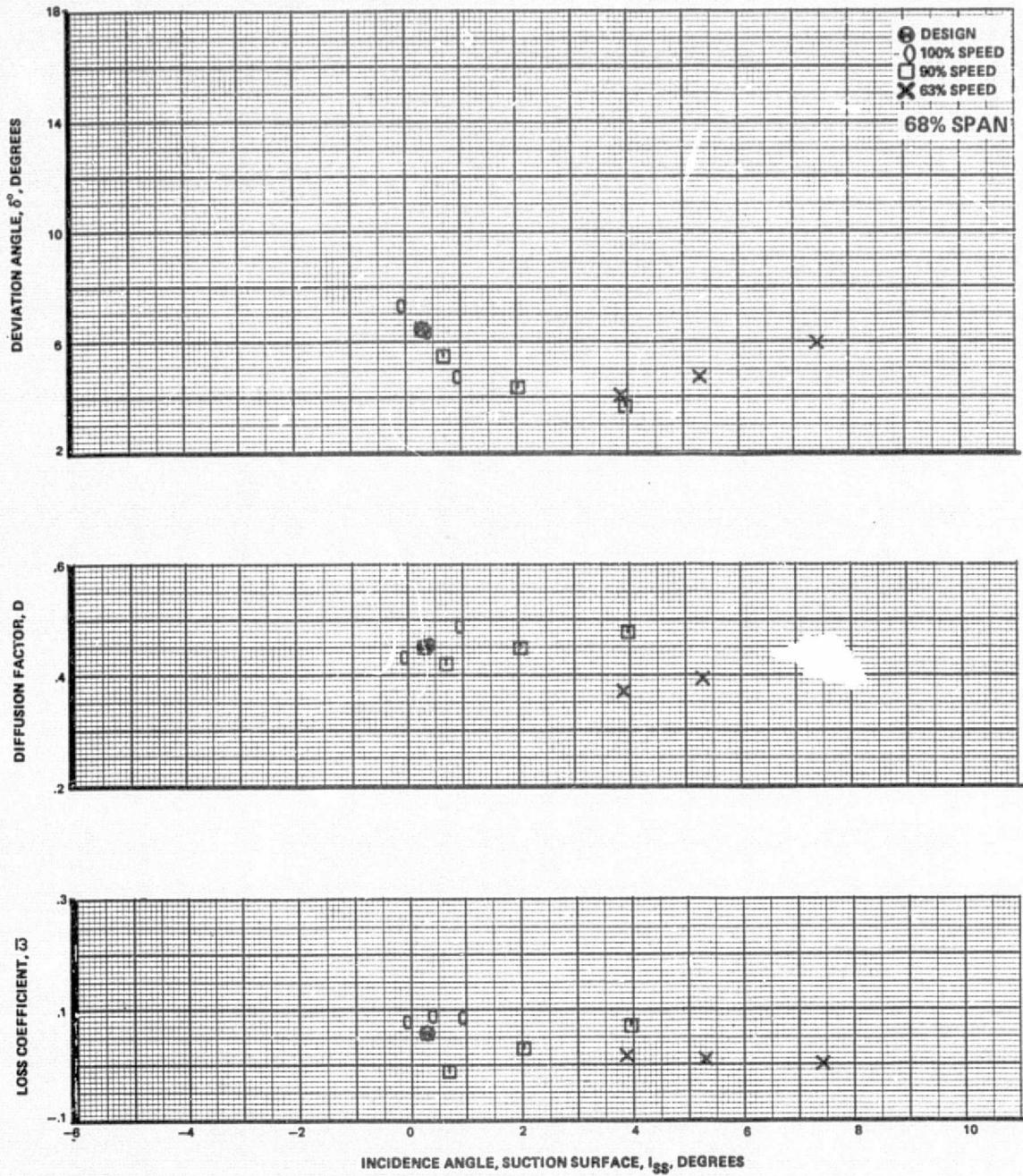


Figure 38d Blade-Element Performance, Baseline Configuration, Tip Radially Distorted Inlet Flow – First-Stage Rotor

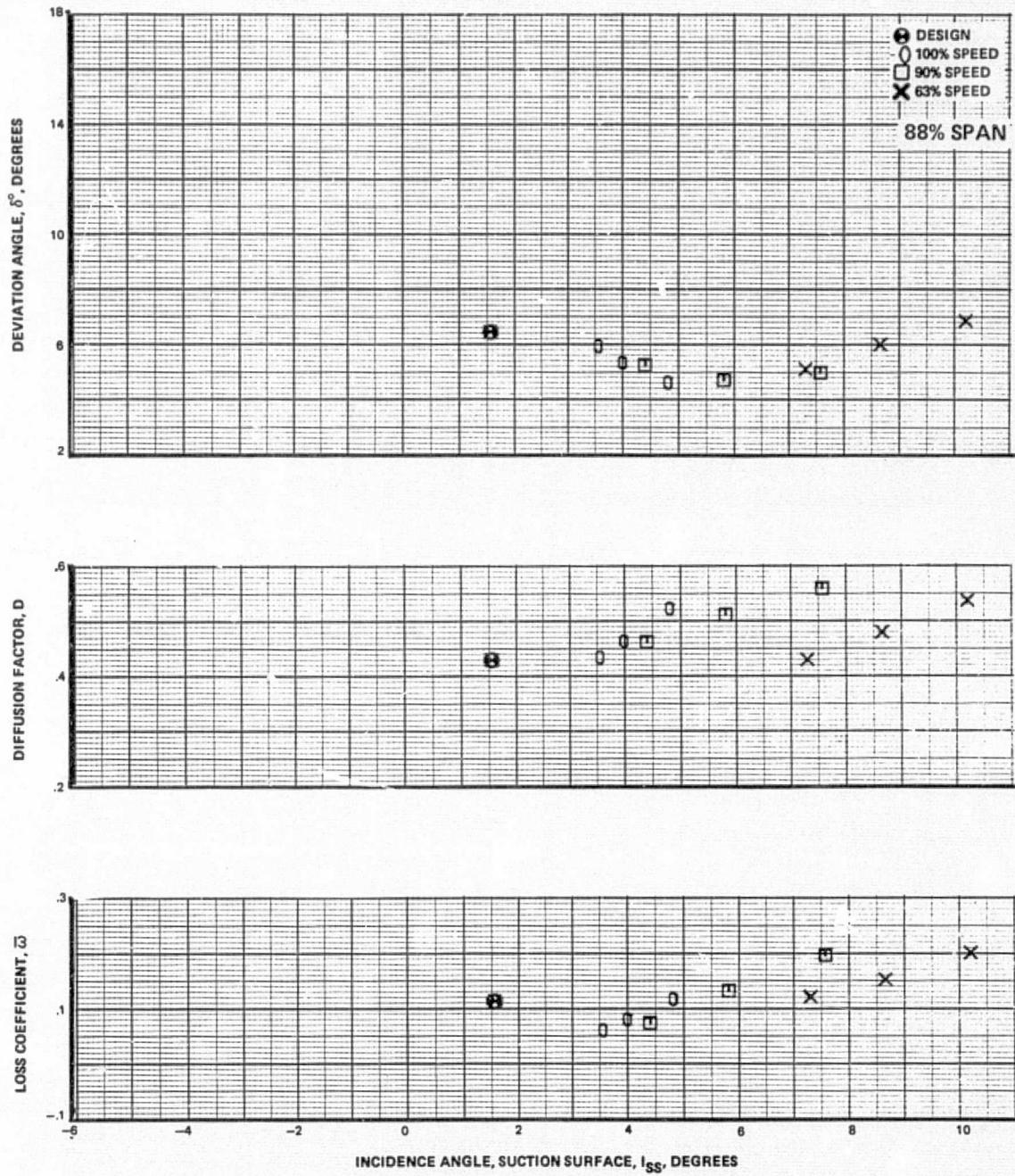


Figure 38e Blade-Element Performance, Baseline Configuration, Tip Radially Distorted Inlet Flow – First-Stage Rotor

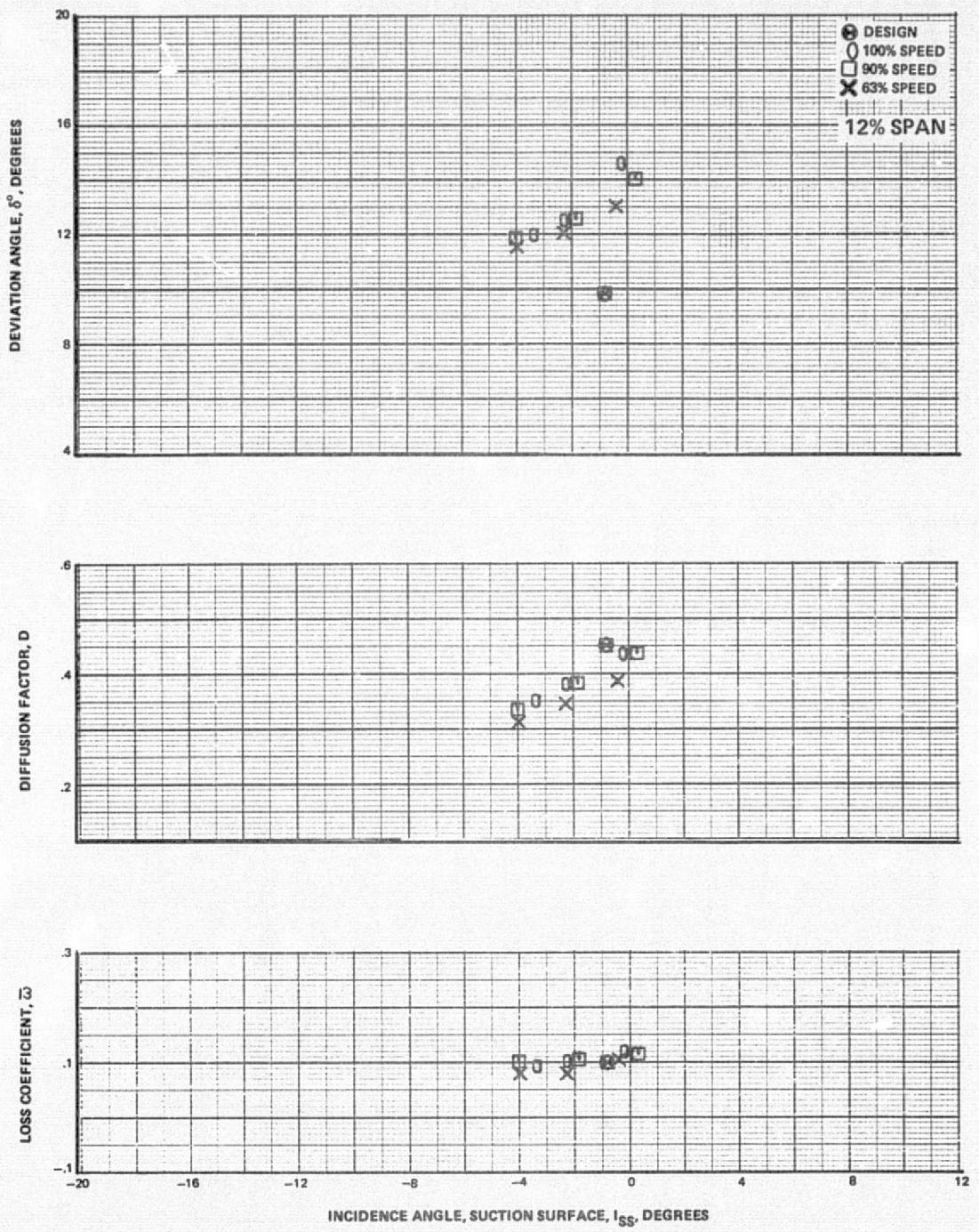


Figure 39a Blade-Element Performance, Baseline Configuration, Tip Radially Distorted Inlet Flow – First-Stage Stator

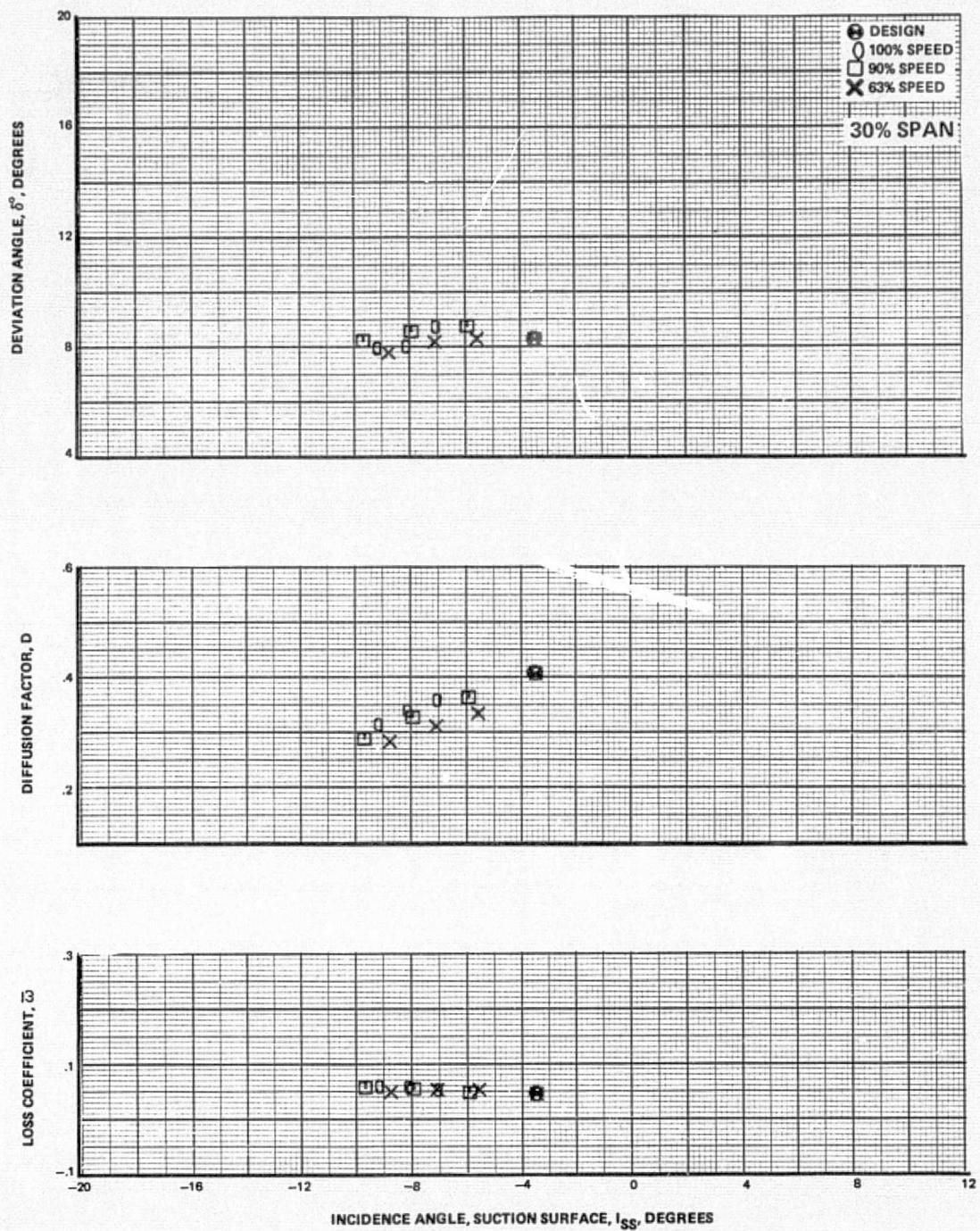


Figure 39b Blade-Element Performance, Baseline Configuration, Tip Radially Distorted Inlet Flow – First-Stage Stator

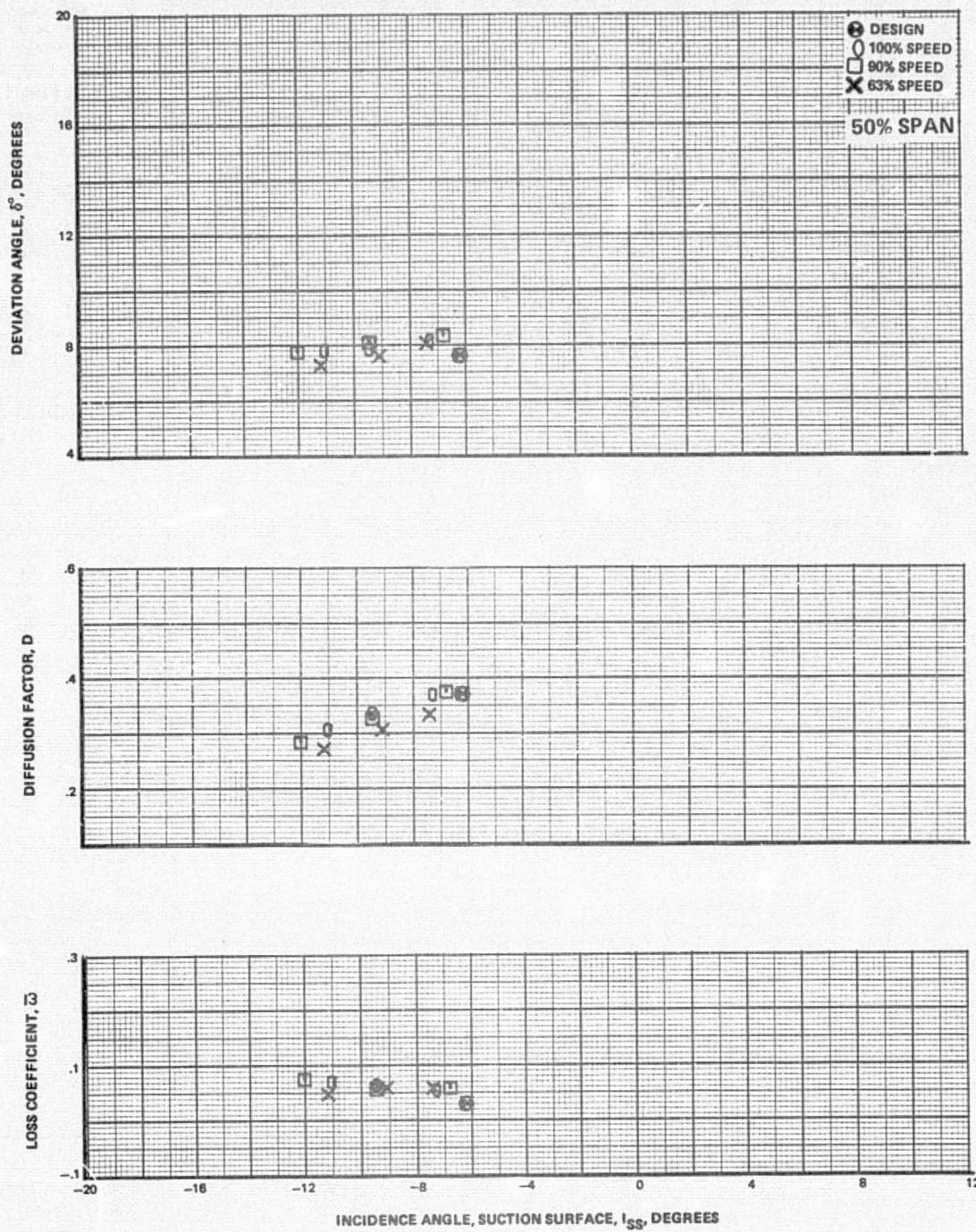


Figure 39c Blade-Element Performance, Baseline Configuration, Tip Radially Distorted Inlet Flow – First-Stage Stator

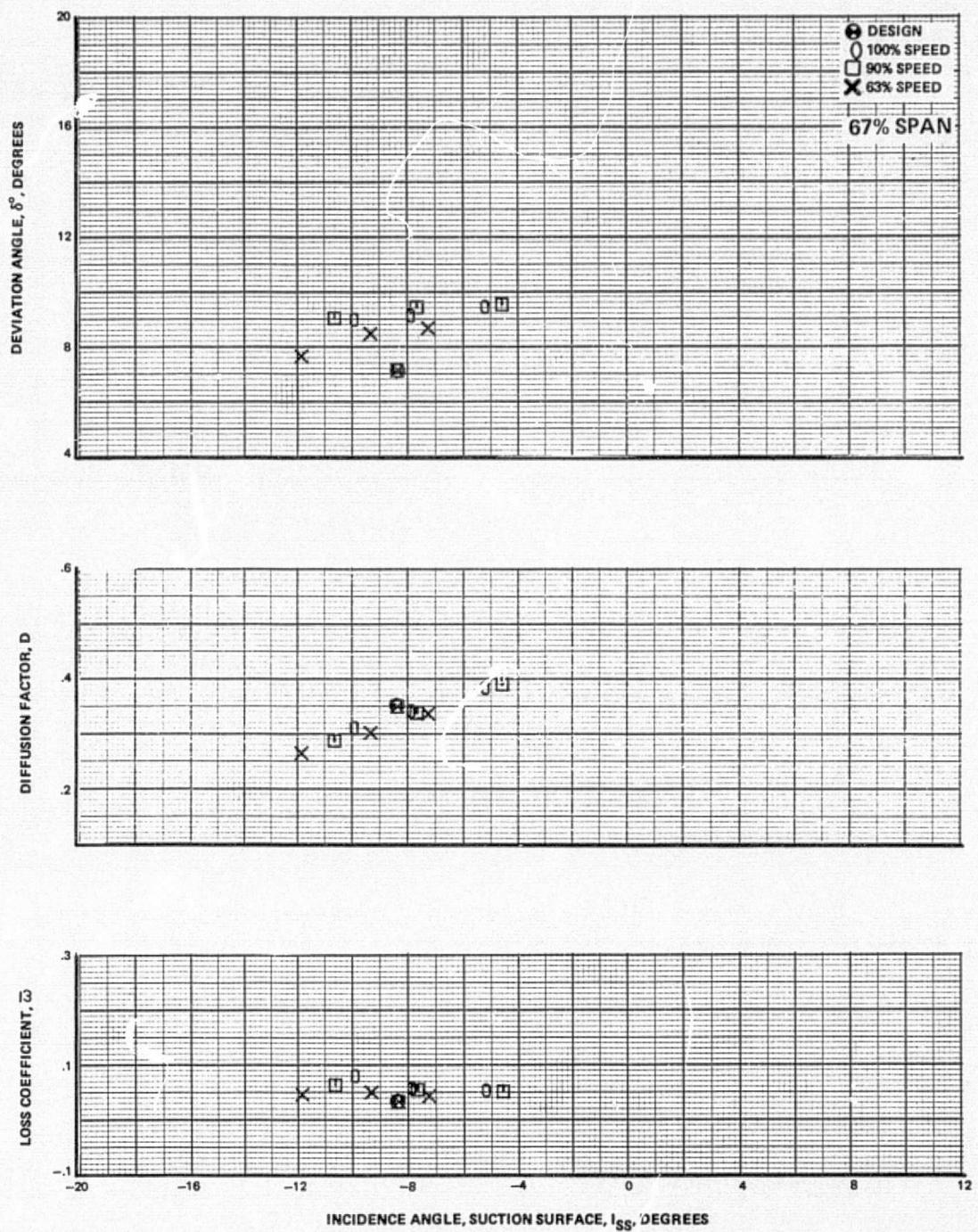


Figure 39d Blade-Element Performance, Baseline Configuration, Tip Radially Distorted Inlet Flow – First-Stage Stator

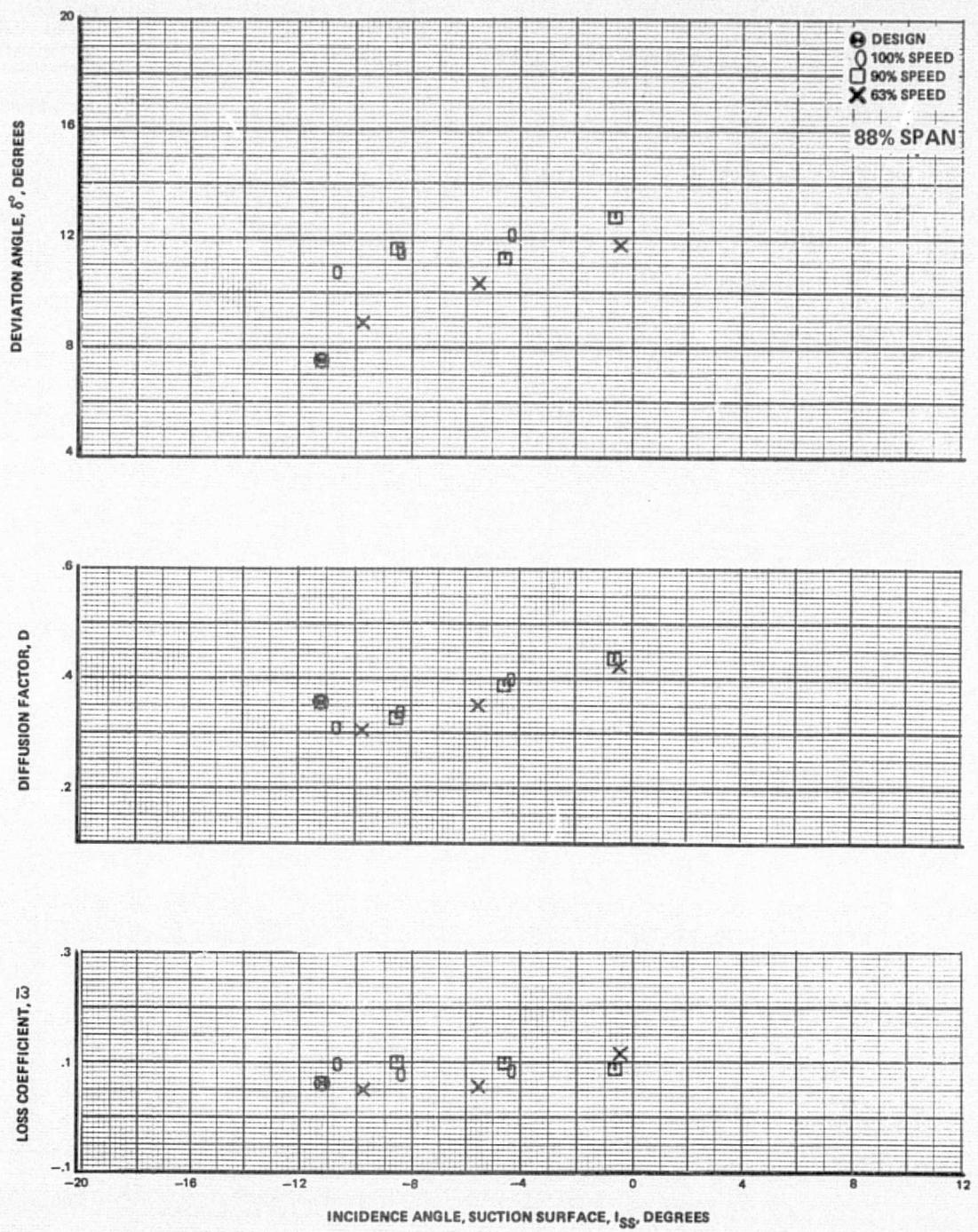


Figure 39e Blade-Element Performance, Baseline Configuration, Tip Radially Distorted Inlet Flow – First-Stage Stator

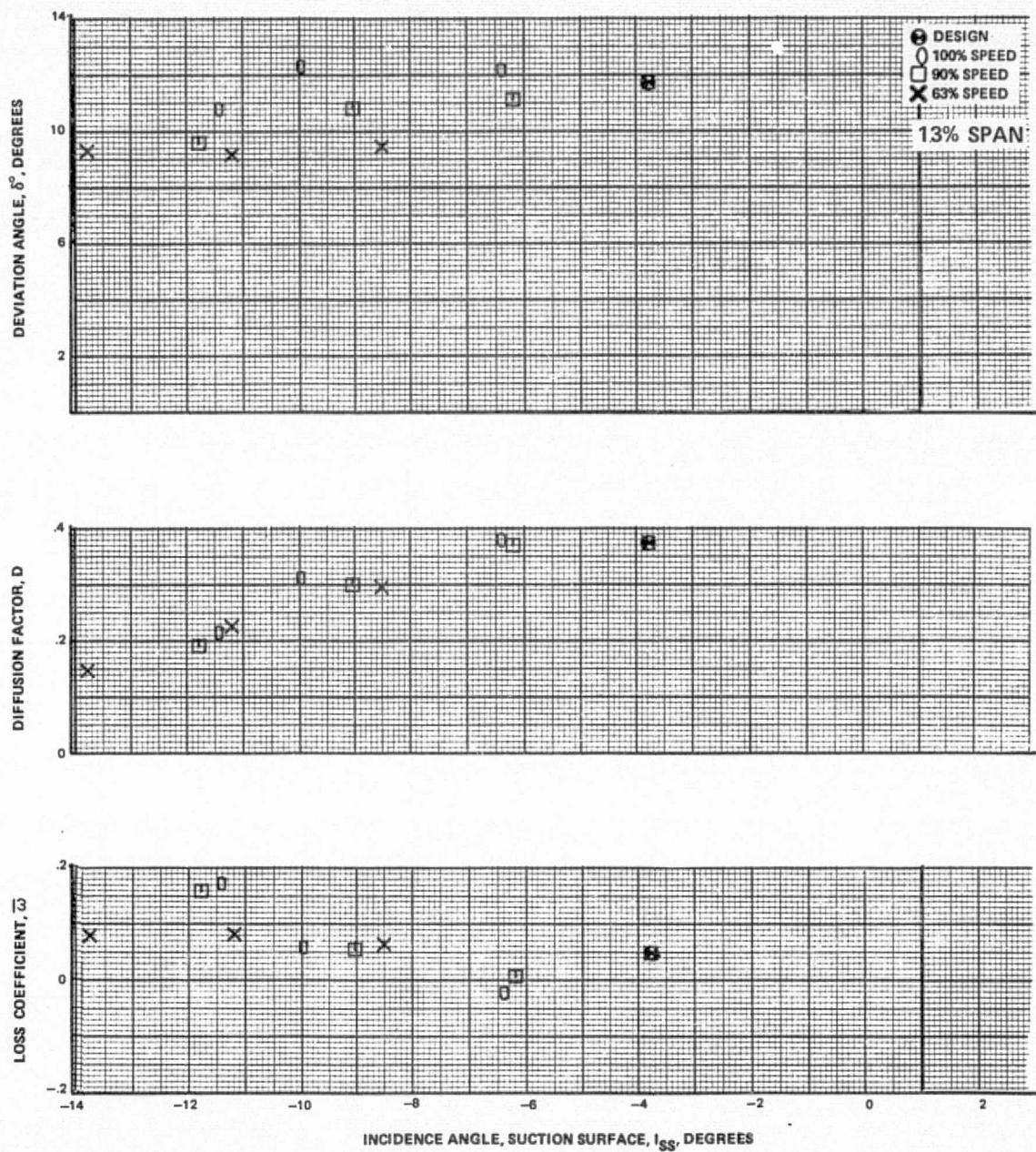


Figure 40a Blade-Element Performance, Baseline Configuration, Tip Radially Distorted Inlet Flow – Second-Stage Rotor

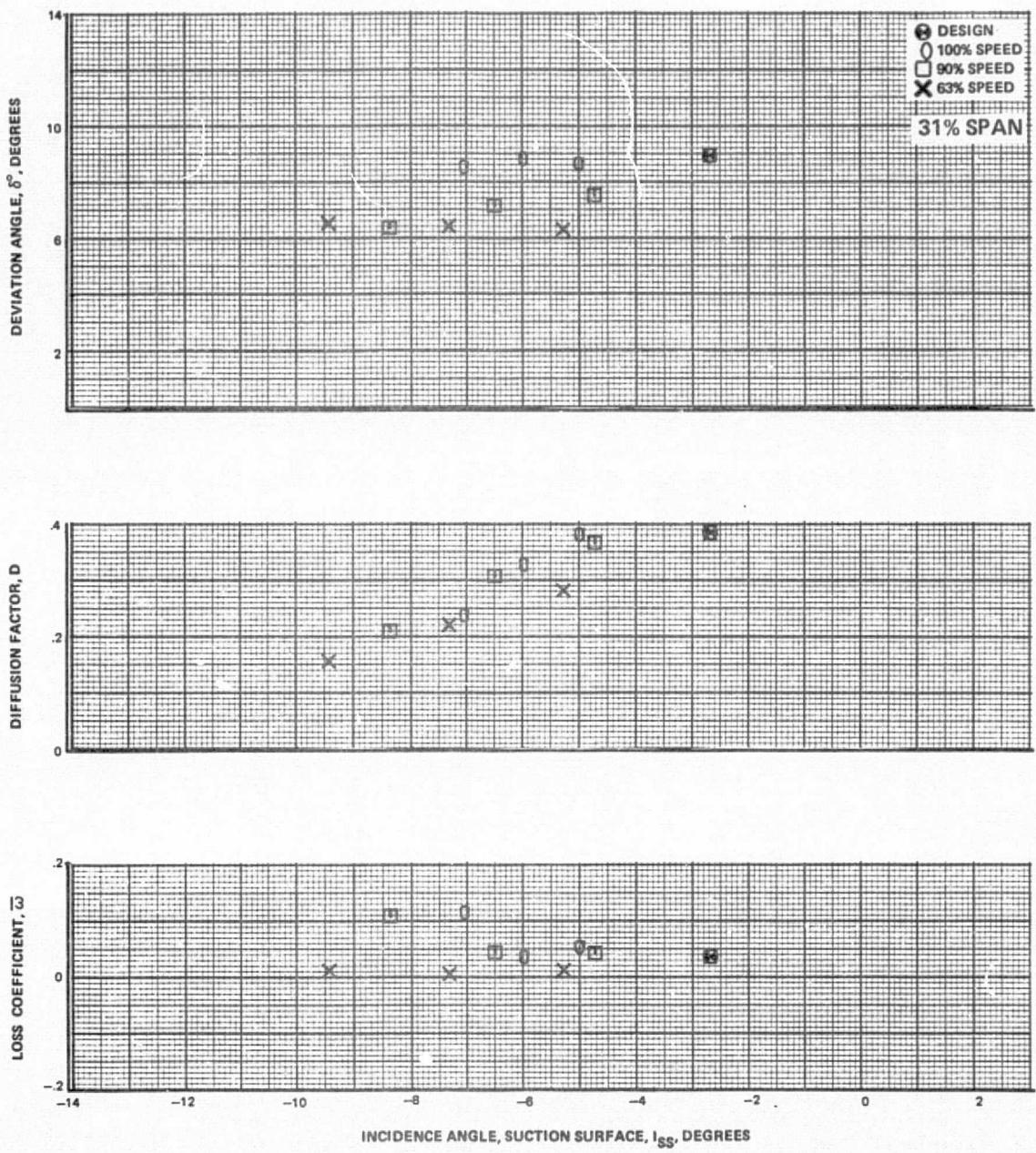


Figure 40b Blade-Element Performance, Baseline Configuration, Tip Radially Distorted Inlet Flow – Second-Stage Rotor

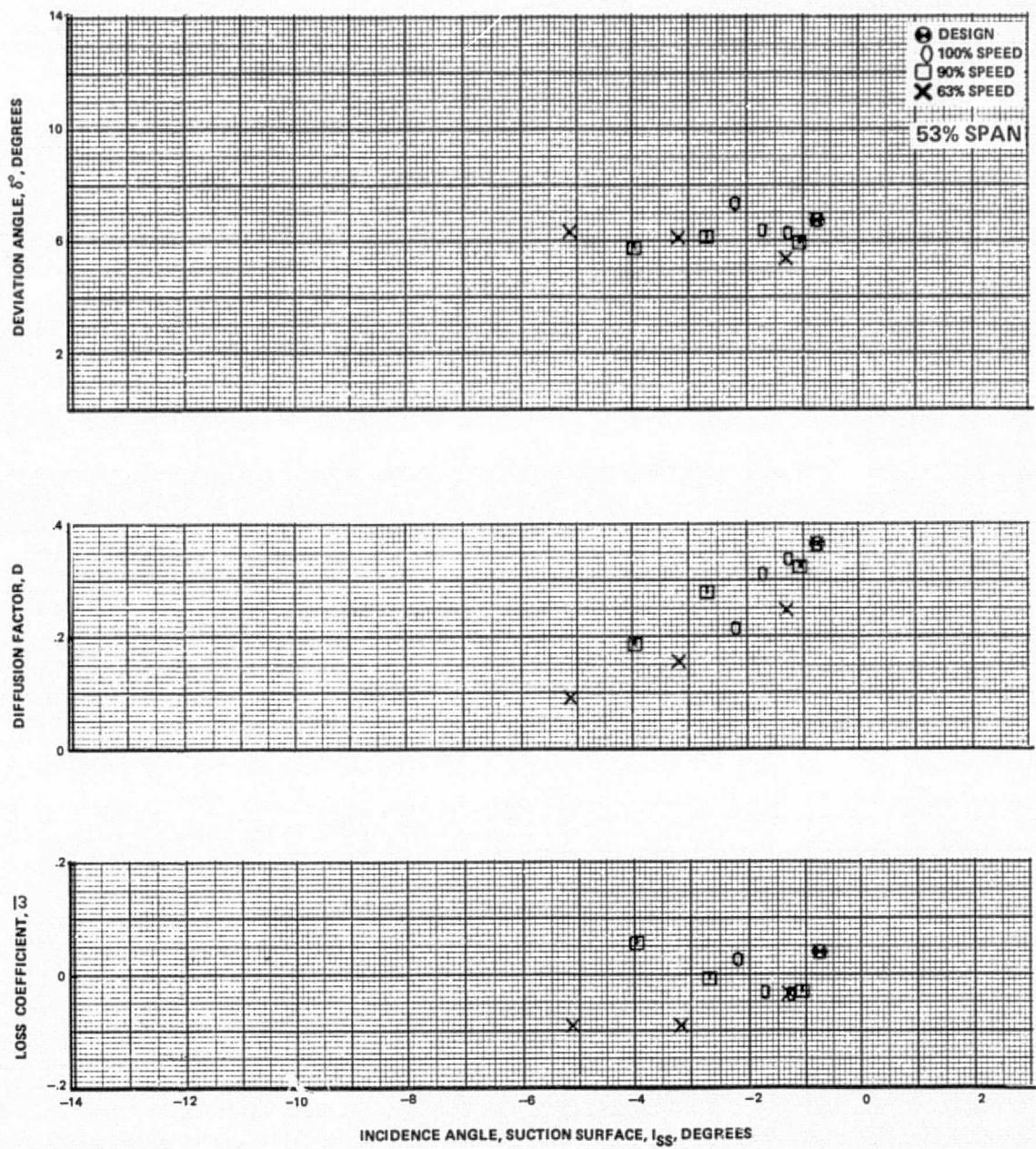


Figure 40c Blade-Element Performance, Baseline Configuration, Tip Radially Distorted Inlet Flow – Second-Stage Rotor

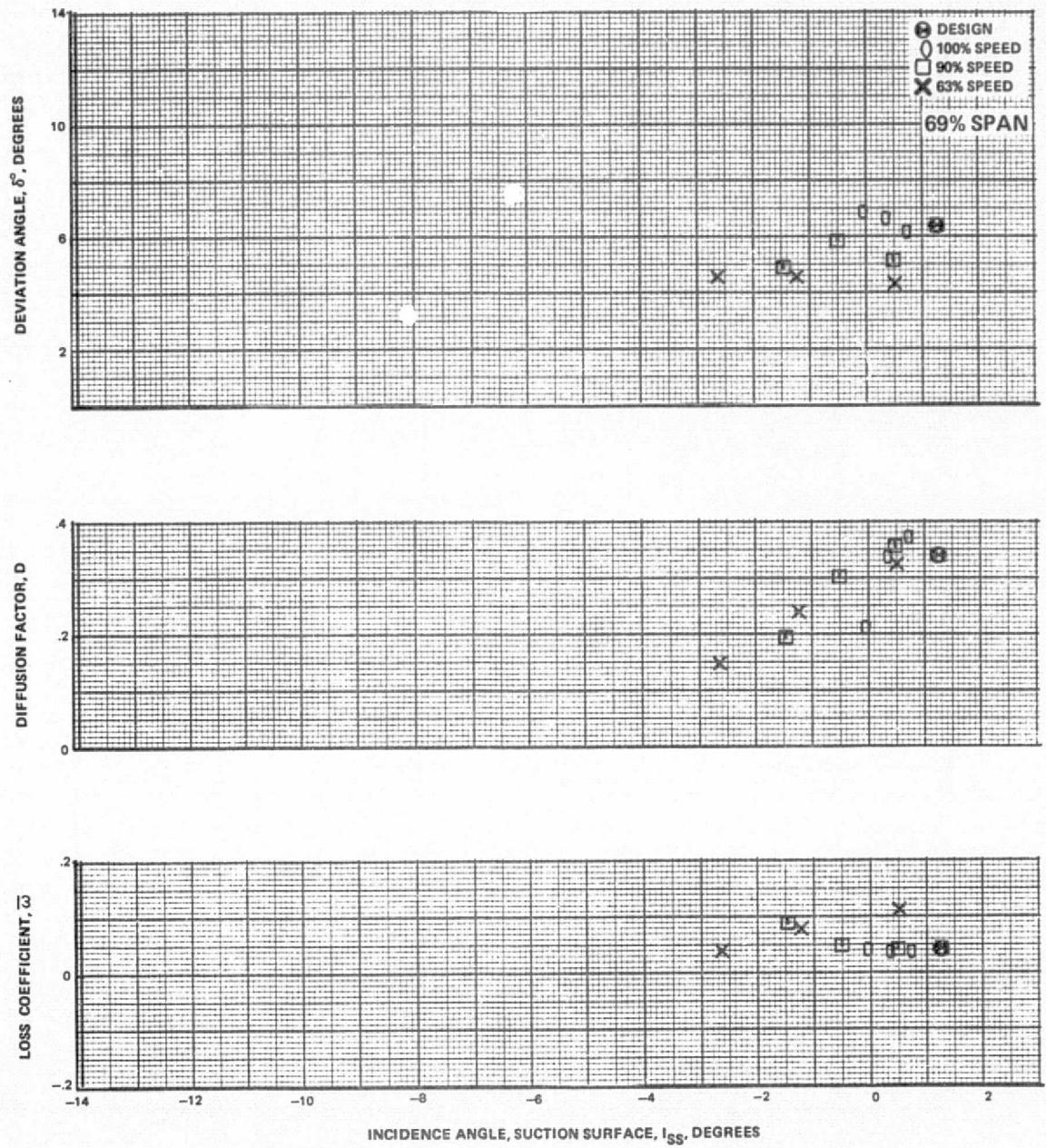


Figure 40d Blade-Element Performance, Baseline Configuration, Tip Radially Distorted Inlet Flow – Second-Stage Rotor

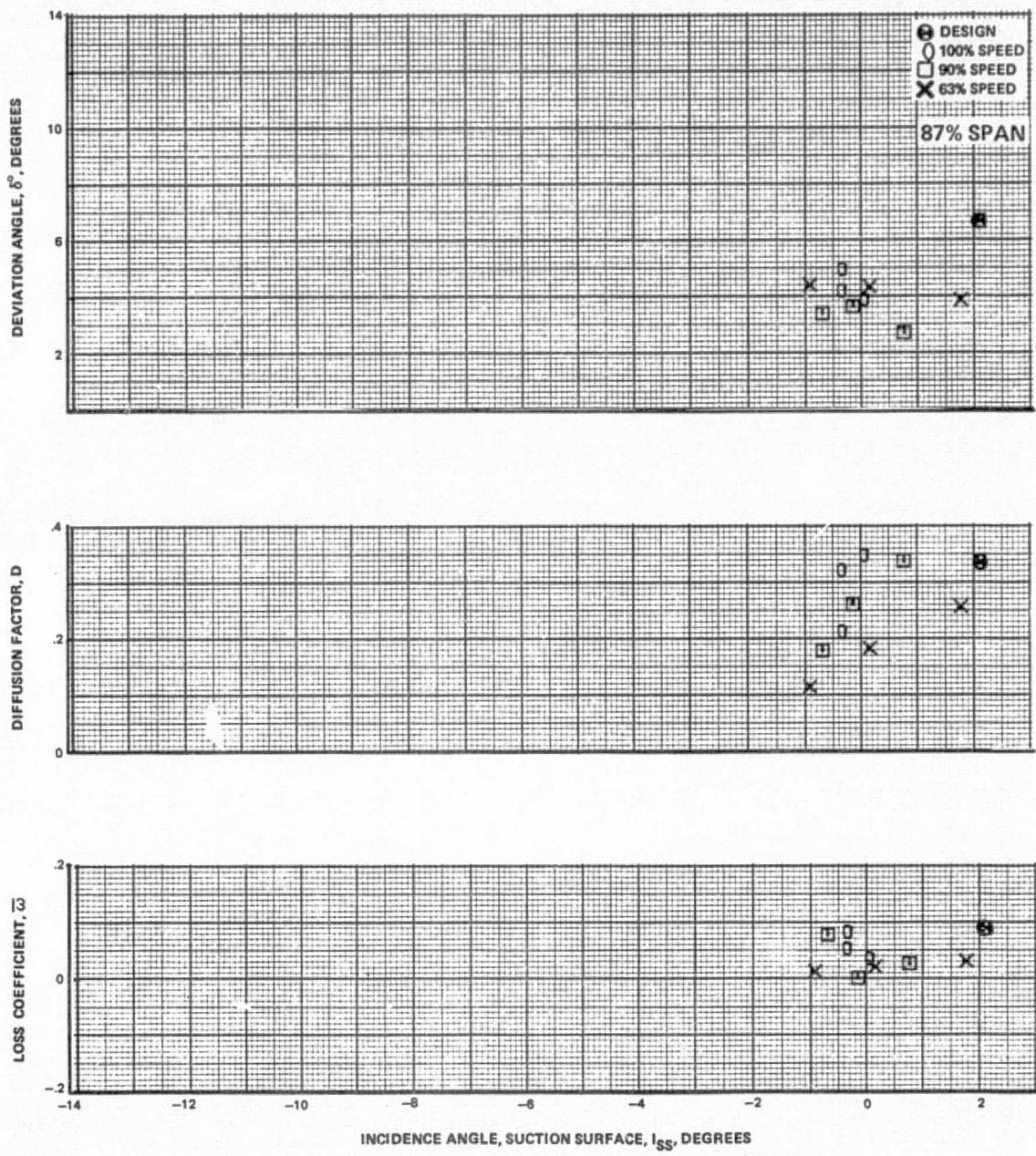


Figure 40e Blade-Element Performance, Baseline Configuration, Tip Radially Distorted Inlet Flow – Second-Stage Rotor

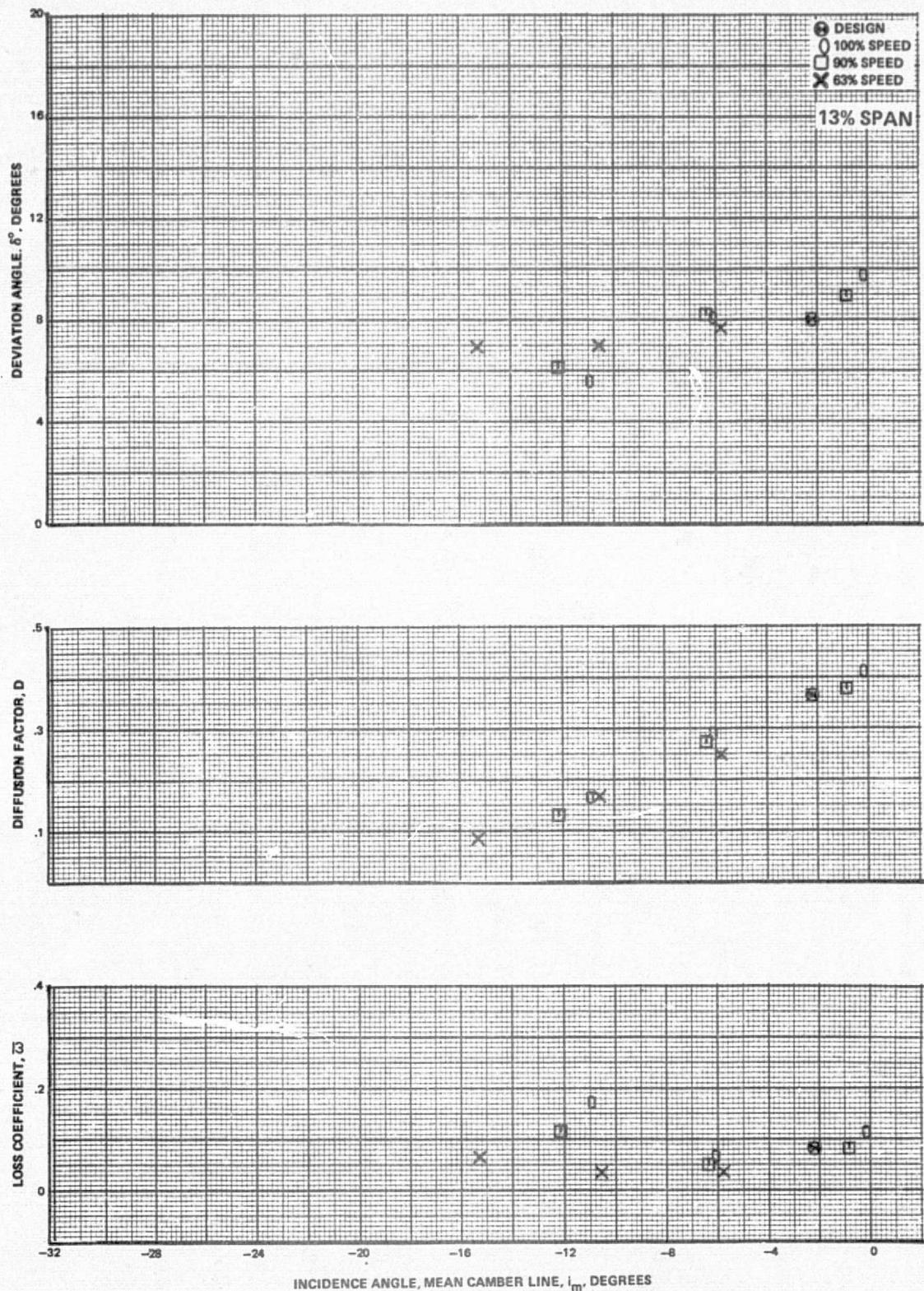


Figure 41a Blade-Element Performance, Baseline Configuration, Tip Radially Distorted Inlet Flow – Second-Stage Stator

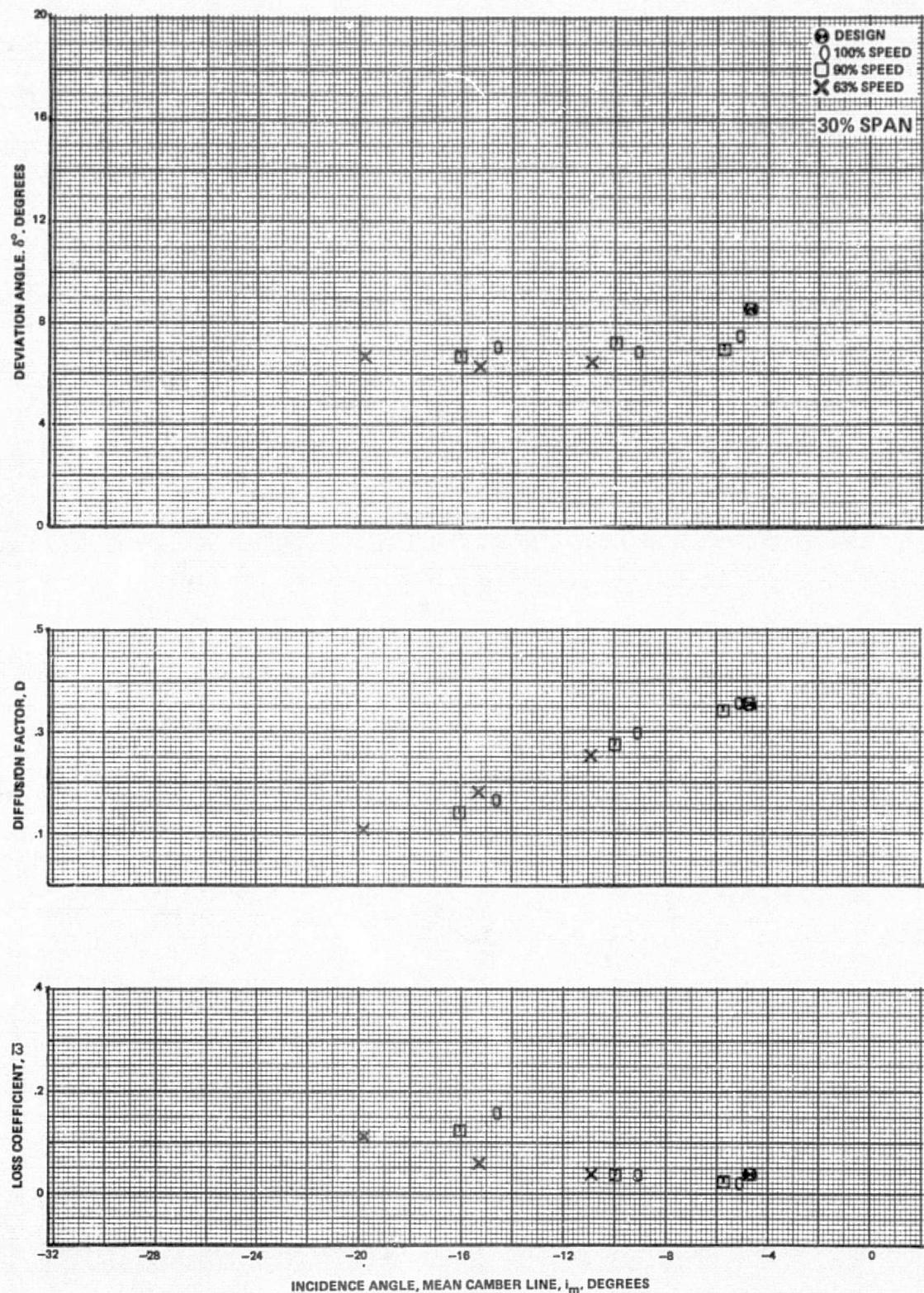


Figure 41b Blade-Element Performance, Baseline Configuration, Tip Radially Distorted Inlet Flow – Second-Stage Stator

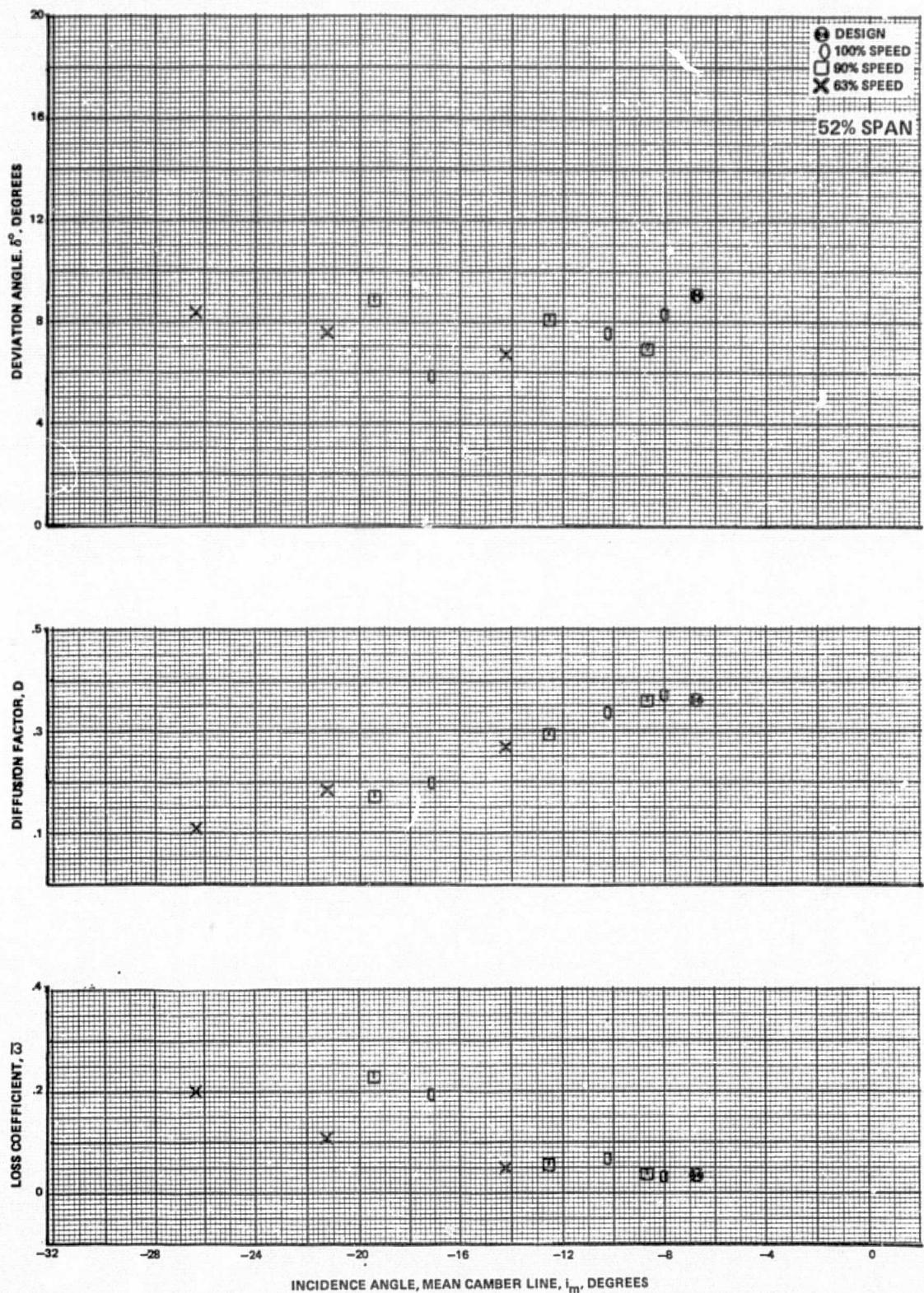


Figure 41c Blade-Element Performance, Baseline Configuration, Tip Radially Distorted Inlet Flow – Second-Stage Stator

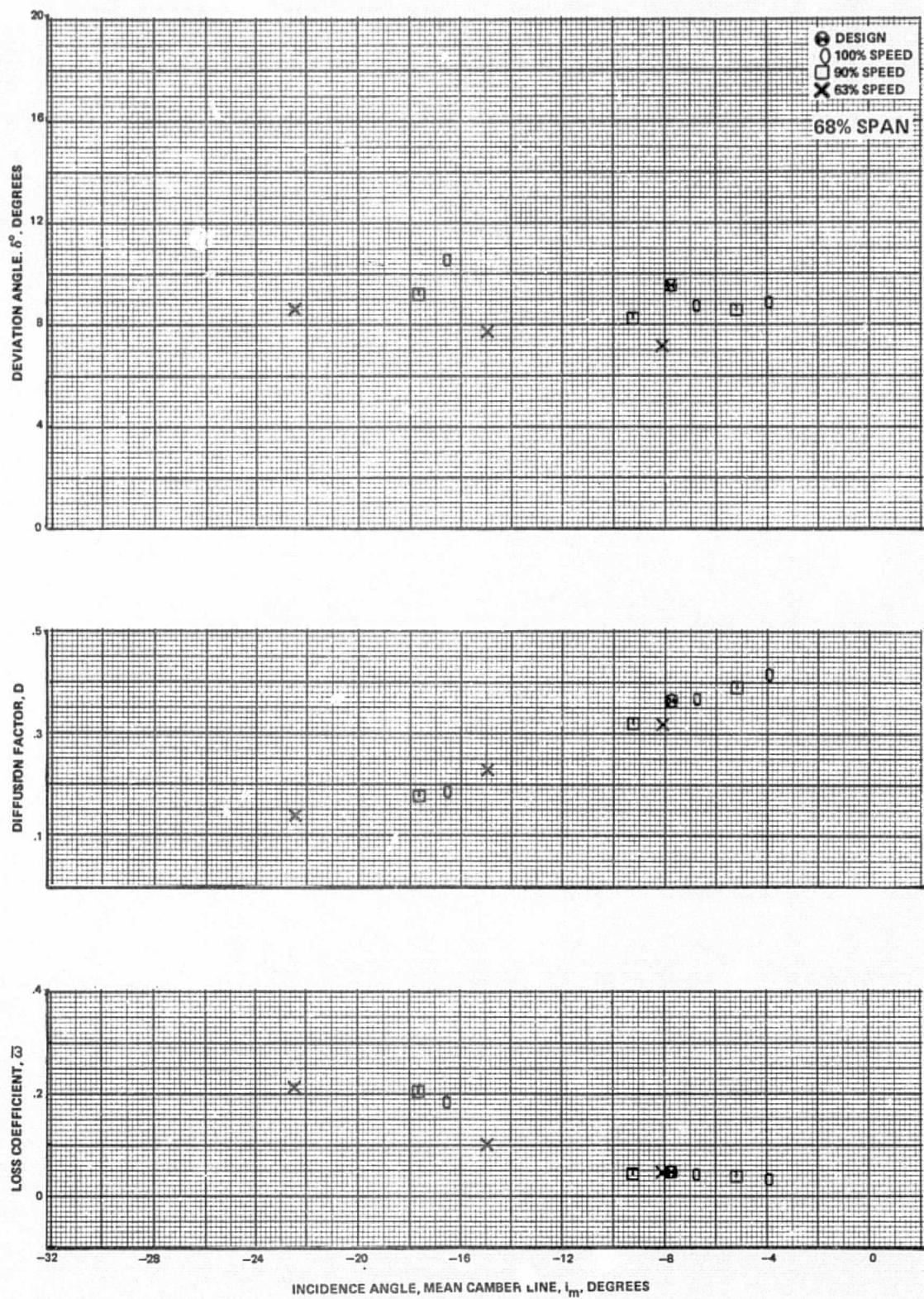


Figure 41d Blade-Element Performance, Baseline Configuration, Tip Radially Distorted Inlet Flow -- Second-Stage Stator

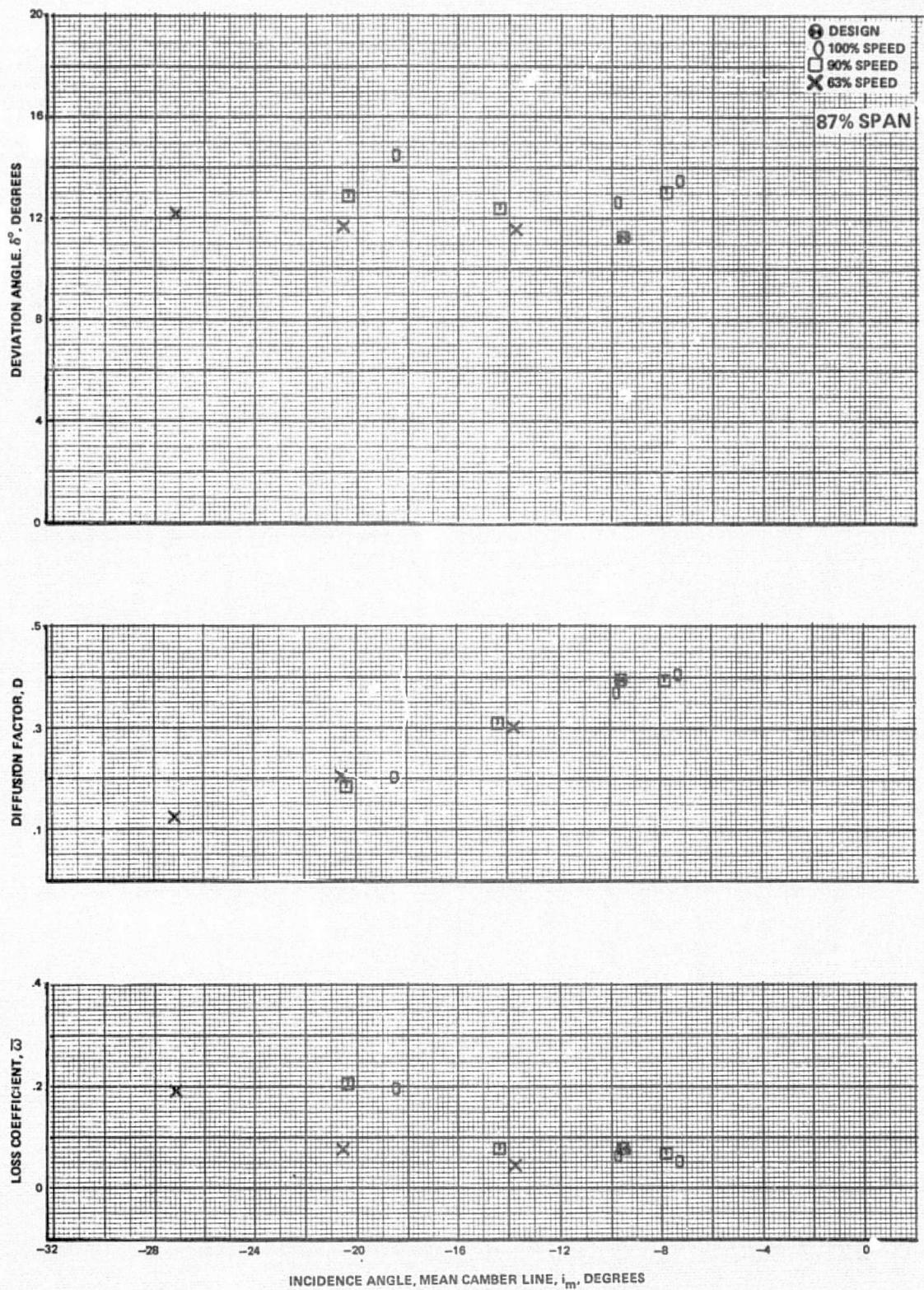


Figure 41e Blade-Element Performance, Baseline Configuration, Tip Radially Distorted Inlet Flow – Second-Stage Stator

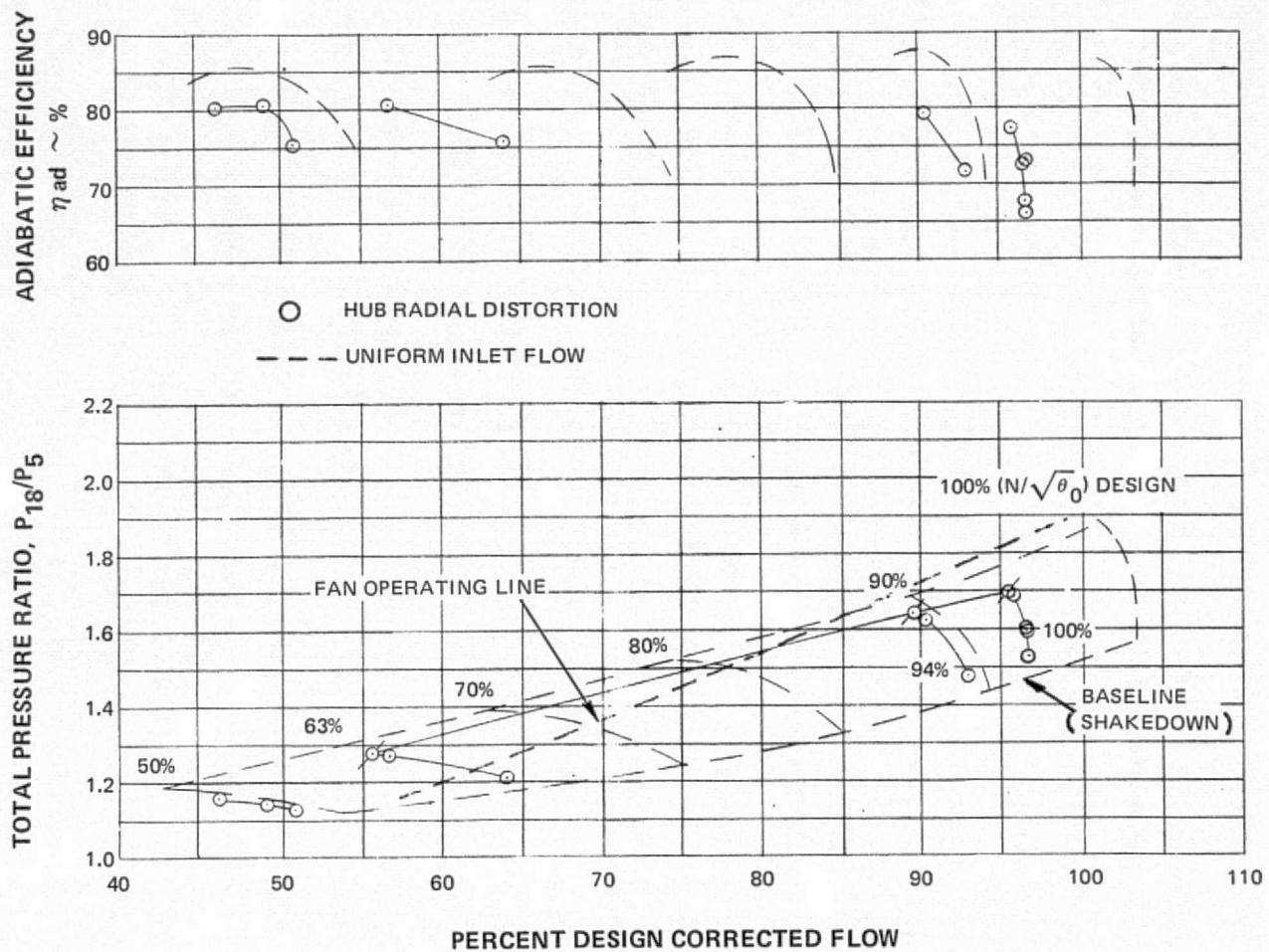


Figure 42 Fan Overall Performance With Hub Radially Distorted Inlet Flow

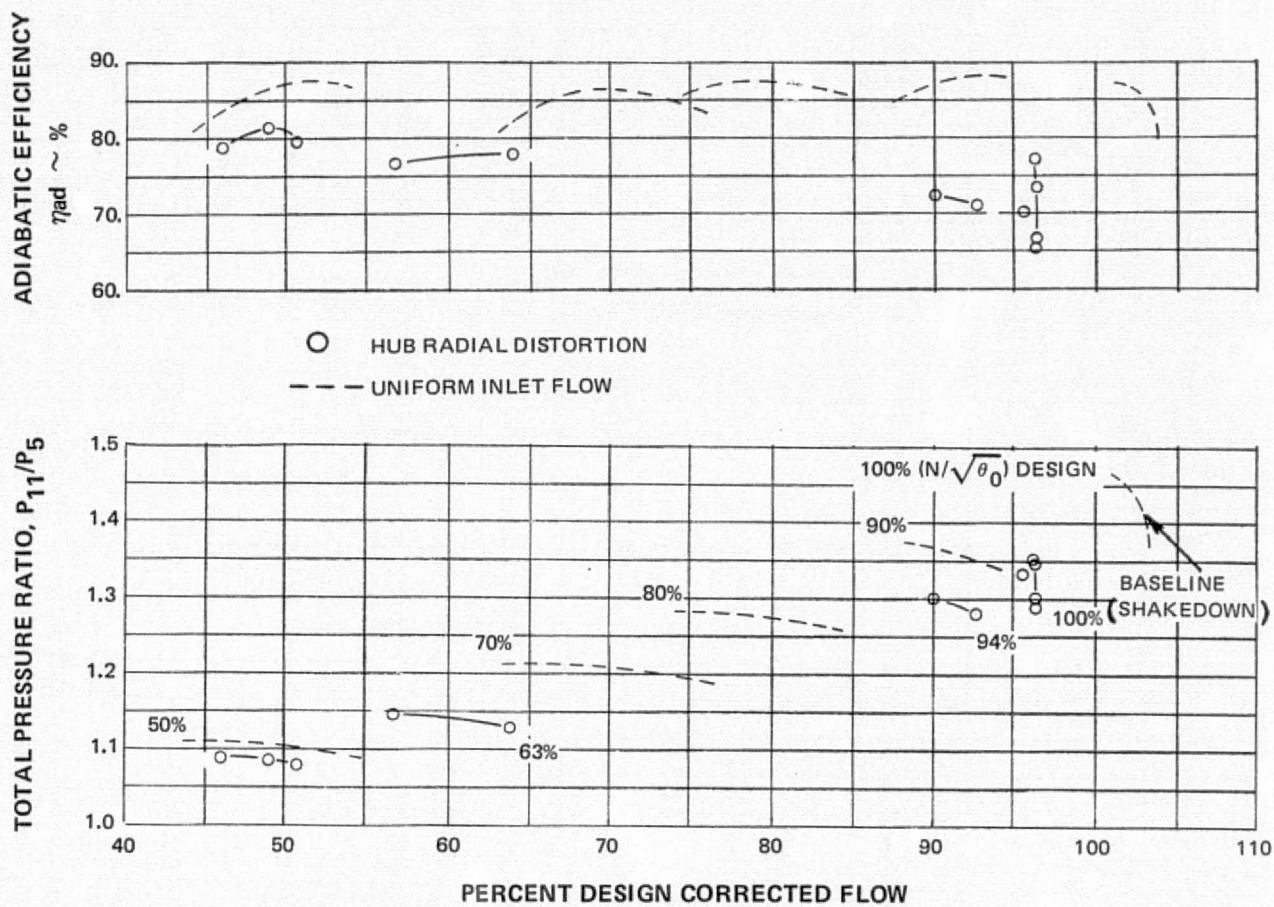


Figure 43 First-Stage Performance With Hub Radially Distorted Inlet Flow

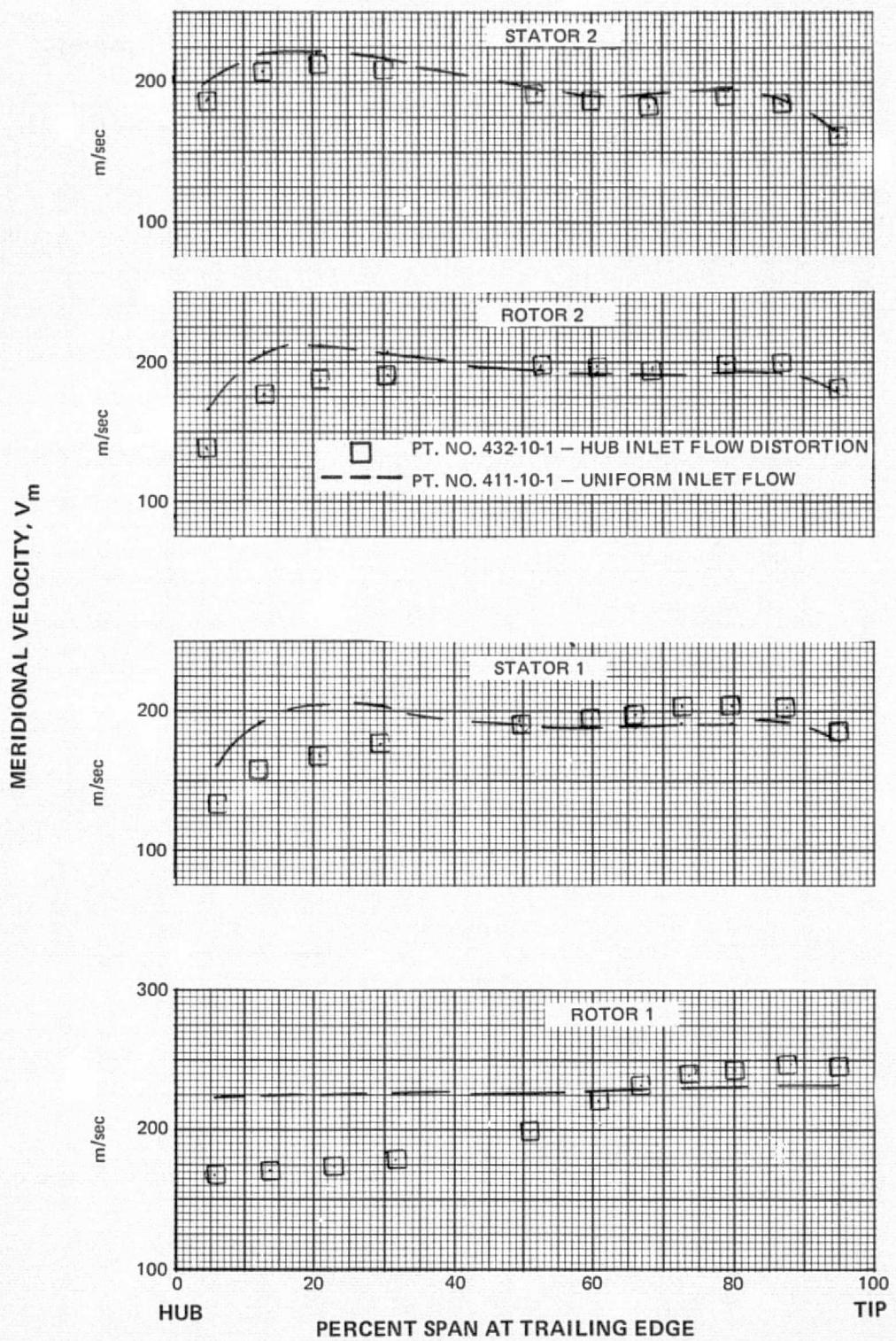


Figure 44 Blade Row Inlet Meridional Velocity Versus Span for Hub Radially Distorted Inlet Flow

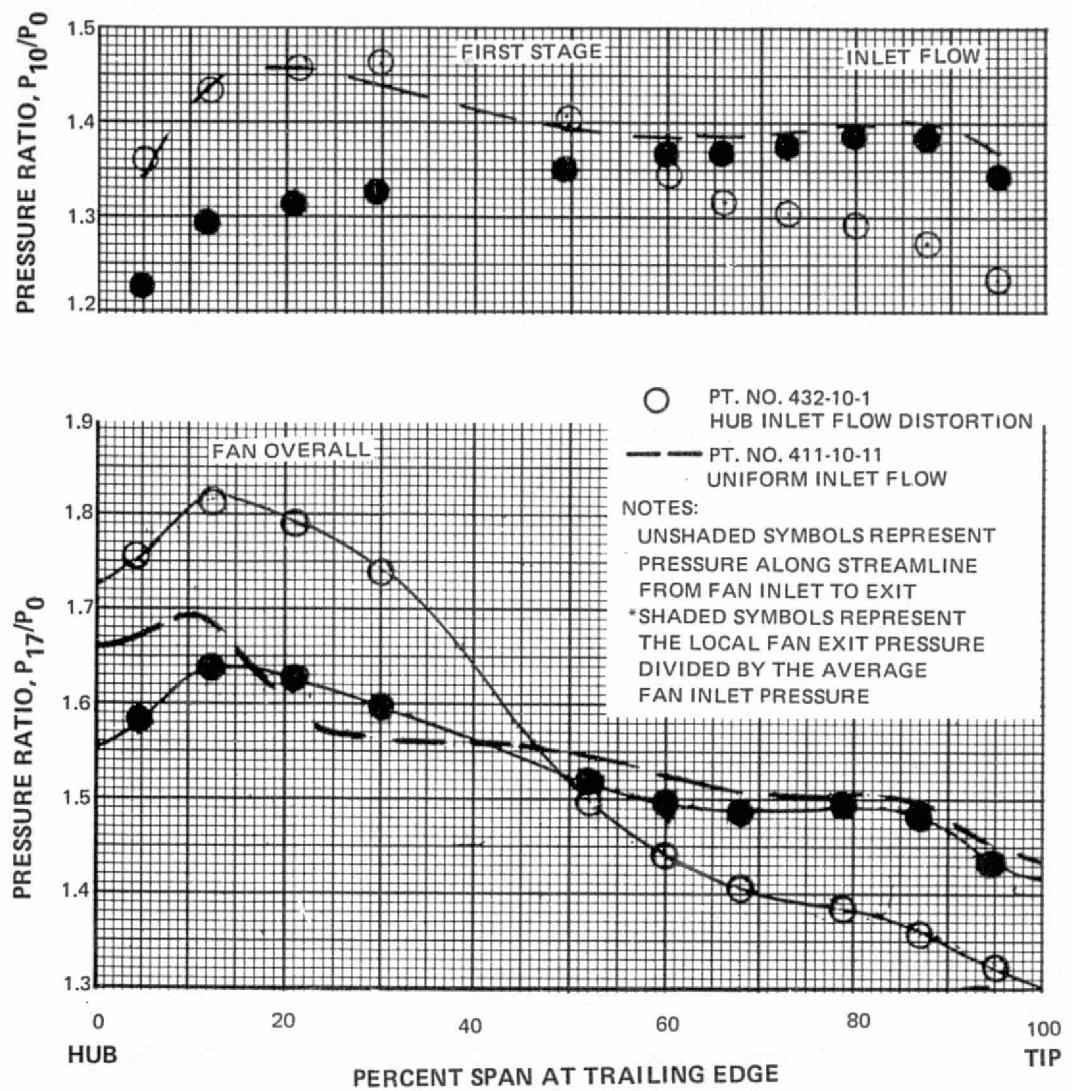


Figure 45 Overall Fan and First-Stage Pressure Ratio Versus Span for Hub Radially Distorted Inlet Flow

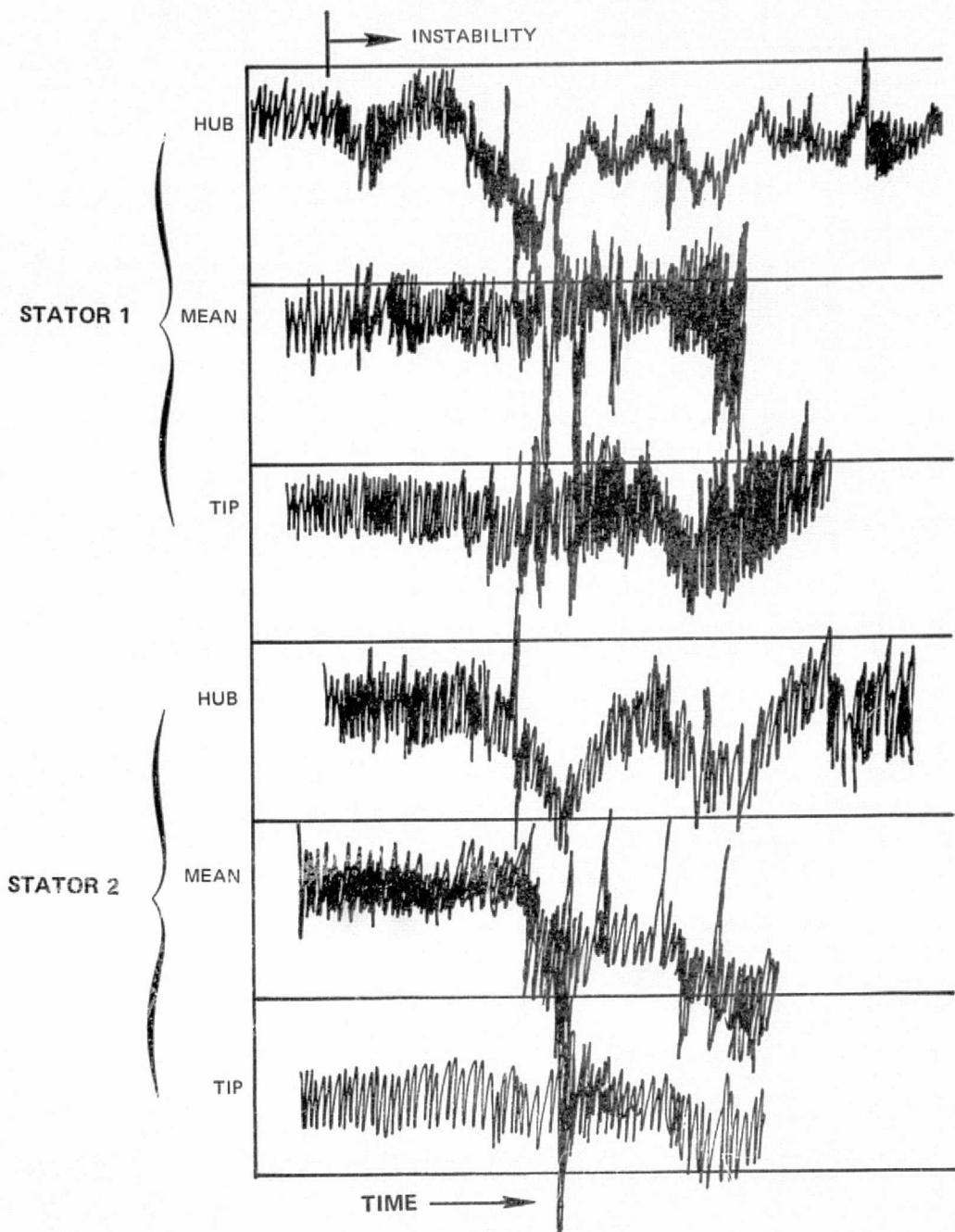


Figure 46 Hot-Film Traces at Stator Inlets, Uniform Inlet Flow, Baseline Configuration, 90 Percent of Design Speed

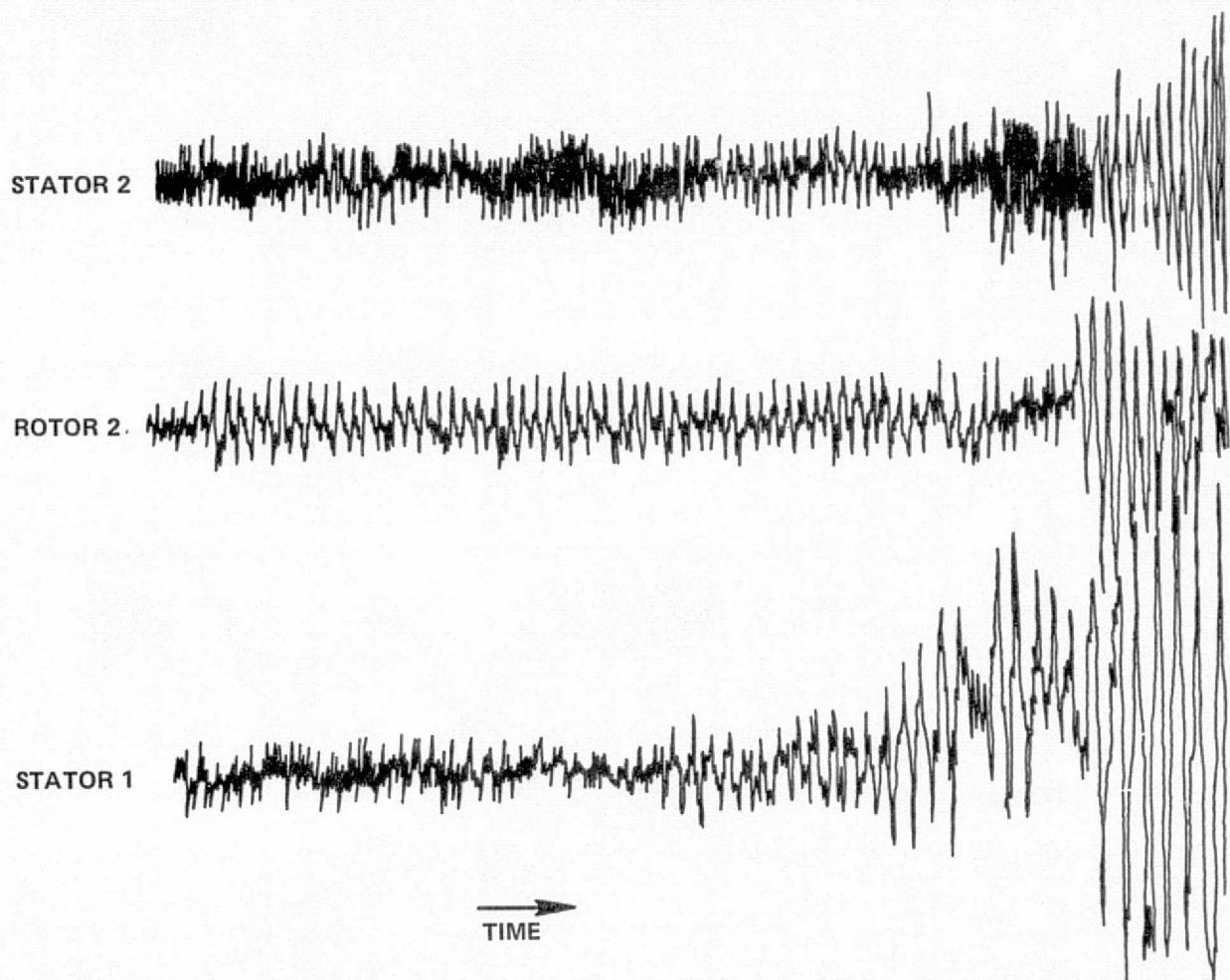


Figure 47 Strain-Gage Traces of Blade During Uniform Inlet Flow, Baseline Configuration, 100 Percent of Design Speed

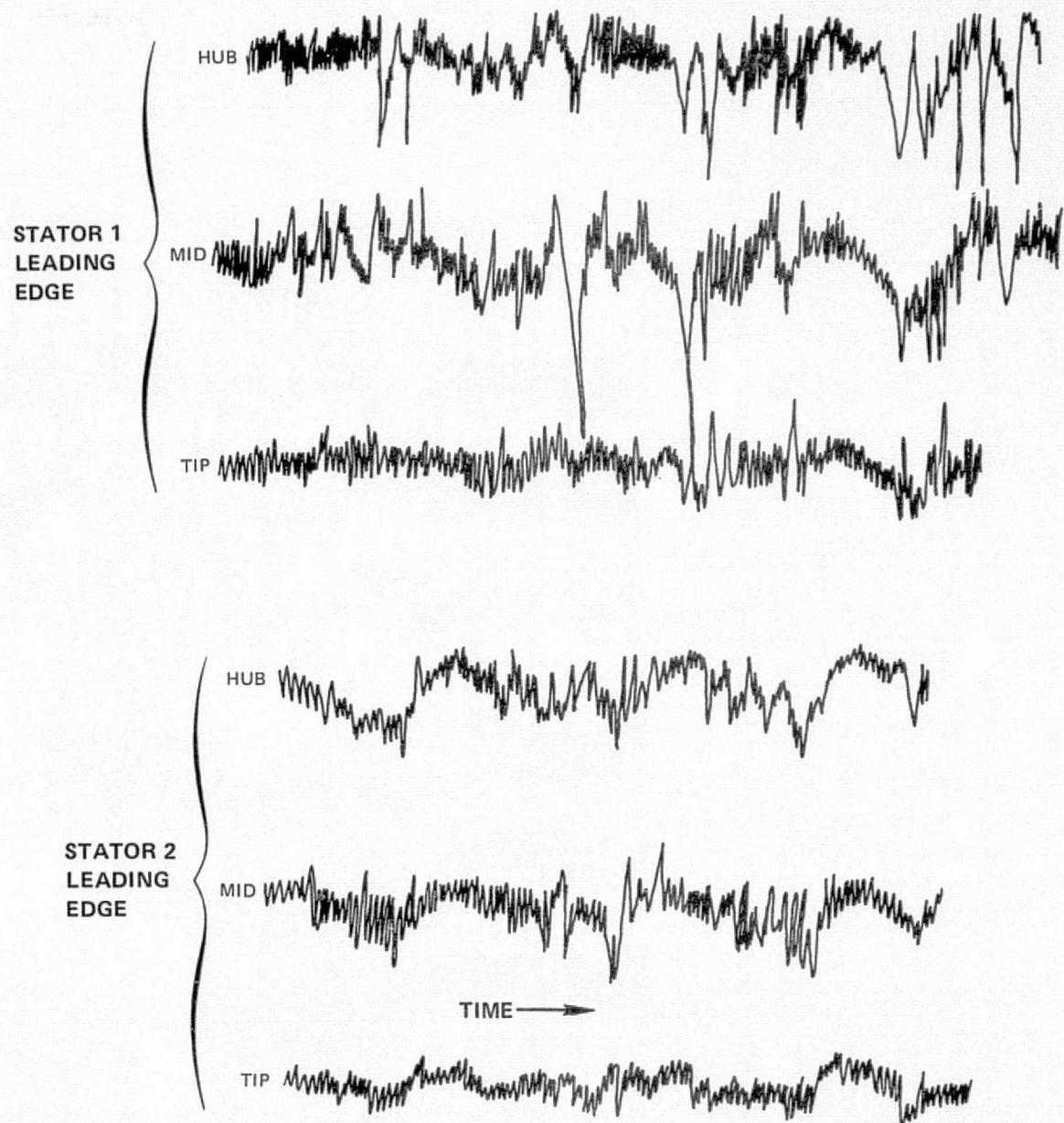


Figure 48 Hot-Film Traces at Stator Inlets, Uniform Inlet Flow, 50 Percent of Design Speed

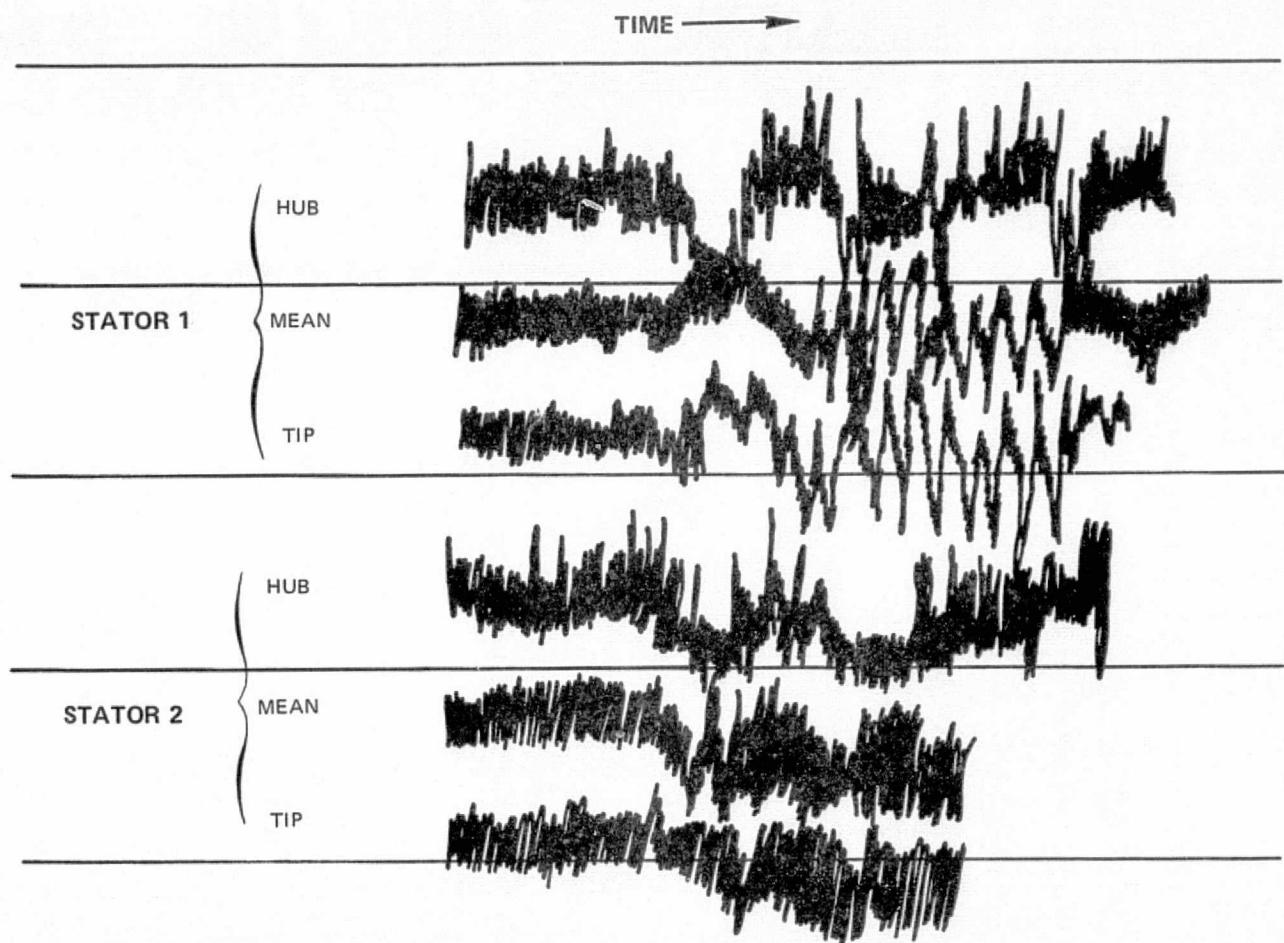


Figure 49 Hot-Film Traces at Stator Inlets, Tip Radially Distorted Inlet Flow, 100 Percent of Design Speed

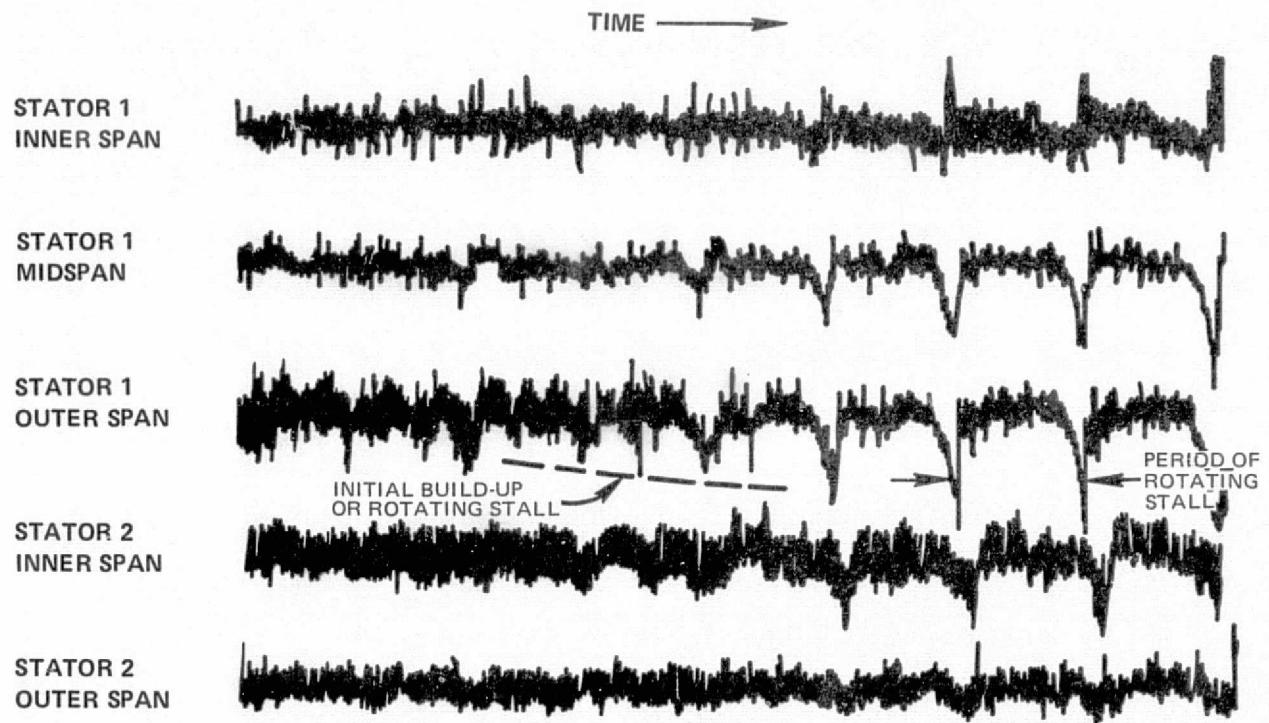


Figure 50 Hot-Film Traces at Stator Inlets, Tip Radially Distorted Inlet Flow, 63 Percent of Design Speed

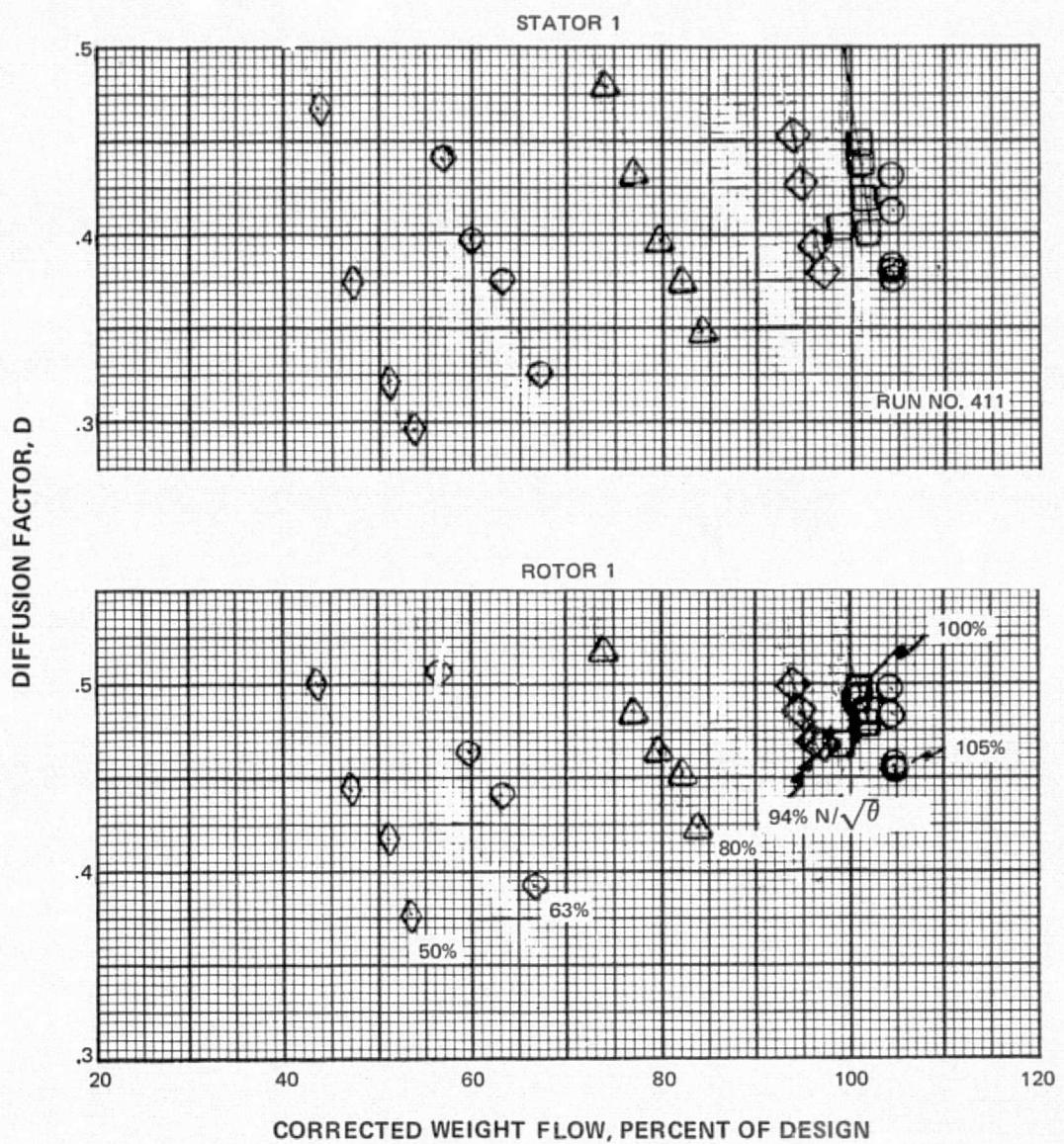


Figure 51 Diffusion Factor of First-Stage Rotor and Stator Versus Weight Flow, Baseline Configuration, Uniform Inlet Flow, 13 Percent Span

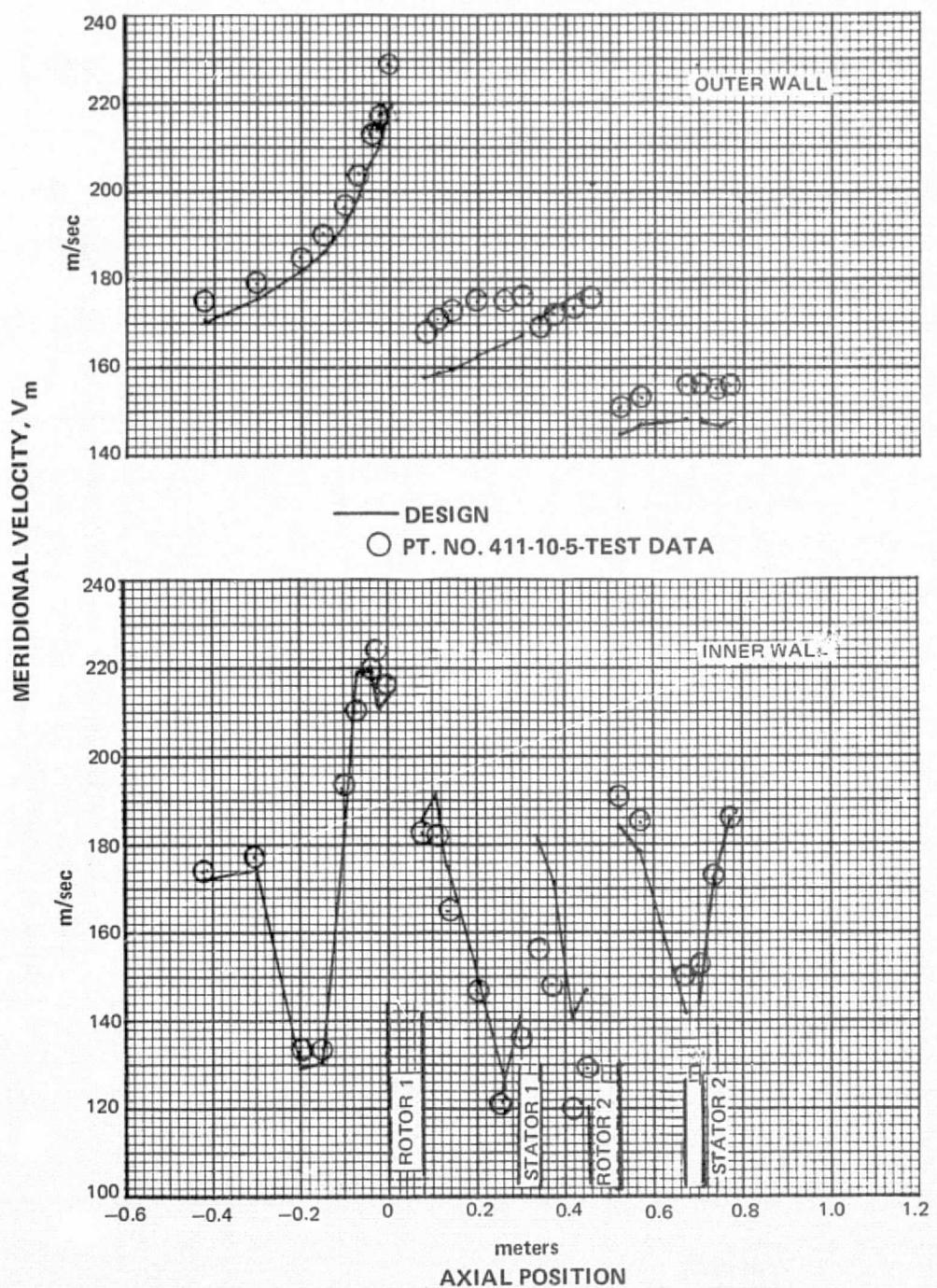


Figure 52 Calculated Meridional Velocity Along Inner and Outer Casing Wall, Baseline Configuration, Uniform Inlet Flow

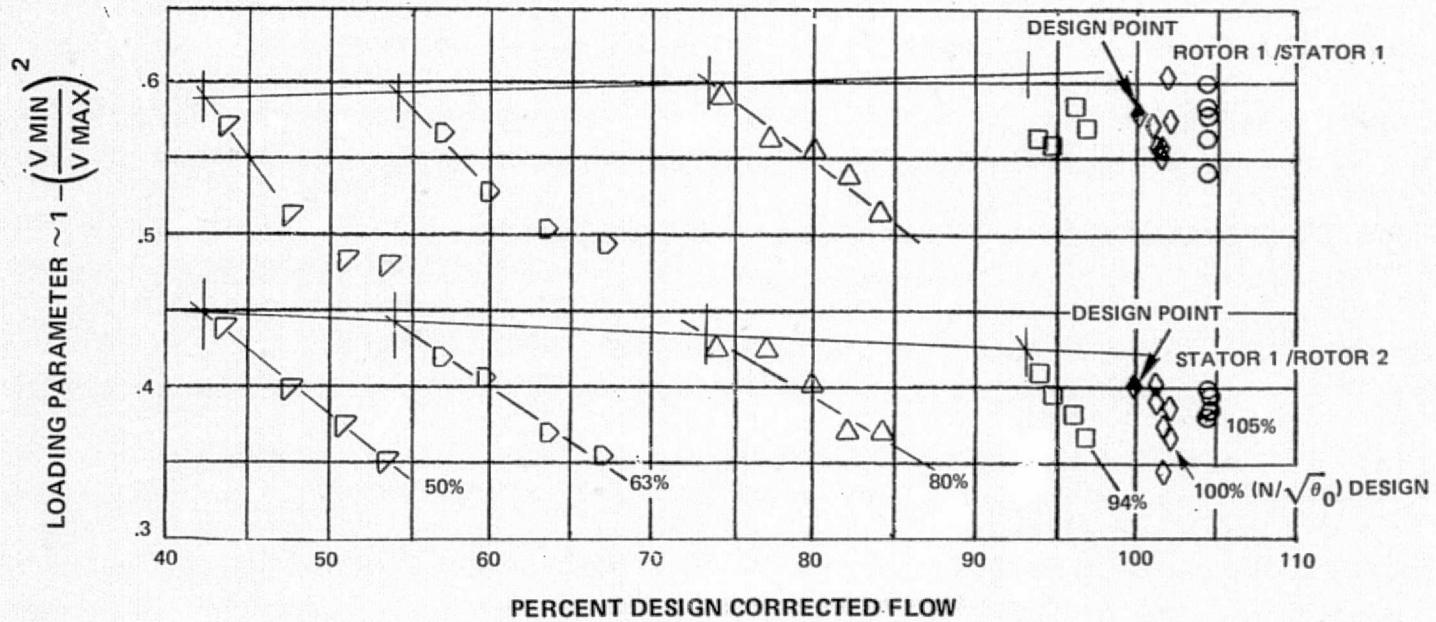


Figure 53 Inner Casing Wall Loading Between the First-Stage Rotor and First-Stage Stator and Between the First-Stage Stator and Second-Stage Rotor, Baseline Configuration, Uniform Inlet Flow

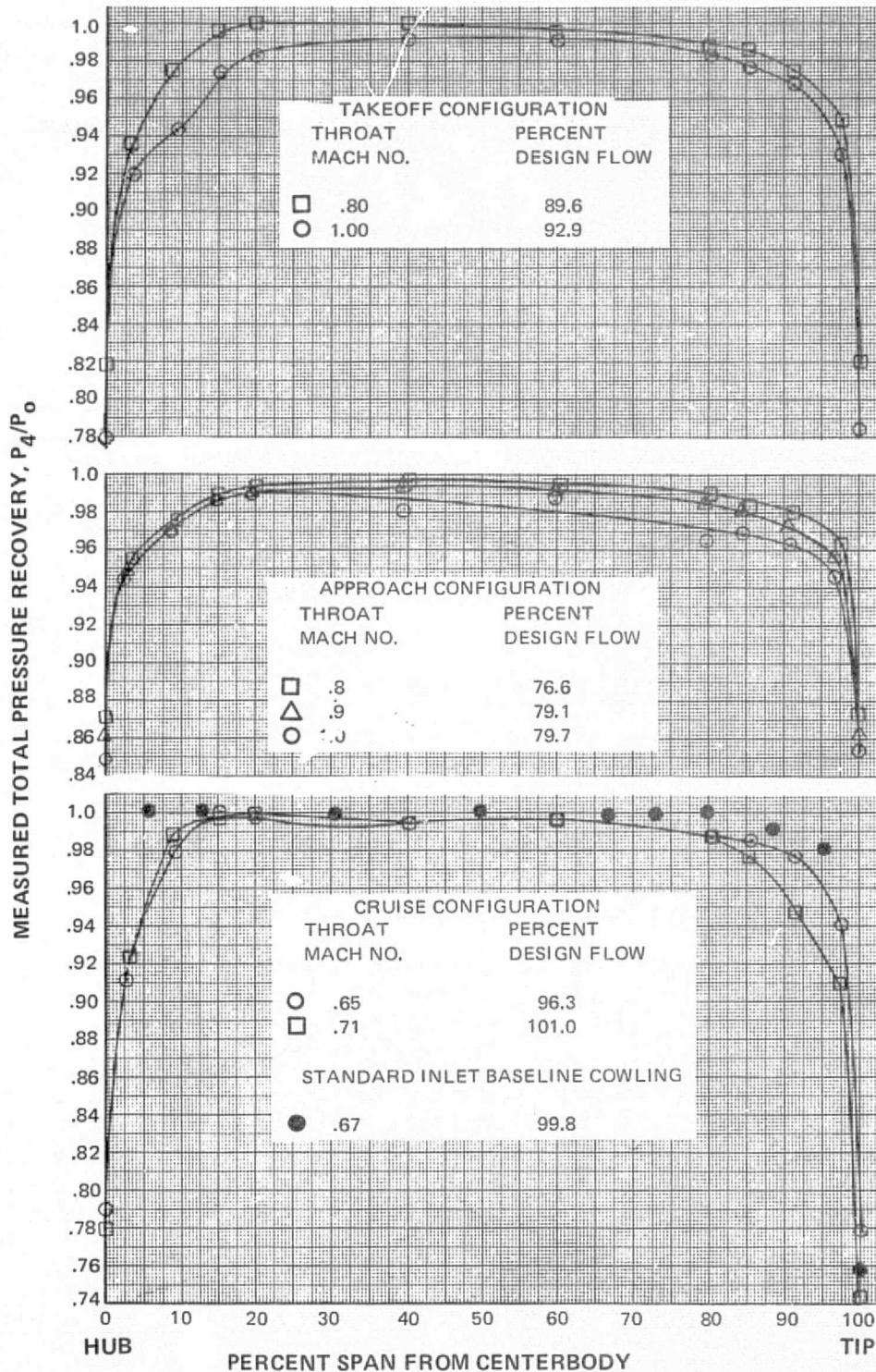


Figure 54 Radial Distributions of Pressure Recoveries of the Baseline and Sonic Configurations

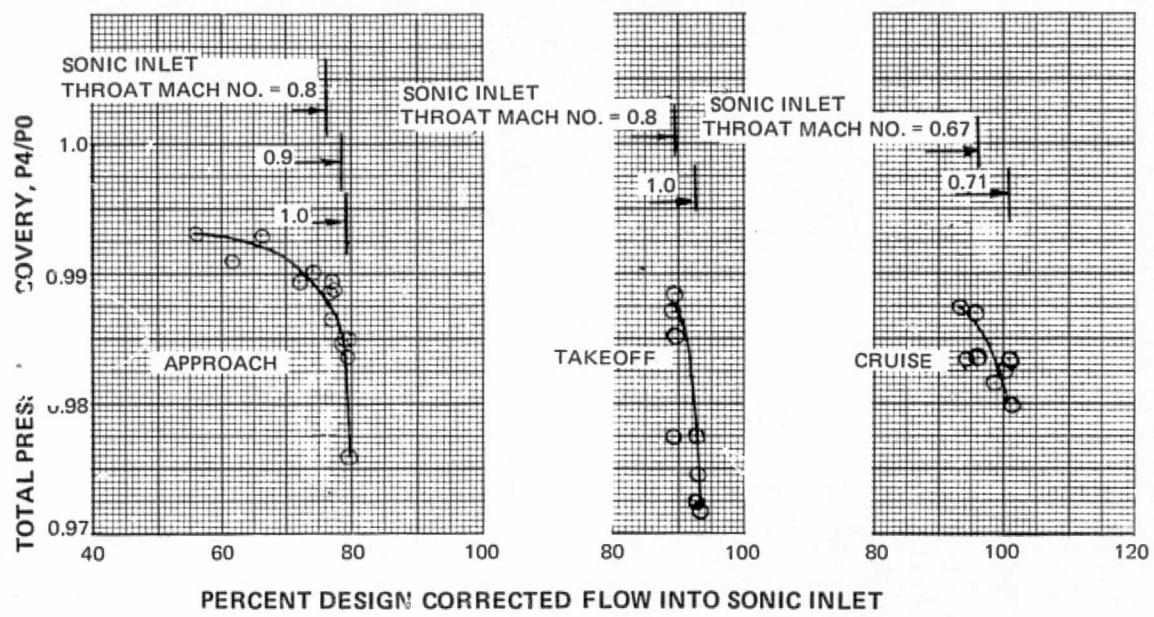


Figure 55 Measured Mass Averaged Recovery of Sonic Inlet

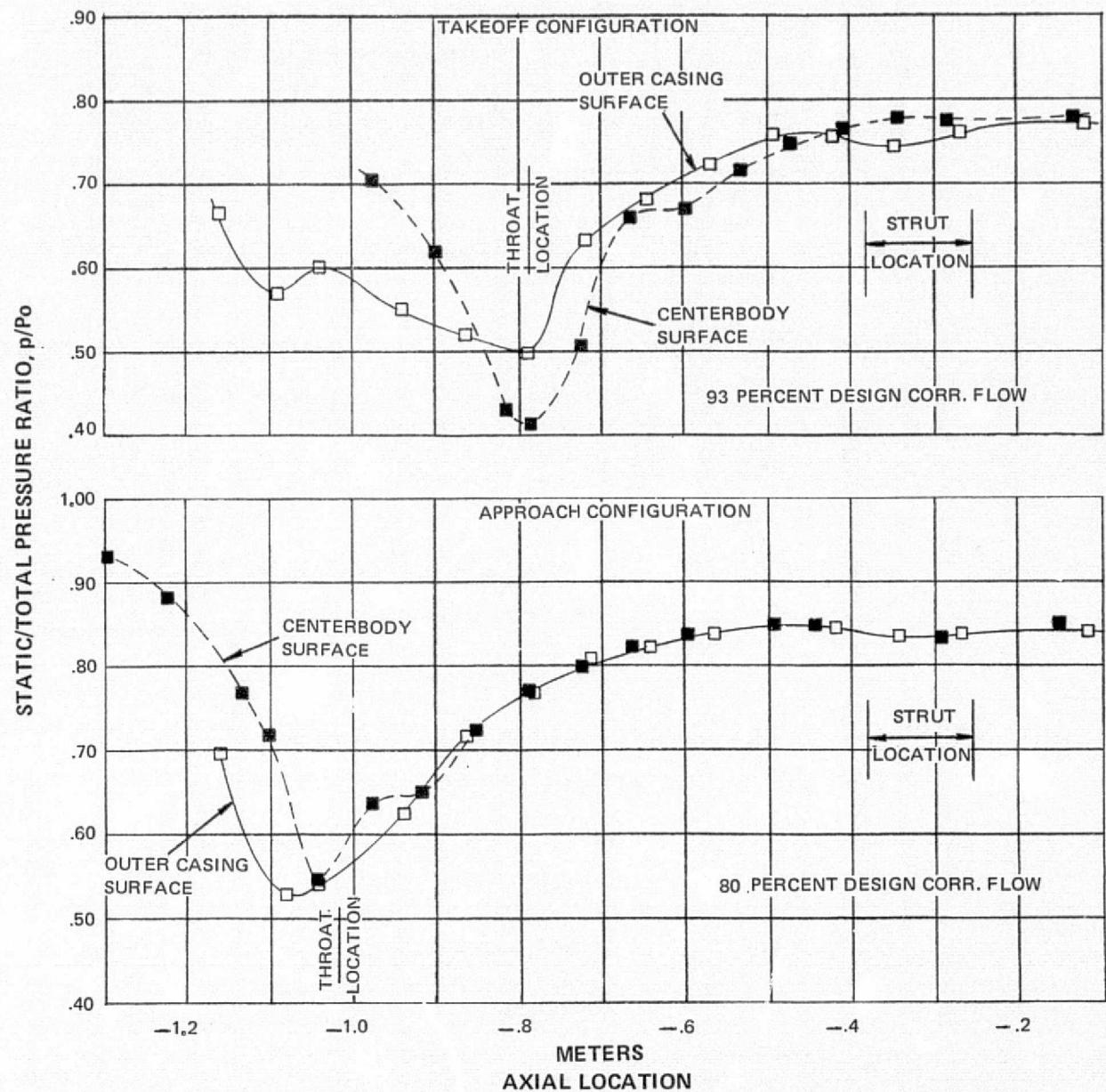


Figure 56 Axial Distribution of Static Pressure on the Sonic Inlet – Throat Mach Number 1.0

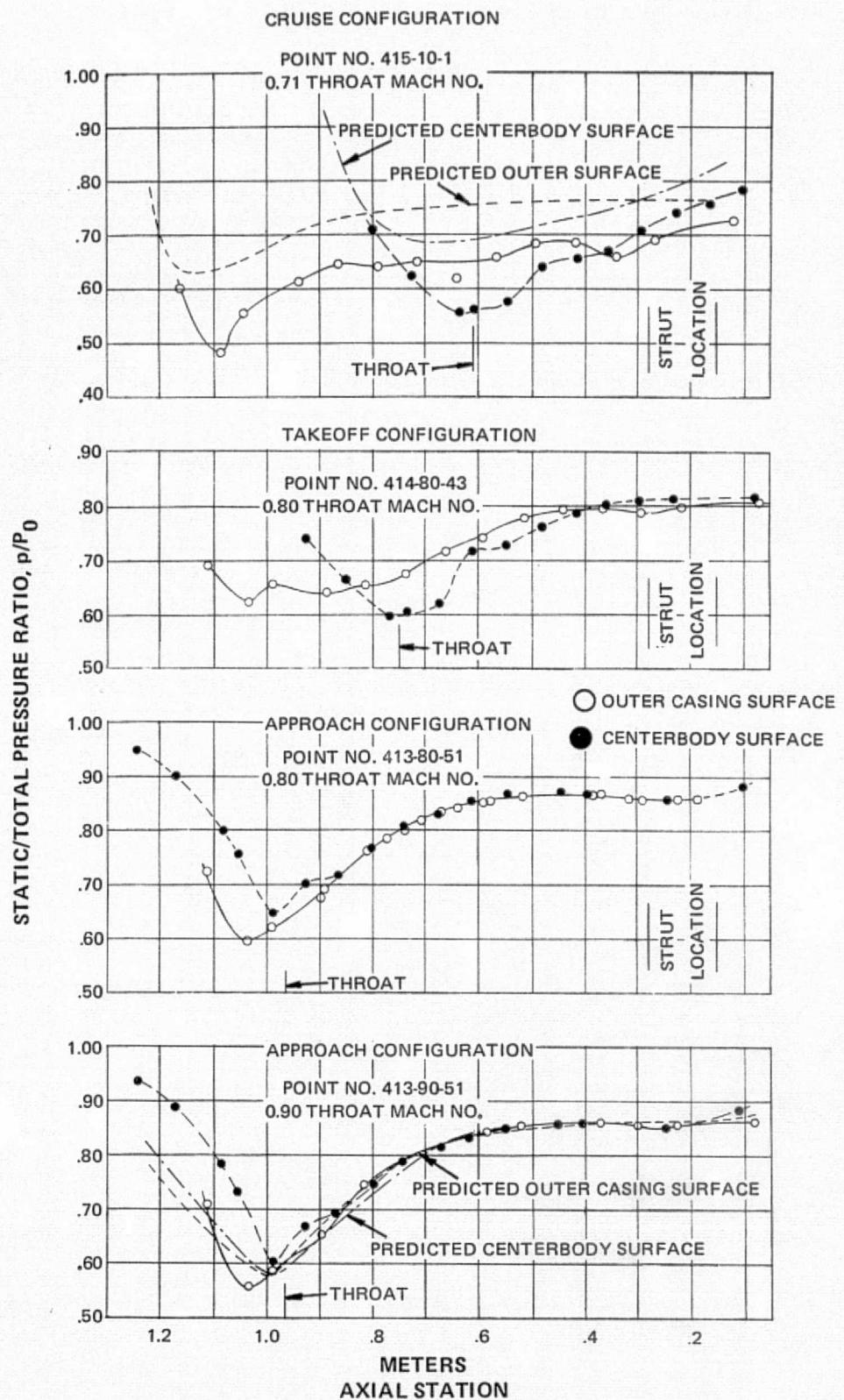


Figure 57 Axial Distribution of Static Pressure on the Inner and Outer Surface of the Sonic Inlet – Throat Mach Number Subsonic

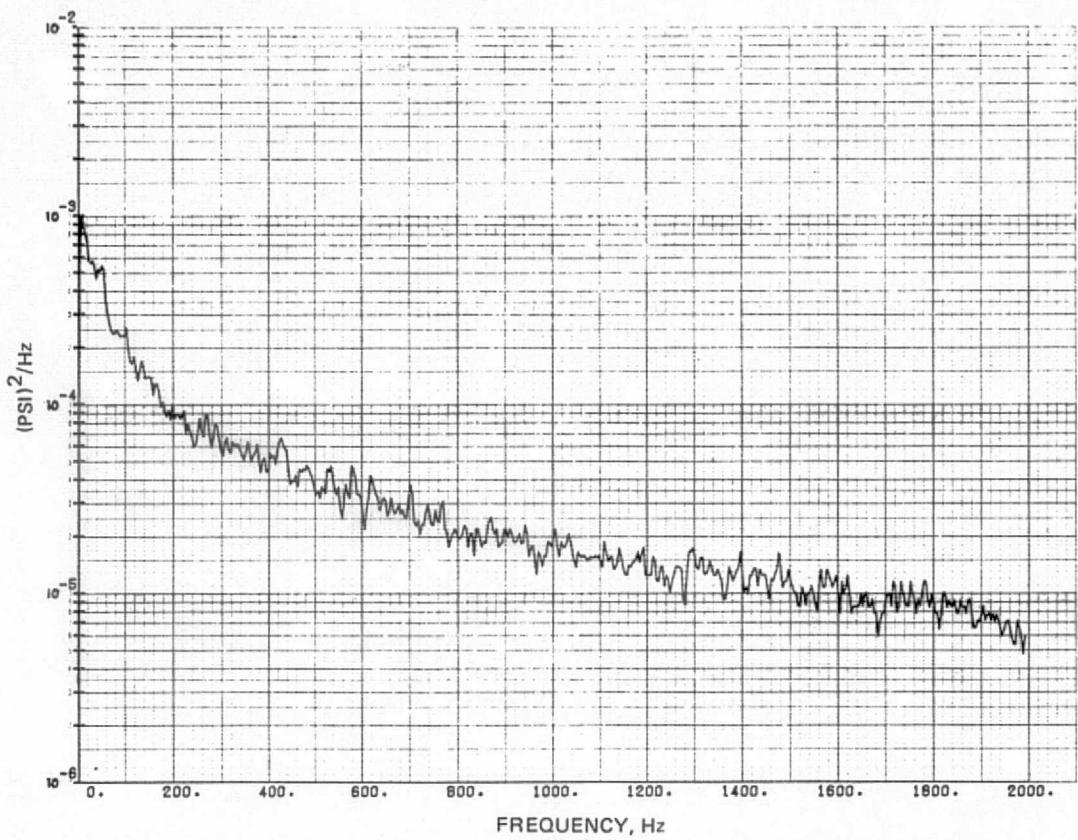


Figure 58 Power Spectral Density Measured Downstream of the Sonic Inlet, Approach Configuration, 0.9 Throat Mach Number, Three Percent Span From Hub

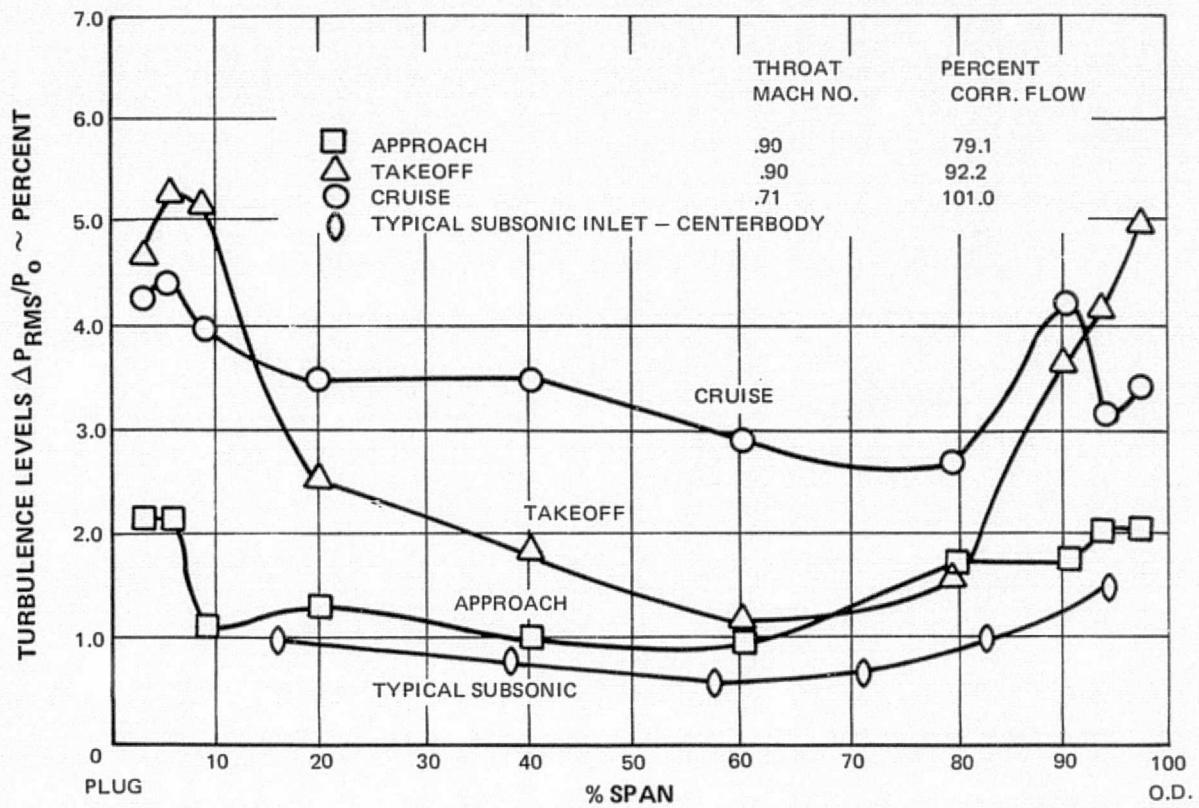


Figure 59 Radial Distribution of Turbulence Levels Measured Downstream of Sonic Inlet

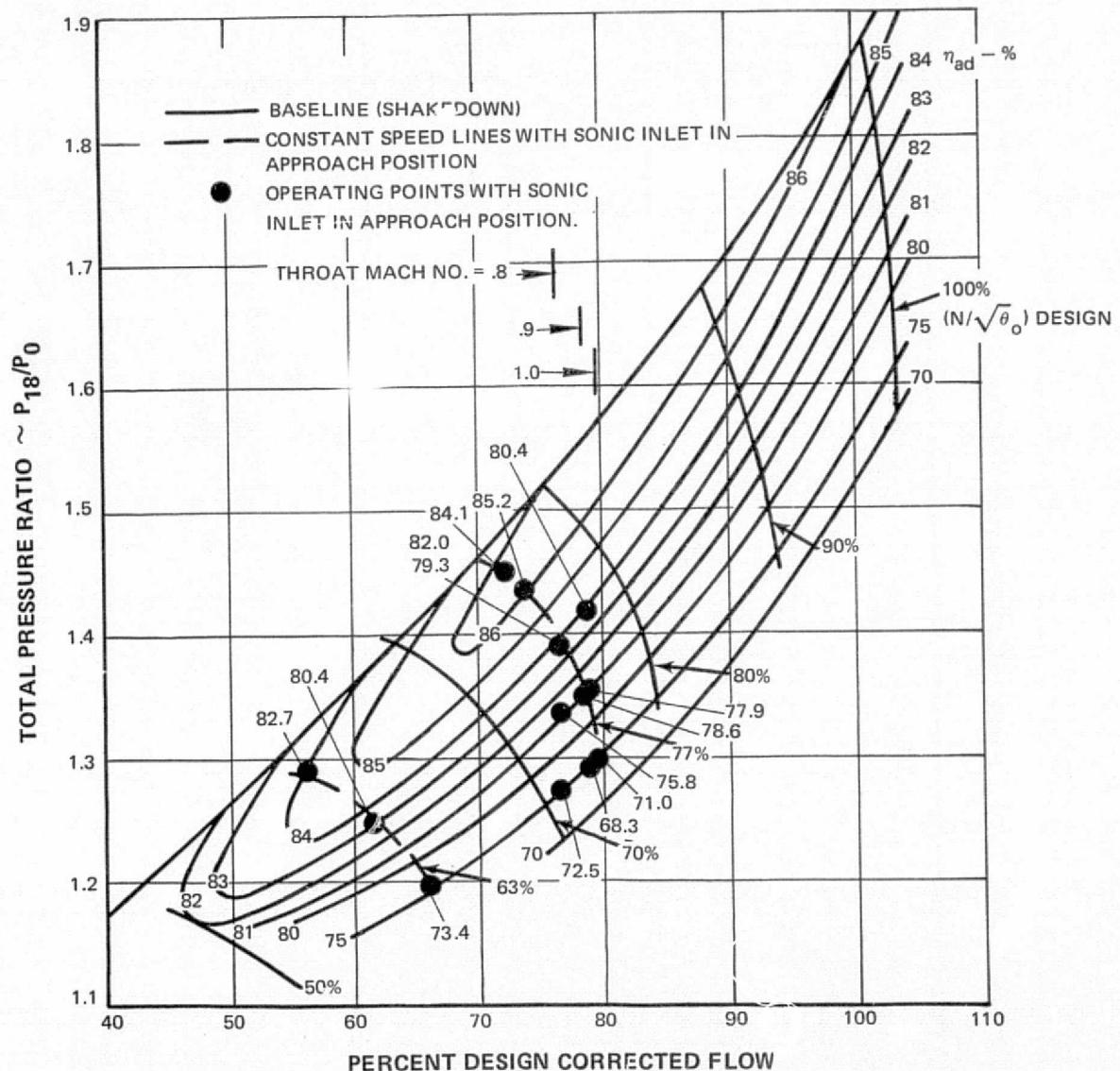


Figure 60a System Performance of Fan and Sonic Inlet Compared to Baseline (Shake-down) – Approach Sonic Inlet Position

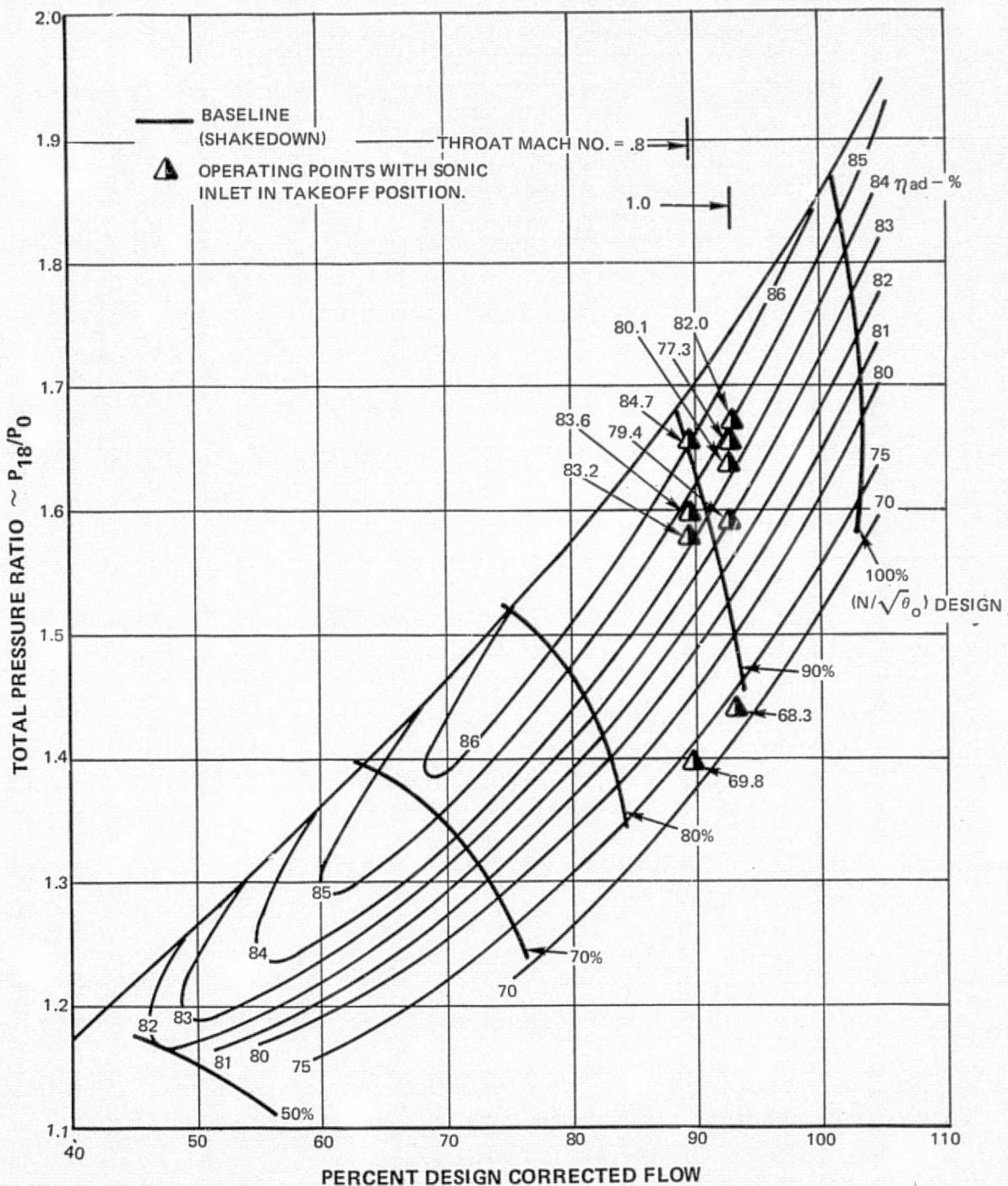


Figure 60b System Performance of Fan and Sonic Inlet Compared to Baseline (Shakedown) – Takeoff Sonic Inlet Position

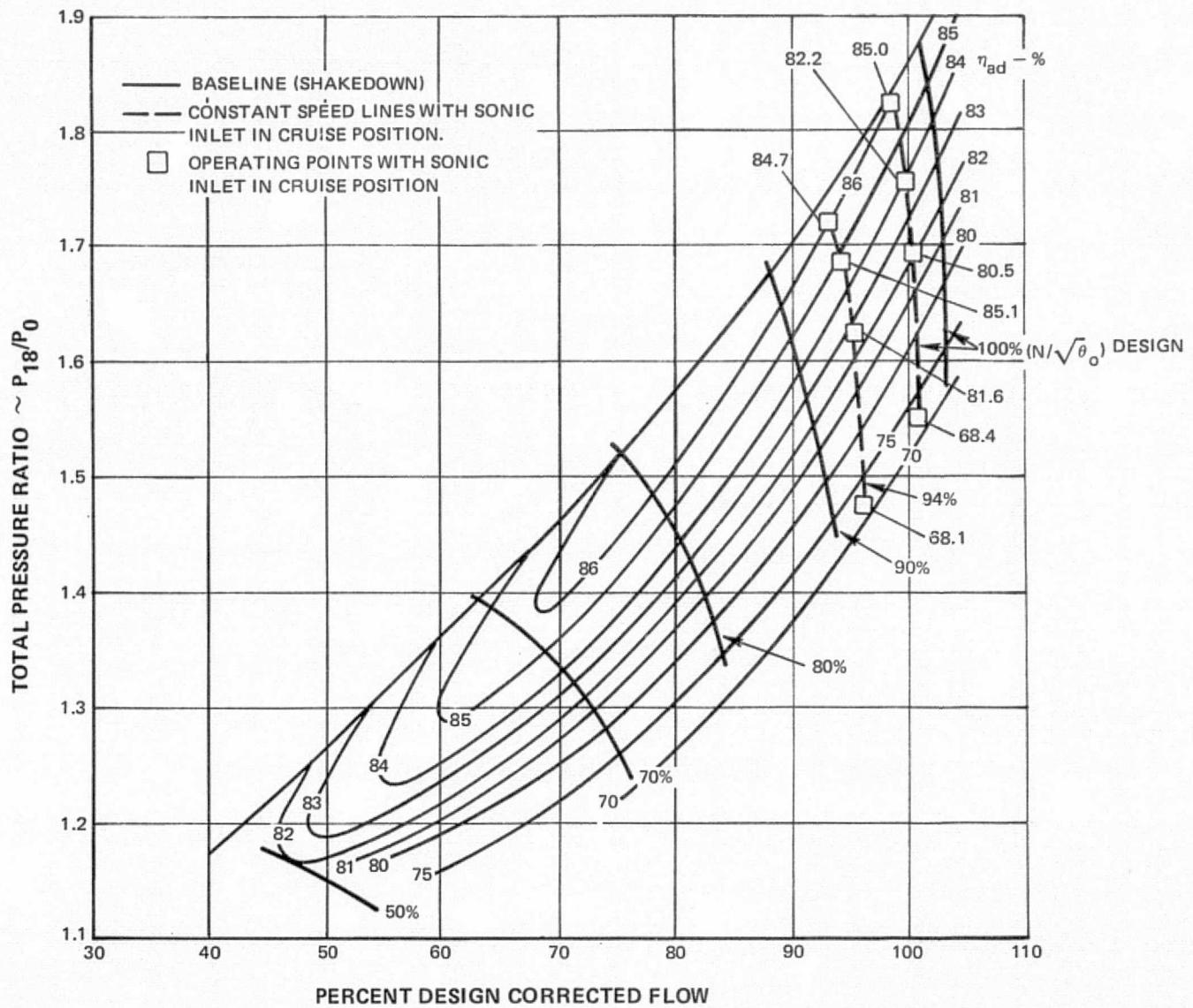


Figure 60c System Performance of Fan and Sonic Inlet Compared to Baseline (Shakedown) – Cruise Sonic Position

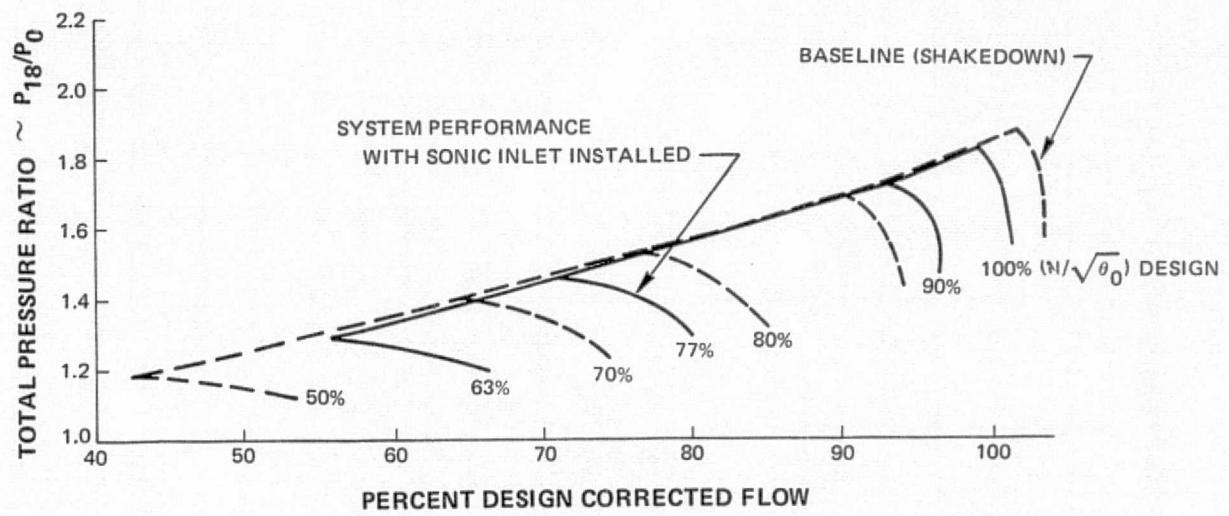


Figure 61 Stall Line Comparison With and Without Sonic Inlet

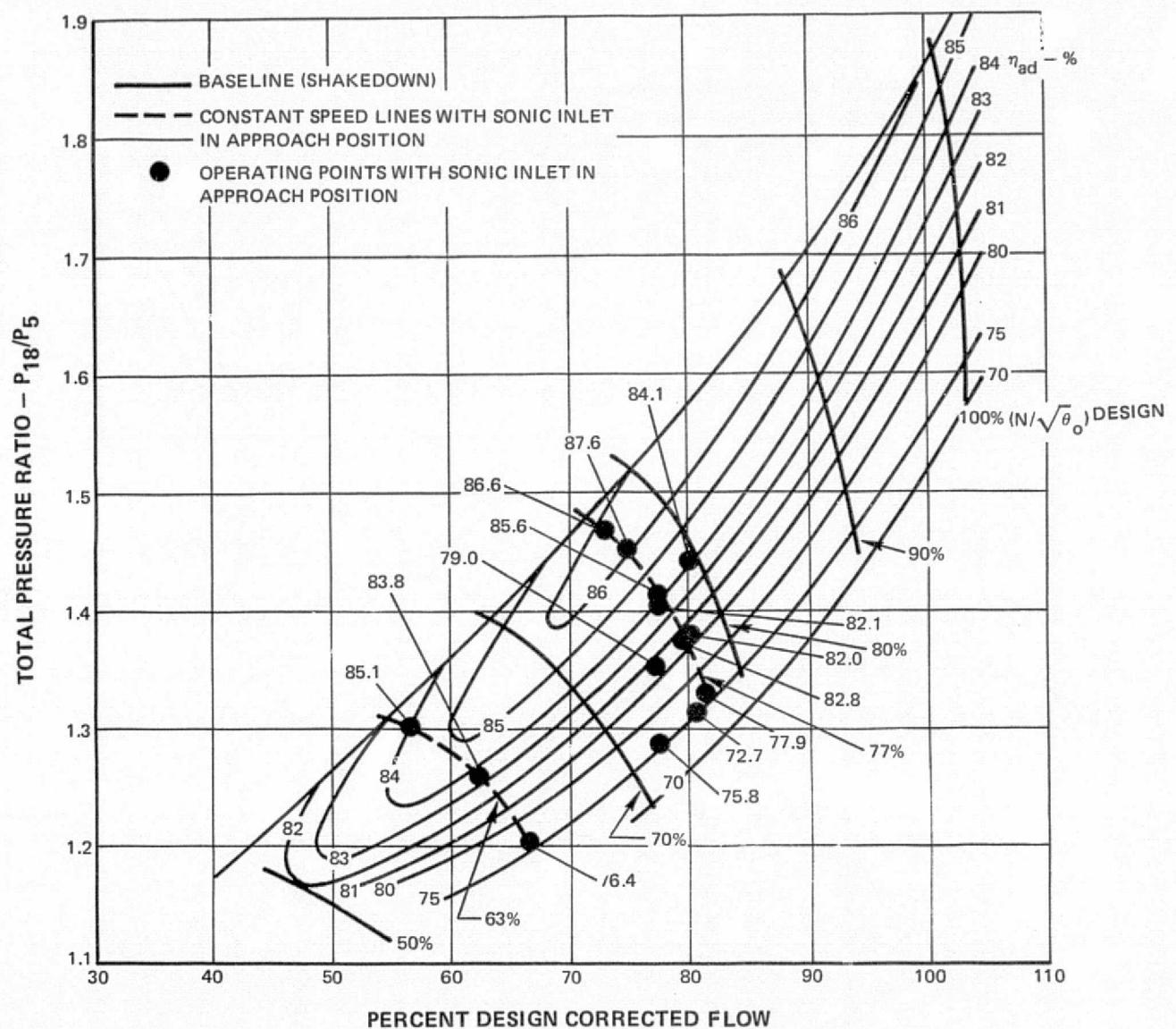


Figure 62a Fan Alone Performance Considering Sonic Inlet as Source of Distortion Compared to Baseline (Shakedown) – Approach Sonic Inlet Position

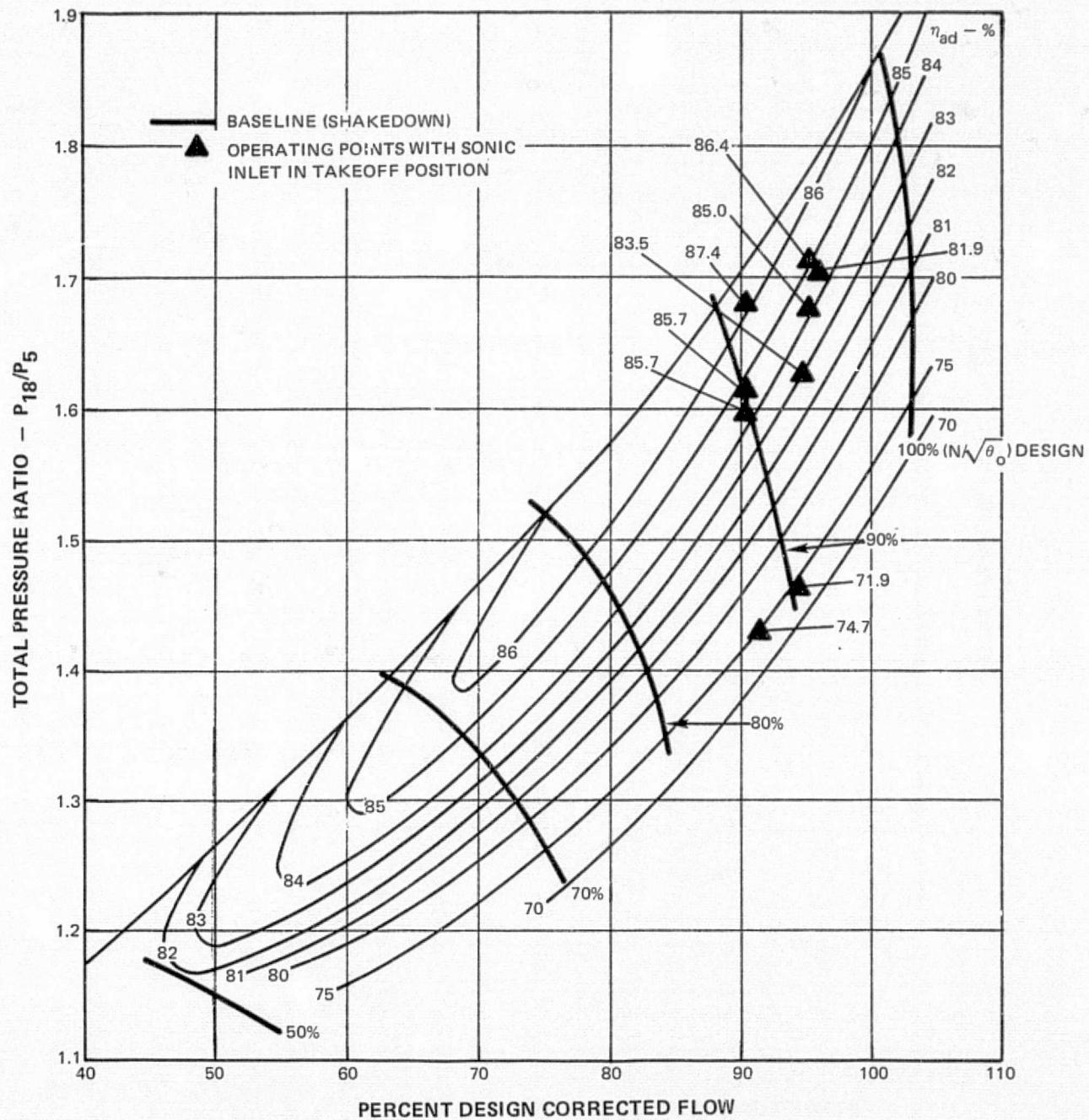


Figure 62b Fan Alone Performance Considering Sonic Inlet as Source of Distortion Compared to Baseline (Shakedown) – Takeoff Sonic Inlet Position

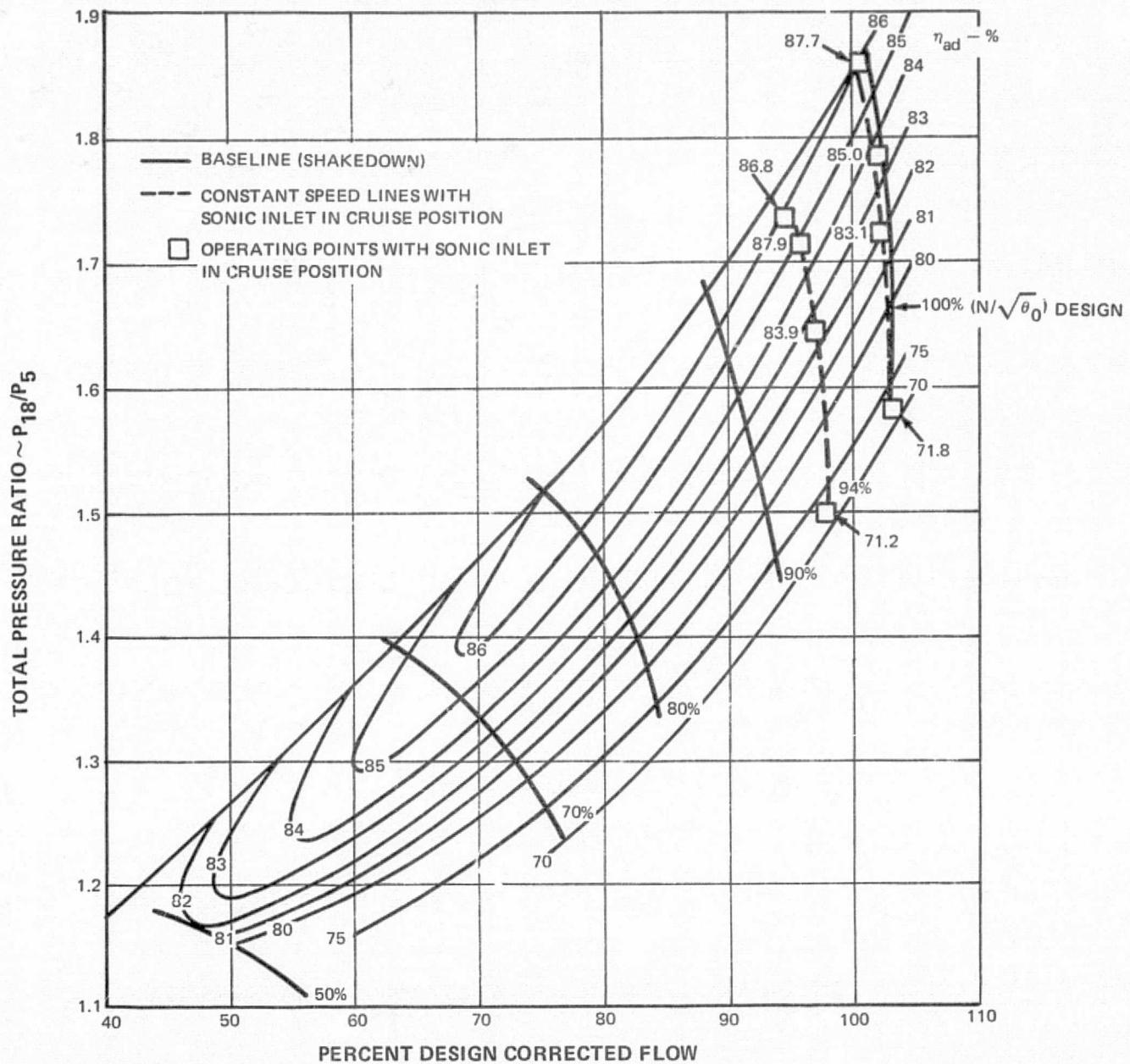


Figure 62c Fan Alone Performance Considering Sonic Inlet as Source of Distortion Compared to Baseline (Shakedown) – Cruise Sonic Inlet Position

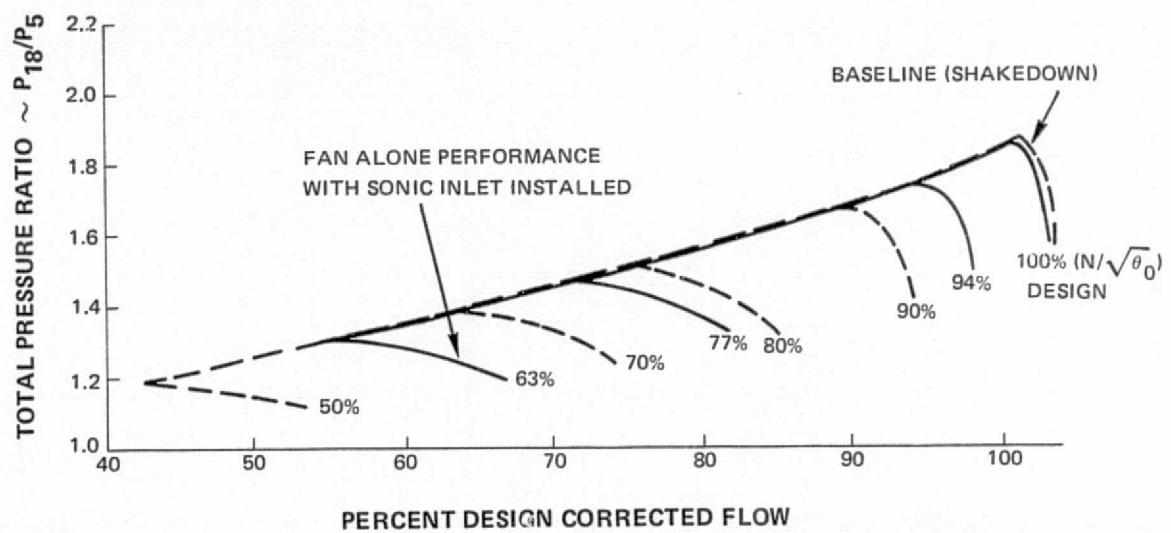


Figure 63 Stall Line of Fan Only, Showing Effect of Sonic Inlet

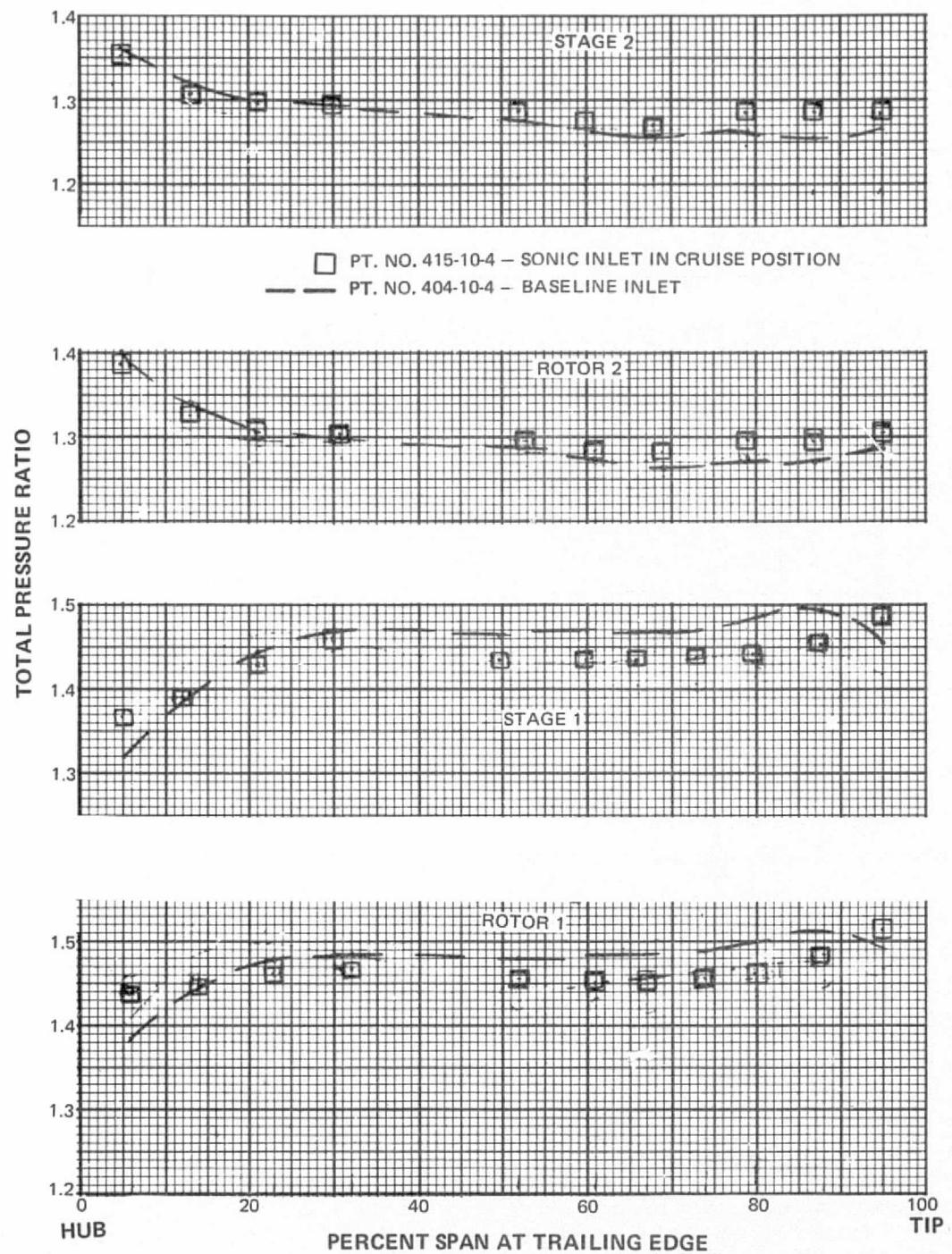


Figure 64 Rotor and Stage Pressure Ratio Versus Span for a Near Design Point With Sonic Inlet in Cruise Position

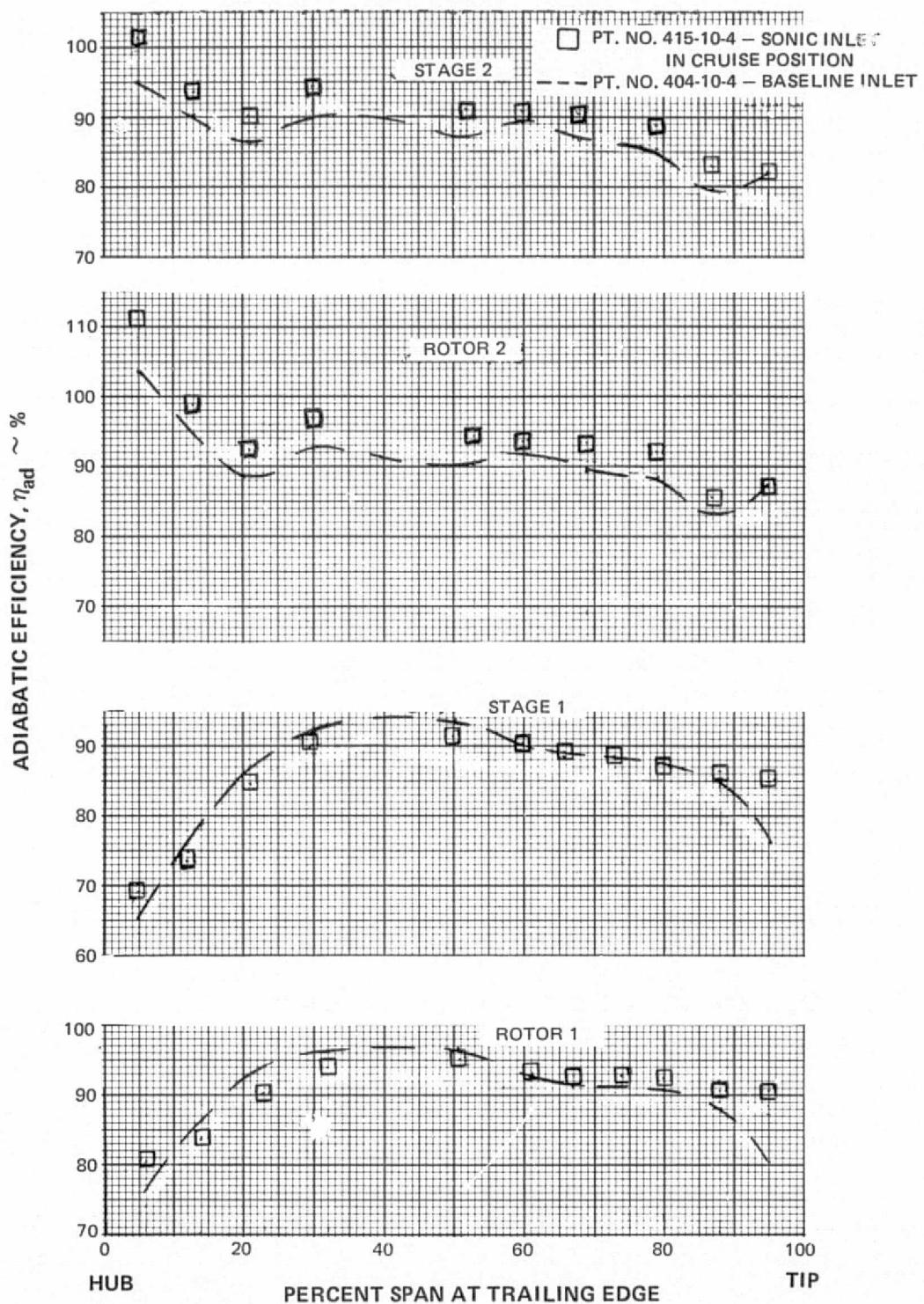


Figure 65 Rotor and Stage Efficiency Versus Span for a Near Design Point With Sonic Inlet in Cruise Position

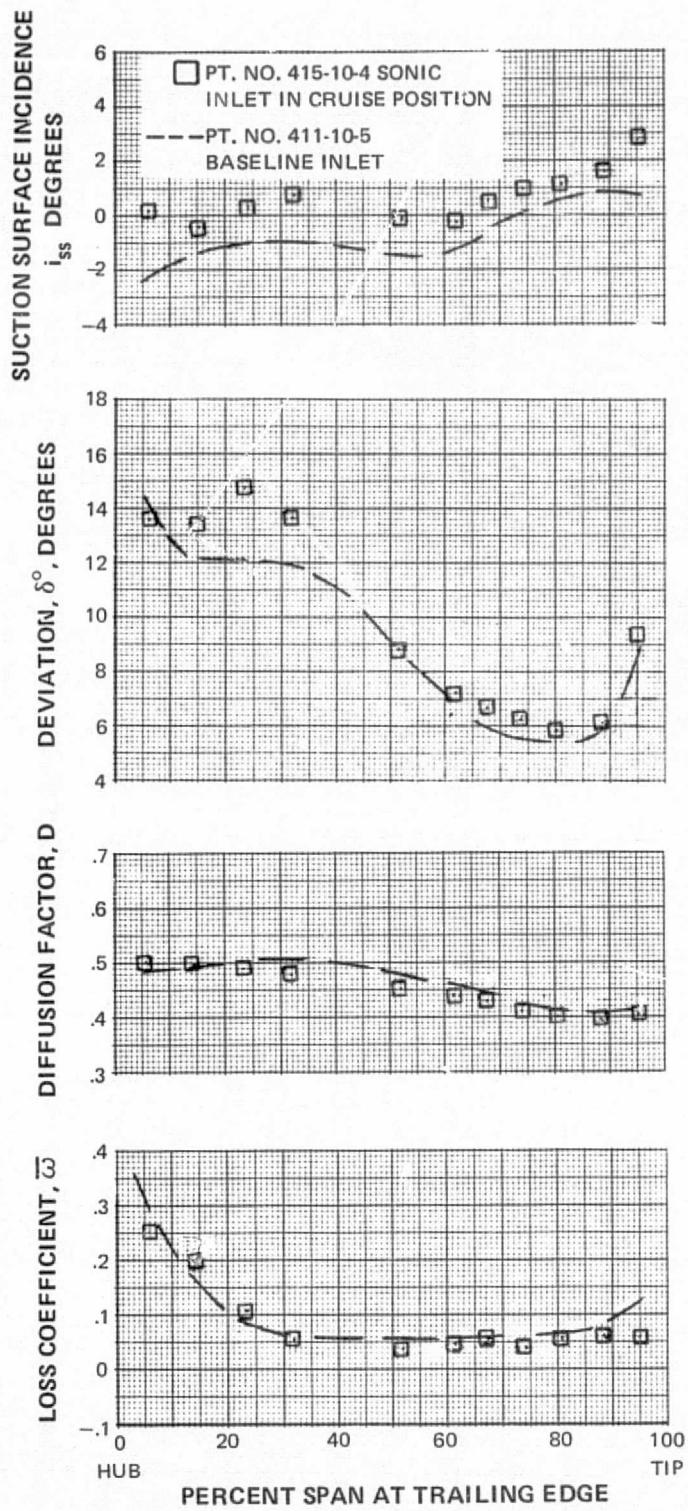


Figure 66 Spanwise Distribution of Loss Coefficient, Diffusion Factor, and Deviation and Incidence Angles For Data Point During Cruise Sonic Inlet Tests – First-Stage Rotor

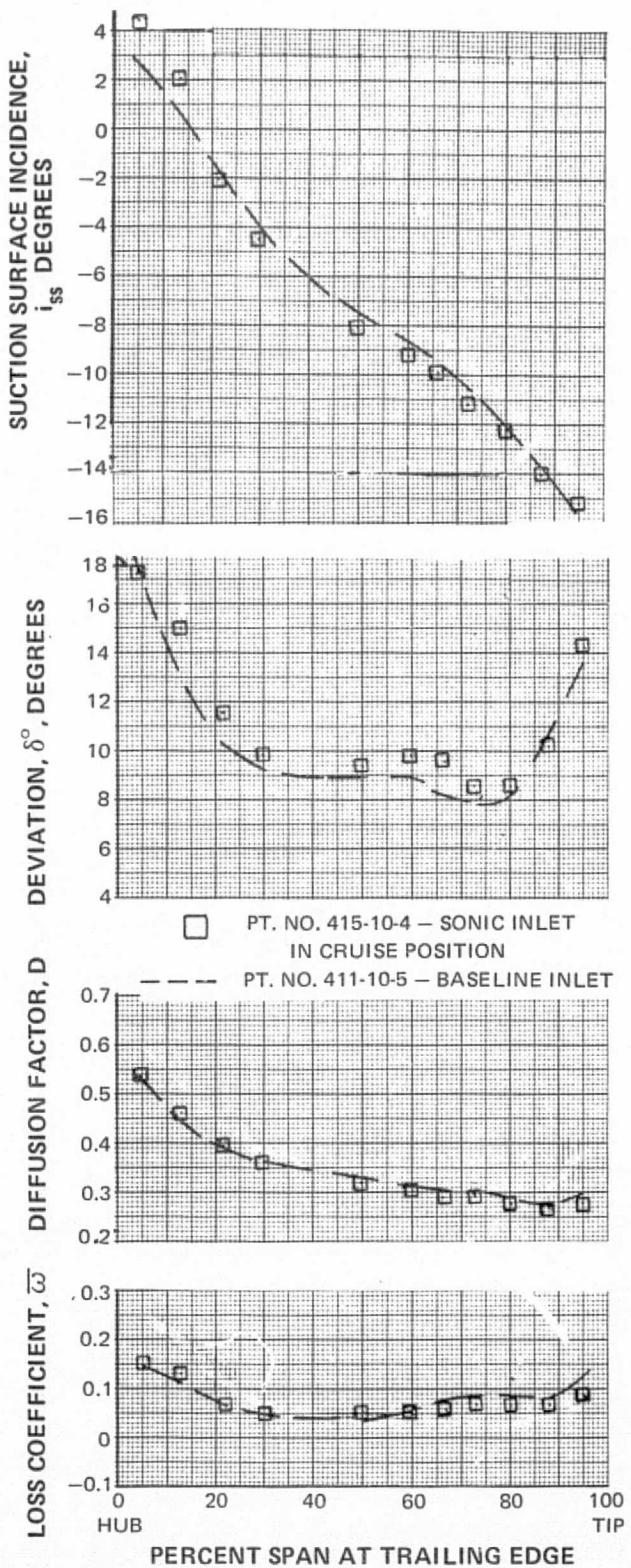


Figure 67 Spanwise Distribution of Loss Coefficient, Diffusion Factor, and Deviation and Incidence Angles for Data Point During Cruise Sonic Inlet Tests – First-Stage Stator

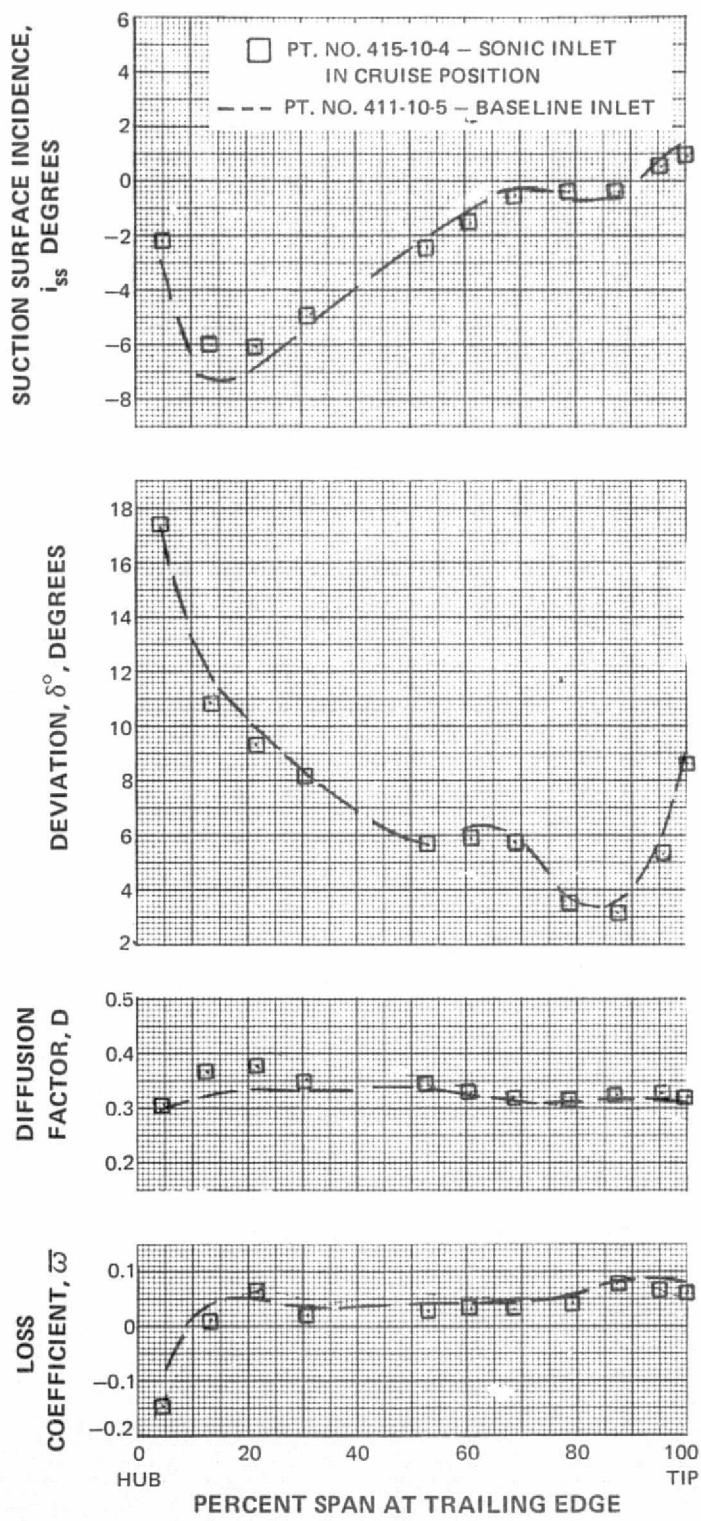


Figure 68 Spanwise Distribution of Loss Coefficient, Diffusion Factor, and Deviation and Incidence Angles for Data Point During Cruise Sonic Inlet Tests – Second-Stage Rotor

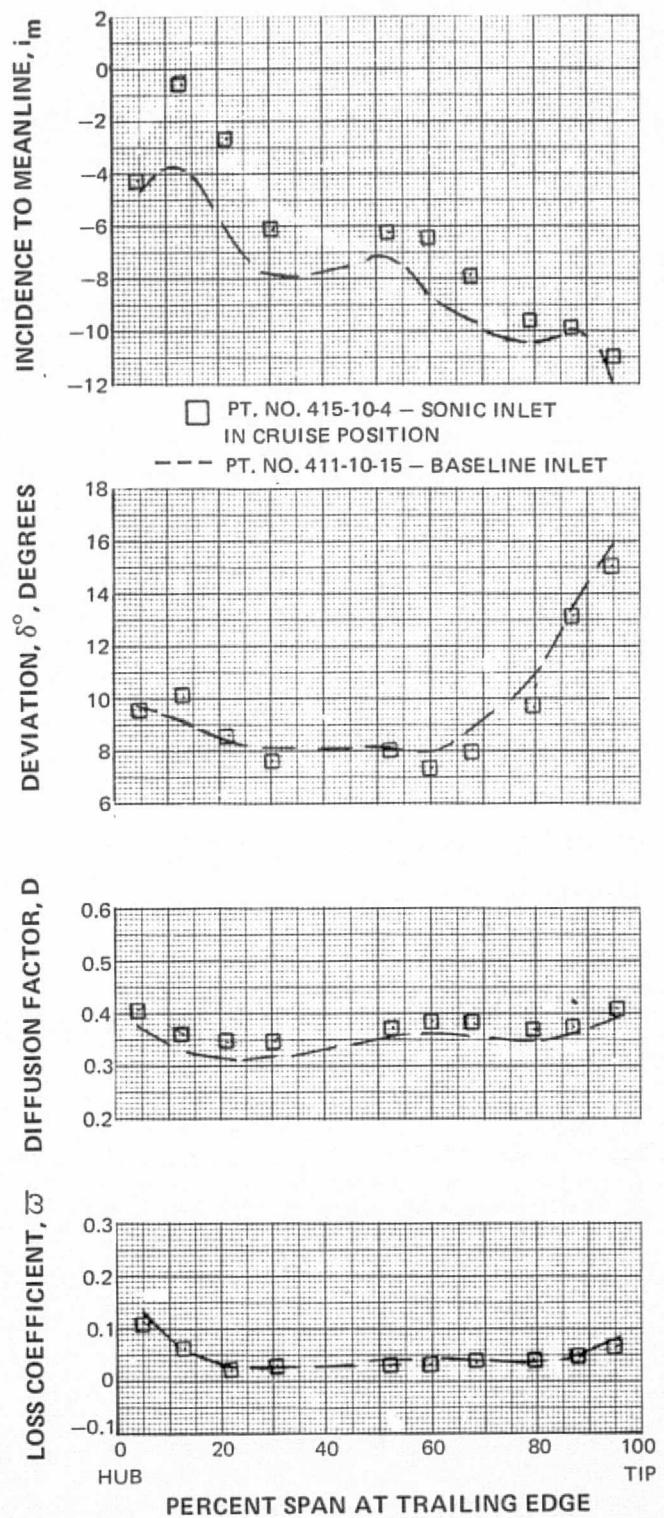


Figure 69 Spanwise Distribution of Loss Coefficient, Diffusion Factor, and Deviation and Incidence Angles for Data Point During Cruise Sonic Inlet Tests – Second-Stage Stator

PT. NO. 415-10-4 – SONIC INLET IN CRUISE POSITION
 — PT. NO. 404-10-4 – BASELINE INLET
 NOTE: UNSHADE SYMBOLS REPRESENT
 PRESSURE ALONG STREAMLINE FROM
 FAN INLET TO EXIT
 SHADED SYMBOLS REPRESENT THE
 LOCAL FAN EXIT PRESSURE DIVIDED
 BY THE AVERAGE FAN INLET PRESSURE

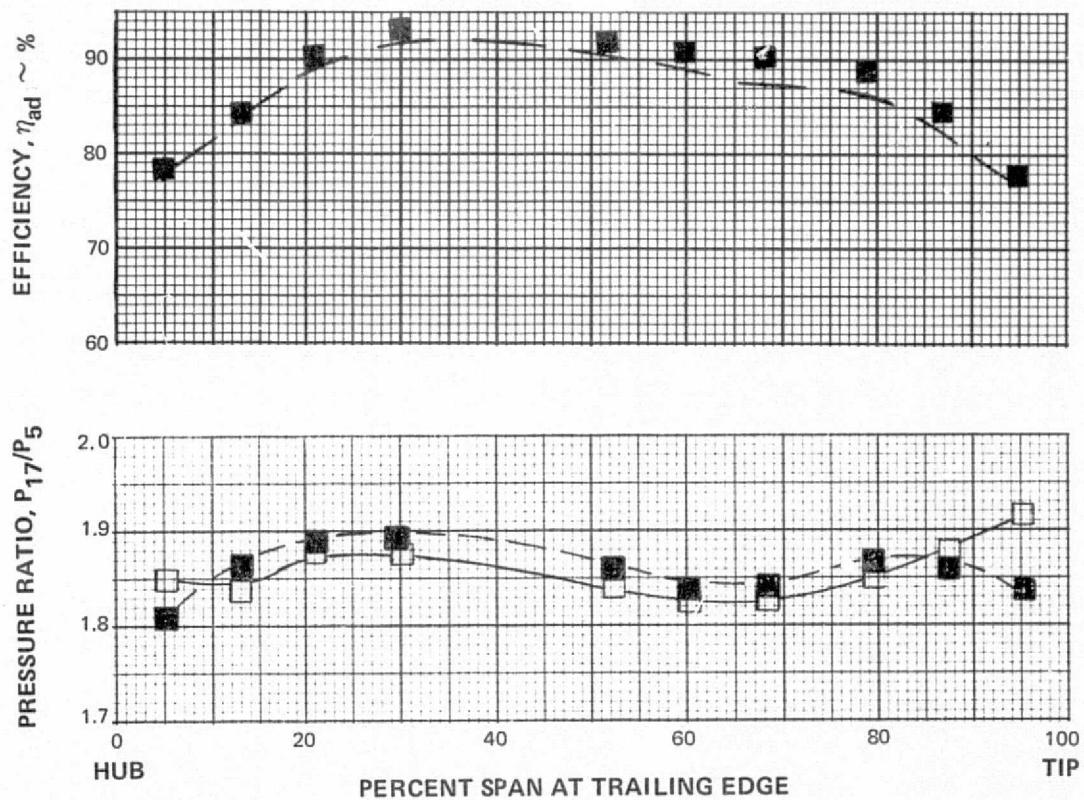


Figure 70 Fan Overall Pressure Ratio and Adiabatic Efficiency for Near Design Point With Sonic Inlet in Cruise Position

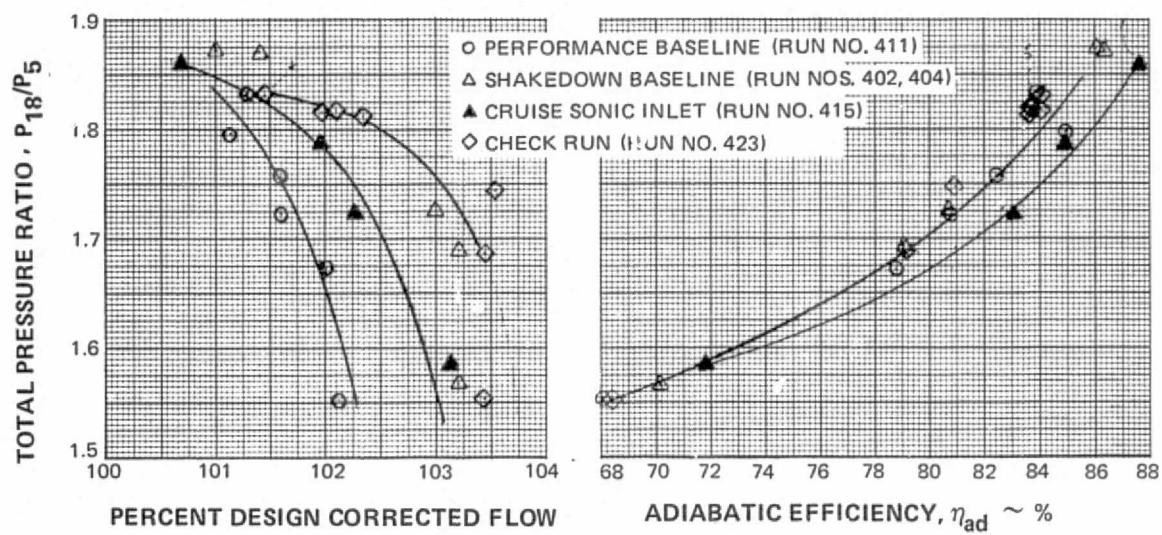


Figure 71 Overall Performance of Fan Alone at Design Speed Comparing Tests of Check Run, Shakedown, Performance, and Cruise Sonic Inlet

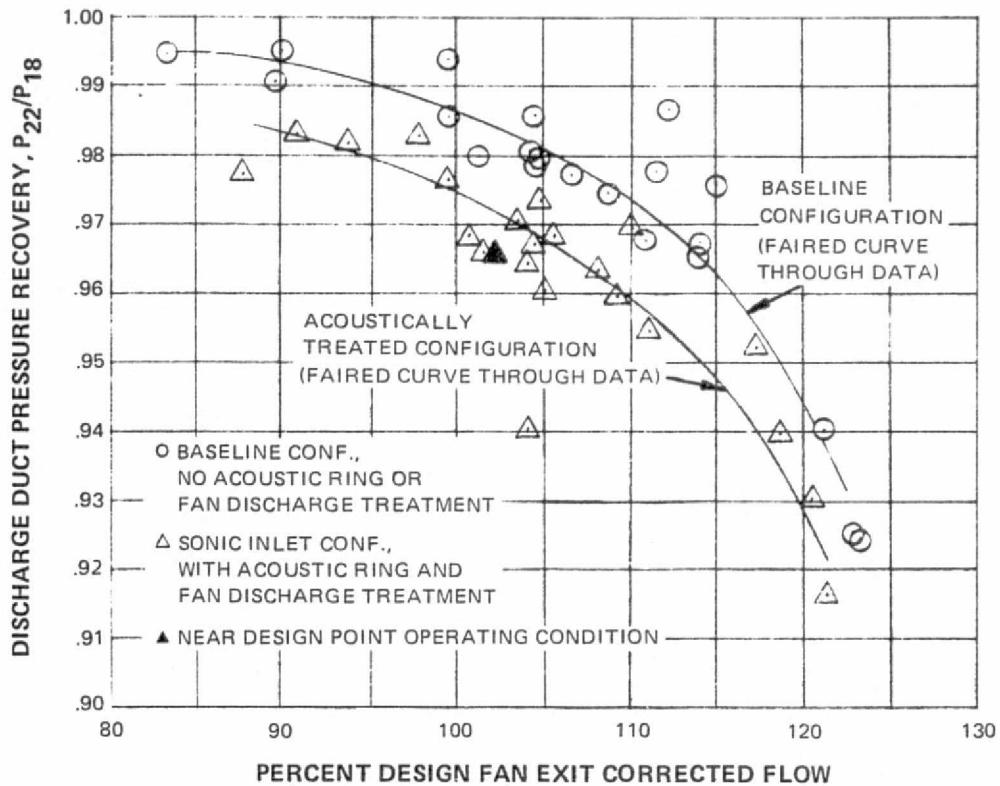


Figure 72 Fan Discharge Duct Recovery With and Without Acoustic Ring and Treatment

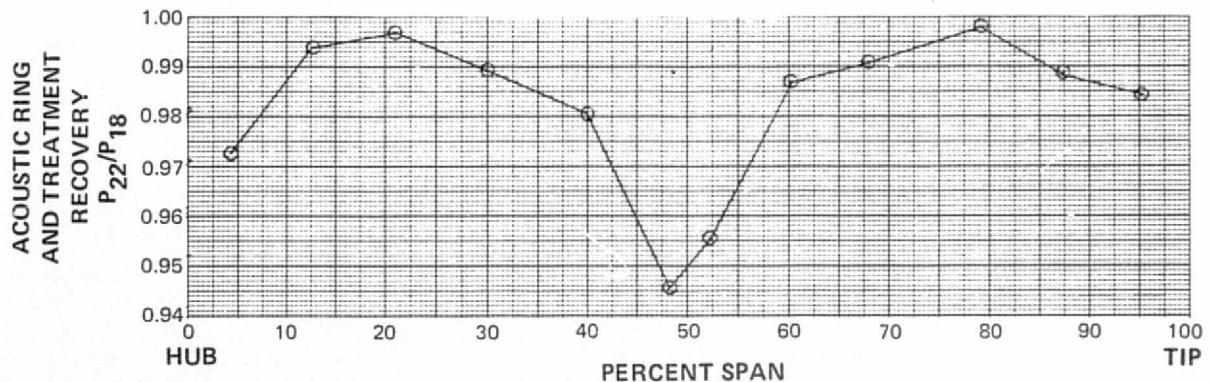


Figure 73 Spanwise Recovery of Fan Discharge Duct, Showing Effect of Acoustic Ring and Treatment